A TWO ELEMENT LAMINAR FLOW AIRFOIL OPTIMIZED FOR CRUISE

A Thesis

by

GREGORY GLEN STEEN

Submitted to the Office of Graduate Studies of
Texas A&M University
in partial fulfillment of the requirements for the degree of

MASTER OF SCIENCE

August 1994

Major Subject: Aerospace Engineering

A TWO ELEMENT LAMINAR FLOW AIRFOIL OPTIMIZED FOR CRUISE

A Thesis

by

GREGORY GLEN STEEN

Submitted to Texas A&M University
in partial fulfillment of the requirements
for the degree of

MASTER OF SCIENCE

Approved as to style and content by:

Leland A. Carlson
(Co-Chair of Committee)

Kenneth D. Korkan
(Co-Chair of Committee)

Gerald L. Morrison
(Member)

Walter E. Haisler
(Head of Department)

August 1994

Major Subject: Aerospace Engineering

ABSTRACT

A Two Element Laminar Flow Airfoil Optimized for Cruise. (August 1994)

Gregory Glen Steen, B.S., Texas A&M University

Co-Chairs of Advisory Committee: Dr. Leland A. Carlson
Dr. Kenneth D. Korkan

Numerical and experimental results are presented for a new two element, fixed geometry natural laminar flow airfoil optimized for cruise Reynolds numbers on the order of three million. The airfoil design consists of a primary element and an independent secondary element with a primary to secondary chord ratio of three to one. The airfoil was designed to improve the cruise lift-to-drag ratio while maintaining an appropriate landing capability when compared to conventional airfoils. The airfoil was numerically developed utilizing the NASA Langley Multi-Component Airfoil Analysis computer code running on a personal computer. Numerical results show a nearly 11.75% decrease in overall wing drag with no increase in stall speed at sailplane cruise conditions when compared to a wing based on an efficient single element airfoil.

Section surface pressure, wake survey, transition location, and flow visualization results were obtained in the Texas A&M University Low Speed Wind Tunnel. Comparisons between the numerical and experimental data, the effects of the relative position and angle of the two elements, and Reynolds number variations from $8x10^5$ to $3x10^6$ for the optimum geometry case are presented.

ACKNOWLEDGMENTS

This material is based upon work supported by the NASA-Langley Research Center under Grant No. NAG-1-1522. Sincere thanks are extended to Dr. Michael F. Card at the NASA Langley Research Center for supporting the effort. Acknowledgment is also due to Mr. Harry L. Morgan, Jr. of NASA Langley for providing a copy of the MCARFA computer code and Mr. Bill Cleary of Ciba-Geigy Corporation for donating the Ren Shape used in the wind tunnel model construction.

A great debt of thanks is due to the members of my Advisory Committee Dr. Leland Carlson, Dr. Kenneth Korkan, and Dr. Gerald Morrison. I thank them all for supporting me through the extended period of time required for me to finish this thesis part time and for giving me three outstanding examples of professional success and personal character.

I also wish to thank the staff of the Texas A&M University Low Speed Wind Tunnel for their support and friendship through the completion of my education and the start of my professional career. I would especially acknowledge Mr. Oran Nicks, who served not only as my boss, but also as a trusted advisor and friend. I feel extremely fortunate to have had the opportunity to work with and learn from such a truly exceptional man.

Finally, I would like to thank my family. I am eternally indebted to my parents Harvey and Ila Steen for teaching me everything really important in life and supporting me in anything I ever chose to do. I would like to close by thanking my wife Kathy and son Kyle whom are my reason for life itself. They have helped, pushed, supported, and loved me more than they will ever know.

TABLE OF CONTENTS

Page

LIST OF FIGURES

Page

Page

Page

Page

Page

Page

Page

Page

LIST OF TABLES

Page

NOMENCLATURE

Symbol	Title
C_p	Pressure Coefficient
c	Total Airfoil Chord (defined as $c_1 + c_2$ for two element airfoils)
c/4	Quarter Chord Location
c_1	Primary Element Airfoil Chord
c_2	Secondary Element Airfoil Chord
c_A	Total Airfoil Axial Force Coefficient
c_a	Airfoil Axial Force Coefficient
c_d	Section Drag Coefficient
c_l	Section Lift Coefficient
cm	Centimeter
c_m	Section Moment Coefficient About the Quarter Chord Location
c_N	Total Airfoil Normal Force Coefficient
c_n	Airfoil Normal Force Coefficient
D	Drag Force
kVA	Kilo-Volt Amp
L	Lift Force
L/D	Lift to Drag Ratio
LSWT	Low Speed Wind Tunnel
m	Meter
mm	Millimeter
NACA	National Advisory Committee for Aeronautics
NASA	National Aeronautics and Space Administration

Symbol	Title
Pa	Pascal
p	Local Pressure
p_s	Freestream Static Pressure
p_t	Freestream Total Pressure
q	Dynamic Pressure
Re	Reynolds Number
$Re_{\delta 2}$	Reynolds Number Based on Boundary Layer Momentum Thickness
RPM	Revolutions per Minute
T	Longitudinal Flow Turbulence Intensity
TAMU	Texas A&M University
U_∞	Longitudinal Mean Velocity Component
u'	Longitudinal Fluctuating Velocity Component
x	Longitudinal Airfoil Coordinate
y, z	Vertical Airfoil Coordinate
α	Angle of Attack
α_0	Zero Lift Angle of Attack
δ, δ_2	Relative Angle of Secondary Element
Γ, γ	Circulation
μ	Viscosity
ρ	Density
ψ	Stream Function

INTRODUCTION

Since a wing is the primary source of lift and a major contributor to drag, it is of prime interest in any major attempt to increase aerodynamic performance. A good wing design will provide lift in the most efficient way possible. An important goal in the design of a wing is the selection of an airfoil with a high lift-to-drag ratio, as "the lift-to-drag ratio is a measure of the aerodynamic efficiency..."[1]

The use of flap systems on airfoils can greatly increase the maximum lift coefficient of the system. The primary use of flaps has been to increase the maximum lift for take-off and landing while maintaining a reasonably small wing for cruise conditions. Many low Reynolds number aircraft, including the new World Class glider[2], have been specifically designed without moveable flap systems. Since they must cruise, take-off, and land with the same wing, design trade-offs must be considered in the selection of an airfoil configuration.

The current effort reports on the viability of a two element fixed geometry airfoil designed to provide low drag for cruise conditions and high lift for landing. The airfoil under study consists of two distinct elements arranged similar to wings having external airfoil flaps (Fig. 1). Various combinations of profile shape, element location, and relative angle have been explored. The intent of this research has been to develop a two element airfoil with an L/D greater than that for a comparable single element airfoil at cruise lift coefficients, while providing high lift coefficients for the landing configuration. The final configuration must provide the same stall and cruise speed as comparable fixed geometry single element airfoils.

Journal Model is the *AIAA Journal of Aircraft*.

The study has been conducted using widely available numerical tools for multi component airfoil analysis, very fast and accurate numerical tools for single element airfoil analysis, and the Texas A&M University Low Speed Wind Tunnel for experimental verification of the final airfoil design.

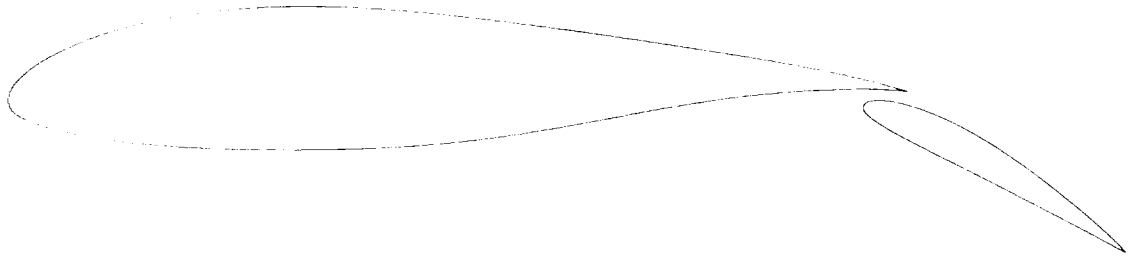

Fig. 1 Concept Airfoil

PROBLEM DESCRIPTION

The original idea for the current study came from experimental data acquired in the early days of airfoil research. National Advisory Committee for Aeronautics (NACA) researchers embarked on a systematic study of various airfoil shapes in the early 1940's. The culmination of this work is the classic NACA Report No. 824 titled "Summary of Airfoil Data."[3,4] Examination of some slotted flap data presented in the NACA report yields an interesting result. Small flap deflections often result in very little increase in drag coefficient but a significant increase in lift coefficient. For example, experimental data from a NACA 63,4-420 airfoil with a 25% chord slotted flap deflected 25° show a nearly 40% increase in cruise L/D over the same airfoil with 0° flap deflection when adjusted for the different maximum lift coefficients. Based on the NACA experimental data, it should be possible to design a new two-element airfoil that will utilize the favorable interactions between the two elements to improve upon the L/D ratio at cruise conditions while maintaining an appropriate take-off and landing capability.

Various airfoil configurations, from simple flaps to complex multi-component Fowler flaps have been extensively explored for use as high lift devices.[5-16] It has even been mathematically proven that n+1 elements are better than n elements for providing maximum lift.[17] However, very little research has been performed on using a multi-element airfoil for cruise conditions since the emphasis has always been on increasing lift and not L/D. Bauer did study the two element airfoil problem using hand launched gliders.[18] His glide slope measurement results, although not definitive, provide support to the basic concept of a low drag two element cruise airfoil.

The current study took a systematic approach to the analysis and design of a two-element cruise airfoil. The concept was first explored analytically using widely accepted numerical methods. The final design was experimentally verified using a wind tunnel model of the airfoil. The overall study consisted of five basic steps. First, the accuracy of the numerical tools was studied by comparing results with published experimental and other numerical data. Next, the effects of relative profile, relative angle, and relative position of the two elements in the configuration were numerically studied. Third, a new two element airfoil was designed based on knowledge gained during the parametric variation study. Fourth, a complete numerical database was obtained on the new two element airfoil at various Reynolds numbers corresponding to actual flight conditions. Finally, a wind tunnel model was built and tested to experimentally verify the final numerical results.

NUMERICAL TOOLS

The new airfoil under study was designed and initially analyzed using commercially available numerical methods. All numerical studies were performed using an Intel 486 based personal computer running at 33 MHz.

The primary numerical tool used for the entire study was the NASA Langley Multi-Component Airfoil Analysis Code (MCARFA). All single element airfoils were also studied using Dr. Richard Eppler's Airfoil Program System (PROFIL) in order to further validate the MCARFA results.

MCARFA Background

The MCARFA computer code was originally developed under NASA contract to the Lockheed-Georgia Company in the early 1970's.[19,20] Major upgrades to the program were completed, again under NASA contract, by the Boeing Company in the late 1970's.[21,22] Currently, the NASA Langley Research Center is the prime source for the code and work on incremental improvements and program maintenance as the need arises.

The MCARFA code is an analytical model which computes the performance characteristics of multi-component airfoils in subsonic, compressible, viscous flow.[23-25] The final converged solution is obtained by successively combining an inviscid solution with a boundary layer displacement thickness. The surface of each airfoil element is approximated by a closed polygon with segments represented by distributed vortex singularities. The boundary layer solution is comprised of mathematical models representing the laminar, transition, turbulent, and confluent boundary layers.

The MCARFA program is composed of three main parts: the geometry specification, the potential flow solution, and the boundary layer solution. The

program uses an iterative procedure to obtain the viscous solution in five basic steps: 1) compute the potential flow solution for the basic airfoil, 2) compute boundary layer properties based on the potential flow solution, 3) construct a modified airfoil by adding the boundary layer displacement thickness to the original airfoil, 4) compute the aerodynamic performance coefficients, and 5) repeat steps 1) through 4) until convergence of the performance coefficients is obtained. Actual convergence is determined by requiring the calculated lift coefficient to converge to within 0.005 of the previous value.

MCARFA Airfoil Geometry Specification

The user inputs the desired airfoil element coordinates into the program. Within the program, the element is modeled as a polygon approximation. This polygon consists of N number of corner points with N-1 straight line segments.

To obtain accurate results, computational surface points are chosen which may differ in number and location from the input surface coordinates. The total number of computational surface points is an input, as is the number of points on each element. The location of the computational surface points is determined based on local surface curvature. To use this method, the curvature at each user input coordinate is computed with the formula:

$$K = \frac{a_1 z^2 - \left(a_1 x + \frac{a_2}{2}\right)^2}{\left[z^2 + \left(a_1 x + \frac{a_2}{2}\right)^2\right]^{3/2}}$$

where a_1, a_2, and a_3 are taken from a curve fit of the airfoil points. A curvature summation is then computed from the following equation and stored for backward interpolation:

$$\overline{K}_i = \int_0^{s_i} |K|^{1/4} \, ds$$

where:

$$s_i = s_{i-1} + \sqrt{(x_i - x_{i-1})^2 + (z_i - z_{i-1})^2}$$

The maximum value of $\overline{K}$ is divided into N equal portions and the s value corresponding to each portion is then determined by backward interpolation between the s_i and $\overline{K}_i$ arrays.

MCARFA Potential Flow Solution

The potential flow solution method used in the MCARFA code is a distributed vortex singularity method first formulated by Oellers[26] to compute the pressure distribution on the surface of airfoils in cascade. Instead of working with induced velocities, as is common in many panel method programs, Oellers' method employs stream functions. The stream function for a uniform stream plus that for a vortex sheet is set to be a constant on the airfoil surface. This is mathematically represented by the Fredholm integral equation:

$$\psi = \frac{1}{2\pi} \int_0^{s_i} \gamma(\xi) \ln[r(s,\xi)] d\xi = U_\infty x(s) \cos\alpha - U_\infty z(s) \sin\alpha$$

where ψ is the unknown stream function constant, $r(s,\xi)$ is the distance between the two points on the airfoil surface, $x(s)$ and $z(s)$ are coordinates of a point on the surface, and $\gamma(\xi)$ is the vortex strength at a point. By dividing the surface into N segments and assuming constant vortex strength for each segment the above equation becomes:

$$\psi - \sum_{j=1}^{N} A_{ij}\gamma_j = U_\infty (x_i \cos\alpha - z_i \sin\alpha)$$

where the influence coefficient A_{ij} is:

$$A_{ij} = \int_{s_j}^{s_{j+1}} \ln[r(s_i,\xi)]d\xi$$

By specifying a control point at the midpoint of each segment, the influence coefficient becomes:

$$A_{ij} = \frac{1}{4\pi}[t_2 \ln(r_2) - t_1 \ln(r_1)] - \frac{\Delta s}{2\pi} + \frac{t_3}{2\pi}\left[\tan^{-1}\left(\frac{t_2}{t_3}\right) - \tan^{-1}\left(\frac{t_1}{t_3}\right)\right] \qquad (i \neq j)$$

$$A_{ij} = \frac{\Delta s}{2\pi}\left[\ln\left(\frac{\Delta s}{2}\right) - 1\right] \qquad (i = j)$$

where:

$$\Delta s = s_{j+1} - s_j$$

$$r_1 = (x_j - x_{c,i})^2 + (z_{j+1} - z_{c,i})^2$$

$$r_2 = (x_{j+1} - x_{c,i})^2 + (z_{j+1} - z_{c,i})^2$$

$$t_1 = \frac{(x_j - x_{c,i})(x_{j+1} - x_j) + (z_j - z_{c,i})(z_{j+1} - z_j)}{\Delta s}$$

$$t_2 = \frac{(x_{j+1} - x_{c,i})(x_{j+1} - x_j) + (z_{j+1} - z_{c,i})(z_{j+1} - z_j)}{\Delta s}$$

$$t_3 = \frac{(x_j - x_{c,i})(z_{j+1} - z_j) + (z_j - z_{c,i})(x_{j+1} - x_j)}{\Delta s}$$

To determine the vortex strength ($\bar{\gamma}$) at the intersection of two segments, the following interpolation formula is used:

$$\bar{\gamma}_j = \frac{\gamma_{j-1}(s_j - s_{j-1}) + \gamma_j(s_{j+1} - s_j)}{s_{j+1} - s_{j-1}} \qquad (j \neq 1 \text{ or } N)$$

The unknowns in the method are now N-1 number of γ's and ψ, therefore an additional equation is needed to obtain an N by N system of equations. The final equation comes from applying the Kutta condition at the trailing edge. The particular formulation of the Kutta condition used requires that the vortex strengths ($\bar{\gamma}$) vary quadratically for the last four segment corners near the upper and lower surface of the trailing edge and that at the trailing edge the upper and lower surface vortex strengths are equal in magnitude but opposite in sign.

The N by N system of simultaneous equations is now solved and the incompressible surface velocities are obtained from the resulting values of the vortex strengths and the stream function. The well know Karman-Tsien compressibility correction law is applied to convert the incompressible pressure coefficients to the equivalent answers at the desired freestream Mach number. No stretching of the chord is performed.

MCARFA Boundary Layer Solution

Using the isentropic flow relations, the local Mach number is computed and input into the boundary layer portion of the program. The boundary layer consists of

an ordinary boundary layer (nonmerging boundary layer), and a confluent boundary layer (merging boundary layer). The ordinary boundary layer is composed of laminar, transition, and turbulent regions. The confluent boundary layer model was developed by Goradia[27] from the Lockheed-Georgia Company and is one of the unique features of the MCARFA program. The critical parameters output from the boundary layer routines are the displacement thickness, the momentum thickness, the shape factor, and the skin friction coefficient. The theoretical development of the boundary layer methods used in this program constituted a doctoral dissertation and therefore will only be briefly summarized here.

A flat plate boundary layer analysis is performed on each surface of an airfoil element, and the leading edge stagnation point is the plate leading edge. An initial laminar boundary layer region exists from the stagnation point to the point of transition from laminar to turbulent flow. The laminar boundary layer model used is the method of Cohen and Reshotko[28] for a compressible laminar boundary layer with heat transfer and an arbitrary pressure gradient. After computing the laminar boundary layer characteristics at a discrete point a check for transition is made. If transition has occurred, a check for the formation of a long or short transition bubble and for laminar stall is made. An initial check is made to determine if the laminar boundary layer is stable or unstable based on the instability criterion of Schlichting and Ulrich who have solved the Orr-Sommerfeld equation assuming a Polhausen laminar profile.[29] If the boundary layer is unstable, a transition check is made based on an empirically derived transition prediction curve developed by Goradia.[27] If transition has occurred, the initial parameters necessary to start the turbulent calculations are computed. If transition has not occurred, the formation of either a long bubble with laminar stall, or a

short bubble with reattachment is determined. The user can also input a fixed transition location, and a check will be made to determine whether this location has been reached.

After computing the transition location and initial boundary layer properties, the turbulent boundary layer calculations are made. The turbulent boundary layer model is that of Truckenbrodt.[30] The Truckenbrodt turbulent boundary layer analysis is an incompressible integral method based on the momentum integral equation and the energy integral equation. An additional turbulent boundary layer method as derived by Nash and Hicks[31] is used on the last iteration for the sole purpose of predicting separation.

If a slot exit plane is reached during the turbulent boundary layer computations, the confluent boundary layer analysis is initiated. The confluent boundary layer is a result of the mixing from the slot efflux and the wake of the forward element. It can exist from the slot exit to the trailing edge depending on the pressure gradient. The confluent boundary layer model was formulated by Goradia.[27] The model is based on the assumption that the merging fore and aft element boundary layers will have similar profiles if nondimensionalized in a way analogous to that for a free-jet flow. Several empirical constants were needed to establish the similar boundary layer profiles and were experimentally derived from tests performed by Goradia.

None of the boundary layer methods used in this program include curvature effects. All the methods are basically integral methods which are often less accurate than finite-difference methods but require less computer time. No attempt to model separated flow exists, so the numerical results are only valid for cases with very small amounts of separated flow.

MCARFA Program Accuracy

Studies were performed to document the MCARFA program accuracy on cases similar to the current airfoil design. Williams has developed an exact test case for the plane potential flow about two adjacent lifting airfoils.[32] MCARFA results of Williams' two test cases are presented in Figures 2 and 3. Test Case A is at an angle of attack of 0° with the flap deflected 30° and test Case B is at an α of 0° and a flap deflection of 10°. The calculated pressure distributions show excellent agreement with the theory. Aerodynamic load data from the exact test case and the MCARFA results are presented in Table 1. Close agreement is obtained for the lift coefficient values, but the MCARFA results show some inaccuracy in the drag coefficient calculations.

NACA external airfoil flap data were used to test the viscous MCARFA results on airfoil designs similar to the current study.[33-36] A NACA 23012 airfoil with a 20% chord 23012 external airfoil flap deflected 20° was tested at a Reynolds number of 1.05×10^6 by NACA researchers. MCARFA lift coefficient results show good agreement overall with the program predicting a 12% higher $c_{l_{max}}$ value than the experiment (Fig. 4). The $c_{l_{max}}$ difference is due to the program not predicting the slope change in the lift curve at a c_l of approximately 1.2 as in the experimental data. The program predicts a higher c_d at the lower lift coefficients and a lower c_d at the higher c_l values than the experimental results show (Fig. 5). The L/D ratio results follow the c_d trends (Fig. 6). Moment coefficient results are generally within 5% (Fig. 7).

The MCARFA code does not predict a true maximum lift coefficient. It instead continues to predict increasing lift with increasing angle of attack after stall. Comparisons with numerous sets of experimental and other numerical data for both single and multi element airfoils has led to an empirical $c_{l_{max}}$ criterion. The airfoil is

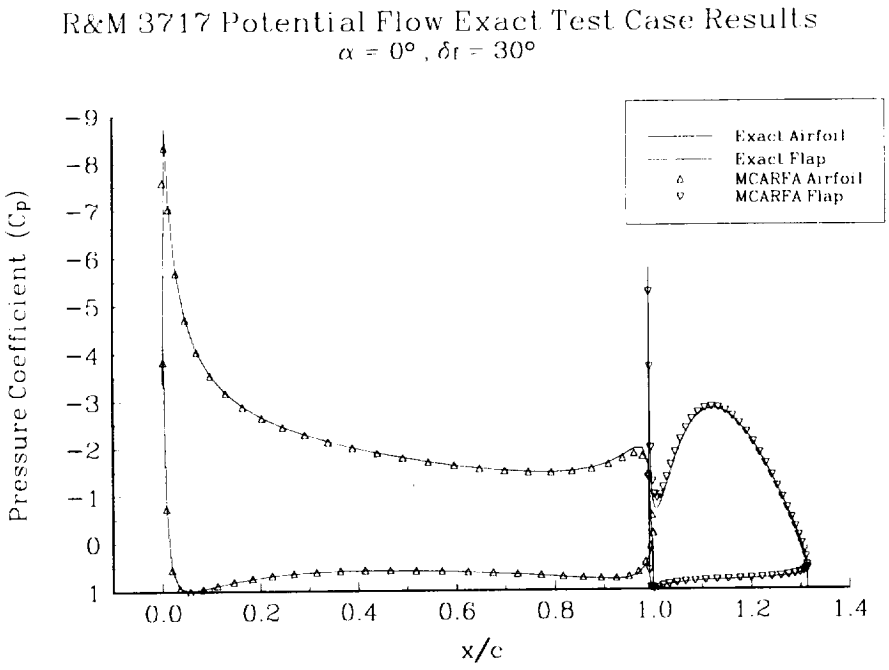

Fig. 2 MCARFA exact test Case A results

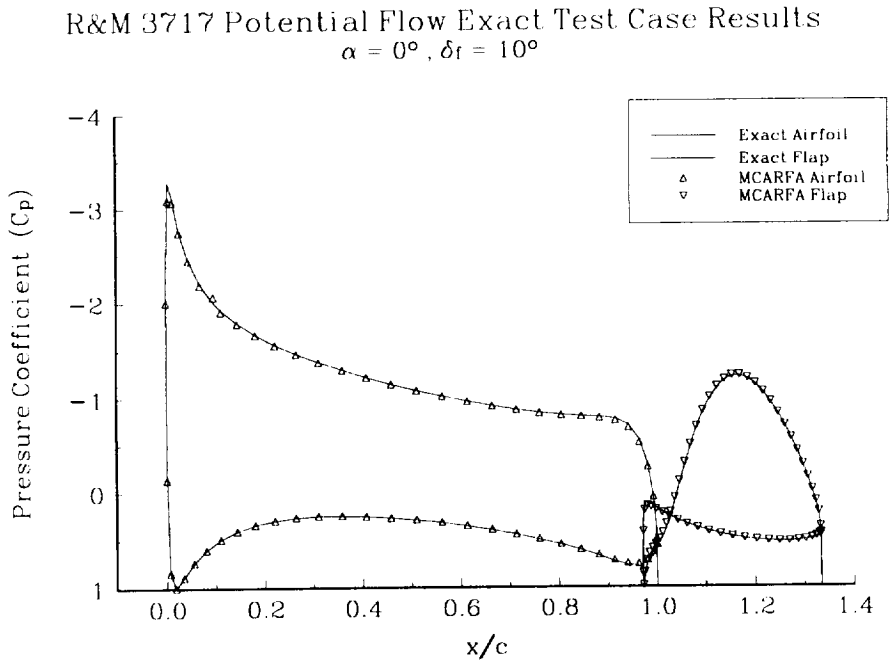

Fig. 3 MCARFA exact test Case B results

Table 1 MCARFA and Williams' exact aerodynamic load results

Component	Case A c_l	c_d
Exact Main	2.9065	-0.3839
MCARFA Main	2.8705	-0.3686
Exact Flap	0.8302	0.3838
MCARFA Flap	0.8453	0.3836
Exact Total	3.7367	-0.0001
MCARFA Total	3.7158	0.0150

Component	Case B c_l	c_d
Exact Main	1.6915	-0.0898
MCARFA Main	1.6758	-0.0847
Exact Flap	0.3366	0.0897
MCARFA Flap	0.3435	0.0900
Exact Total	2.0281	-0.0001
MCARFA Total	2.0193	0.0054

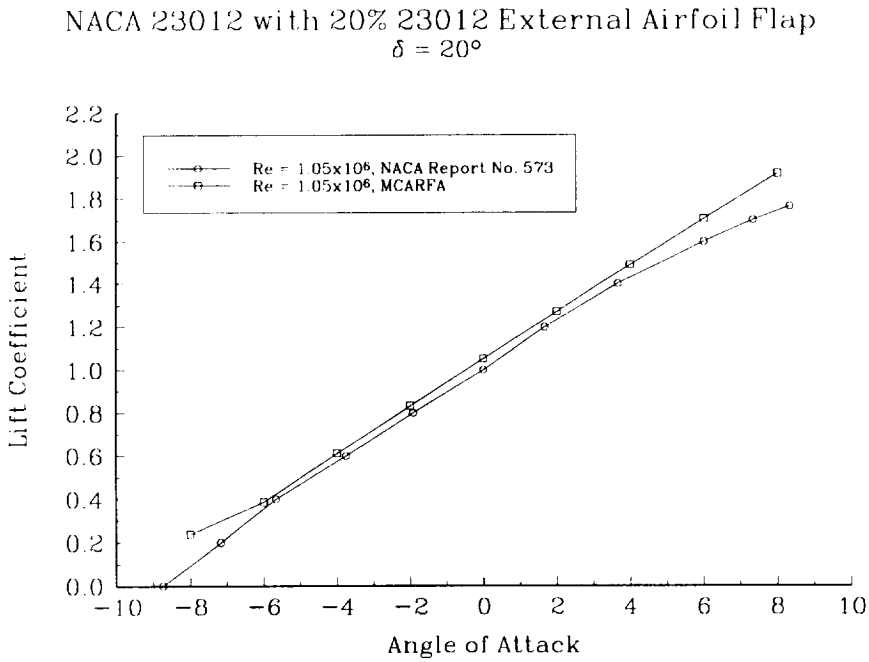

Fig. 4 NACA 23012 with 23012 flap lift coefficient results

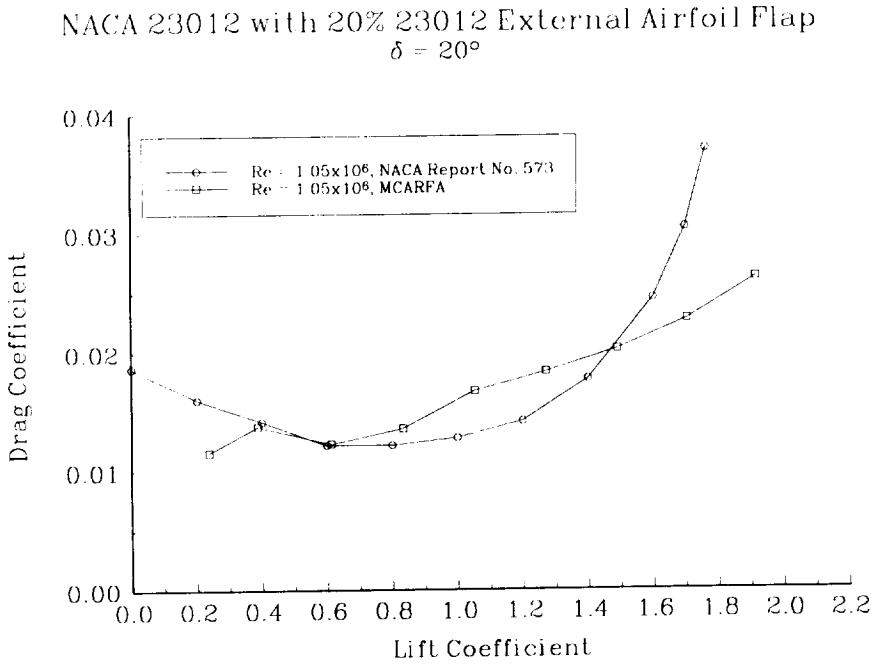

Fig. 5 NACA 23012 with 23012 flap drag coefficient results

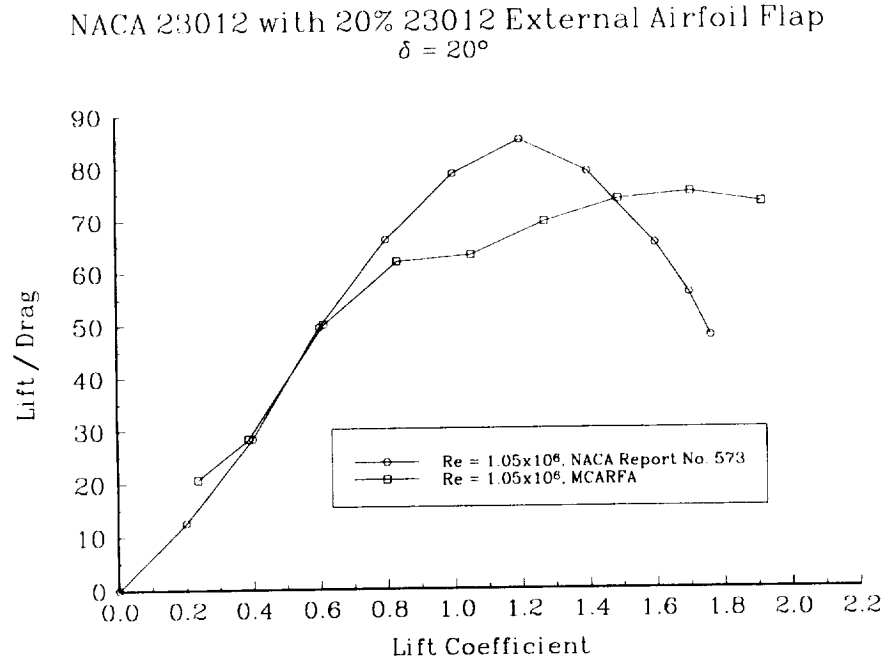

Fig. 6 NACA 23012 with 23012 flap L/D ratio results

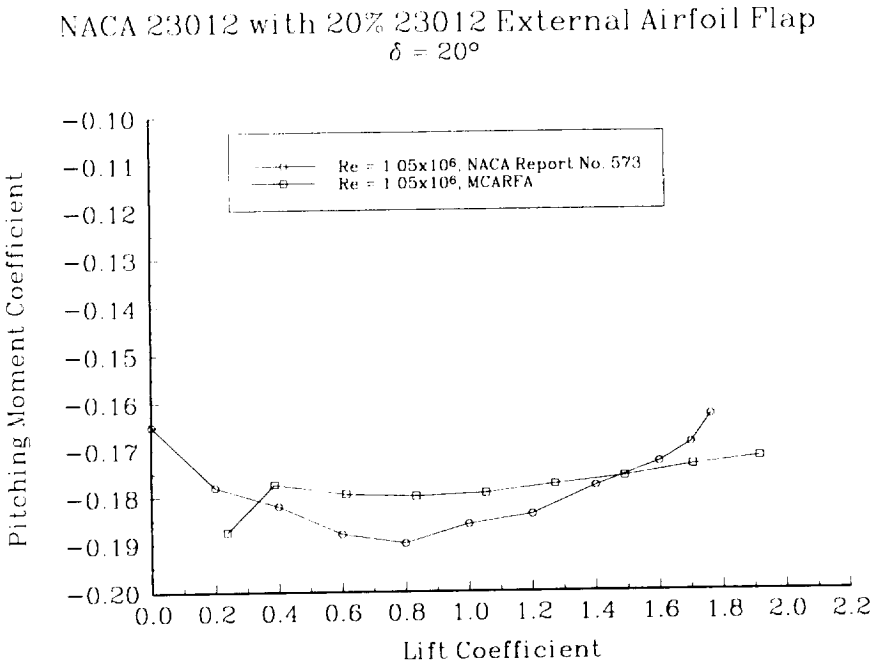

Fig. 7 NACA 23012 with 23012 flap moment coefficient results

said to have stalled when the MCARFA code predicts separated flow over more than 10% of the upper surface area on a given element.

PROFIL Background

The PROFIL computer program is a two dimensional incompressible viscous flow program developed over the last several years primarily by Dr. Richard Eppler of the University of Stuttgart.[37,38] Because of his lead role in the program development, the code is often referred to as the Eppler code. A major step in the program history occurred when, under collaboration with the NASA Langley Research Center, a User's Manual and program description were published in the early 1980's.[39,40] The code is still being continually updated and improved. The latest version is commercially available directly from Dr. Eppler.

The PROFIL code has two primary modes of operation: airfoil design and airfoil analysis. In the airfoil design mode, the program solves the inverse design problem through a conformal mapping routine which computes an airfoil geometry based on input velocity distributions. In the airfoil analysis mode, a panel method routine to solve the potential flow and boundary layer effects of a flow field on a given shape is completed. The airfoil analysis portion of the program was all that was used during the current study.

Previous experience has shown the program to be an extremely fast and reliable source for performance characteristics of single element airfoils.[41,42] The primary drawback to the PROFIL code is the fact that it only computes results for single element airfoils or airfoils with simple flap systems. No provision is made to analyze complex or multi element airfoils. Because of this limitation, the PROFIL code was used to analyze all single element airfoils and provide a check on the single element results of the MCARFA code, but none of the final two element airfoil cases were examined with the PROFIL code.

PROFIL Potential Flow Solution

The potential flow airfoil analysis method employs panels with distributed surface singularities. The geometry of the panels is determined by a spline fit of the input airfoil coordinates. The singularities used are vortices distributed parabolically along each panel. The flow condition, which requires the inner tangential velocity to be zero, is satisfied at each input airfoil coordinate. Angles of attack of 0° and 90° are analyzed. The flow for an arbitrary angle of attack is derived by superposition from these two solutions. The numerical method is based upon determination of the velocity vector induced at a point by the vorticity distribution along a straight panel according to the well known Biot-Savart law.[43]

PROFIL Boundary Layer Solution

An integral method for the calculation of standard boundary layer properties is employed. The standard definitions of the displacement thickness, the momentum thickness, the energy thickness, and the two shape factors are employed as with the MCARFA code.

For the laminar boundary layers, some Hartree profiles are used as velocity distributions.[29] Based on these velocity distributions, the critical parameters are calculated using the momentum thickness and the H_{32} shape factor as the independent quantities. The H_{12} shape factor, the skin friction, the transition location, and the separation location are all polynomial fit solutions based on the H_{32} shape factor.

The turbulent boundary layer calculations of the critical parameters are not as straightforward as the laminar boundary layers. Results for the required boundary layer parameters are obtained by empirical relations derived by Wieghardt, Ludwieg-Tillman, and Rotta.[44]

Turbulent separation is determined by the value of H_{32}; separation is said to have occurred when H_{32} is equal to 1.46. Laminar separation is predicted if H_{32} is equal to 1.51509. One benefit of the PROFIL program is it does continue to model the flow after some separation has occurred, applying an empirical correction based on the amount of separation to both the angle of attack and the lift curve. Transition from laminar to turbulent flow and the corresponding switch in equations is initiated by the following relation:

$$\ln \mathrm{Re}_{\delta_2} \geq 18.4 H_{32} - 21.74 - 0.36r$$

where r is a roughness factor with a value of zero corresponding to natural transition on a smooth surface.

PROFIL Accuracy

Studies similar to those conducted for the MCARFA computer program were carried out to determine the accuracy of the PROFIL results. This step also served as a check of the MCARFA single element results and as a basis for the understanding of both computer programs.

Graphical results of all aerodynamic performance characteristics as calculated by both the PROFIL and MCARFA computer codes and experimentally tested by the NACA or NASA are presented in the Existing Single Element Airfoils section of this paper. In general, the PROFIL compute code agrees very will through the entire lift range with the experimental data. A shift of the α_0 value of approximately 1° is observed between the experimental and PROFIL numerical data. The MCARFA code predicts the low lift coefficient values very well, but slightly overpredicts the lift at higher angles of attack due to the lack of separated flow modeling. Drag coefficient values agree well at the lower lift coefficients for all cases, but the MCARFA code does underpredict the drag at the higher lift coefficients. The PROFIL computer code overpredicts the moment coefficient by about 20% when compared with both the experimental data and the MCARFA computer results.

NUMERICAL RESULTS AND DISCUSSION

Results for various combinations of profile shape, relative angle, and relative position of the two elements of the new airfoil are presented. Numerical results of the systematic study were obtained at Reynolds Numbers of $8x10^5$ through $3x10^6$. Appendix A presents a list of all numerical cases. The MCARFA program was used to analyze all cases. When possible, the PROFIL program was also used to verify MCARFA output. All analytical results were obtained at sea level standard conditions with natural or free transition from laminar to turbulent flow.

Existing Single Element Airfoils

Numerical results were obtained for a variety of existing single element airfoils for possible use in the initial two element configurations. Examining the single element airfoils afforded the opportunity to examine MCARFA results as compared with the PROFIL answers and published experimental data.[4] Experience in the nuances of the MCARFA numerical method was also obtained in this first step.

Five single element candidate airfoils were examined: a NASA NLF(1)-0416, a NACA 0012, a NACA 2412, a NACA 4412, and a NACA 23012. All cases were performed on an airfoil with a 61 cm chord at a Reynolds number of approximately three million. The NLF(1)-0416 airfoil lift coefficient vs. angle of attack results show generally good agreement between the three sources (Fig. 8). The MCARFA program predicts very good results at lower lift coefficients but a slightly higher lift curve slope at the higher angles of attack than experimentally verified. The PROFIL program predicts the shape of the lift curve very well but underpredicts the zero lift angle of attack by about 0.75°. Overall, the drag coefficient results (Fig. 9) show good agreement between all sources, but the MCARFA code does underpredict the drag

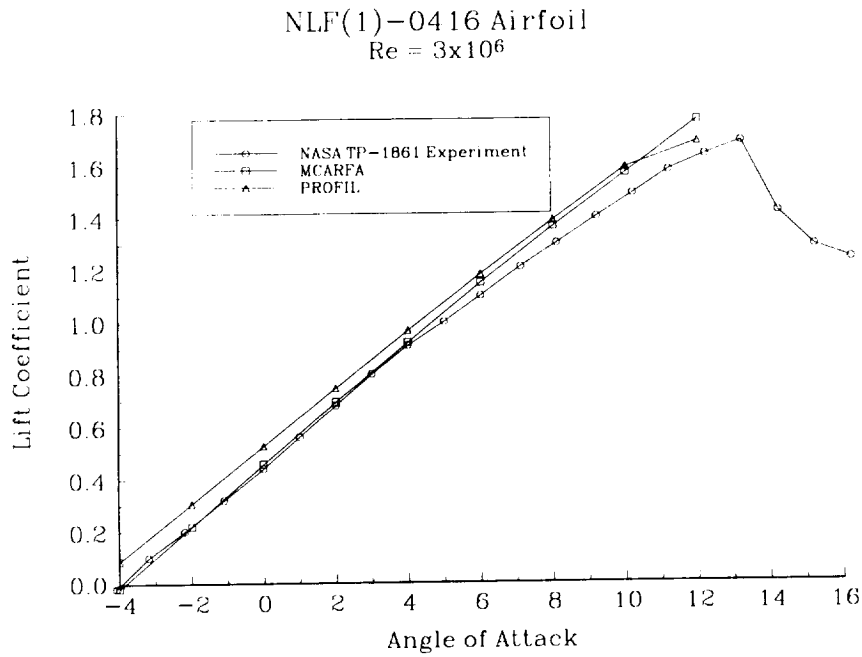

Fig. 8 NLF(1)-0416 airfoil lift coefficient results

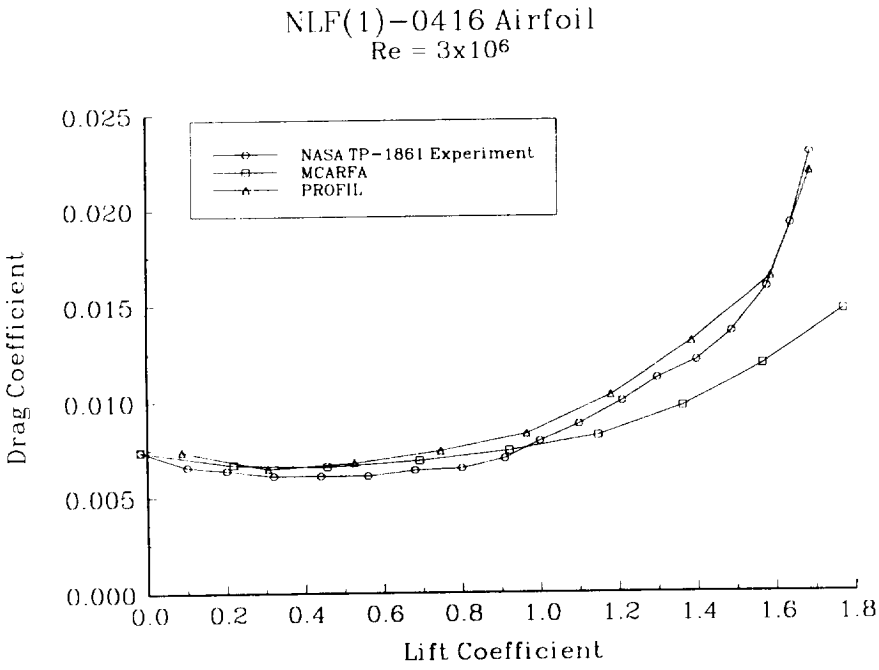

Fig. 9 NLF(1)-0416 airfoil drag coefficient results

coefficient at the higher lift values. Moment coefficient results show excellent agreement between the MCARFA results and the experiment, but the PROFIL code overpredicts the moment coefficient by about 20% (Fig. 10).

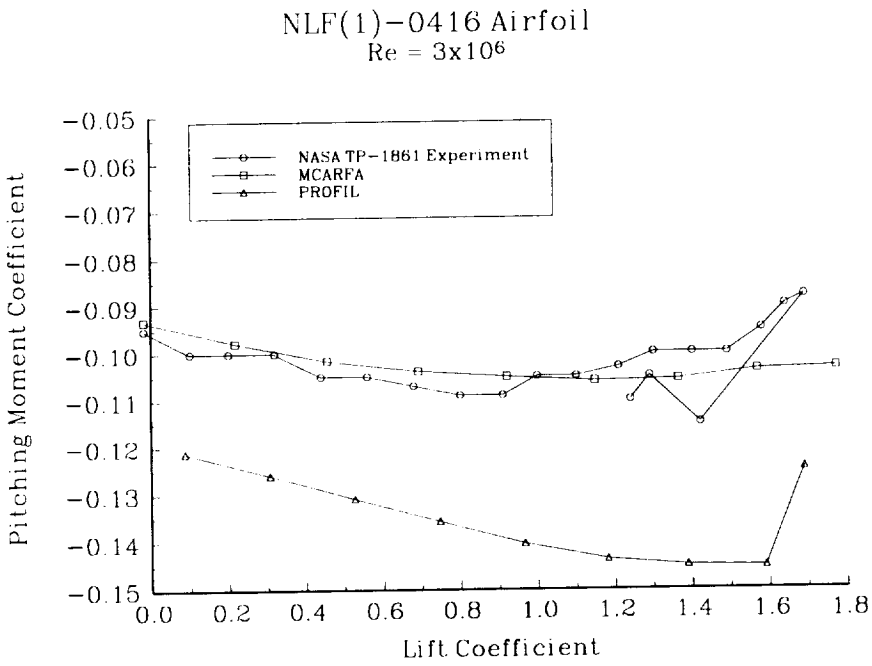

Fig. 10 NLF(1)-0416 airfoil moment coefficient results

Results for the NACA 0012, 2412, 4412, and 23012 airfoils are presented in Figures 11 through 22. Generally good agreement between the two sets of numerical data and the published experimental values were obtained on all cases.

Profile Shape

Various combinations of existing airfoils were explored for use as a two element airfoil. The NASA NLF(1)-0416 airfoil was chosen for use as the primary

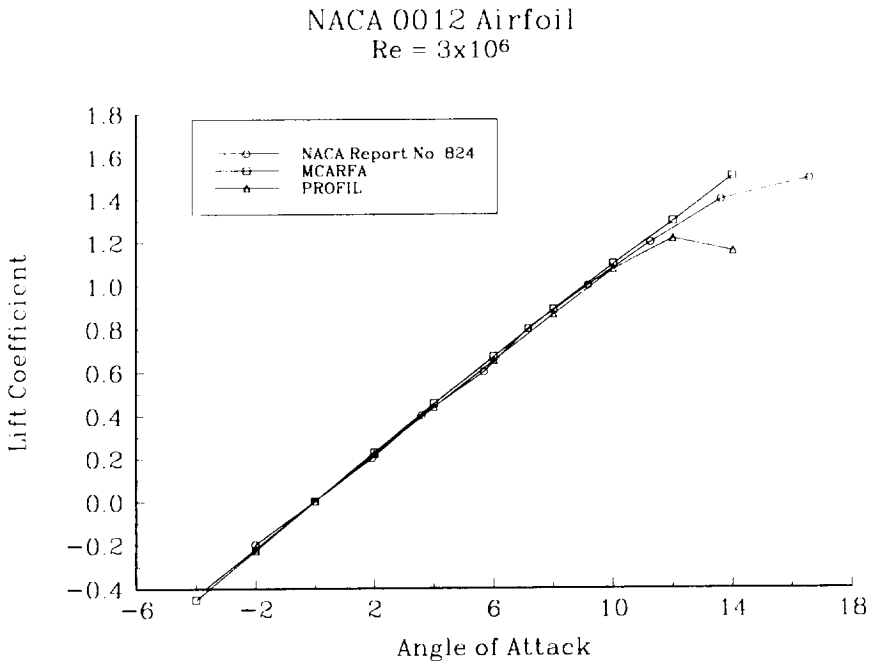

Fig. 11 NACA 0012 airfoil lift coefficient results

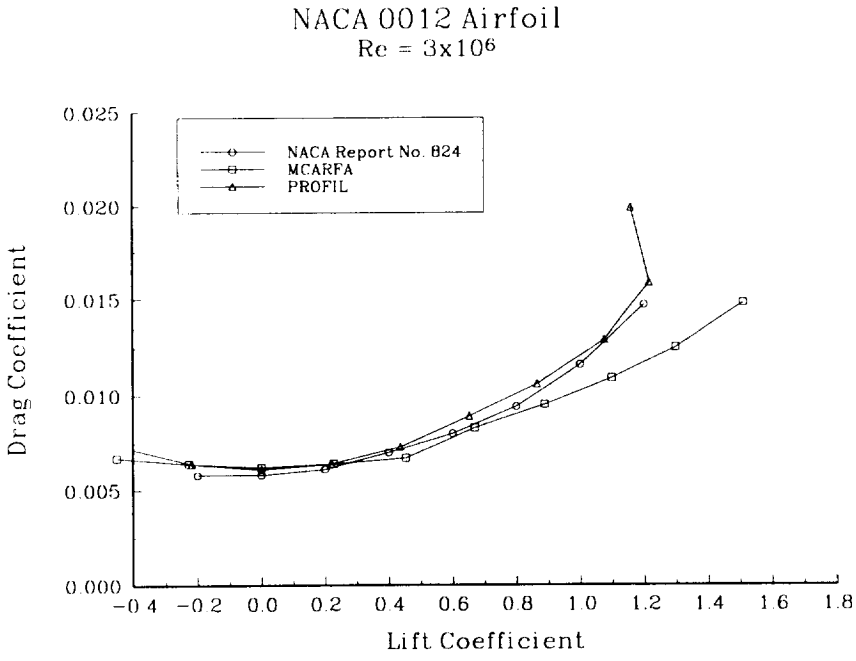

Fig. 12 NACA 0012 airfoil drag coefficient results

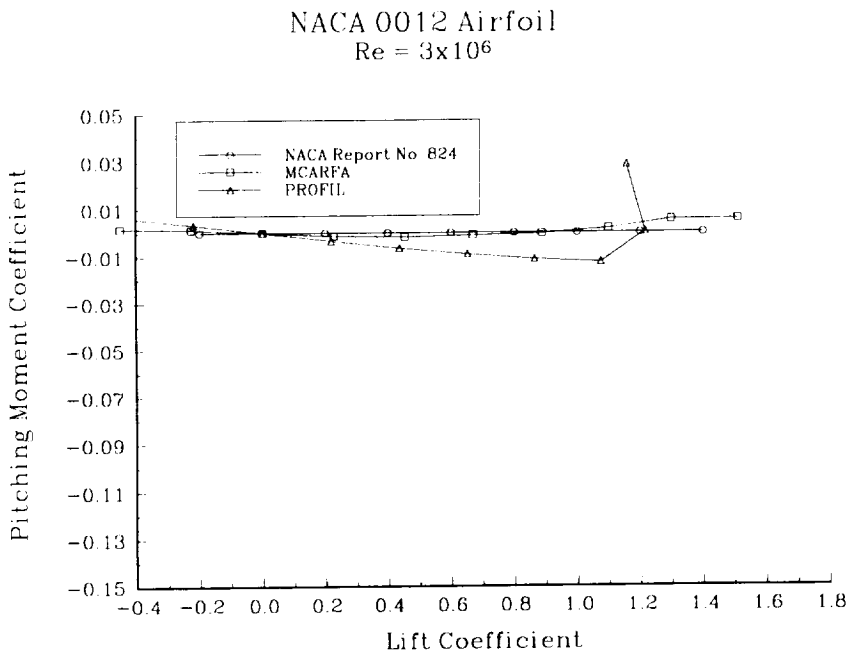

Fig. 13 NACA 0012 airfoil moment coefficient results

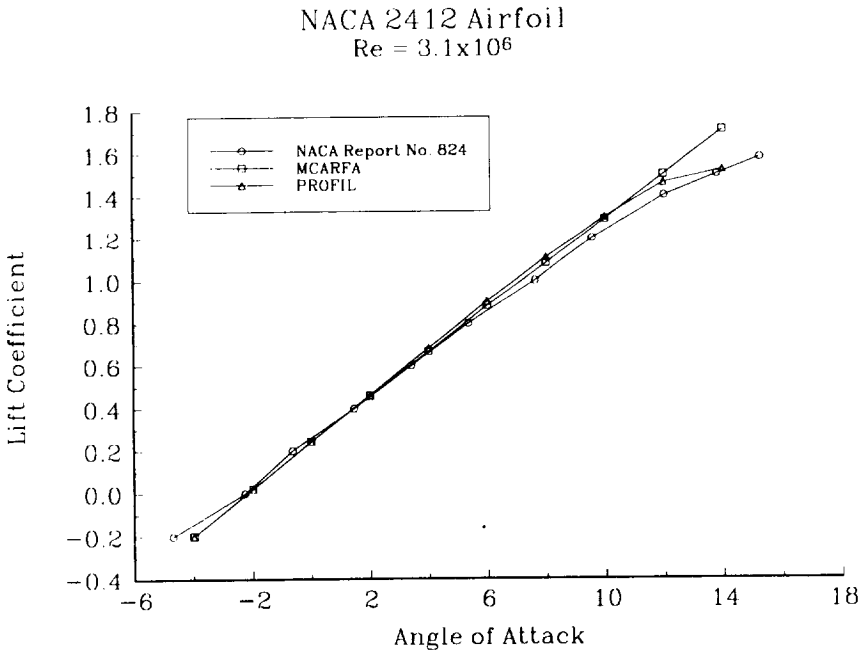

Fig. 14 NACA 2412 airfoil lift coefficient results

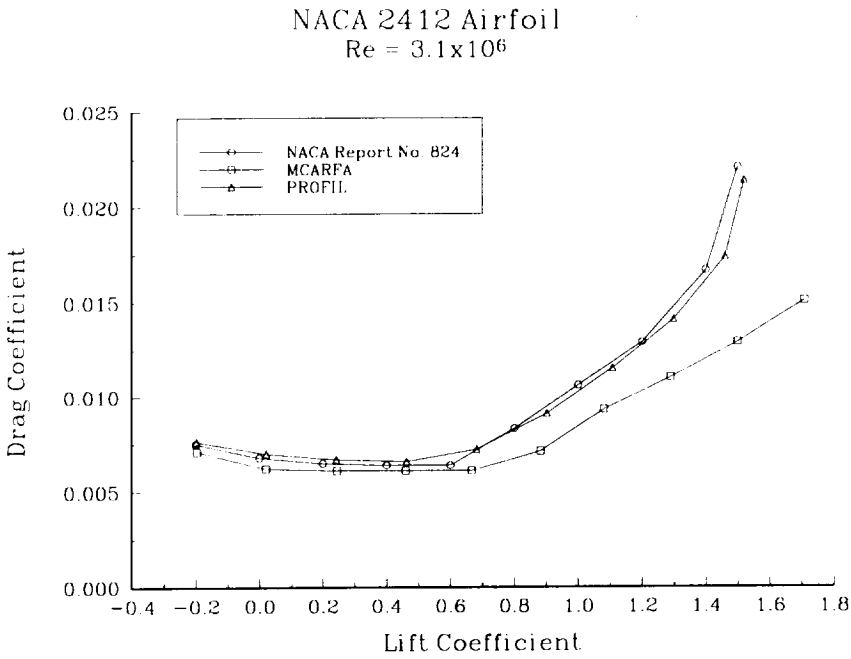

Fig. 15 NACA 2412 airfoil drag coefficient results

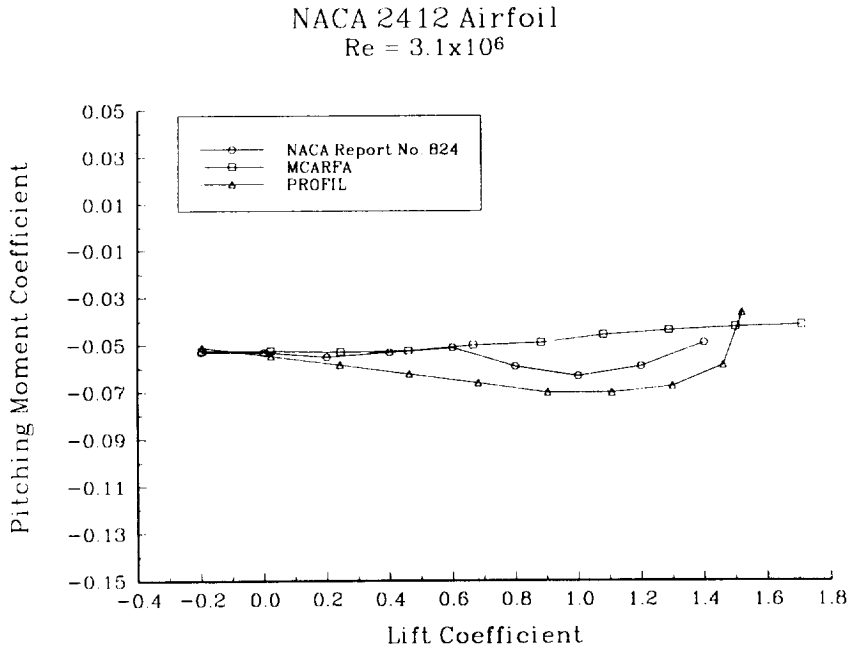

Fig. 16 NACA 2412 airfoil moment coefficient results

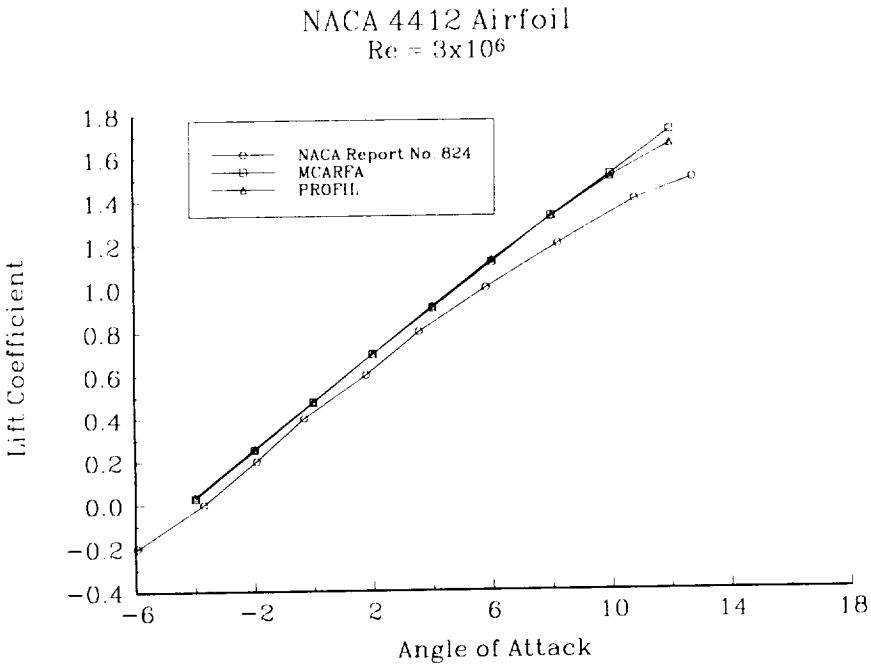

Fig. 17 NACA 4412 airfoil lift coefficient results

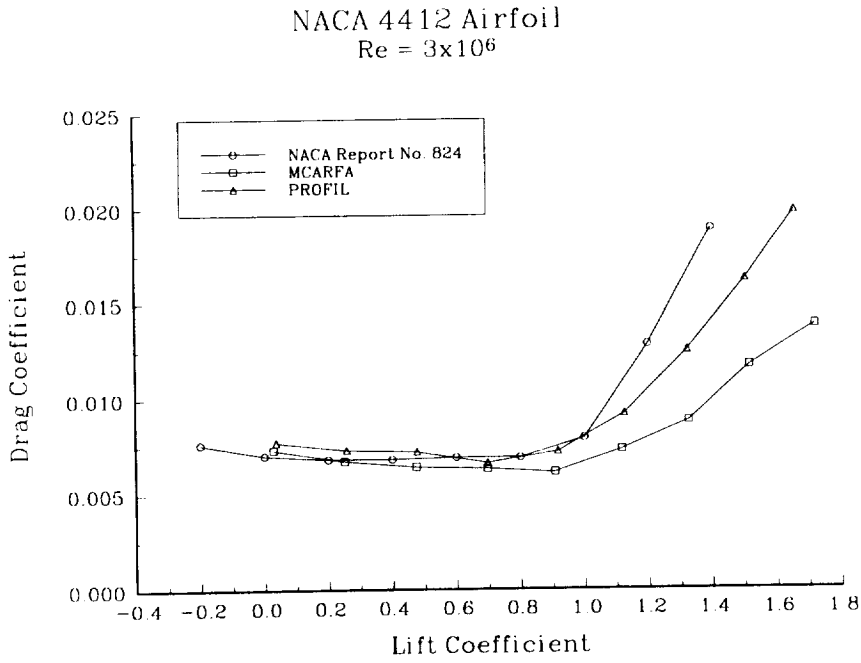

Fig. 18 NACA 4412 airfoil drag coefficient results

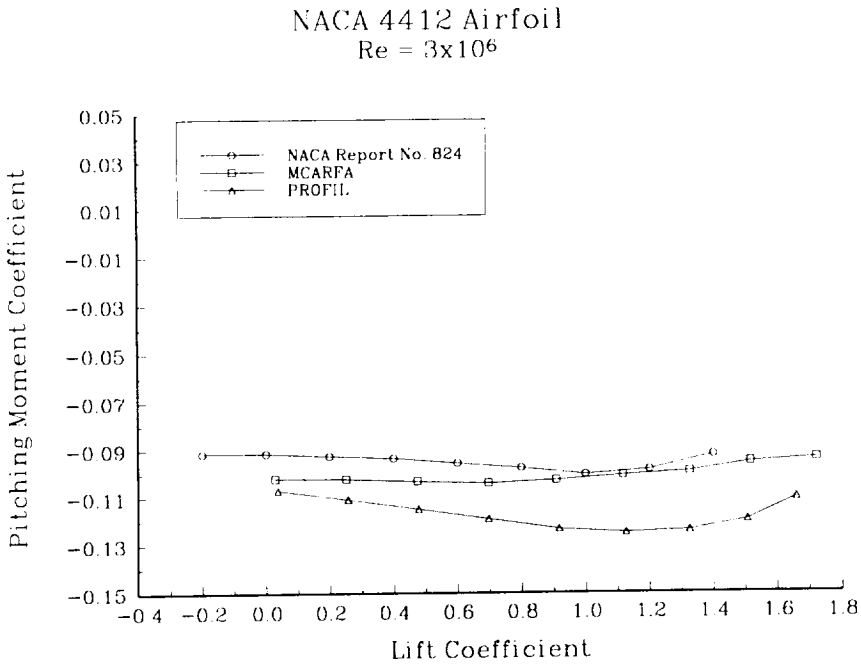

Fig. 19 NACA 4412 airfoil moment coefficient results

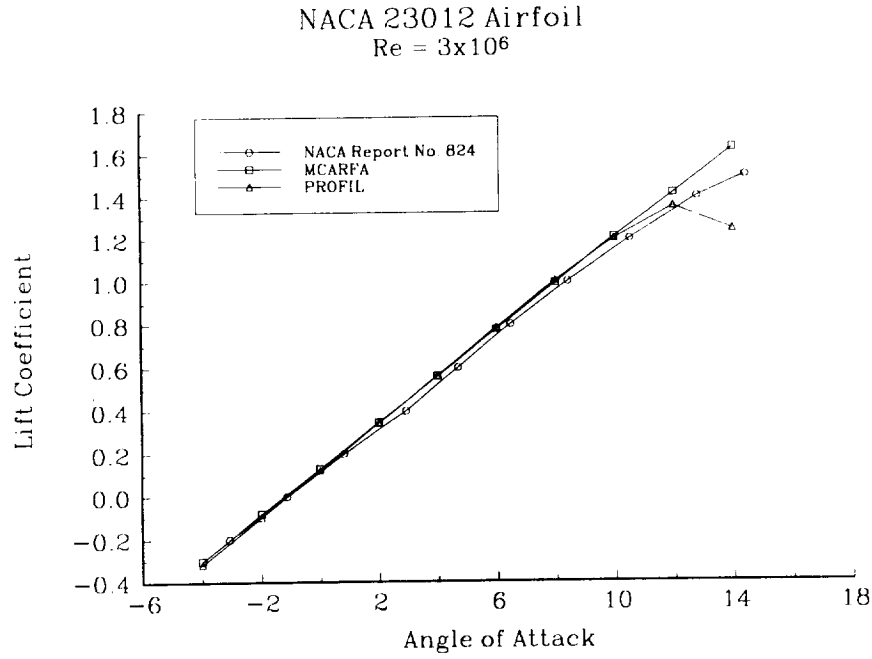

Fig. 20 NACA 23012 airfoil lift coefficient results

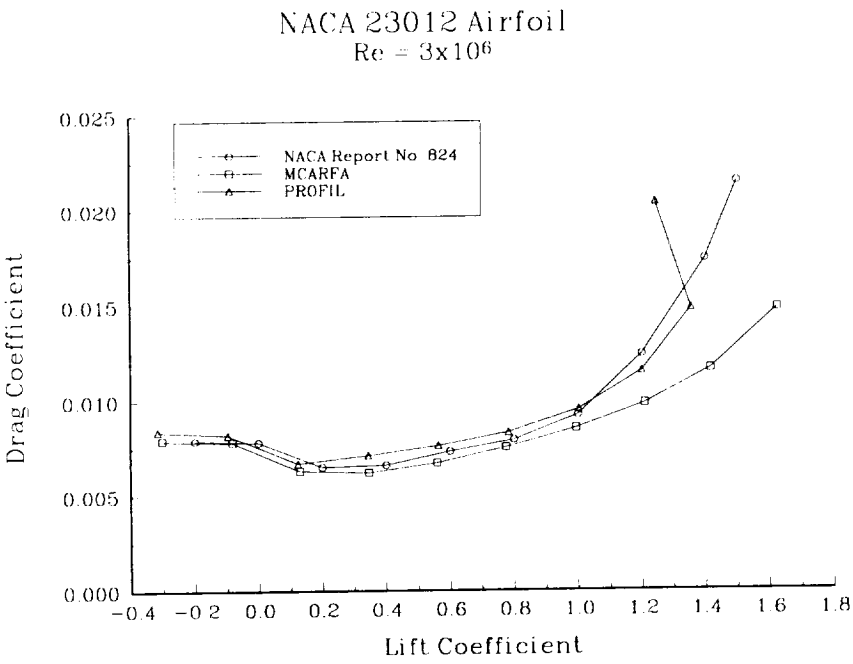

Fig. 21 NACA 23012 airfoil drag coefficient results

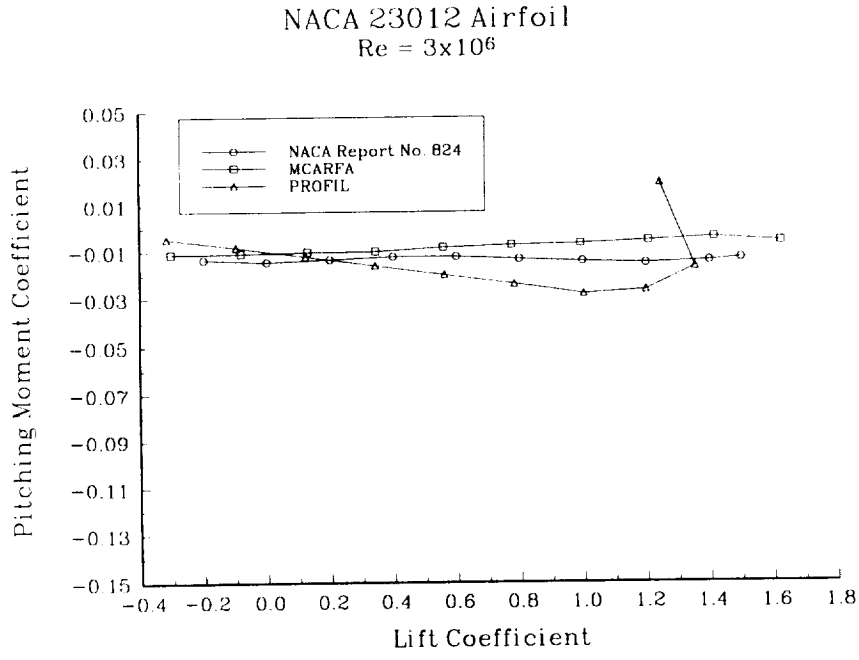

Fig. 22 NACA 23012 airfoil moment coefficient results

element in the initial two element configuration. This choice was made for two reasons. First, the NLF airfoil was designed for similar conditions to the two element airfoil under study.[45] It is an unflapped, reasonably high lift laminar flow airfoil designed for light general aviation applications. The second reason for choosing the NLF airfoil was the well documented set of both experimental and numerical data previously published for the airfoil, thus allowing accurate direct comparisons between the current study results and those independently obtained previously.

The secondary element profile should be a relatively benign section because of the disrupted flow conditions it will be operating in due to the wake and downwash from the primary element. The NACA 0012, 2412, 4412, and 23012 airfoils studied previously were determined to be candidates for the secondary profile. Wentz[46] determined the optimum location for the leading edge of a split flap to be 98% chord behind and 3% chord below the leading edge of the airfoil, this location was used during the initial studies for placement of the secondary airfoil. The NACA found a 25% chord external airfoil flap deflected 20° was the optimum relative size and deflection.[36] Again, these choices were used for initial studies with the two element configuration.

Lift coefficient results for the various secondary element profile shapes show the NASA NLF(1)-0416 with a NACA 4412 provides the highest $c_{l_{max}}$ (Fig. 23). Drag coefficient results show very little difference between the various secondary element profile shapes at low lift coefficients (Fig. 24). The 4412 case has the lowest drag at a given lift for the higher lift coefficient. Lift to Drag ratio results show the highest L/D values with the 4412 case through the entire c_l range (Fig. 25). Moment coefficient results show, as expected, higher moment values with increasing camber (Fig. 26). The

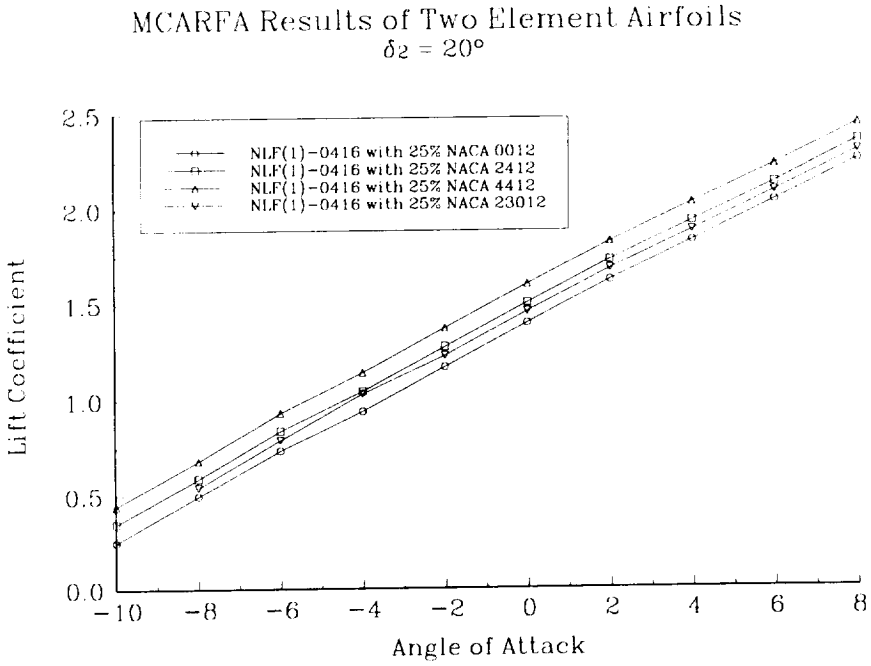

Fig. 23 Secondary element profile effect on lift coefficient results

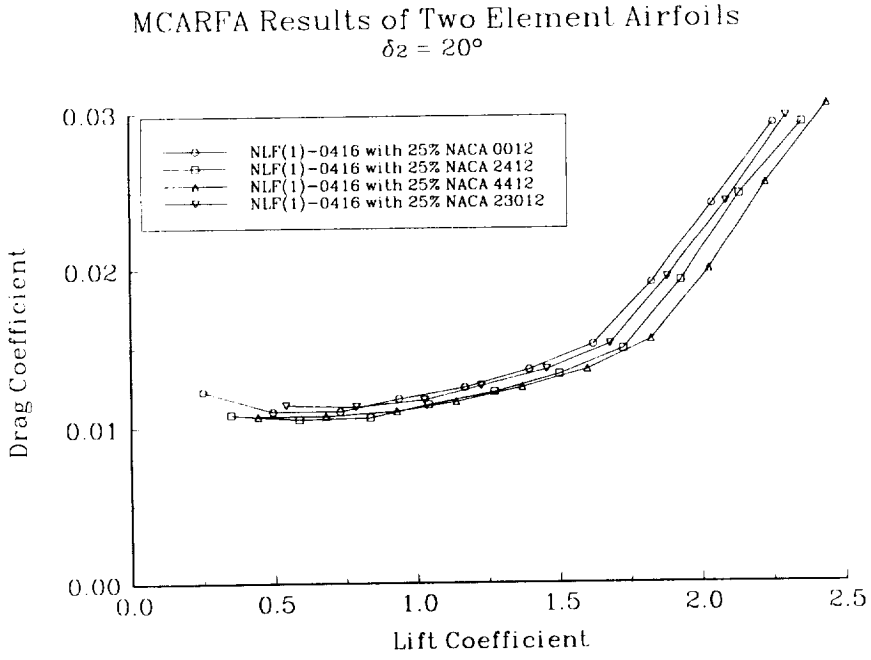

Fig. 24 Secondary element profile effect on drag coefficient results

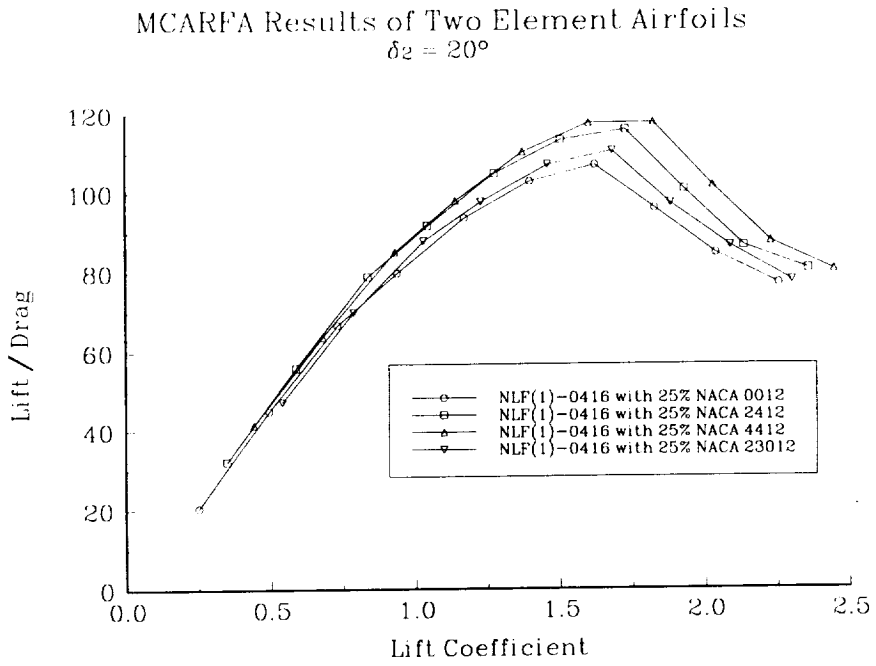

Fig. 25 Secondary element profile effect on L/D ratio results

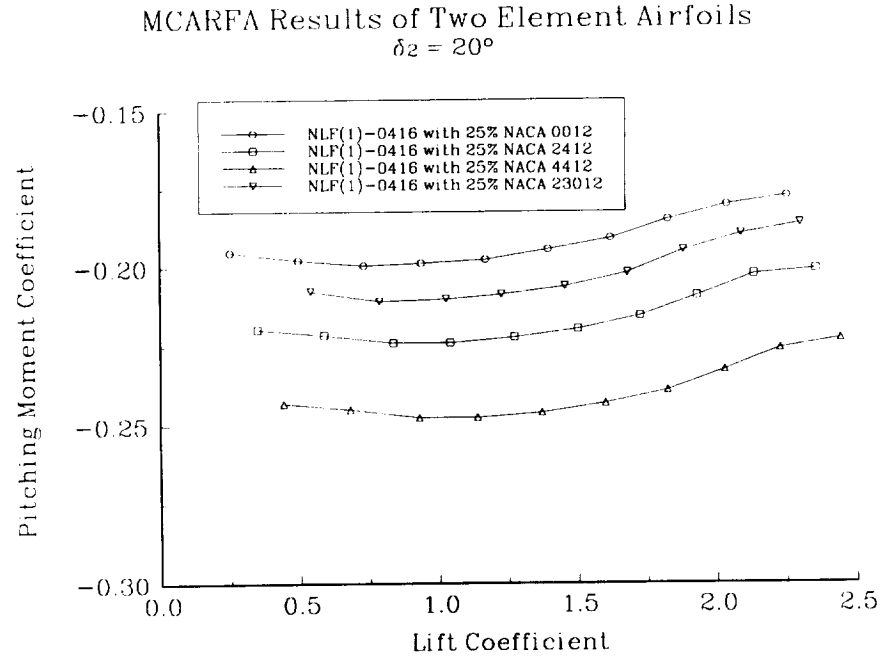

Fig. 26 Secondary element profile effect on moment coefficient results

NACA 4412 case has the most negative moment at roughly 20% higher than the 2412 case. Based on the above data, the NACA 4412 profile was chosen for the secondary element. The 2412 was also chosen for further study because of its reasonably high c_{lmax} and the significantly lower moment coefficient.

Relative Position

The optimum relative position of the two elements was studied in detail by varying the horizontal and vertical position independently while holding all other parameters constant. This variation was studied with both the NACA 4412 and 2412 secondary element at second element deflections of 10°, 15°, 20°, 25°, and 30°. The primary element size was held constant at 38 centimeters or 75% of the total chord and the secondary element chord was kept at 13 centimeters or 25% of the total chord. Position nomenclature used is the location of the leading edge of the secondary element with respect to the leading edge of the primary element in percent of the primary chord.

Lift coefficient results for the 4412 deflected 20° at a vertical position 4% of the primary chord below the primary leading edge show the highest c_l values obtained at a horizontal position of 96% behind the primary leading edge (Fig. 27). Drag coefficient results of the same case show the lowest drag coefficient obtained at a secondary horizontal position of 95% (Fig. 28). The maximum L/D ratio was calculated at a position of 95% (Fig. 29). The moment coefficient increased as the secondary element was moved further aft (Fig. 30). Similar results were obtained with the secondary element at vertical positions of 3% below (Figs. 31-34), 2% below (Figs. 35-38), and 1.5% below (Figs. 39-42) the primary element. Results are also presented for a NACA 2412 secondary element deflected 20° and located 2% below the primary element (Figs. 43-46). Again the optimum horizontal position is seen to be 95% behind the primary leading edge.

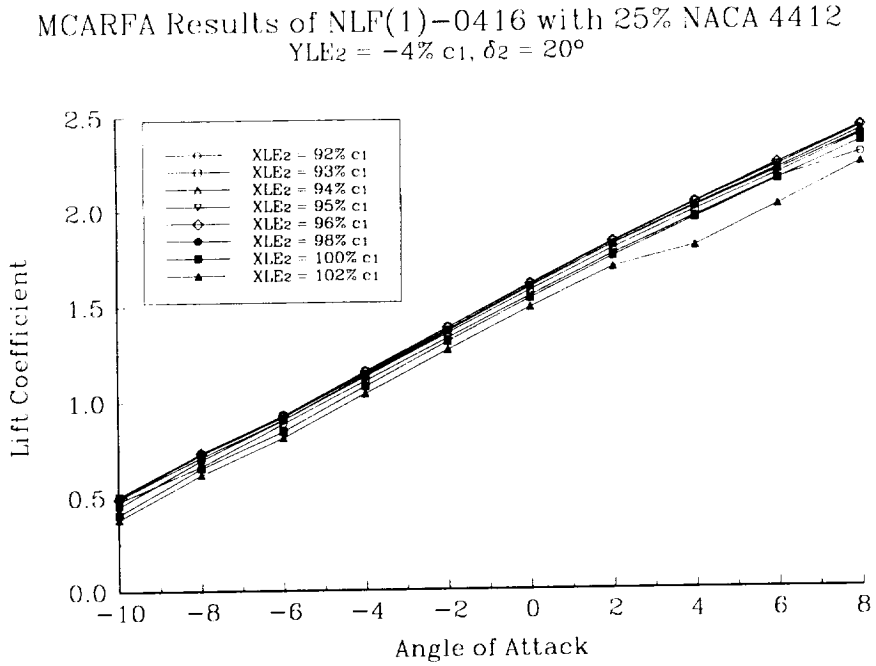

Fig. 27 Horizontal position effect on lift coefficient at -4% and δ = 20°

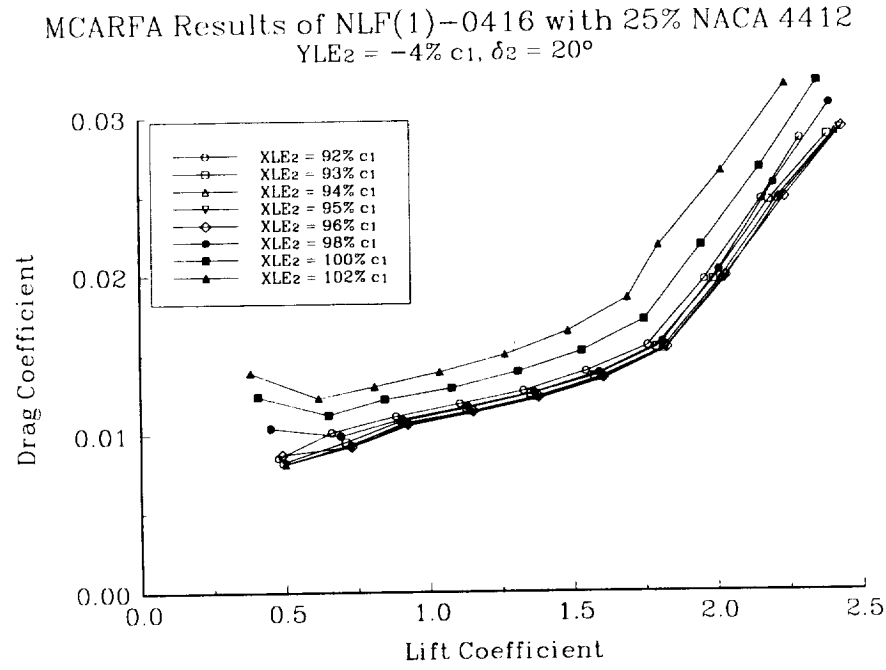

Fig. 28 Horizontal position effect on drag coefficient at -4% and δ = 20°

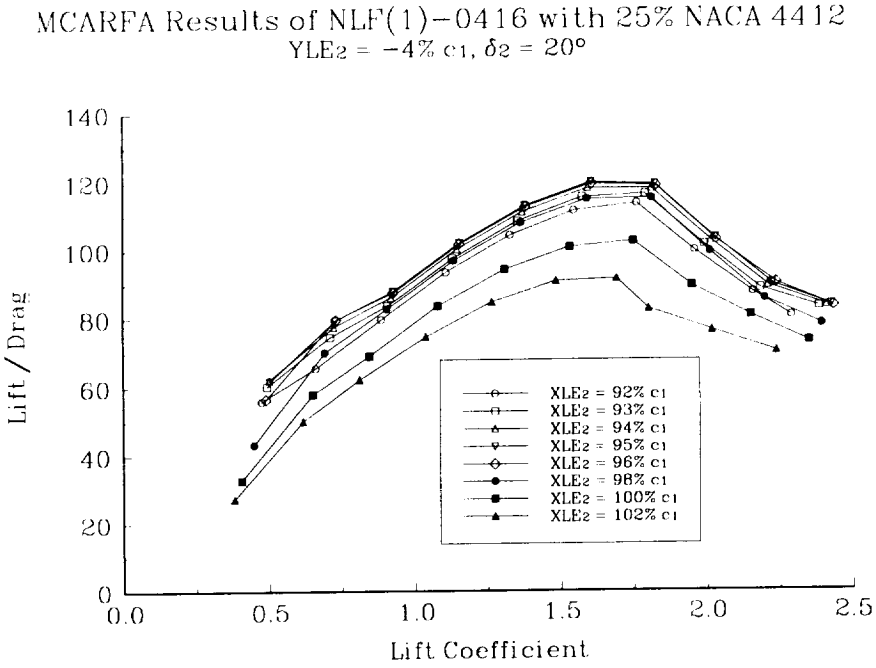

Fig. 29 Horizontal position effect on L/D ratio at -4% and δ = 20°

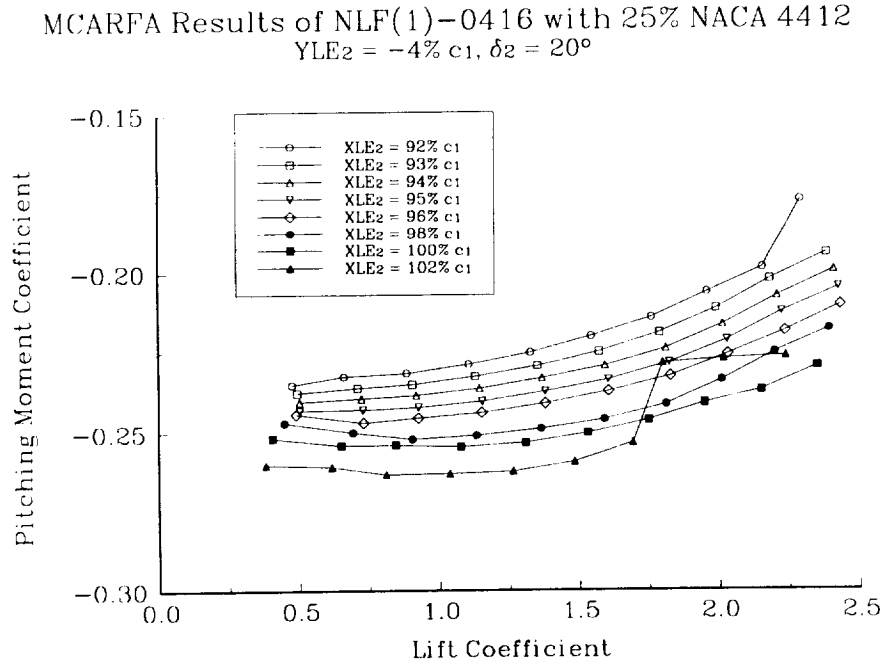

Fig. 30 Horizontal position effect on moment coefficient at -4% and δ = 20°

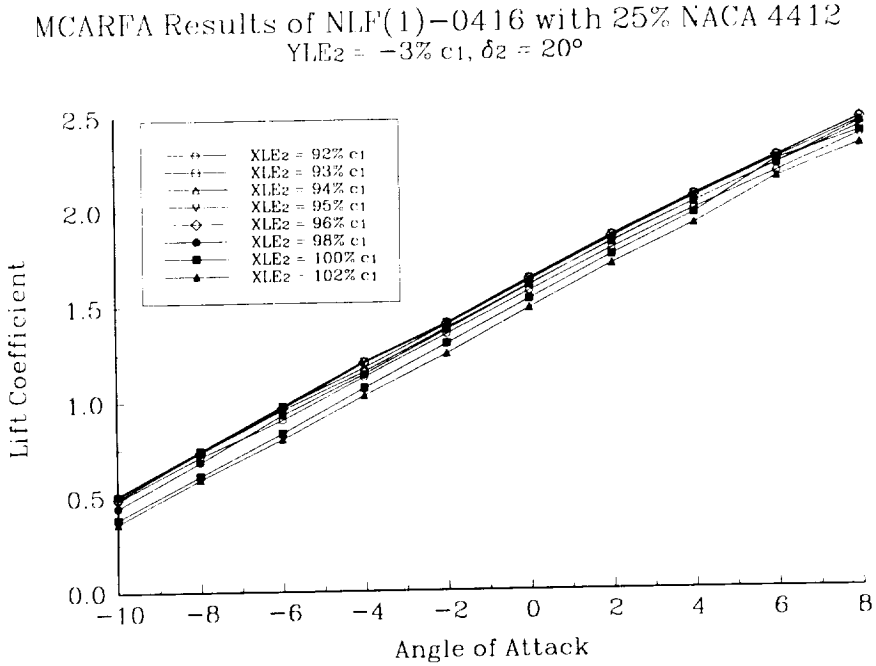

Fig. 31 Horizontal position effect on lift coefficient at -3% and δ = 20°

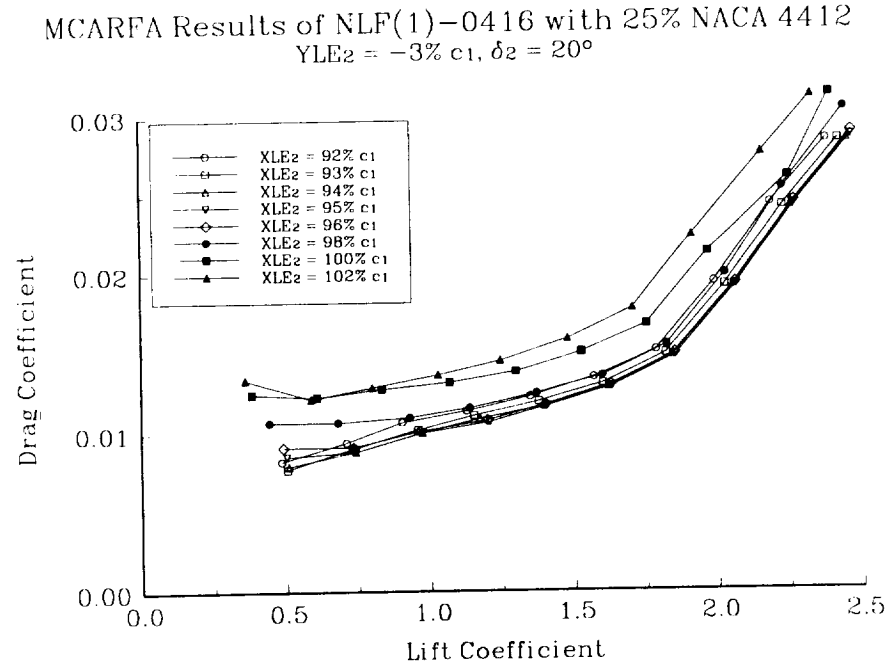

Fig. 32 Horizontal position effect on drag coefficient at -3% and δ = 20°

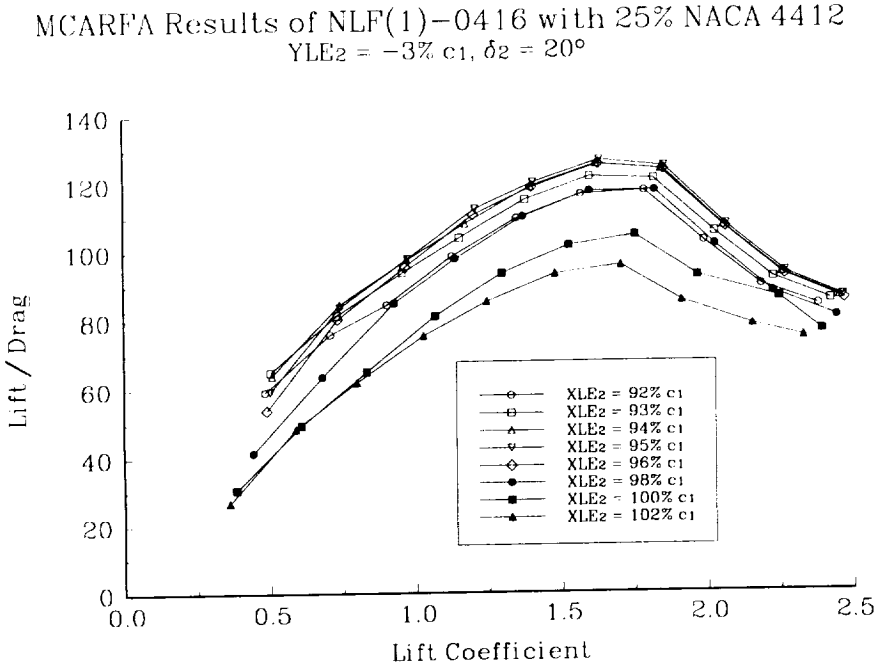

Fig. 33 Horizontal position effect on L/D ratio at -3% and δ = 20°

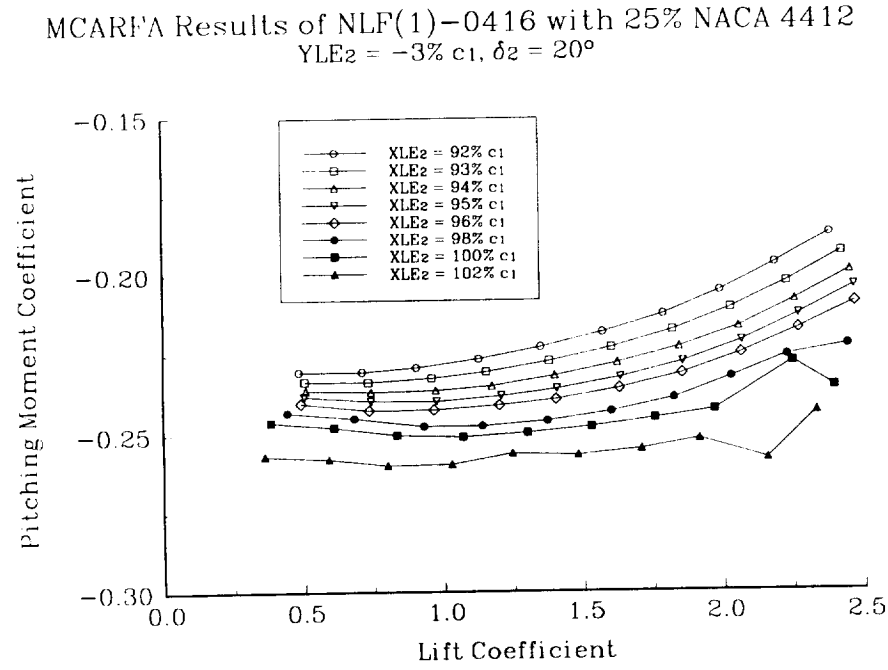

Fig. 34 Horizontal position effect on moment coefficient at -3% and δ = 20°

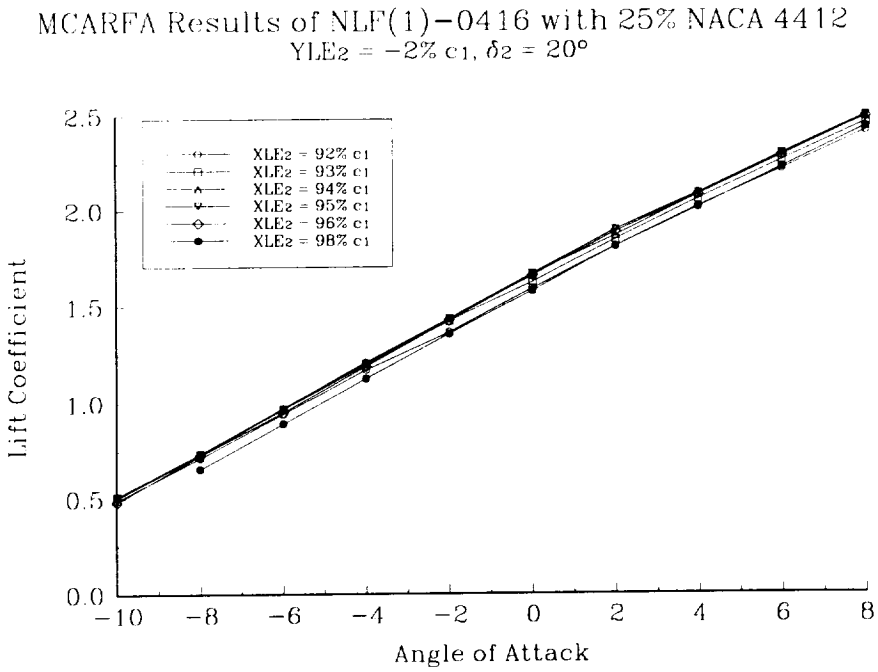

Fig. 35 Horizontal position effect on lift coefficient at -2% and δ = 20°

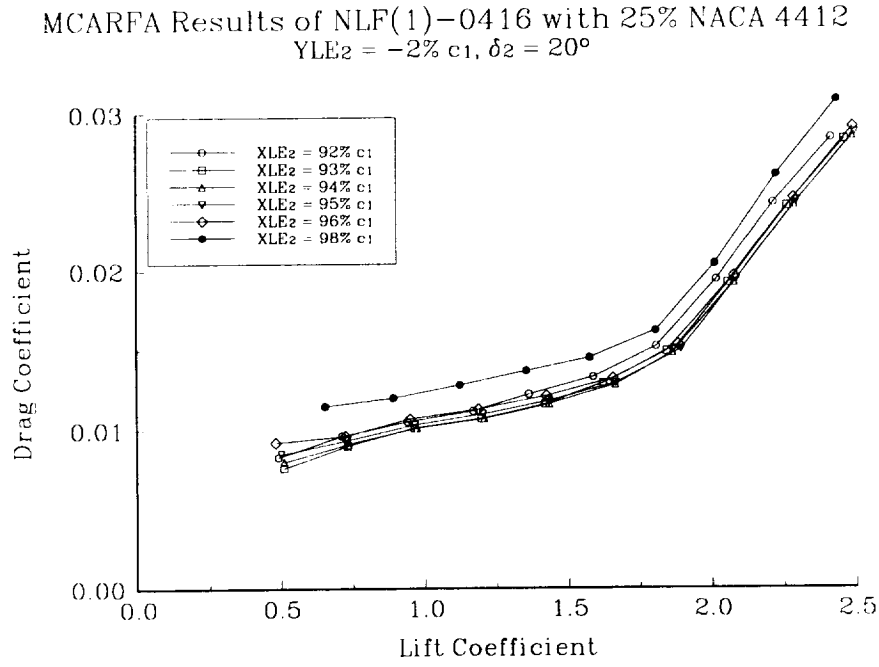

Fig. 36 Horizontal position effect on drag coefficient at -2% and δ = 20°

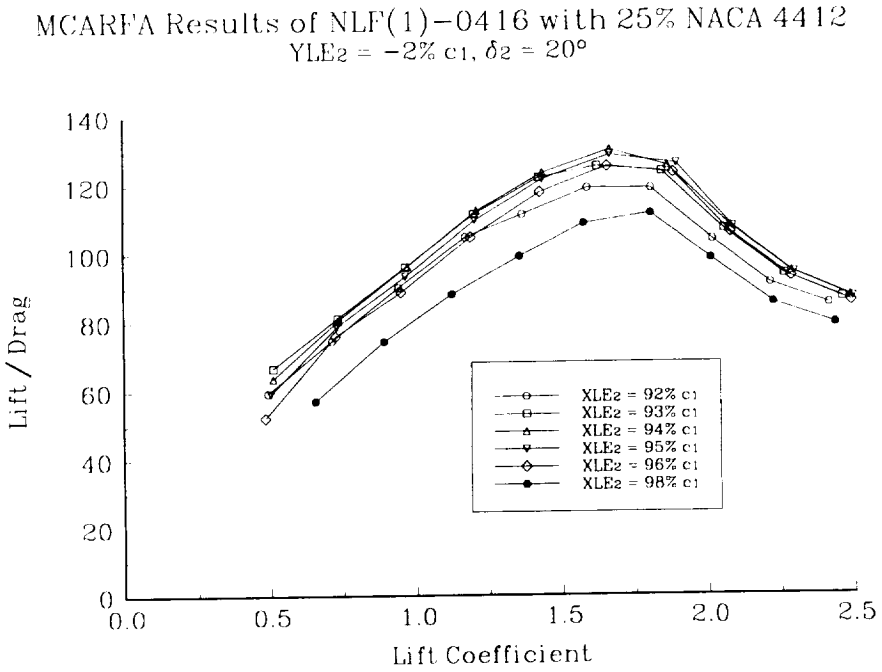

Fig. 37 Horizontal position effect on L/D ratio at -2% and δ = 20°

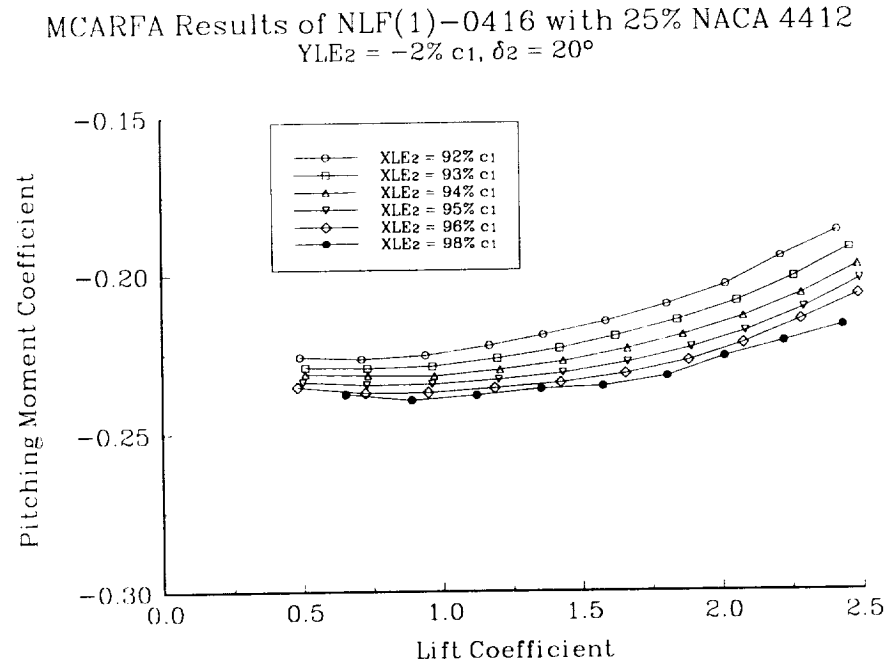

Fig. 38 Horizontal position effect on moment coefficient at -2% and δ = 20°

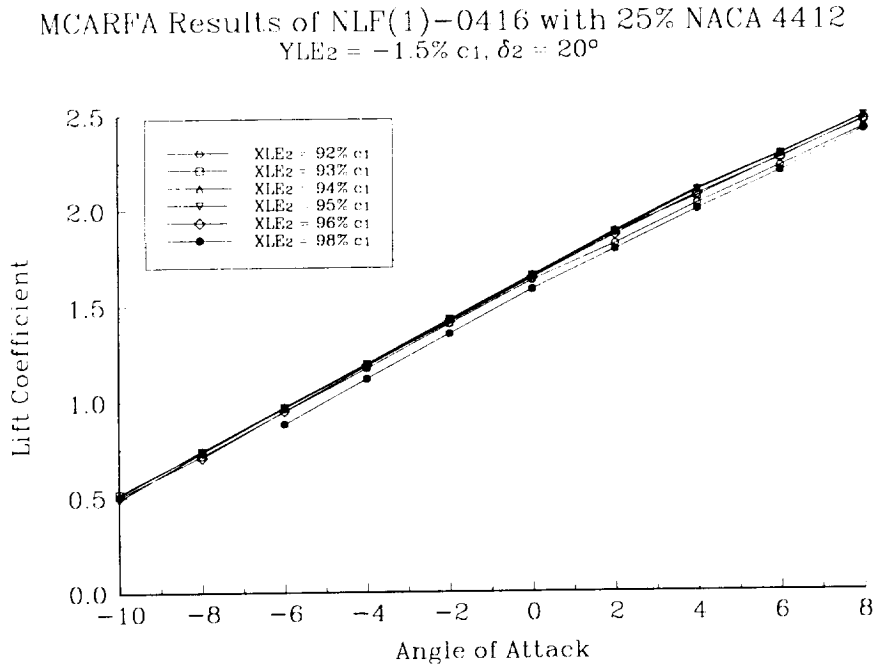

Fig. 39 Horizontal position effect on lift coefficient at -1.5% and δ = 20°

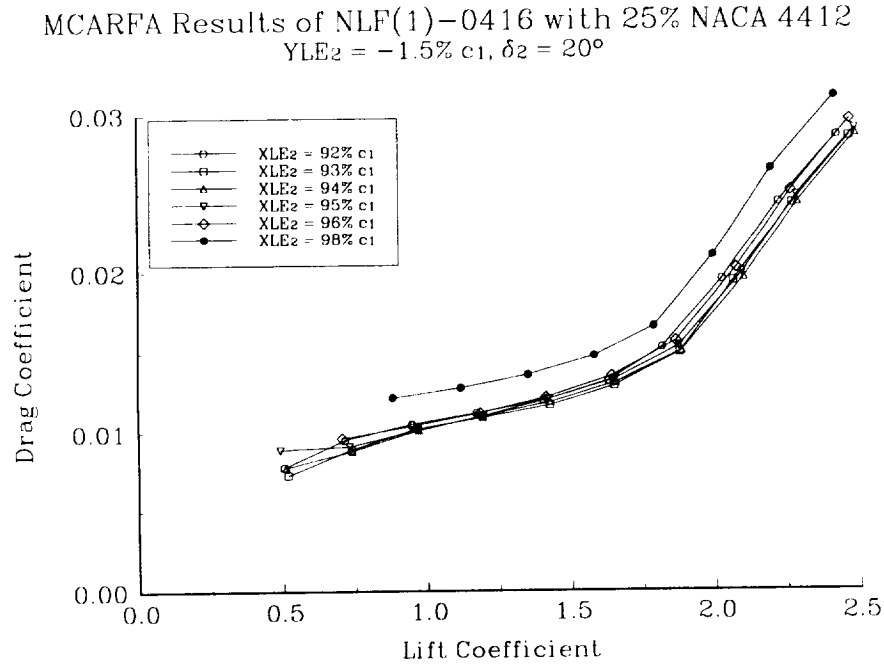

Fig. 40 Horizontal position effect on drag coefficient at -1.5% and δ = 20°

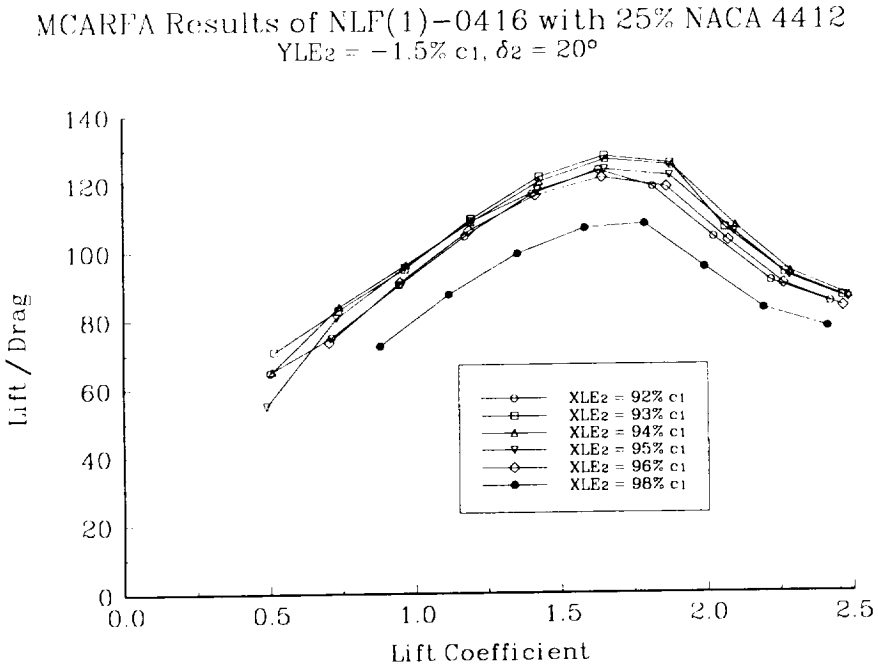

Fig. 41 Horizontal position effect on L/D ratio at -1.5% and δ = 20°

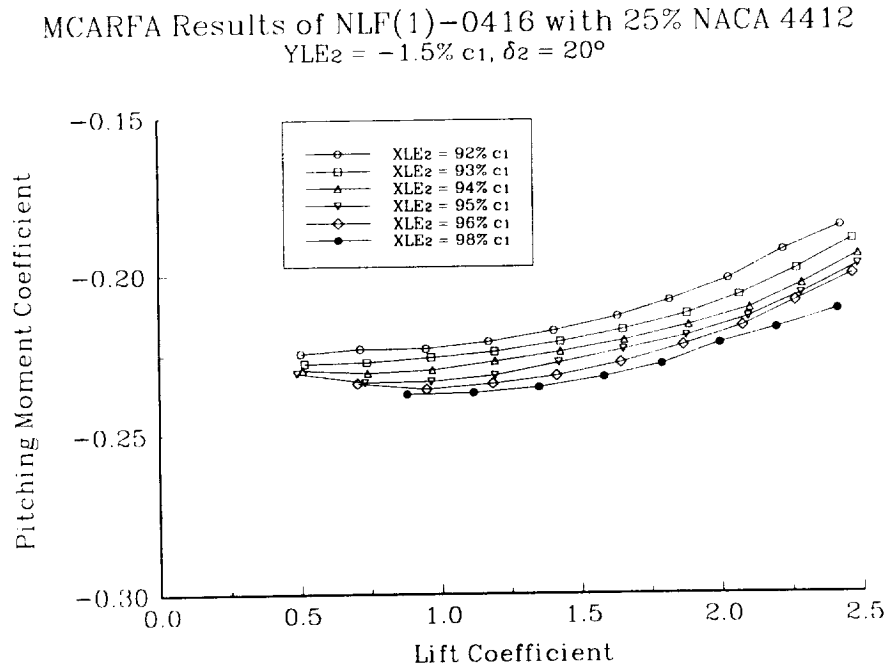

Fig. 42 Horizontal position effect on moment coefficient at -1.5% and δ = 20°

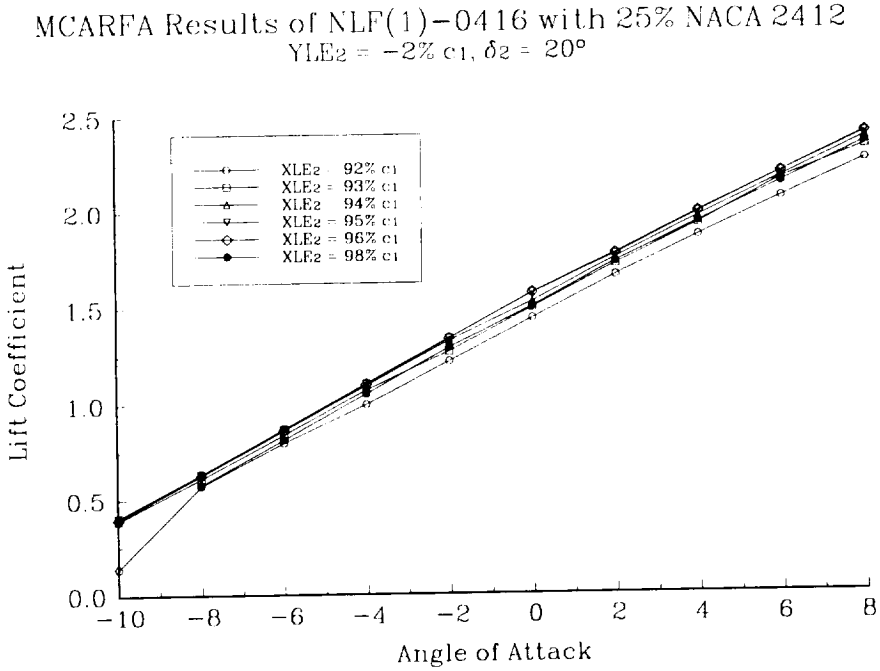

Fig. 43 Horizontal position effect on lift coefficient with NACA 2412

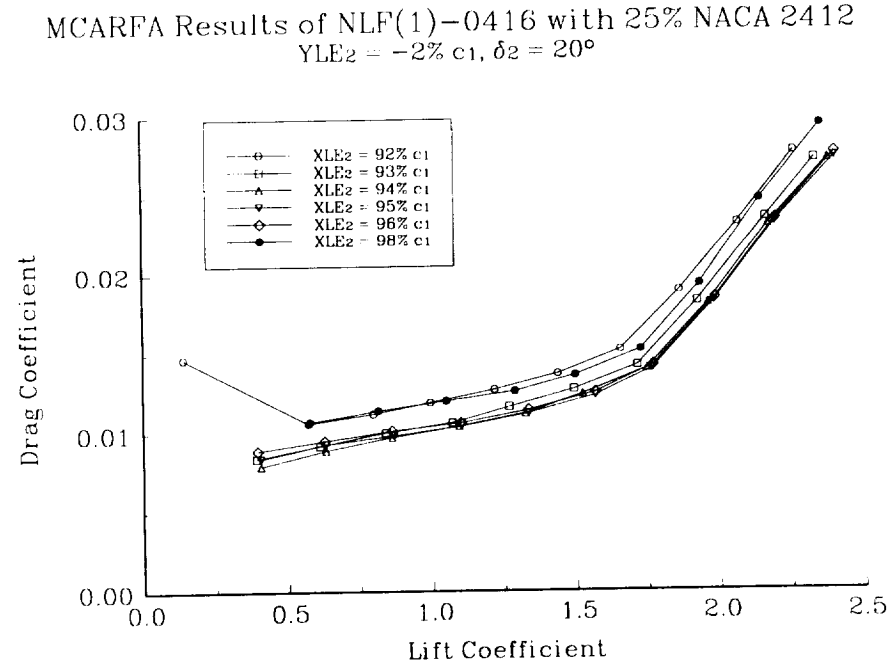

Fig. 44 Horizontal position effect on drag coefficient with NACA 2412

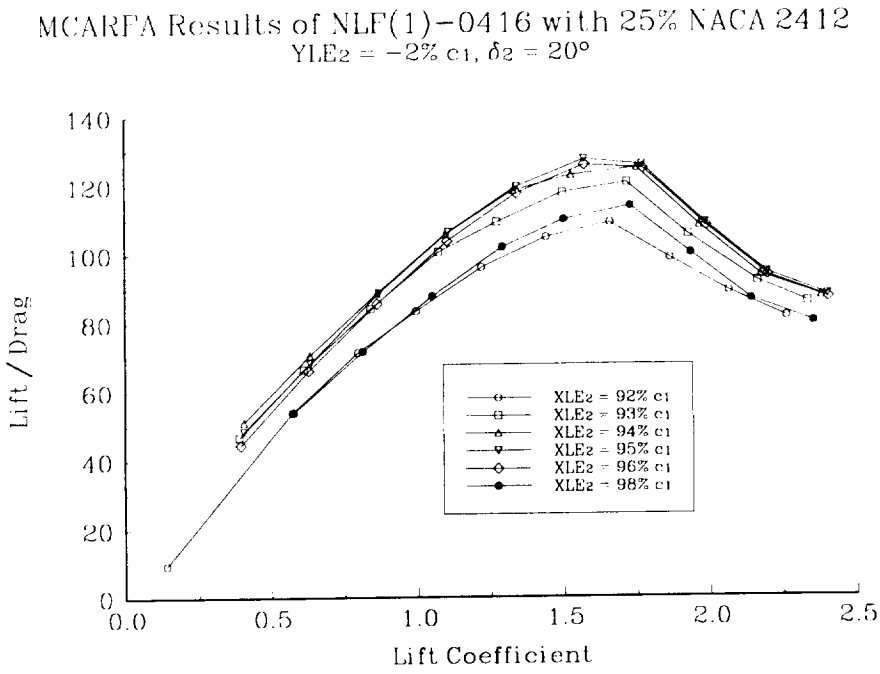

Fig. 45 Horizontal position effect on L/D ratio with NACA 2412

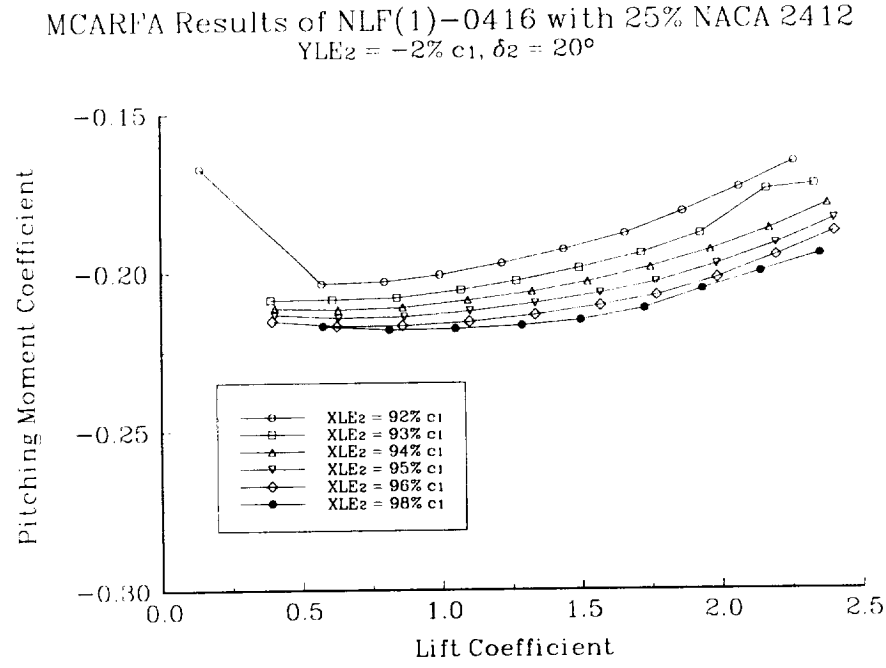

Fig. 46 Horizontal position effect on moment coefficient with NACA 2412

The best relative position was expected to change with various secondary element deflections due to the changing slot geometry so numerical results were obtained for the NACA 4412 deflected relative angles of 10° through 30° at 2% below the primary leading edge.

Lift and drag coefficient results for the 10° deflection case show very small changes with different relative positions (Figs. 47-48). Lift to drag ratio results, however, show a slight L/D improvement with the secondary airfoil located at 93% behind the primary leading edge (Fig. 49). Moment coefficient results, as with previous cases, show the moment increases with the secondary element moved aft (Fig. 50).

The 15° deflection c_l and c_d results show lower lift and higher drag with the 98% position, but no significant change with the other cases (Figs. 51-52). The L/D ratio plot confirms the c_l and c_d results showing no significant change at the 92% through 95% positions (Fig. 53). Again the moment coefficient increases with the further aft position of the secondary element (Fig. 54).

The c_l results for the 25° deflection case show the highest c_{lmax} to be at the 95% and 96% position (Fig. 55). The c_d values are lowest with the 95% and 96% cases (Fig. 56), and the L/D ratio is a maximum for the 95% case through most of the c_l range (Fig. 57). Moment coefficient results show the same trends as previously seen (Fig. 58).

The L/D results show a spike in the curve near a c_l of 0.75. This spike is calculated because the drag is continuing to drop as the lift is linearly increasing. This drag reduction is accompanied by an increase in the amount of laminar flow calculated on both surfaces. As the angle of attack is increased, more and more laminar flow is calculated on the lower surface of the primary element, but the transition has yet to

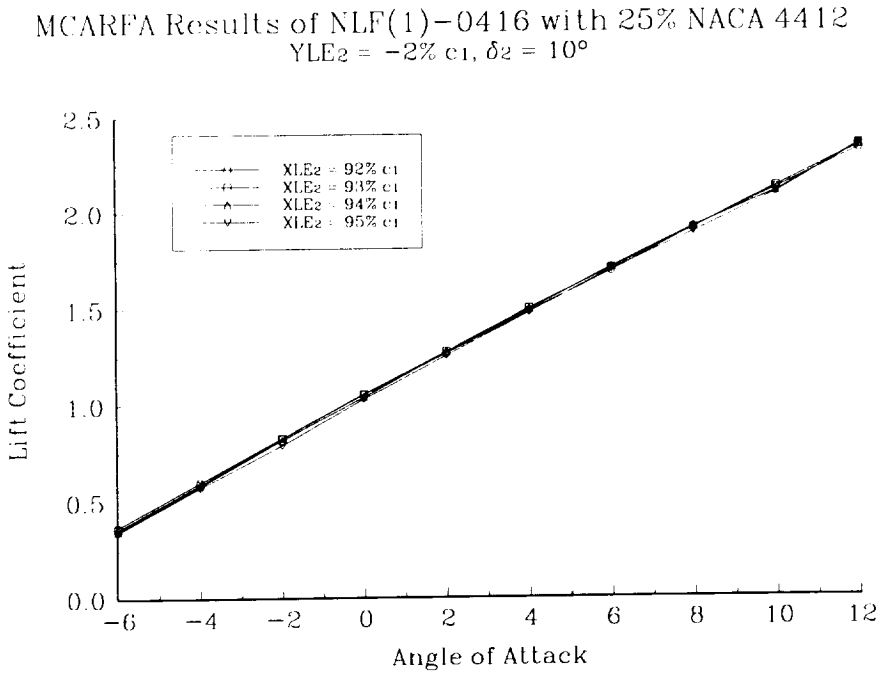

Fig. 47 Horizontal position effect on lift coefficient at -2% and δ = 10°

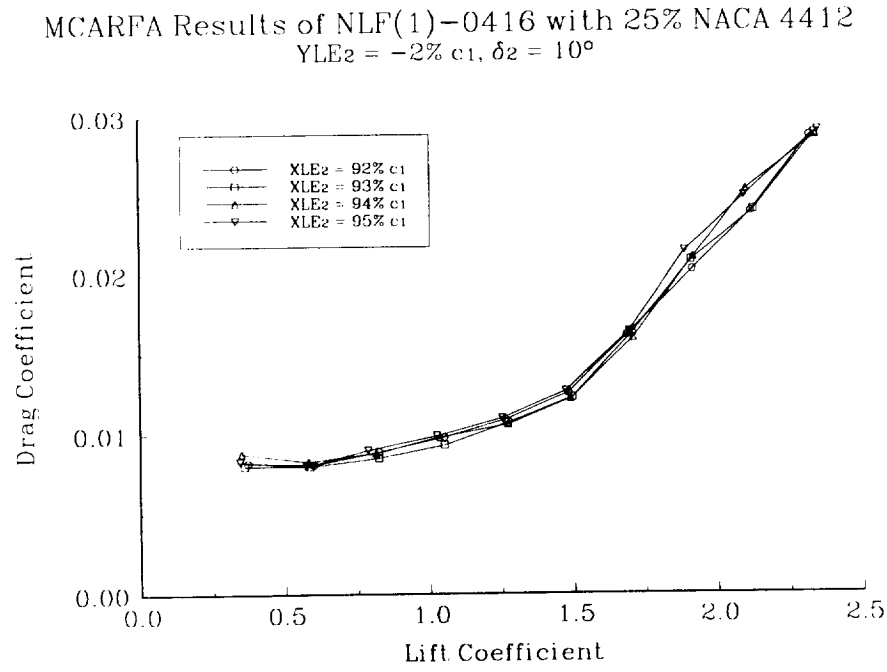

Fig. 48 Horizontal position effect on drag coefficient at -2% and δ = 10°

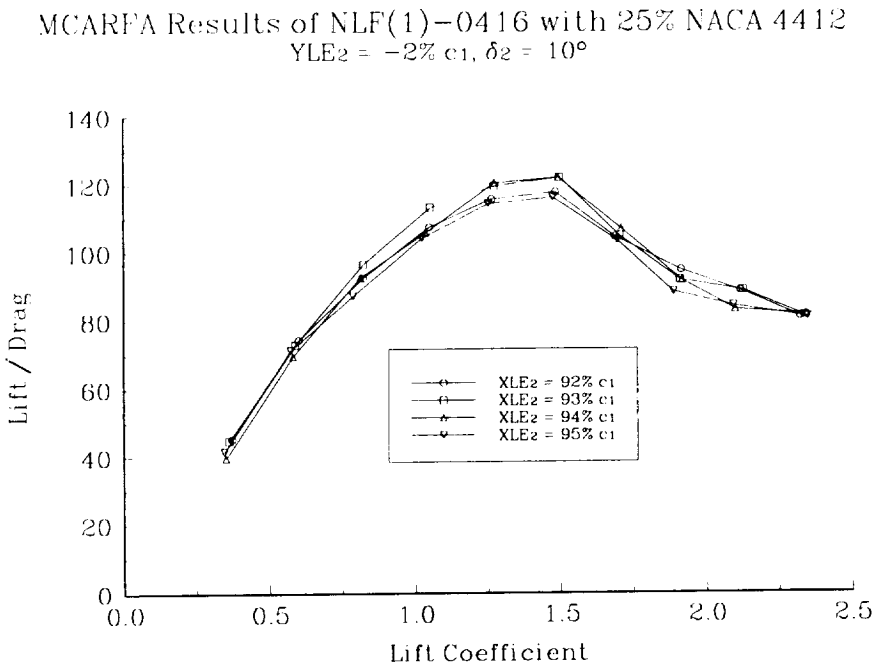

Fig. 49 Horizontal position effect on L/D ratio at -2% and δ = 10°

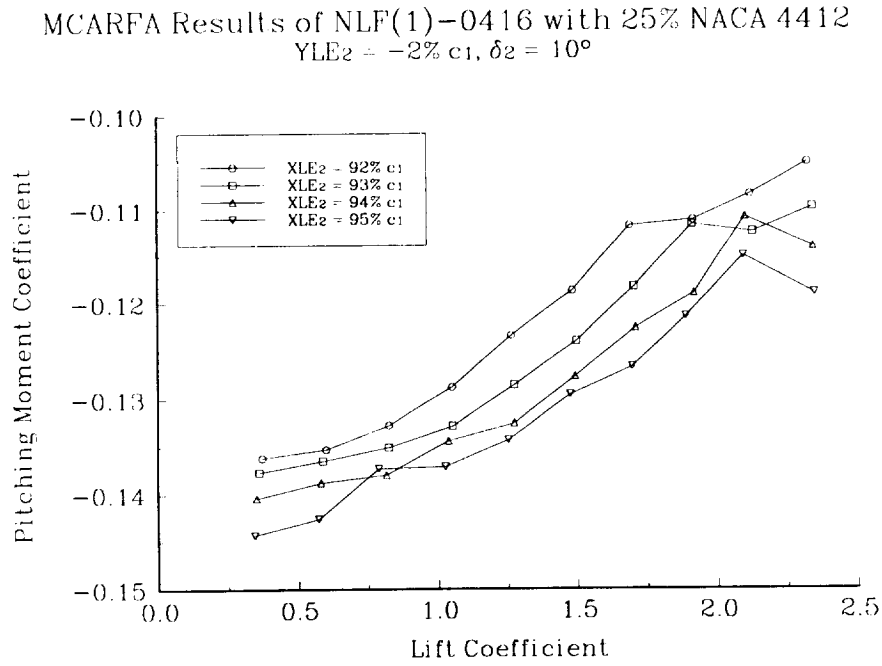

Fig. 50 Horizontal position effect on moment coefficient at -2% and δ = 10°

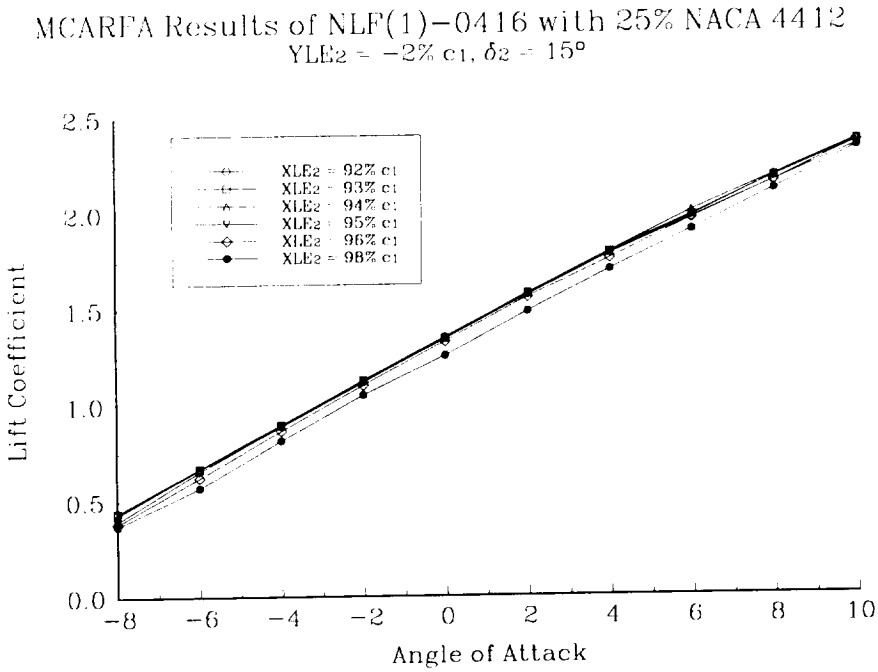

Fig. 51 Horizontal position effect on lift coefficient at -2% and δ = 15°

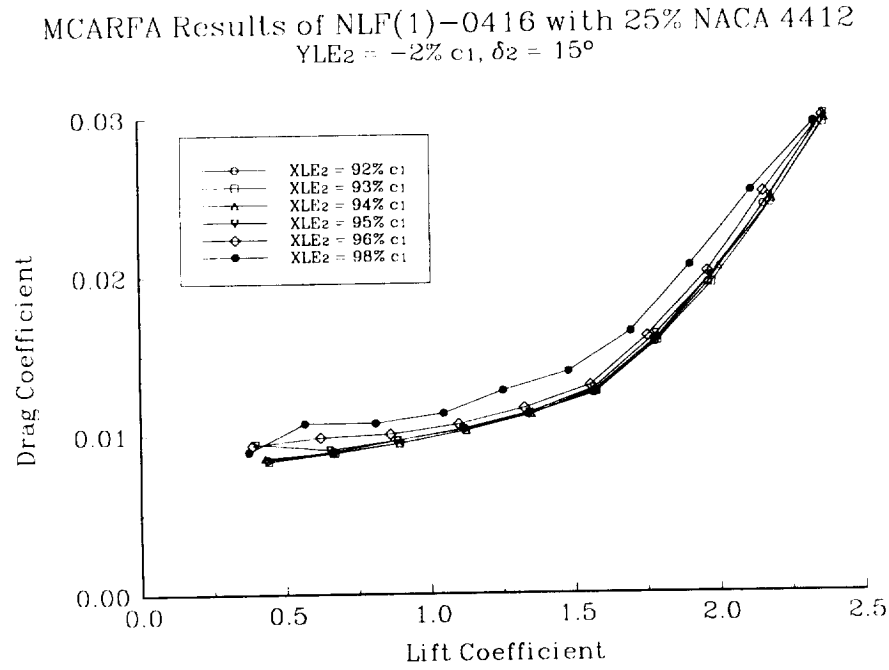

Fig. 52 Horizontal position effect on drag coefficient at -2% and δ = 15°

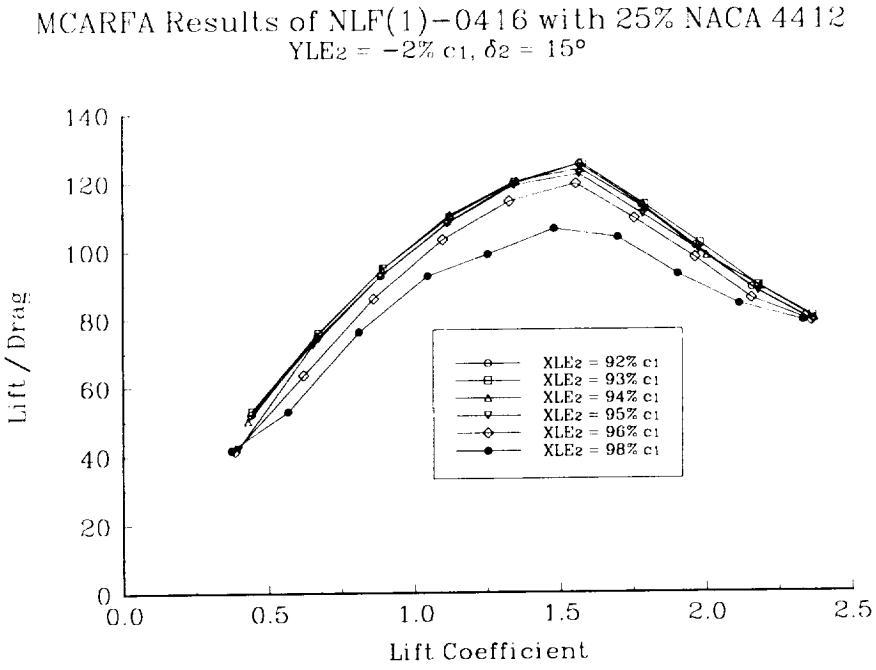

Fig. 53 Horizontal position effect on L/D ratio at -2% and δ = 15°

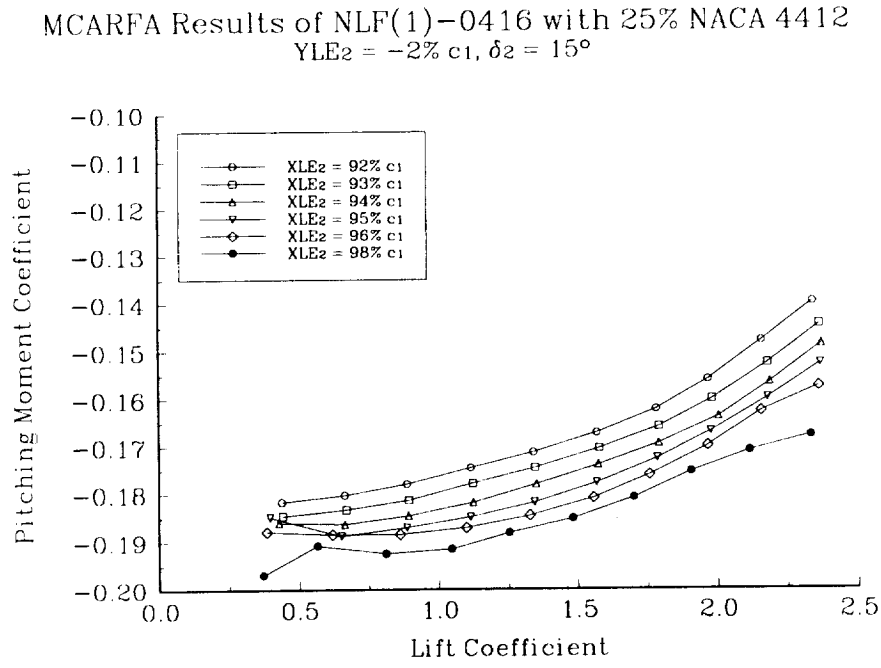

Fig. 54 Horizontal position effect on moment coefficient at -2% and δ = 15°

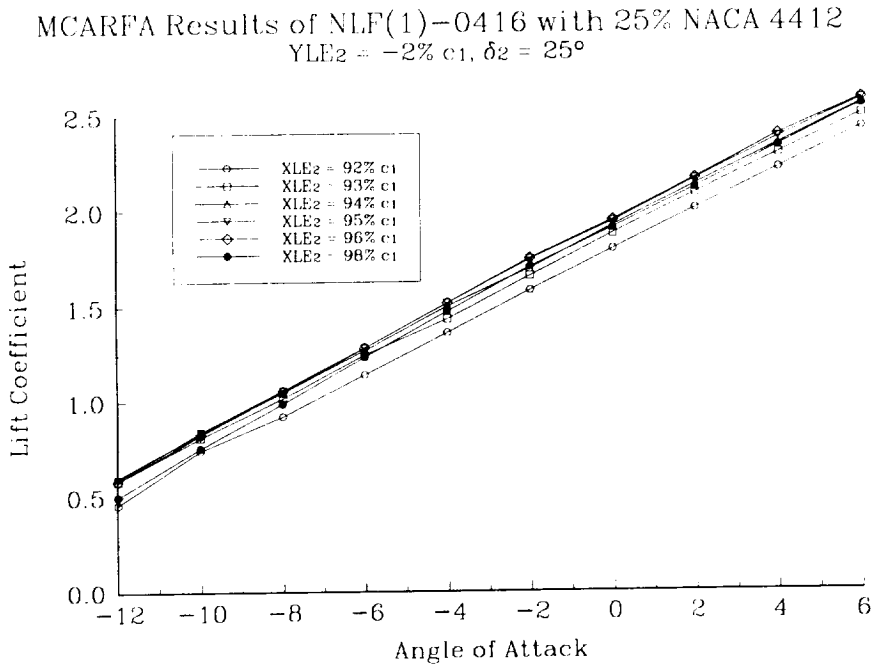

Fig. 55 Horizontal position effect on lift coefficient at -2% and δ = 25°

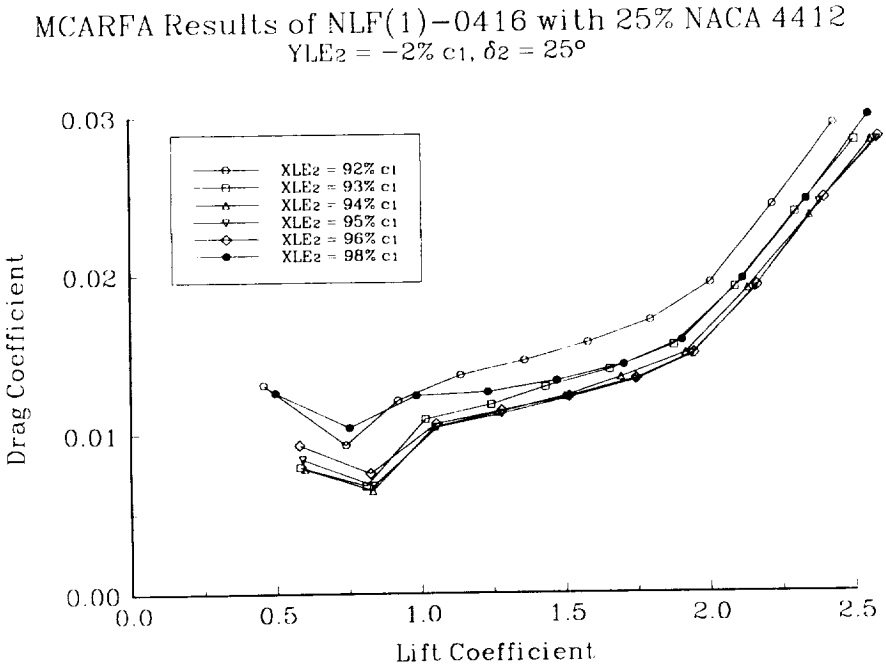

Fig. 56 Horizontal position effect on drag coefficient at -2% and δ = 25°

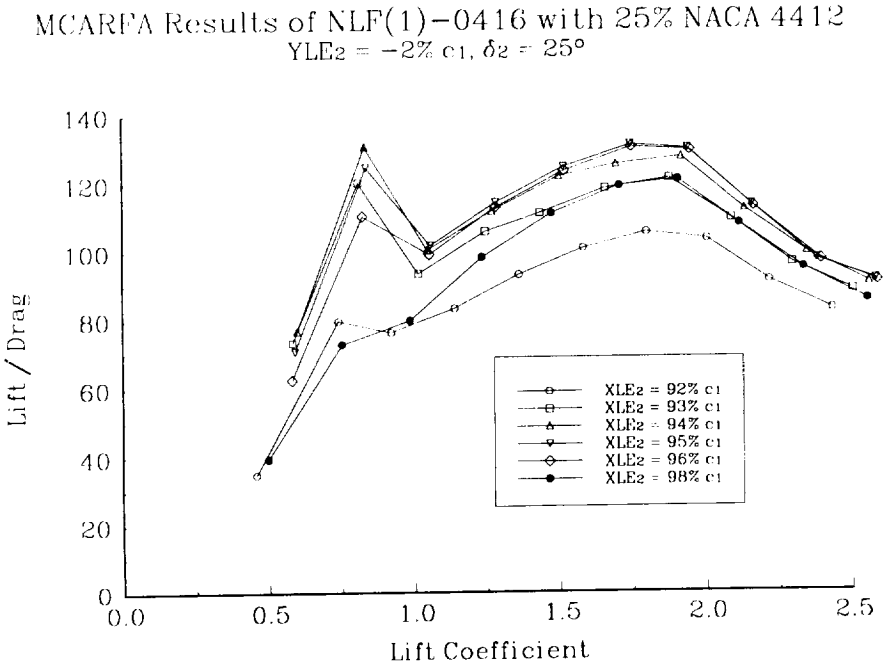

Fig. 57 Horizontal position effect on L/D ratio at -2% and δ = 25°

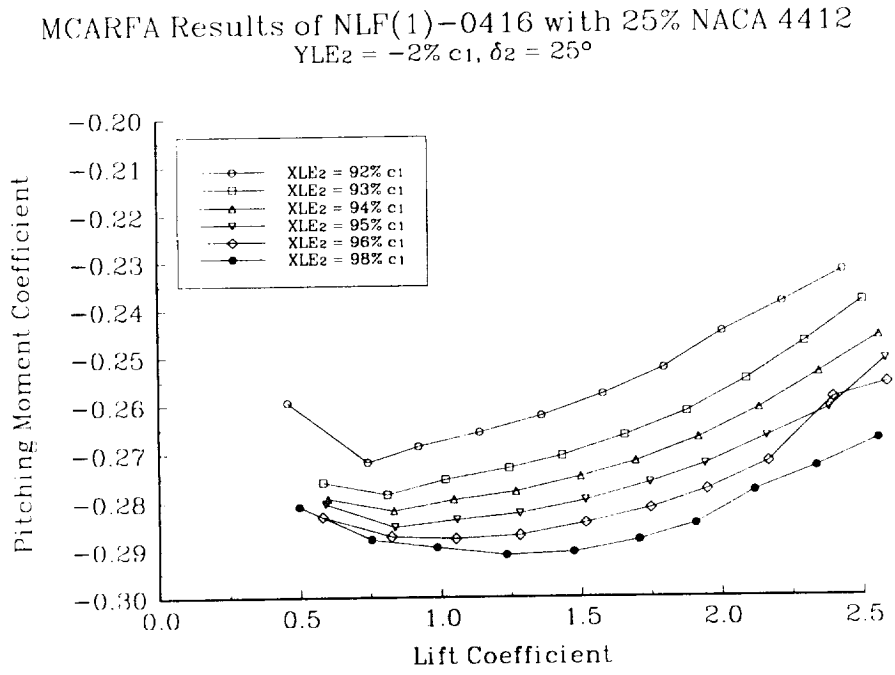

Fig. 58 Horizontal position effect on moment coefficient at -2% and δ = 25°

start moving forward on the upper surface so the net result is a large amount of laminar flow on both surfaces. The point on the L/D curve immediately after the spike is the location where the transition on the upper surface starts to move forward. There is reason to believe this spike in the L/D curve is real. Smith[17] states that the secondary element in a slotted flap system effectively increases the circulation about the primary element and helps to delay the onset of separation. The current data show the secondary element also delays transition.

The 30° deflection c_l results show little difference in the c_{lmax} value with positions of 95% through 98% (Fig. 59). Drag coefficient data shows the lowest c_d at the 95% and 96% positions (Fig. 60) and therefore the highest L/D is also at the 95% and 96% position (Fig. 61). Moment coefficients are again the highest at the most aft secondary element positions (Fig. 62). The 92% position c_m results are quite different than the other position answers with the values the least negative at the lower c_l's and crosses over to be the most negative case at the higher c_l conditions.

Vertical positions of -1.5% and -1% were also examined for the 30° deflection case because the c_{lmax} and L/D values for the -2% case proved to be higher than the 20° deflection case earlier. The -1.5% condition c_l results show the highest lift values at the 96% condition (Fig. 63) and the c_d results show the lowest drag at the 95% position (Fig. 64). The highest L/D for most of the c_l range was at the 95% case (Fig. 65). The moment results showed the largest c_m with the furthest aft position (Fig. 66). The -1% position results are nearly identical to the -1.5% answers (Figs. 67-70).

The optimum position of the leading edge of the second element for the 20° and 25° deflection cases was found to be 95% of the primary chord behind and 2% of the primary chord below the leading edge of the secondary element. The 30° deflection

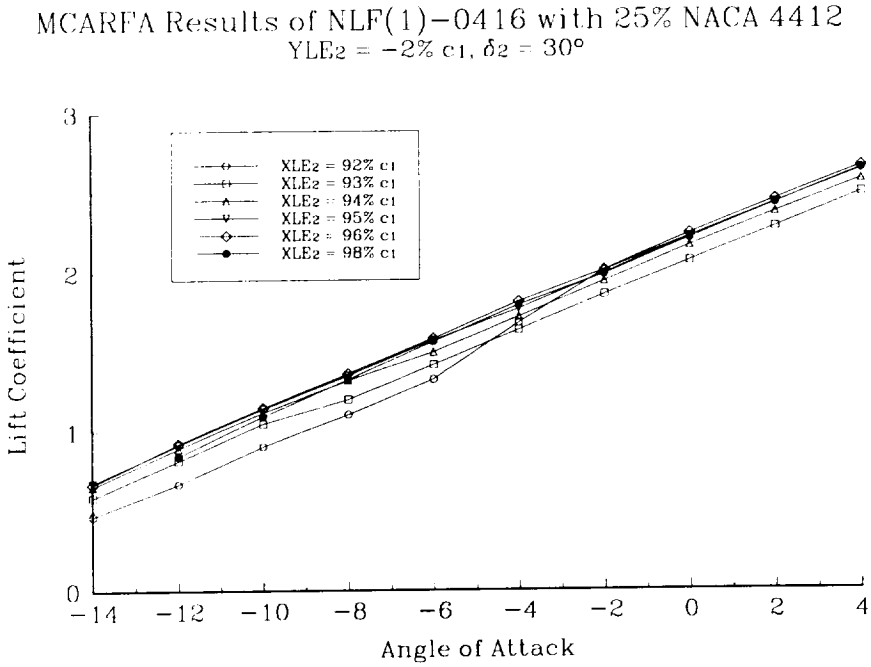

Fig. 59 Horizontal position effect on lift coefficient at -2% and δ = 30°

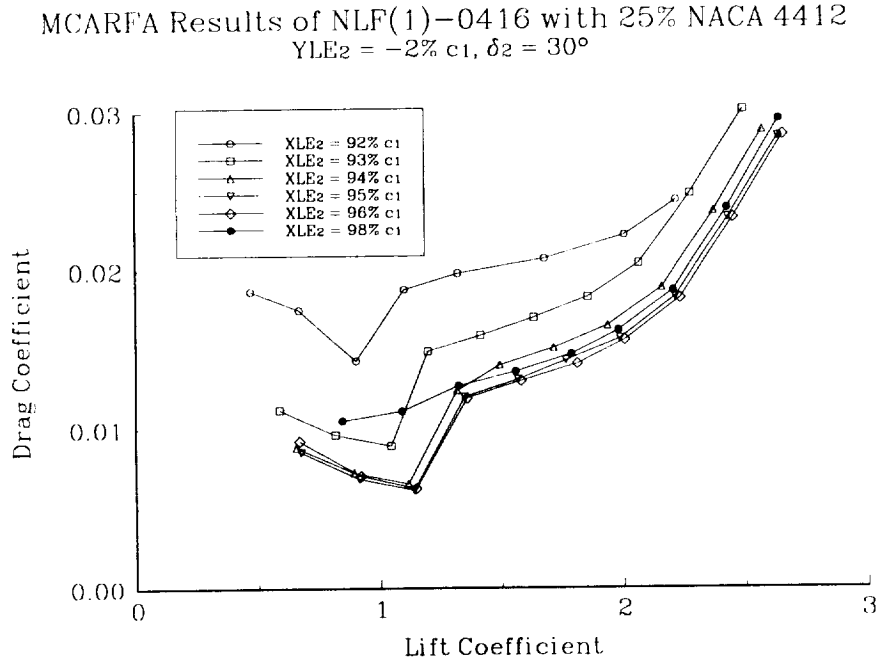

Fig. 60 Horizontal position effect on drag coefficient at -2% and δ = 30°

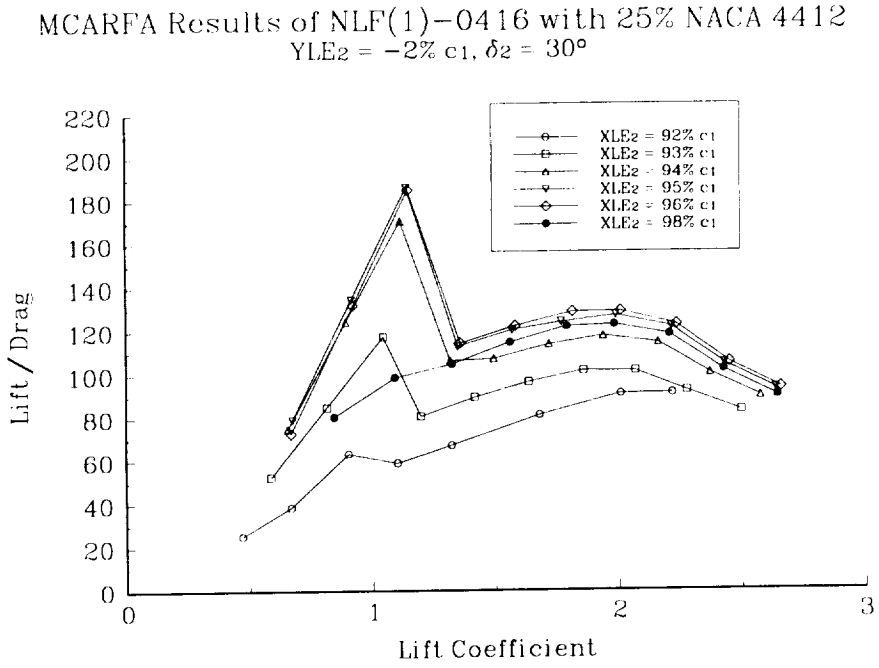

Fig. 61 Horizontal position effect on L/D ratio at -2% and δ = 30°

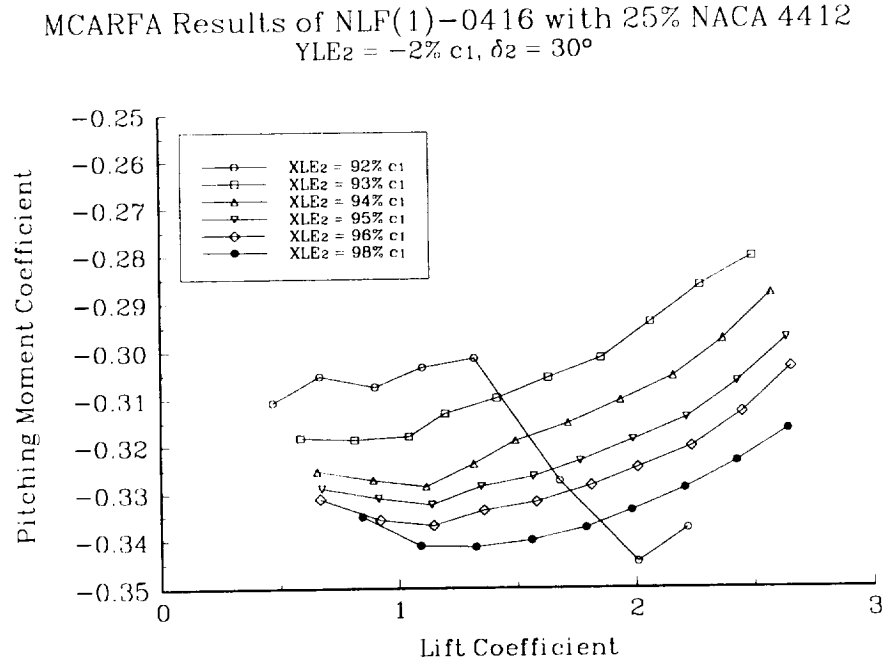

Fig. 62 Horizontal position effect on moment coefficient at -2% and δ = 30°

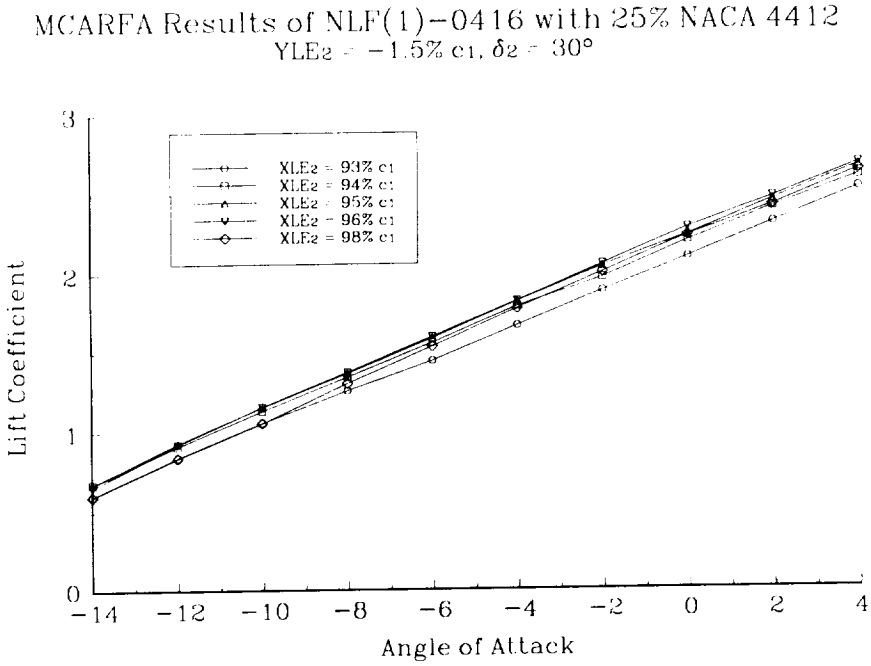

Fig. 63 Horizontal position effect on lift coefficient at -1.5% and δ = 30°

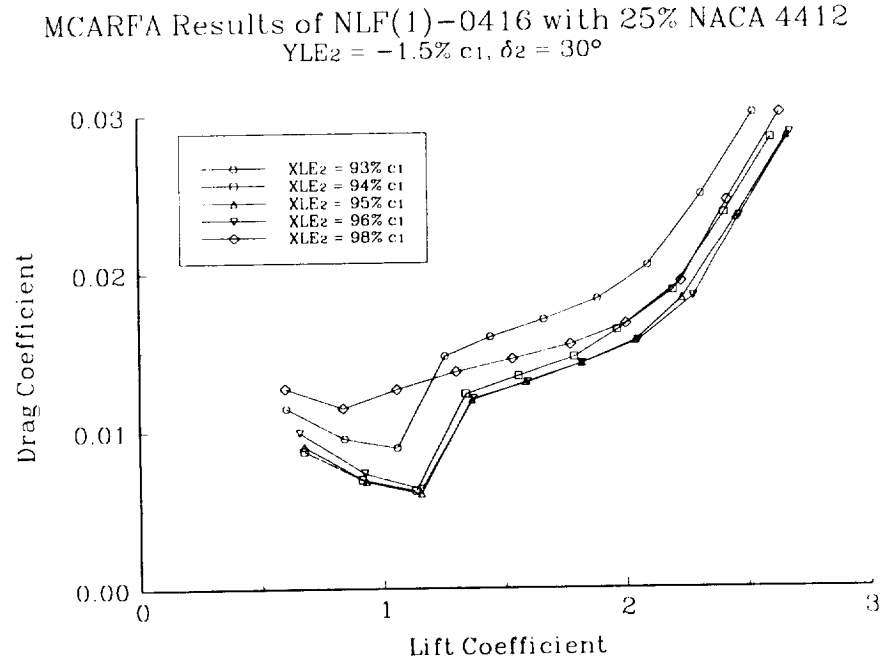

Fig. 64 Horizontal position effect on drag coefficient at -1.5% and δ = 30°

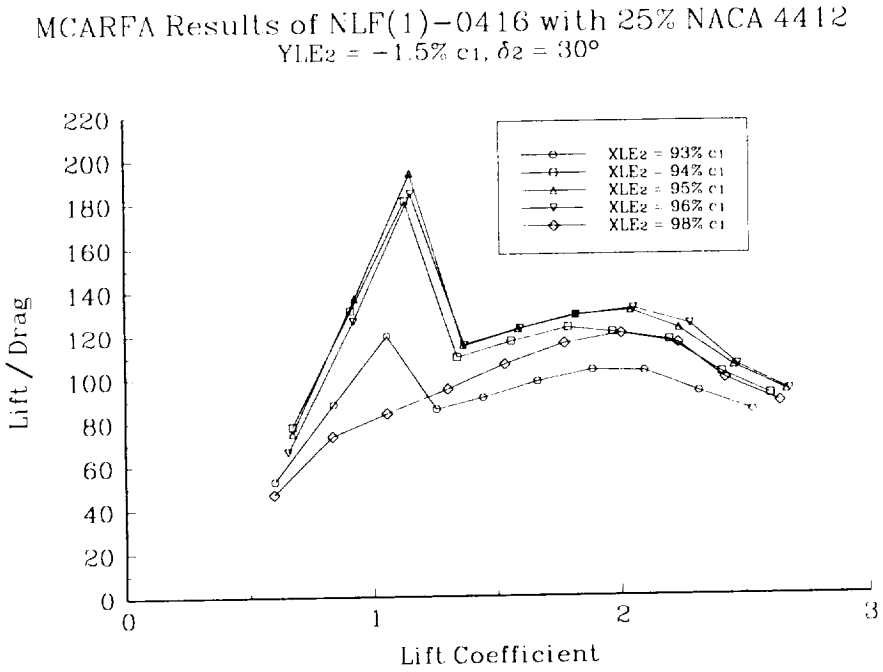

Fig. 65 Horizontal position effect on L/D ratio at -1.5% and δ = 30°

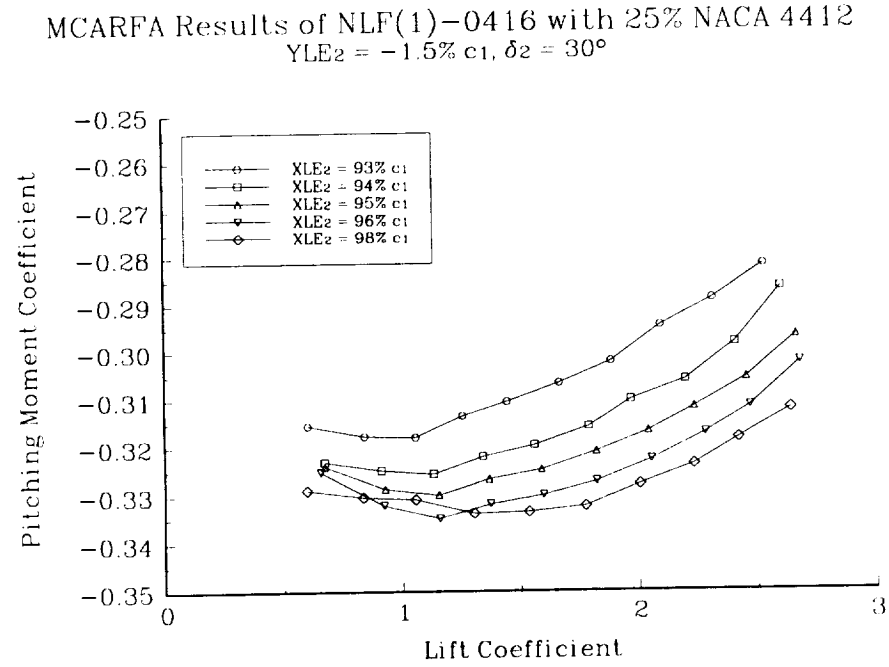

Fig. 66 Horizontal position effect on moment coefficient at -1.5% and δ = 30°

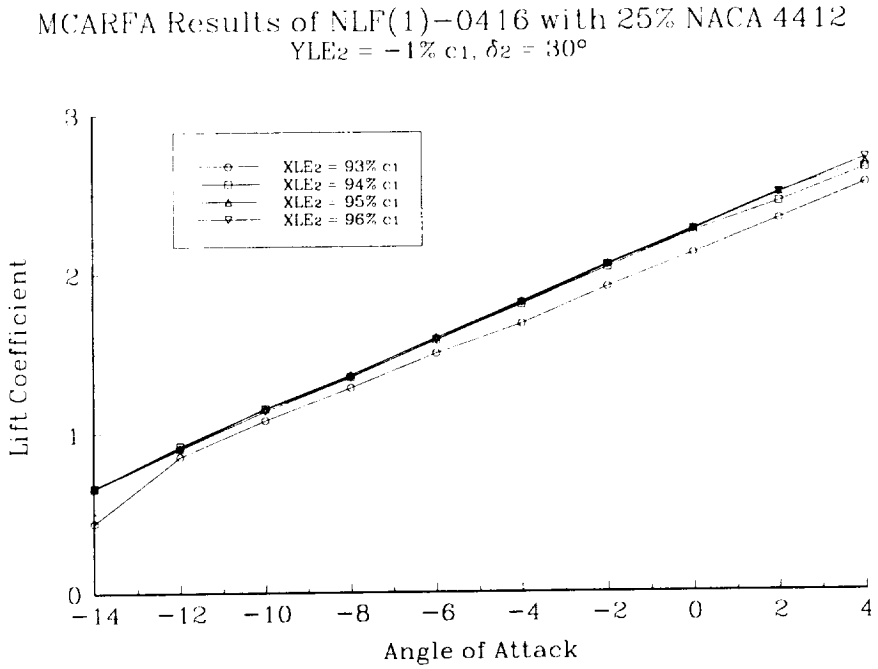

Fig. 67 Horizontal position effect on lift coefficient at -1% and δ = 30°

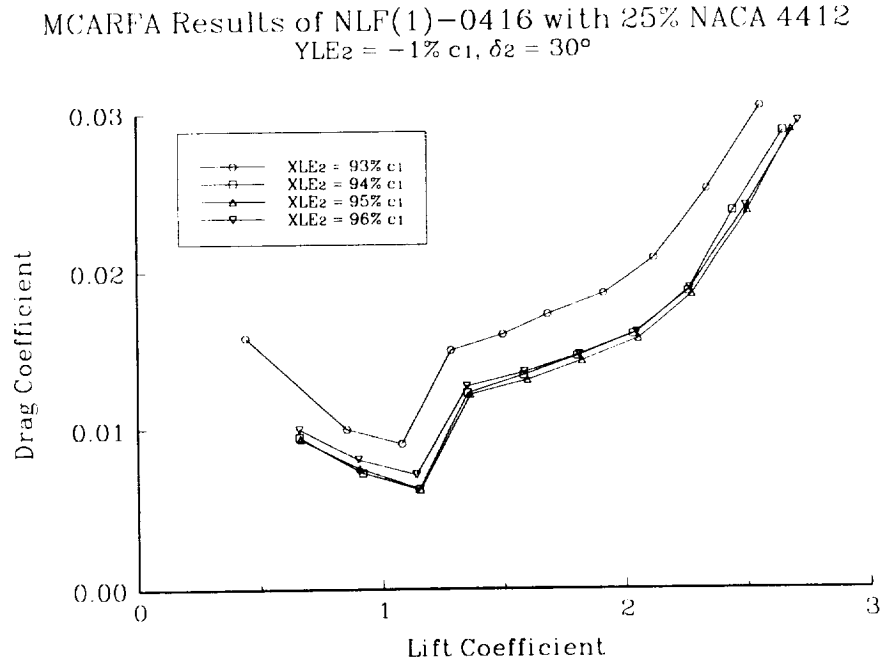

Fig. 68 Horizontal position effect on drag coefficient at -1% and δ = 30°

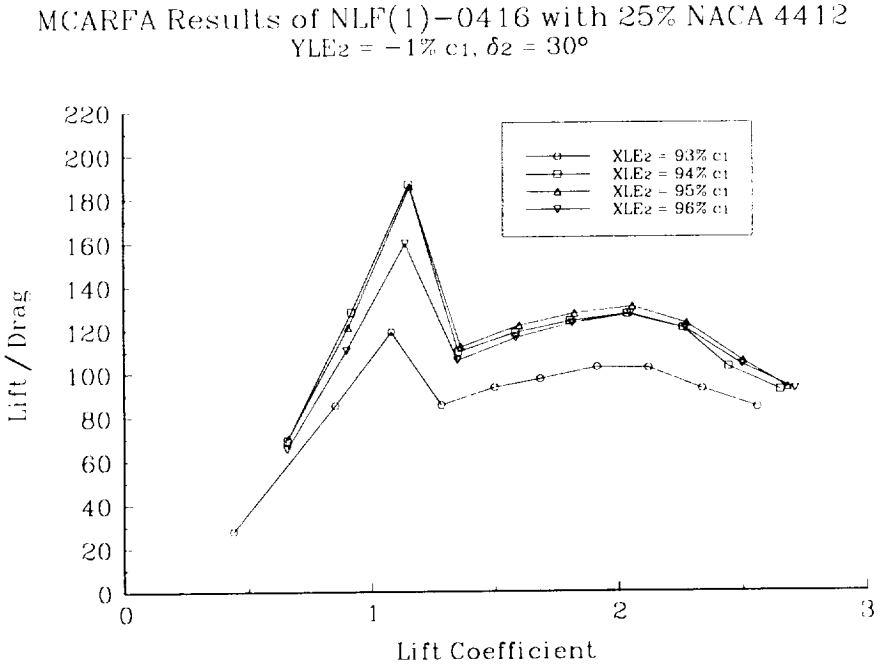

Fig. 69 Horizontal position effect on L/D ratio at -1% and δ = 30°

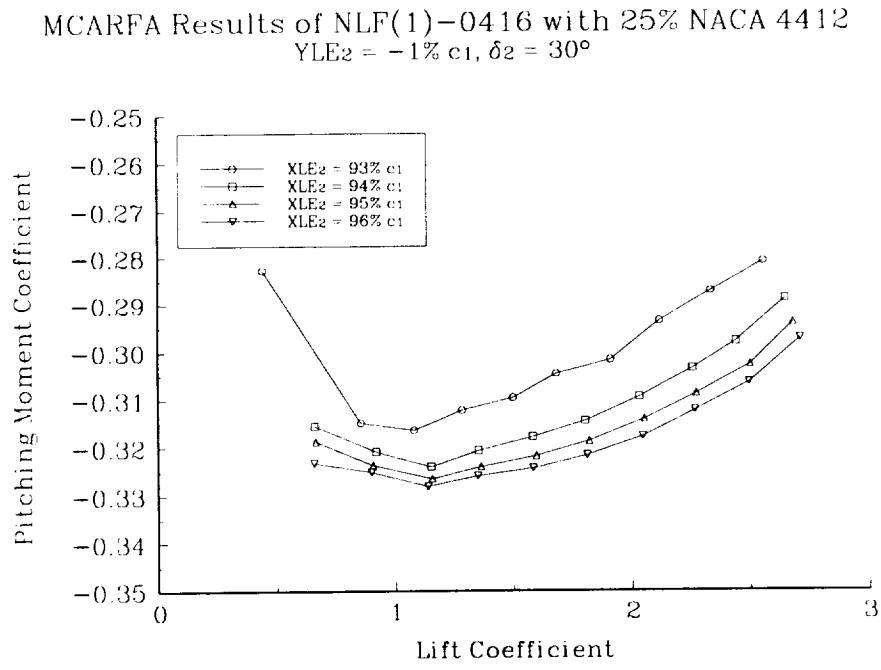

Fig. 70 Horizontal position effect on moment coefficient at -1% and δ = 30°

case optimum position was 95% of the primary chord behind and 1.5% of the primary chord below the primary leading edge.

Relative Angle

The effect of the relative angle on the aerodynamic loads was also studied. The leading edge of the secondary element was positioned 95% of the primary chord behind and 2% below the leading edge of the primary element. The secondary element of NACA 4412 section was deflected from 10° through 30° in 5° increments. The maximum lift coefficient increases with increasing deflection angle so the highest c_{lmax} was obtained with the 30° deflection case (Fig. 71). The lowest drag coefficient was also found at the 30° deflection case for the lower c_l range (Fig. 72). The highest L/D value at expected cruise conditions was obtained with the 30° deflection case (Fig. 73). The spike in the L/D curve discussed earlier is again present at the 25° and 30° deflection cases; without this spike, the 20° deflection case would have the highest L/D at the cruise case. The 20° deflection case also has the highest L/D through much of the mid c_l range. As expected, the moment coefficient results show the largest moments with the greatest second element deflection, increasing approximately 0.05 for each 5° deflection increase (Fig. 74).

Based on the above study, the 30° deflection case was found to be the best because it had the highest c_{lmax} value and the highest L/D at the expected cruise c_l of about 0.6 at a Reynolds number of $3x10^6$. The 20° deflection case was also kept for future study based on the more conservative L/D curve and the nearly 30% lower pitching moment.

Modified Profile Shapes

The parametric variation study above found the optimum geometry for the new two element airfoil to be made up of a primary element with a NASA NLF(1)-0416

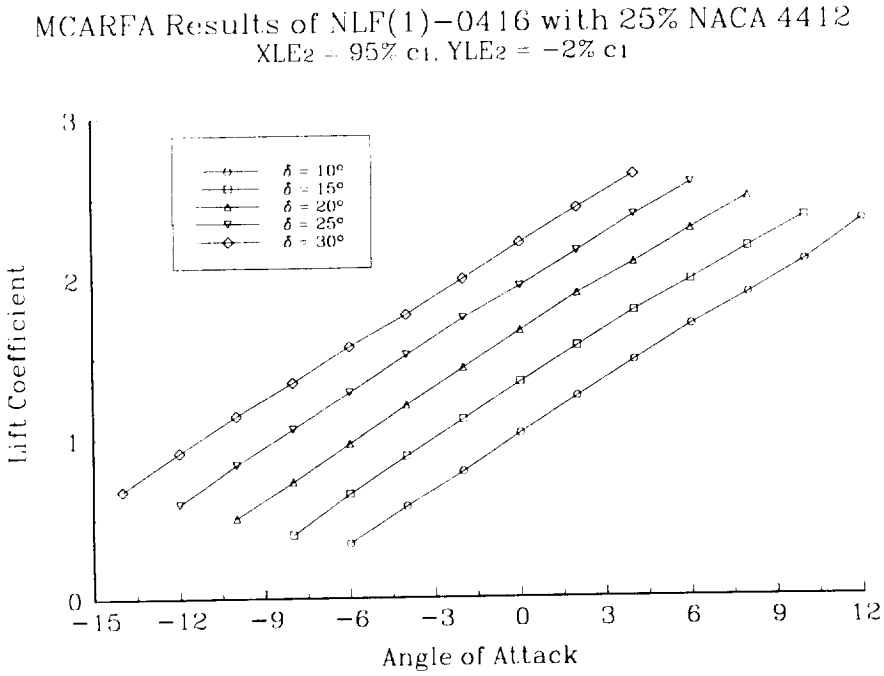

Fig. 71 Relative angle effect on lift coefficient

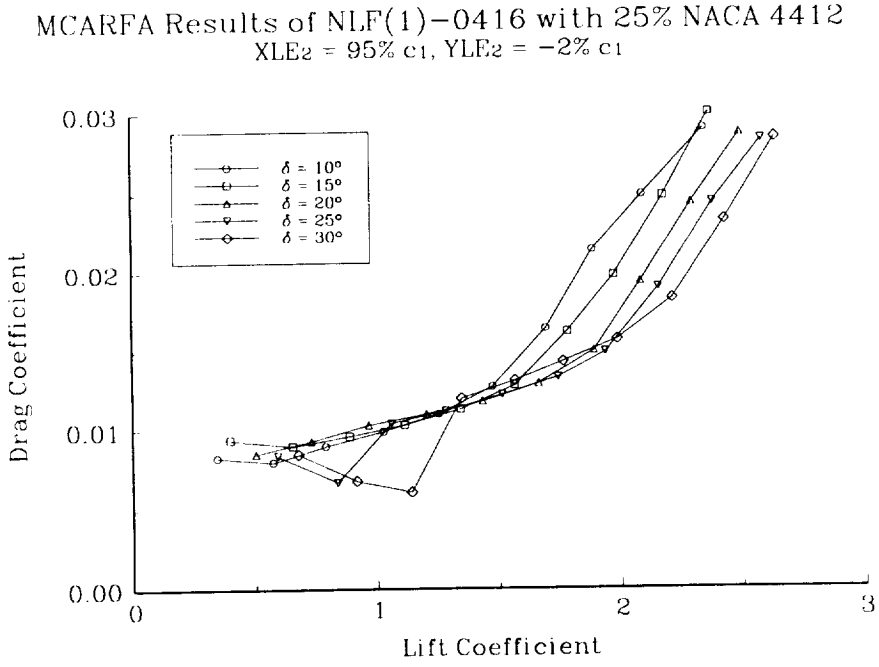

Fig. 72 Relative angle effect on drag coefficient

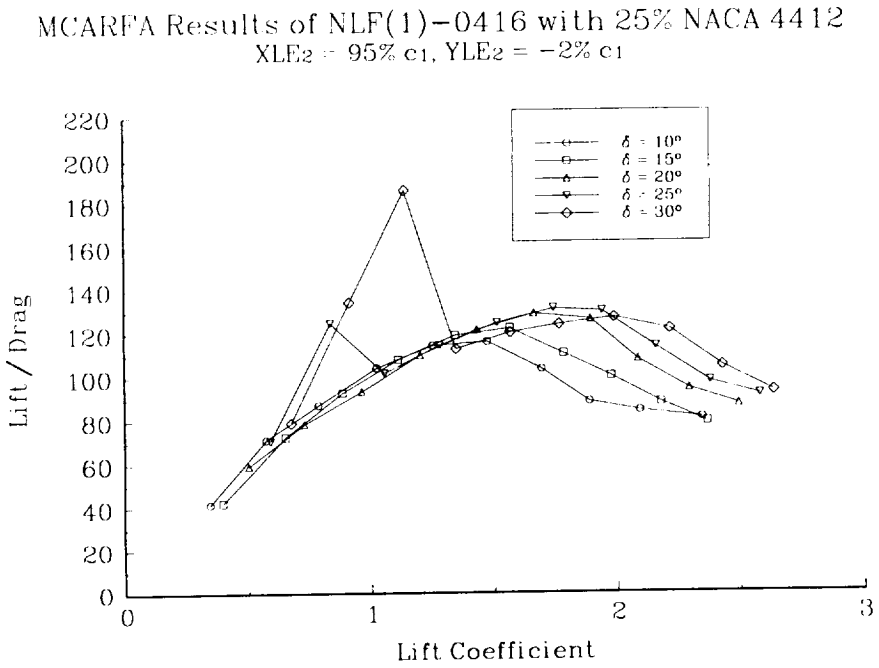

Fig. 73 Relative angle effect on L/D ratio

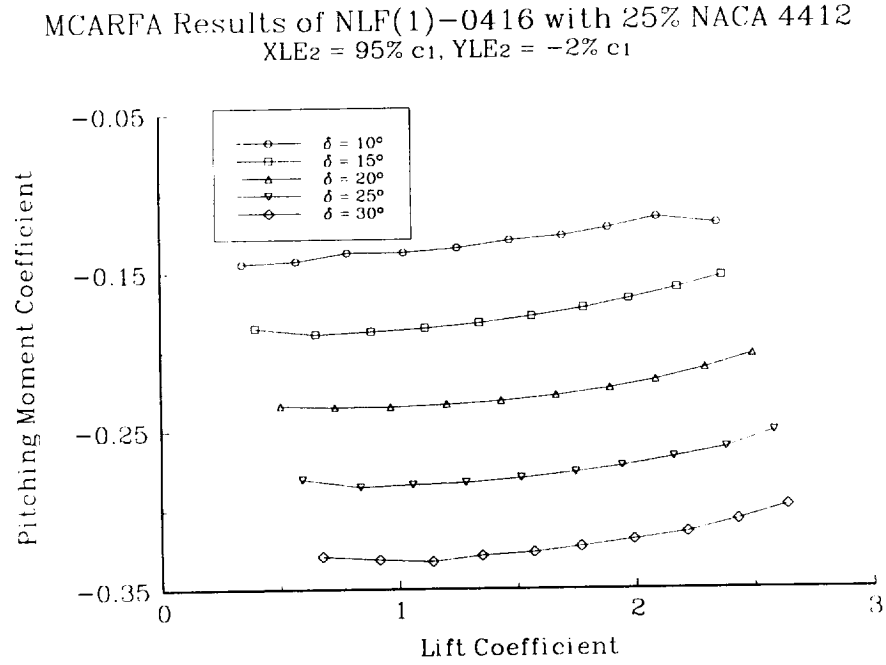

Fig. 74 Relative angle effect on moment coefficient

section 75% of the total chord and a secondary element with a NACA 4412 section 25% of the total chord. The secondary element was deflected 30° with respect to the primary element, although the 20° deflection case was also kept as a candidate. The leading edge of the secondary element was located 95% of the primary chord behind and 1.5% of the primary chord below the primary leading edge.

The next task in the study was to design a new two element airfoil based on the experience gained in the parametric study. The relative geometry between the two elements was kept the same as in the parametric variations. In addition, the NACA 4412 secondary profile shape was working well so it was also kept the same. The primary region of possible improvement was in the profile shape of the primary element. In particular, the primary element was operating at a negative angle of attack for the cruise case so the major thrust of the new design was to obtain more laminar flow on the primary element at the cruise c_l values.

Nomenclature for the new airfoils is GS01 for the first iteration of the two element airfoil configuration. The name followed by an A as in GS01A refers to the primary element only of the two element configuration. The first new primary element, named the GS01A, attempted to lower the drag of the system by creating a cut-out near the trailing edge of the primary element to shield the secondary element from the freestream (Fig. 75). The second primary element GS02A was an attempt to obtain more laminar flow on the primary element lower surface by thickening the NASA NLF(1)-0416 airfoil from the leading edge back to approximately 85% of the local chord and then faired to meet the old trailing edge. The upper surface remained unchanged from the NLF airfoil. The GS03A airfoil lower surface was the same as the NLF airfoil back to about 20% chord and then thicker to the trailing edge. In addition, the trailing edge cusp was removed; the upper surface was again unchanged from the

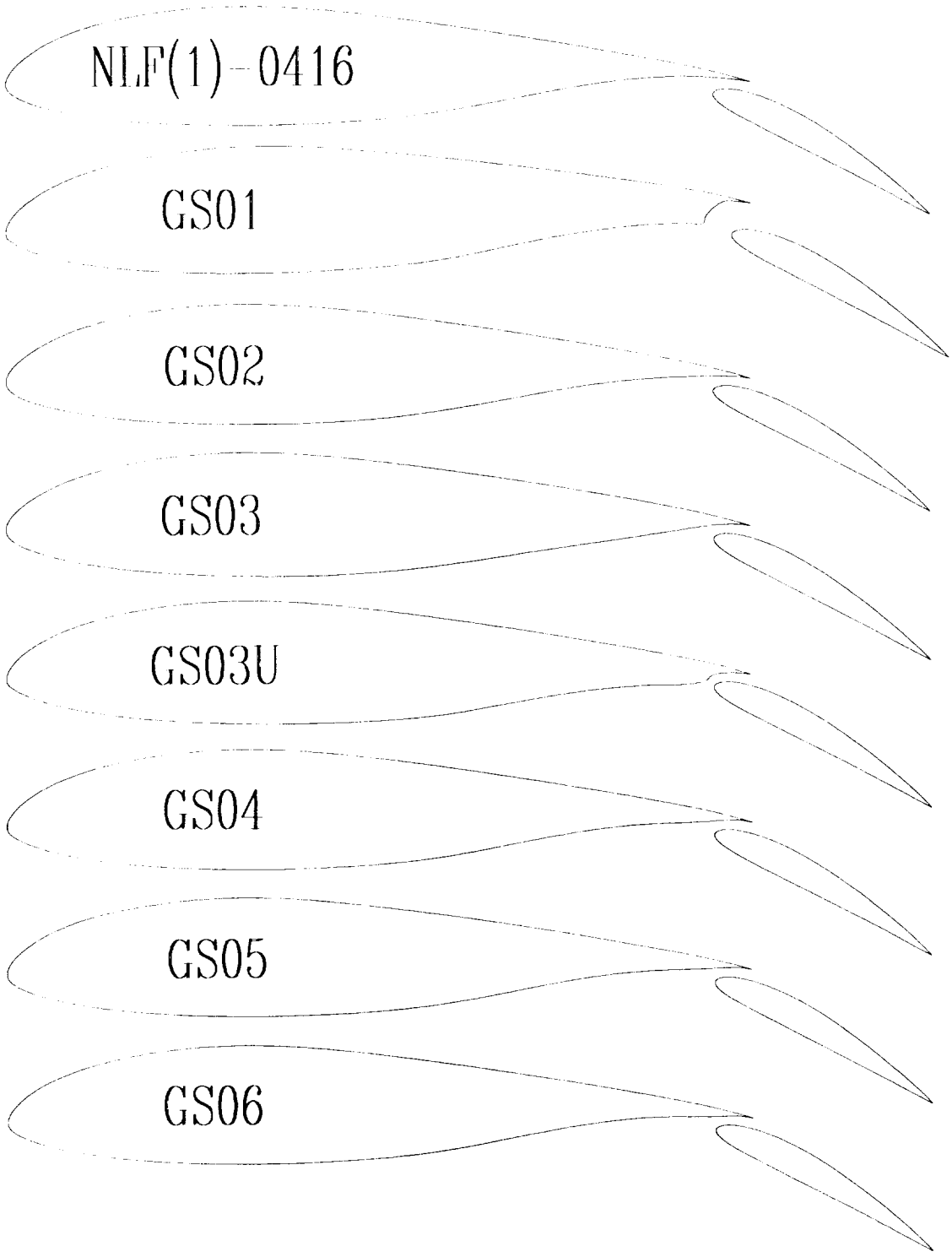

Fig. 75 Modified profile shapes

original NLF shape. The GS03UA profile was the same as the GS03 but a cutout matching the shape of the NACA 4412 leading edge was faired into the last 10% of the lower surface. The GS02A airfoil was further modified by again thickening the lower surface back to about 85% chord and called the GS04A airfoil. The GS05A and GS06A were again thicker modifications of the GS02A airfoil but respectively thinner than the GS04A profile.

Numerical results are presented for the various modified profile shapes and the original NLF(1)-0416 primary profile, all with a NACA 4412 secondary profile deflected 30°. Lift coefficient results show the lowest c_{lmax} values for the GS01, the GS03U, and the GS03 profiles, with very little difference in the lift curves between the other cases (Fig. 76). The c_d results show the highest drag values on the three worst lift cases. The lowest drag was obtained on the GS02 configuration with slight improvements over the other cases (Fig. 77). Lift to drag ratio results show the highest L/D values with the GS02 case at lower lift coefficients but the NLF airfoil case had the best L/D ratio at the highest lift coefficients (Fig. 78). Pitching moment coefficient results were nearly identical for all of the best cases (Fig. 79).

AG9301 Airfoil

Based on the c_{lmax} value and the highest L/D at the lower lift coefficients, the GS02 airfoil was chosen as the final modified profile shape. In order to match the chord in the numerical cases with the wind tunnel results, the numerical case total chord was extended from 51 centimeters in the GS02 case to 61 centimeters for the final shape. The final shape was named the AG9301 airfoil for the first (01) Texas A&M University Aggie (AG) airfoil of 1993 (93).

A small grid varying the relative position of the NACA 4412 secondary element with respect to the AG9301A primary element was studied to verify the optimum

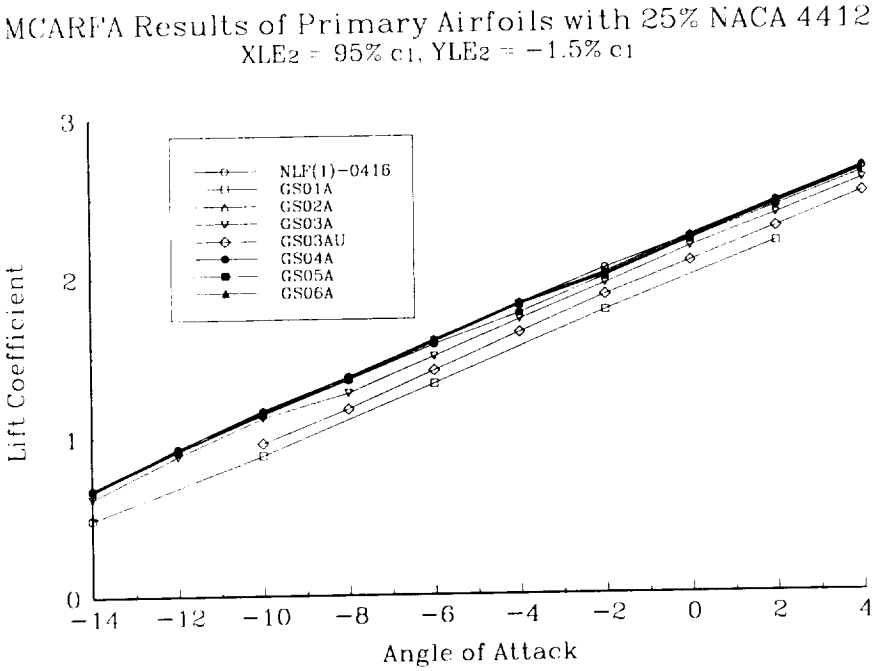

Fig. 76 Modified primary profile shape effect on lift coefficient

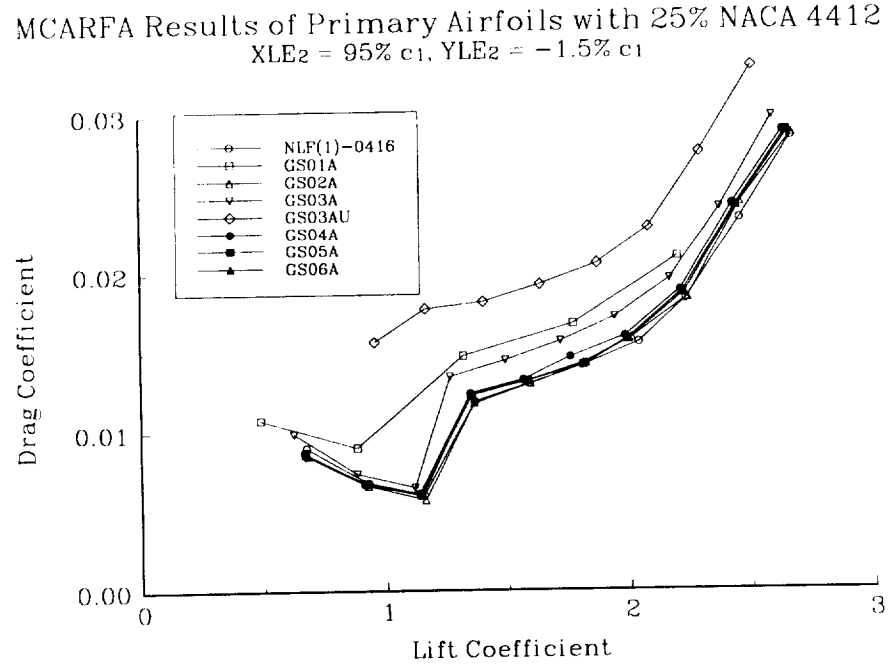

Fig. 77 Modified primary profile shape effect on drag coefficient

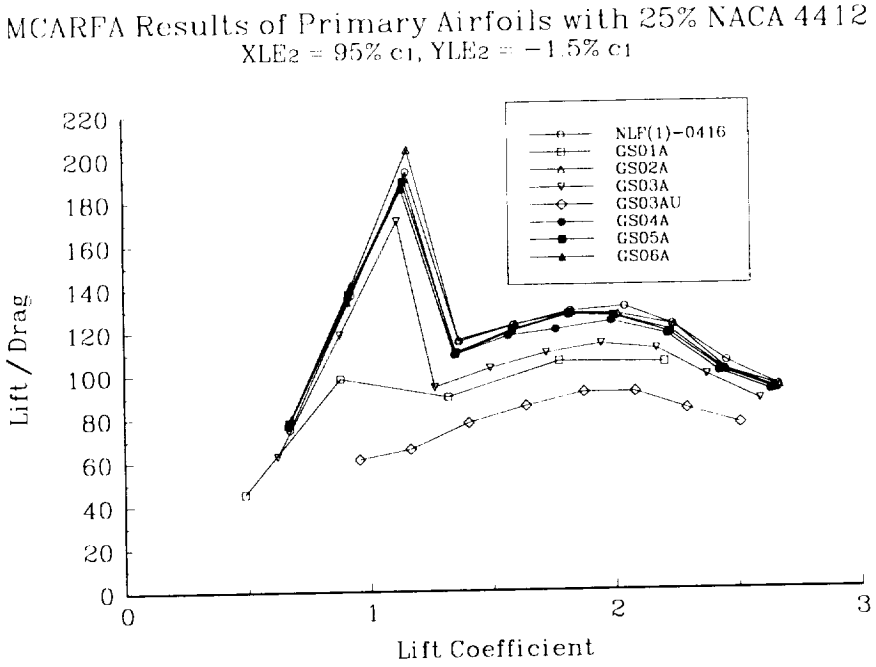

Fig. 78 Modified primary profile shape effect on L/D ratio

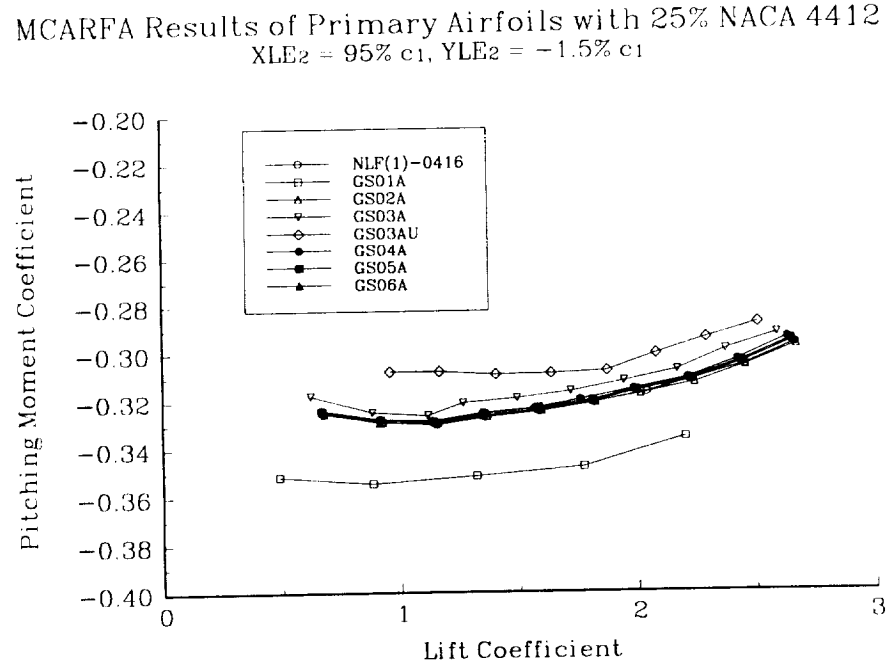

Fig. 79 Modified primary profile shape effect on moment coefficient

relative position. The secondary element leading edge was varied from 94% through 96% of the primary chord behind and 1% through 2% below the primary leading edge at a secondary element deflection of 30° and a Reynolds number of $3x10^6$.

Lift coefficient results for the secondary element at a vertical position 1% below the primary element show very little change with the different horizontal positions (Fig. 80). Drag coefficient values (Fig. 81) show the lowest c_d through most of the lift range at the 95% position. Lift to drag ratio results, as the c_d, show the best L/D through most of the c_l range at the 95% configuration (Fig. 82). Moment coefficient values increase with the further aft positioning of the secondary element (Fig. 83).

Lift coefficient values for the 1.5% below case show slightly higher c_l values for the 95% and 96% cases than the 94% condition (Fig. 84). The lowest c_d was obtained at the 95% case (Fig. 85) and, therefore, the highest L/D ratio was observed at the 95% condition as well (Fig. 86). Moment coefficient values again increased with further aft positioning (Fig. 87).

The 2% below lift coefficient values again show the highest c_l results at the 95% and 96% positions (Fig. 88). Drag coefficients were again the lowest (Fig. 89) and the L/D ratio was the highest (Fig. 90) for the 95% condition. Moment coefficient results were the same as previously observed (Fig. 91).

Based on the AG9301 position results, the optimum position of the NACA 4412 secondary element leading edge was verified to be 95% of the primary chord behind and 1.5% of the primary chord below the primary element leading edge.

The final AG9301 profile shape was therefore determined to be a two element airfoil with a primary profile of AG9301A section and a secondary element profile of NACA 4412 section. Airfoil coordinates for the AG9301A and the NACA 4412 are given in Tables 2 and 3, respectively. The primary element has a local chord 75% of

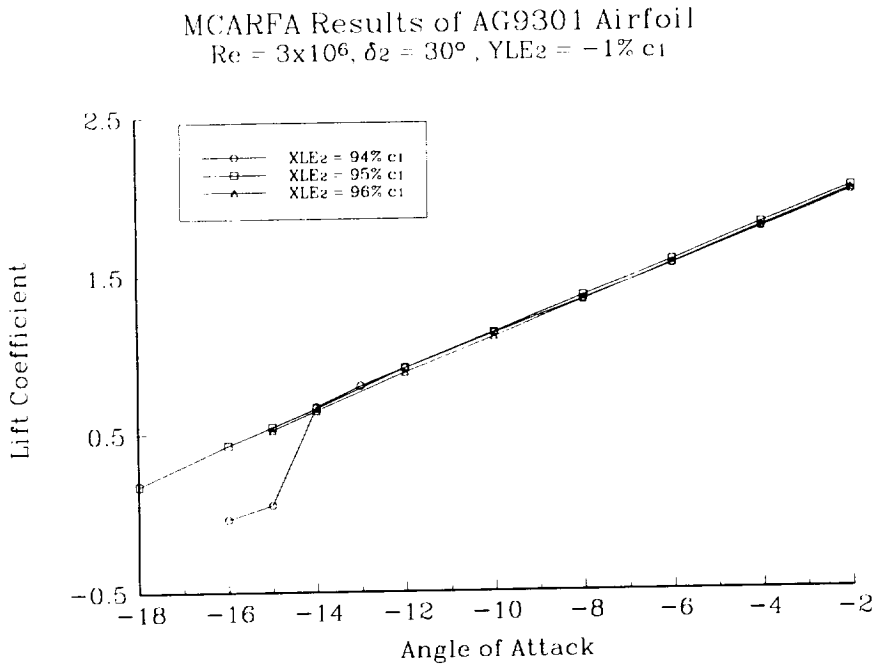

Fig. 80 AG9301 horizontal position effect on lift coefficient at -1%

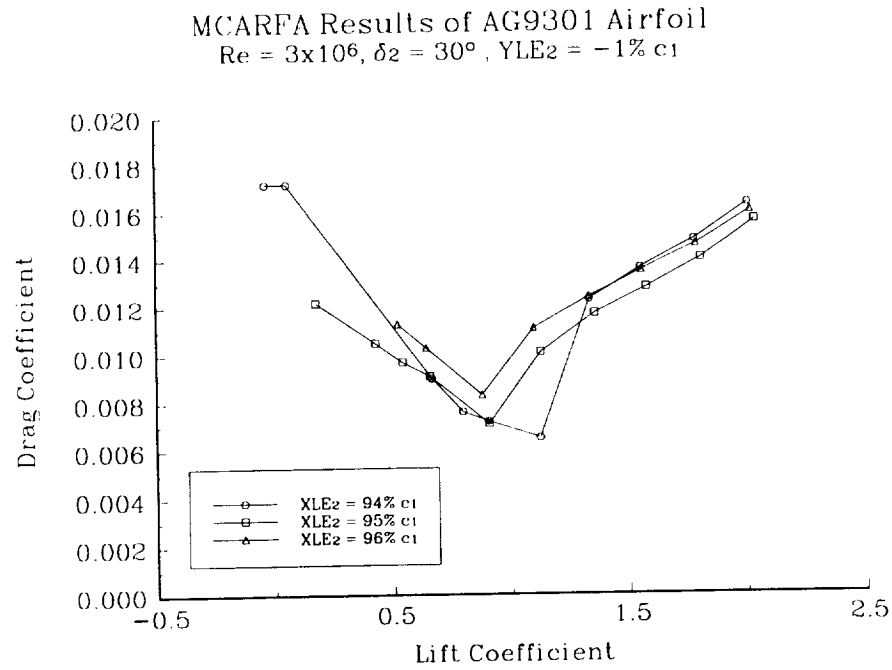

Fig. 81 AG9301 horizontal position effect on drag coefficient at -1%

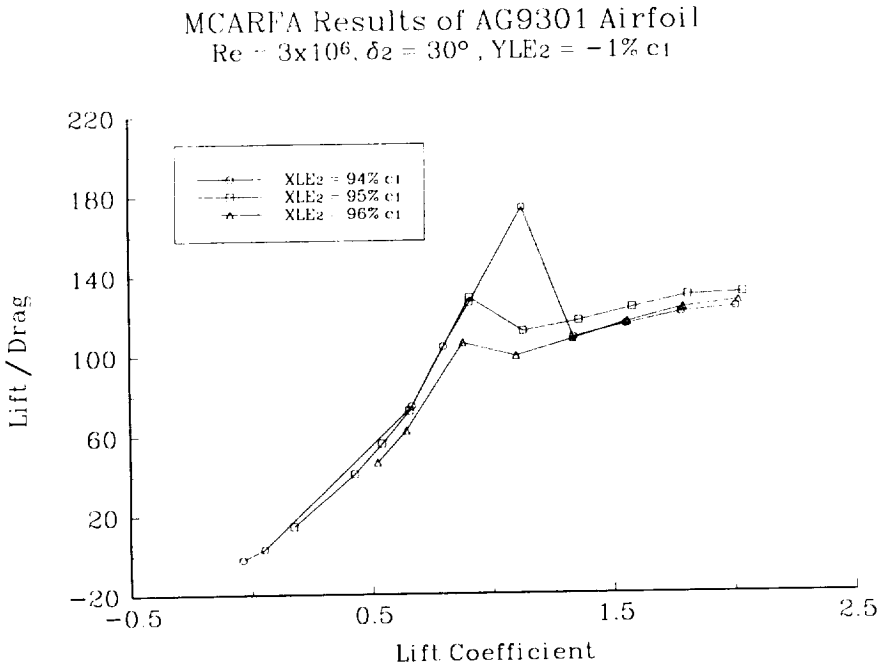

Fig. 82 AG9301 horizontal position effect on L/D ratio at -1%

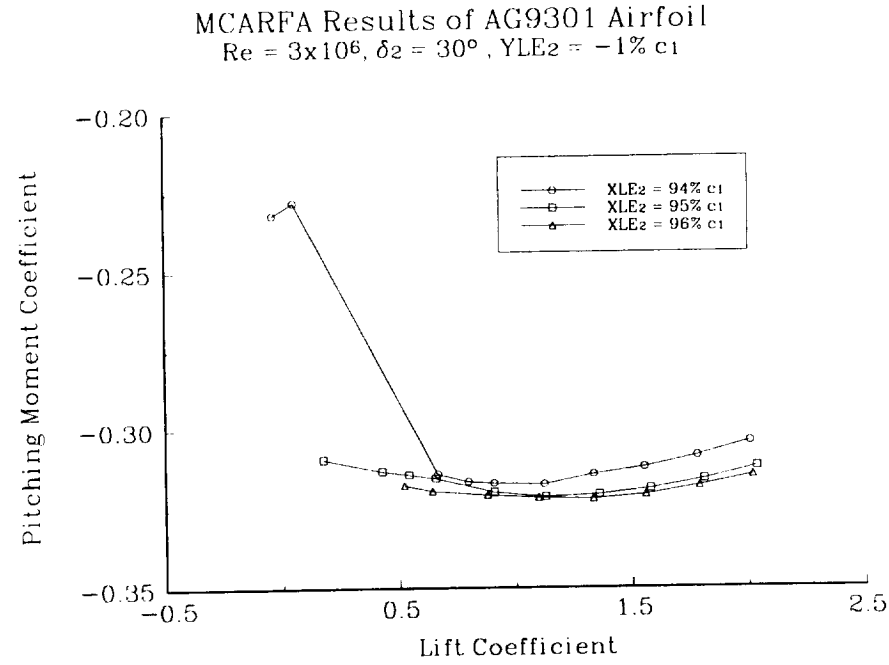

Fig. 83 AG9301 horizontal position effect on moment coefficient at -1%

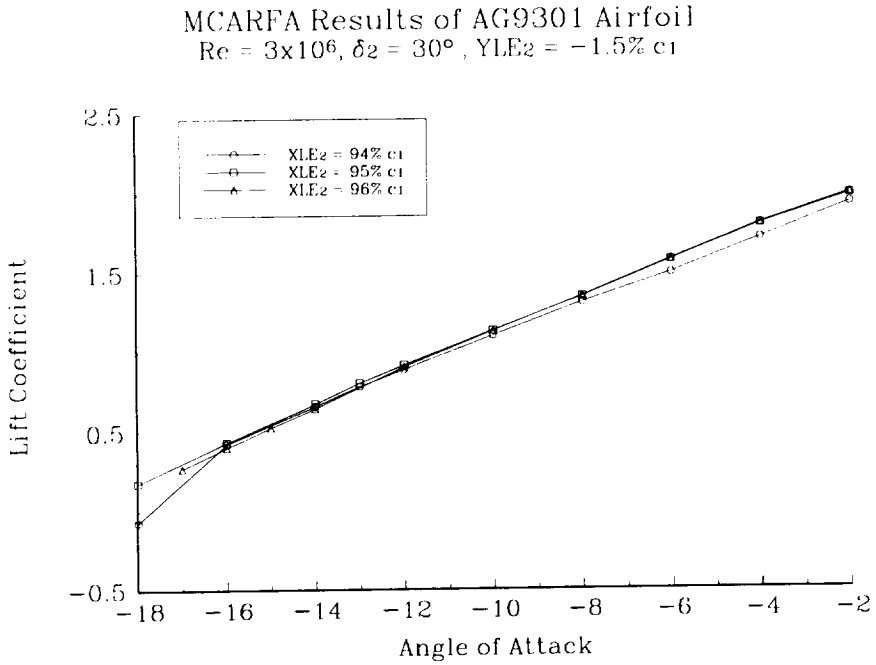

Fig. 84 AG9301 horizontal position effect on lift coefficient at -1.5%

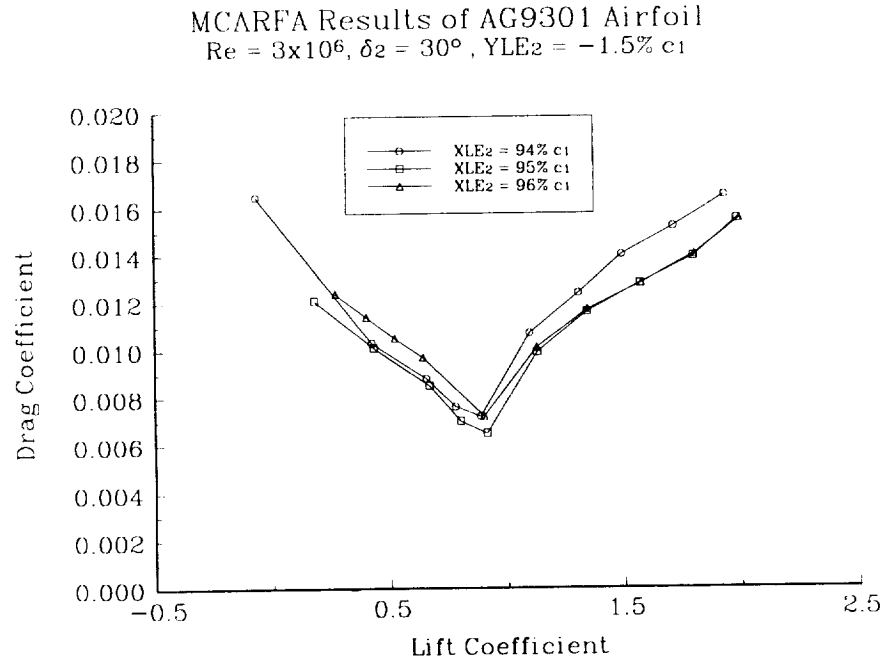

Fig. 85 AG9301 horizontal position effect on drag coefficient at -1.5%

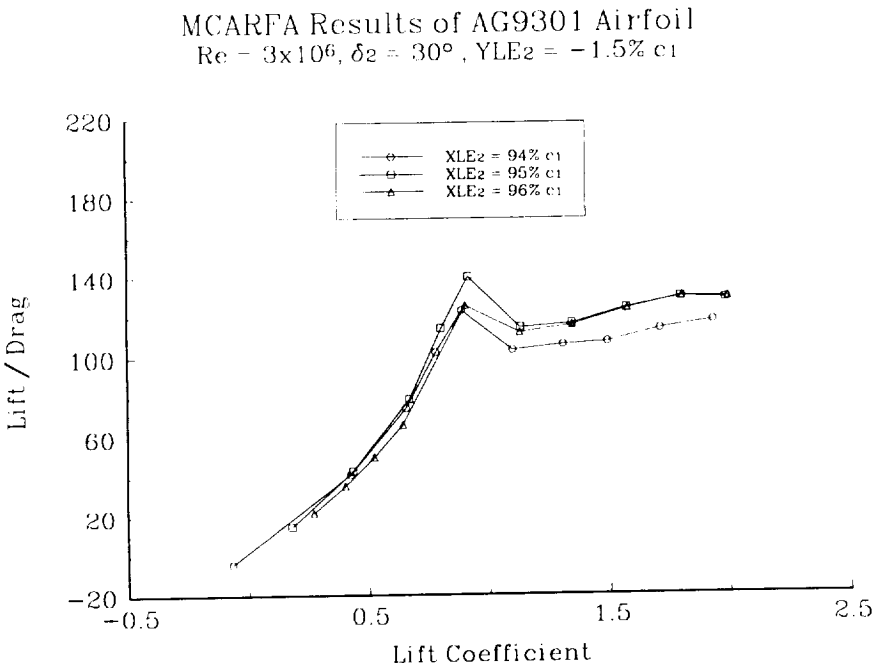

Fig. 86 AG9301 horizontal position effect on L/D ratio at -1.5%

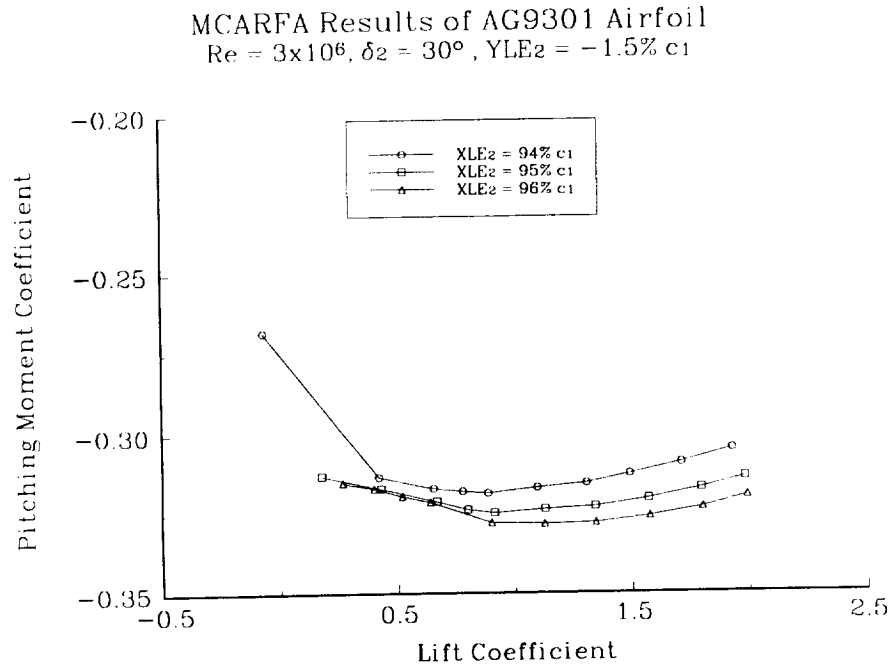

Fig. 87 AG9301 horizontal position effect on moment coefficient at -1.5%

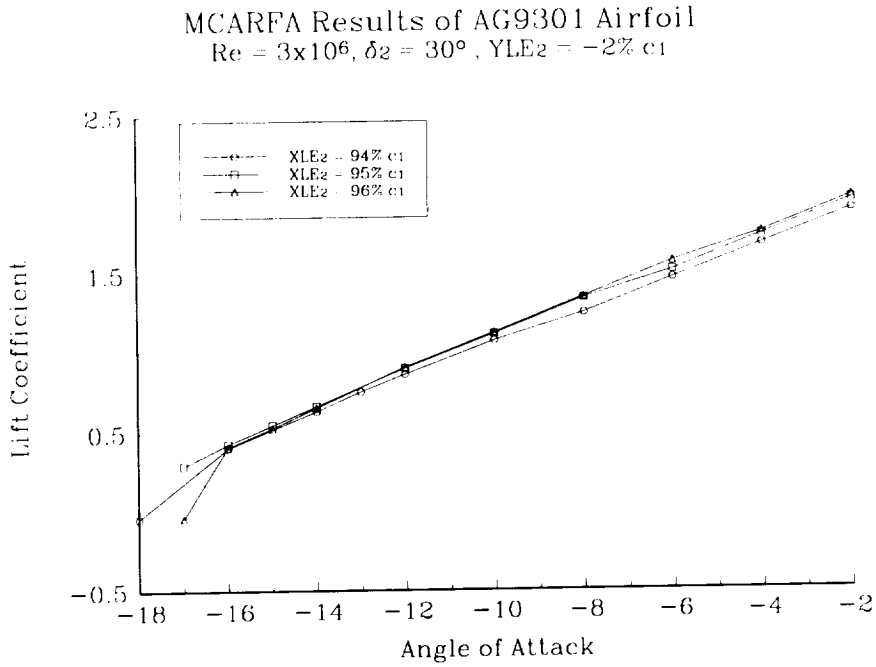

Fig. 88 AG9301 horizontal position effect on lift coefficient at -2%

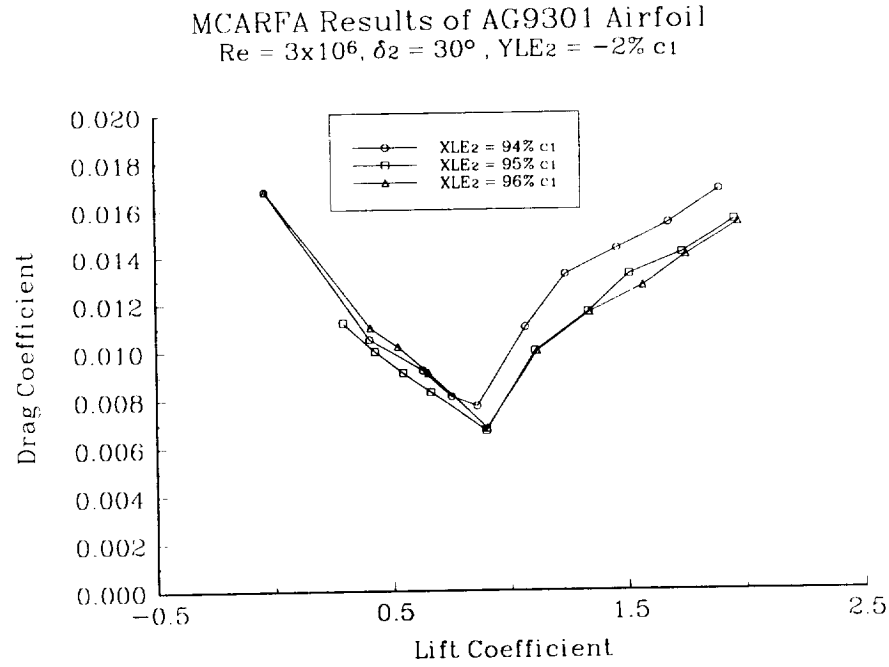

Fig. 89 AG9301 horizontal position effect on drag coefficient at -2%

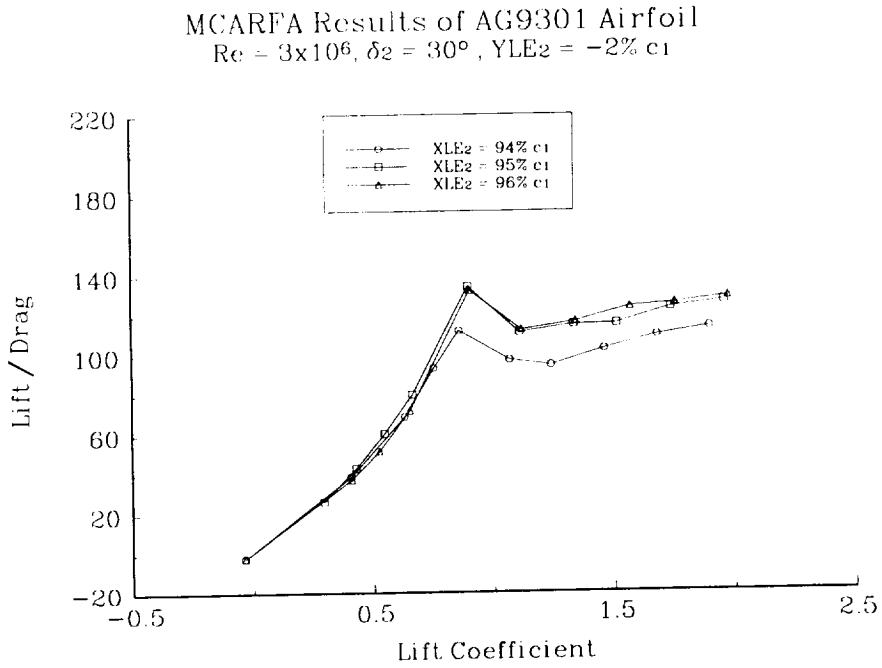

Fig. 90 AG9301 horizontal position effect on L/D ratio at -2%

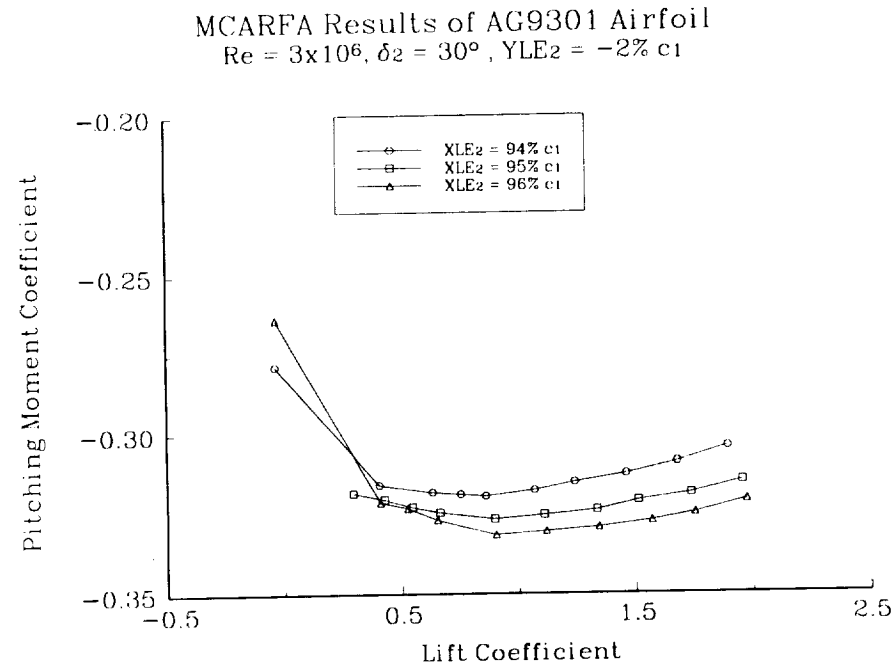

Fig. 91 AG9301 horizontal position effect on moment coefficient at -2%

Table 2 AG9301A airfoil coordinates

x/c_1	y_{upper}/c_1	y_{lower}/c_1
0.000000	0.000000	0.000000
0.005000	0.015343	-0.009706
0.010000	0.021783	-0.013944
0.020000	0.031484	-0.019655
0.030000	0.039238	-0.023882
0.040000	0.045860	-0.027367
0.050000	0.051674	-0.030383
0.075000	0.063694	-0.036594
0.100000	0.073149	-0.041499
0.125000	0.080766	-0.045440
0.150000	0.086964	-0.048604
0.200000	0.096023	-0.053100
0.250000	0.101412	-0.055799
0.300000	0.103663	-0.057221
0.350000	0.103217	-0.057582
0.400000	0.100539	-0.056845
0.450000	0.096122	-0.054783
0.500000	0.090432	-0.051083
0.550000	0.083849	-0.045551
0.600000	0.076645	-0.038302
0.650000	0.069000	-0.029832
0.700000	0.061018	-0.020924
0.750000	0.052737	-0.012478
0.800000	0.044130	-0.005385
0.850000	0.035066	-0.000372
0.875000	0.030278	0.001232
0.900000	0.025239	0.002271
0.925000	0.019857	0.002893
0.950000	0.013996	0.003286
0.975000	0.007467	0.002872
1.000000	0.000000	0.000000

Table 3 NACA 4412 airfoil coordinates

x/c_2	y_{upper}/c_2	y_{lower}/c_2
0.000000	0.000000	0.000000
0.005000	0.013918	-0.010384
0.010000	0.019946	-0.014175
0.020000	0.028815	-0.018737
0.030000	0.035767	-0.021612
0.040000	0.041635	-0.023640
0.050000	0.046753	-0.025147
0.075000	0.057305	-0.027543
0.100000	0.065712	-0.028727
0.125000	0.072659	-0.029131
0.150000	0.078473	-0.028998
0.200000	0.087386	-0.027695
0.250000	0.093296	-0.025662
0.300000	0.096706	-0.023356
0.350000	0.097999	-0.020980
0.400000	0.097486	-0.018618
0.450000	0.095388	-0.016325
0.500000	0.091916	-0.014126
0.550000	0.087237	-0.012044
0.600000	0.081483	-0.010095
0.650000	0.074756	-0.008302
0.700000	0.067117	-0.006688
0.750000	0.058610	-0.005282
0.800000	0.049220	-0.004103
0.850000	0.038906	-0.003164
0.875000	0.033359	-0.002766
0.900000	0.027520	-0.002397
0.925000	0.021359	-0.002028
0.950000	0.014806	-0.001596
0.975000	0.007756	-0.000991
1.000000	0.000000	0.000000

the total chord and the secondary element has a local chord 25% of the total. The position of the 4412 leading edge was optimized to be 95% of the primary chord behind and 1.5% of the primary chord below the primary element leading edge. The optimum deflection of the secondary element with respect to the primary element was determined to be 30°, but the 20° case will still be considered because of the somewhat more conservative design. The primary element AG9301A is a 16.13% thick airfoil with a chord of 46 centimeters. The final AG9301 airfoil, with both the 30° and 20° deflections, is shown in Figure 92.

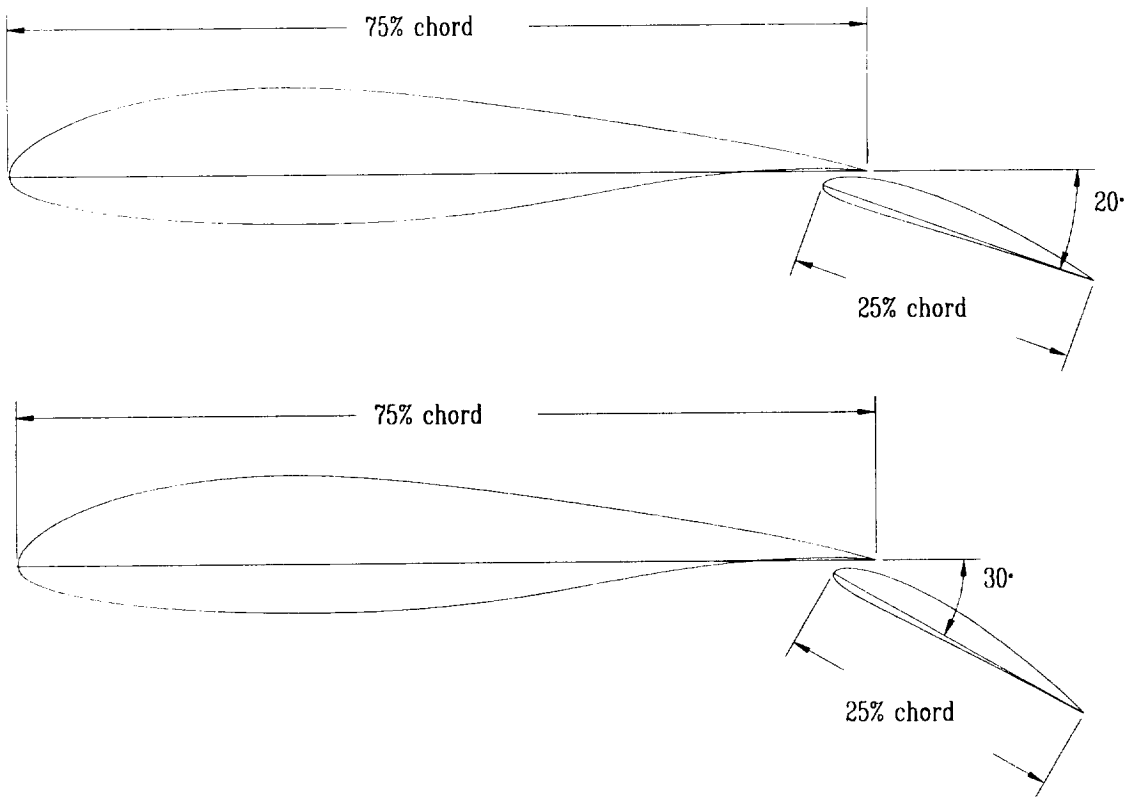

Fig. 92 AG9301 airfoil

Numerical results for the final AG9301 airfoil with both the 30° and 20° deflection cases are presented for various Reynolds numbers across the entire expected operating envelope.

Lift coefficient results for the AG9301 30° deflection case at Reynolds numbers ranging from $8x10^5$ to $3x10^6$ show the c_{lmax} does not change significantly with the various Reynolds numbers, but the slope of the lift curve does increase, especially at higher c_l values, with increasing Reynolds number (Fig. 93). The drag coefficient decreases with increasing Reynolds number as expected (Fig. 94). The L/D ratio (Fig. 95) and the moment coefficient (Fig. 96) also increase with increasing Reynolds numbers.

The AG9301 20° deflection results are also presented for Reynolds numbers ranging from $1x10^6$ through $3x10^6$. Results follow generally the same trends as the 30° deflection cases. The lift curve slope increases with increasing Reynolds number with very little change in the c_{lmax} values (Fig. 97). The drag coefficient decreases with increasing Reynolds number (Fig. 98). The L/D ratio (Fig. 99) and the moment coefficient (Fig. 100) both increase with increasing Reynolds numbers. In addition to the L/D ratio which is critical to the maximum range performance, results are also presented for $c_l^{3/2}/c_d$ which is the driving parameter in the maximum endurance equations for propeller driven aircraft or gliders (Fig. 101). These results also show an increase in performance with an increase in Reynolds number.

Comparison With Other Airfoils

The AG9301 airfoil was compared with three other similar use airfoils. Both the 30° and 20° deflection cases are used for this comparison. The AG9301 was compared with the NASA NLF(1)-0416 airfoil, the SM701 airfoil, and the Wortmann FX 79-K-144/17 airfoil. The NASA NLF(1)-0416 was the profile shape that the

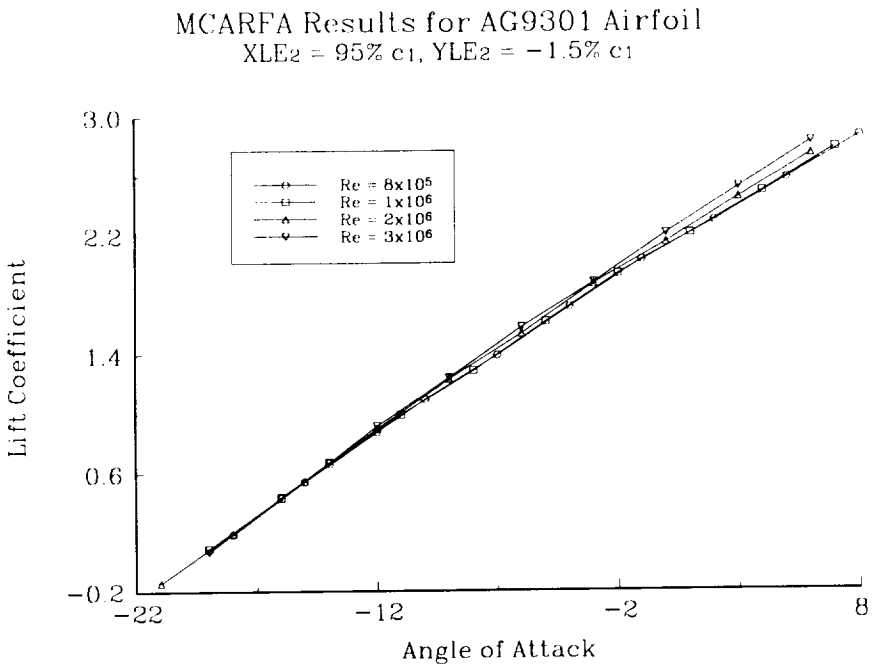

Fig. 93 Reynolds number effect on numerical lift coefficient, δ=30°

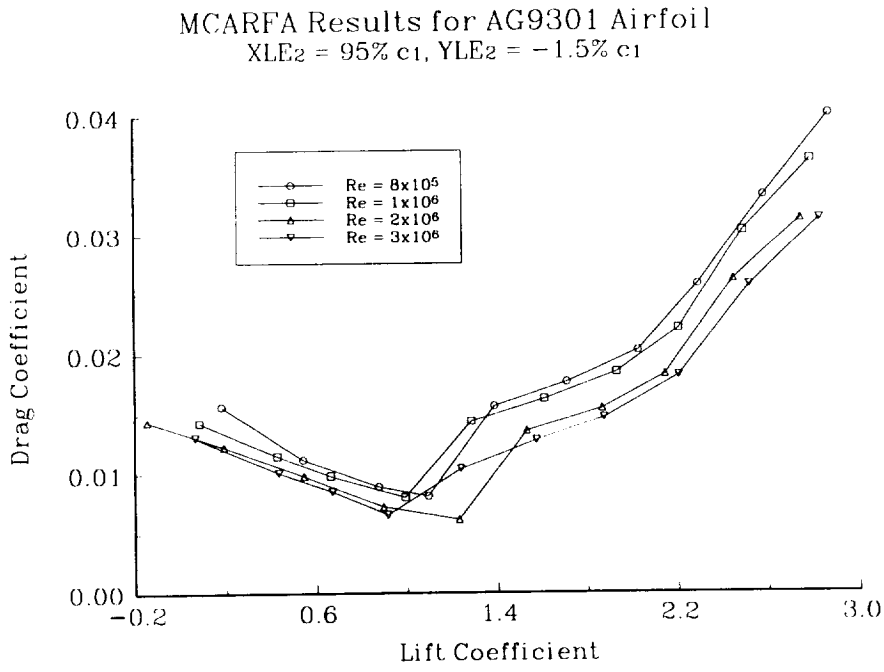

Fig. 94 Reynolds number effect on numerical drag coefficient, δ=30°

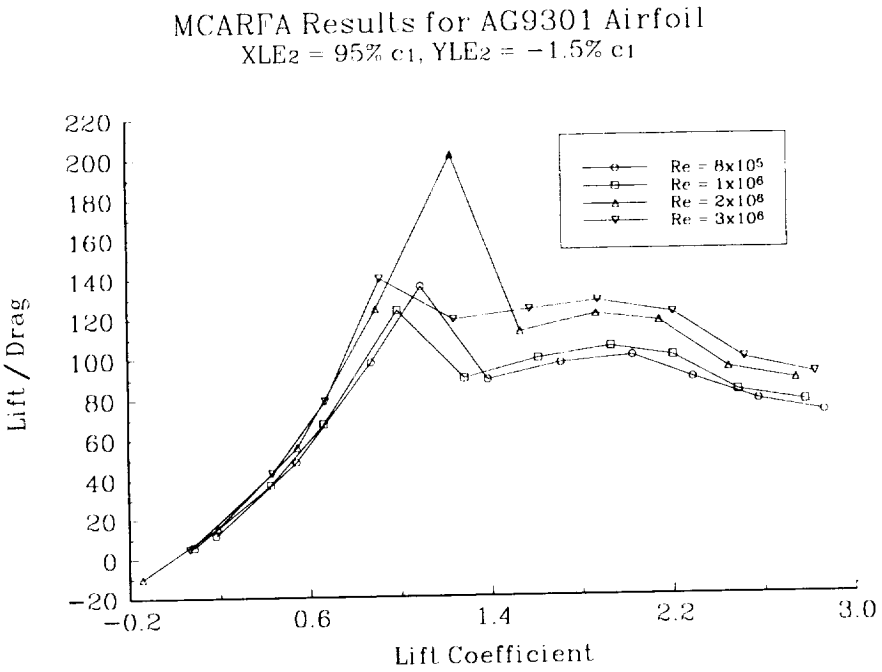

Fig. 95 Reynolds number effect on numerical L/D ratio, δ=30°

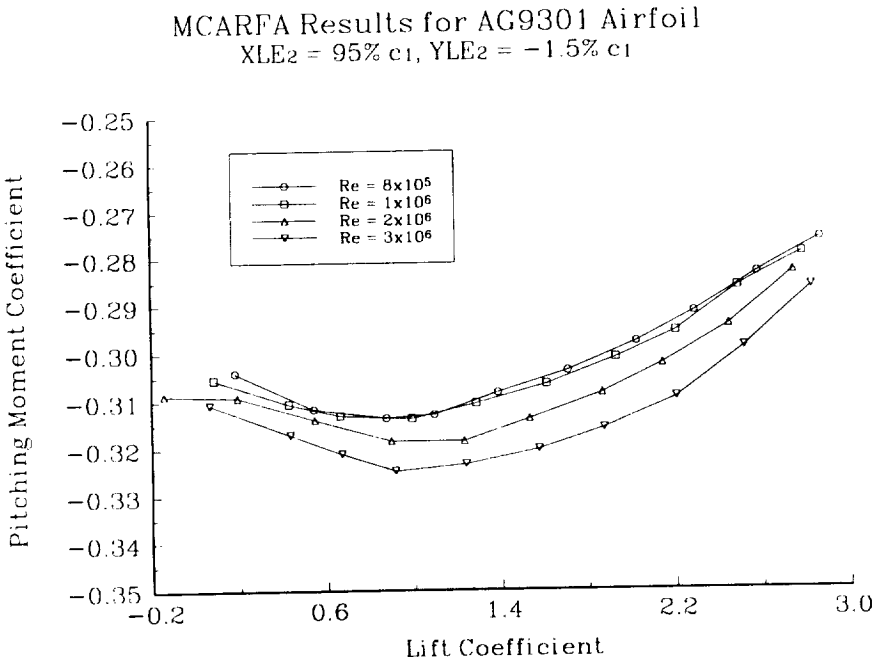

Fig. 96 Reynolds number effect on numerical moment coefficient, δ=30°

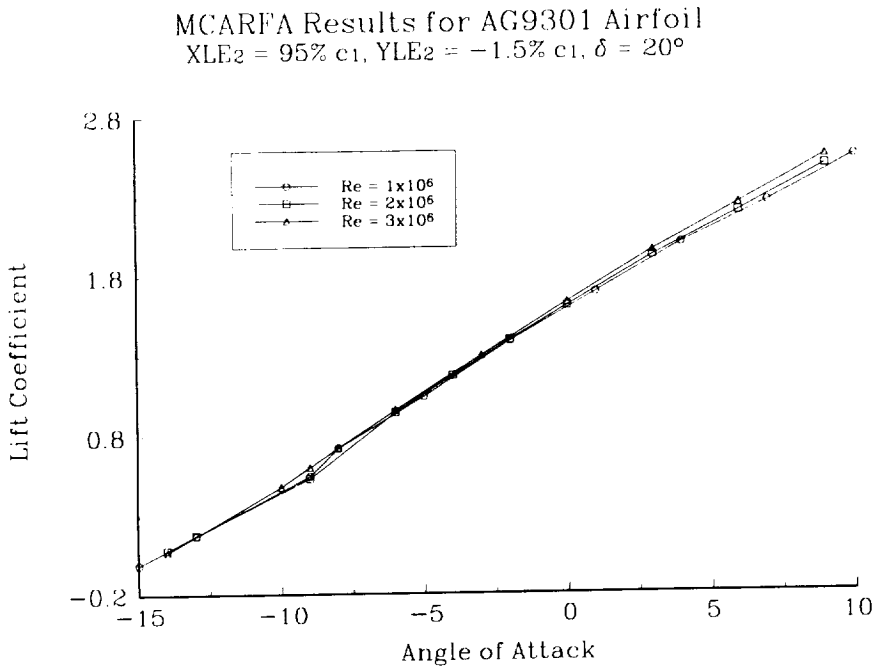

Fig. 97 Reynolds number effect on numerical lift coefficient, δ=20°

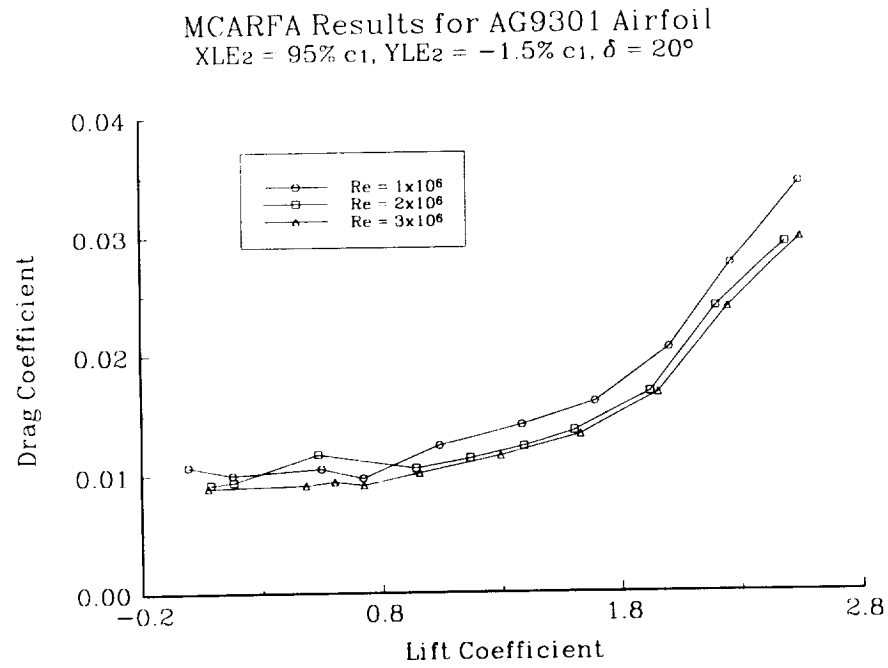

Fig. 98 Reynolds number effect on numerical drag coefficient, δ=20°

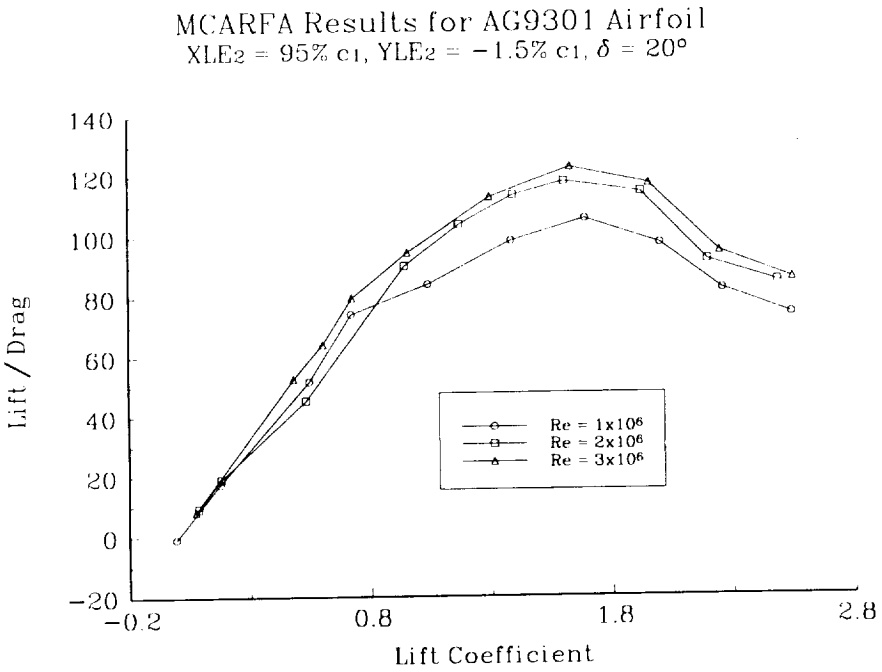

Fig. 99 Reynolds number effect on numerical L/D ratio, δ=20°

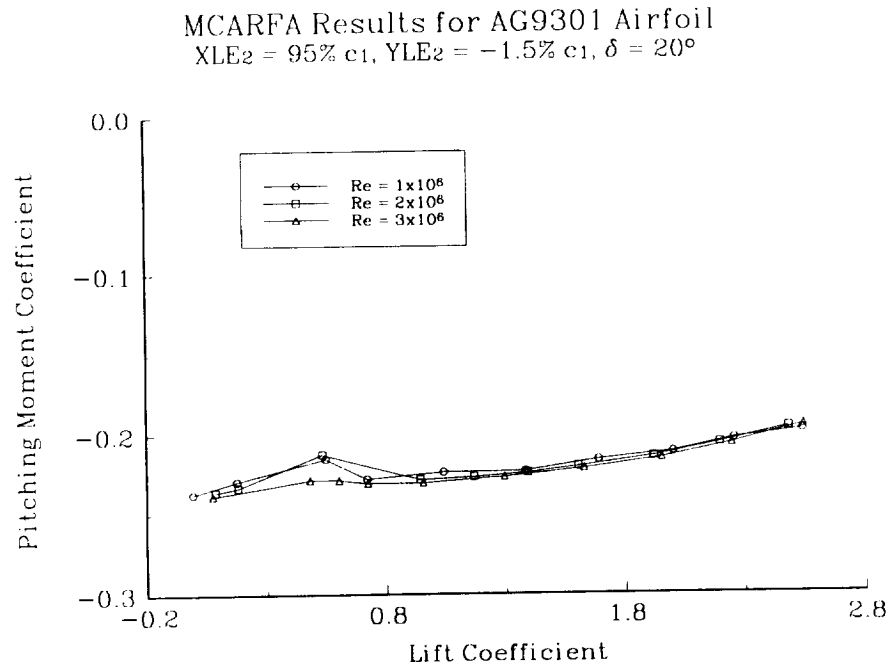

Fig. 100 Reynolds number effect on numerical moment coefficient, δ=20°

C-2

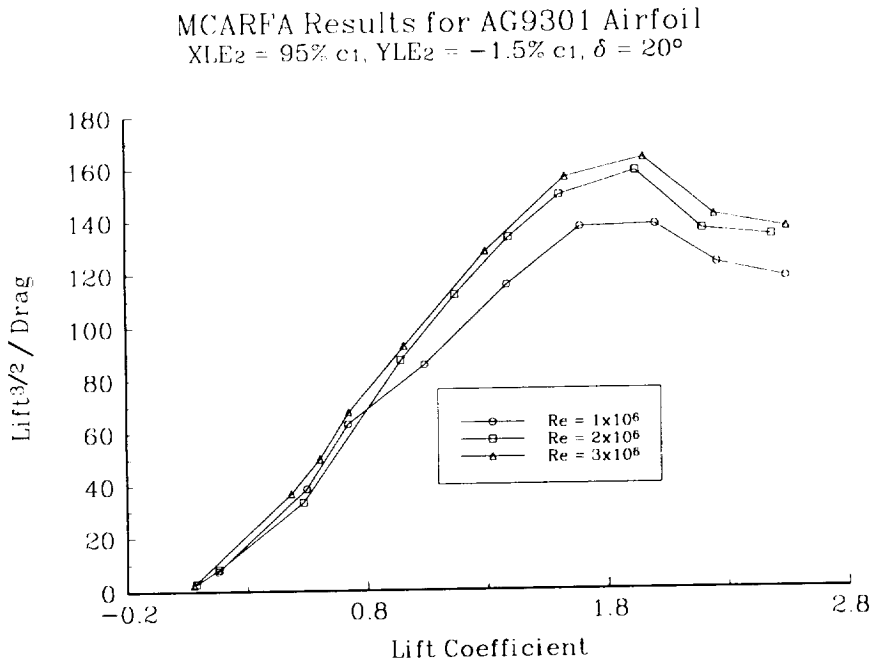

Fig. 101 Reynolds number effect on numerical $c_l^{3/2}/c_d$, δ=20°

AG9301A was modified from. It was originally chosen for study because it was a reasonably high lift single element airfoil designed for light general aviation applications. The SM701 airfoil is a fixed geometry single element airfoil designed by Mr. Dan Somers and Dr. Mark Maughmer specifically for the new World Class Gliders.[47] The Wortmann FX-79-K-144/17 is a state of the art sailplane cruise airfoil used on many of the current high performance gliders including the Ventus and the Nimbus.[48] It has a 17% chord simple flap deflected -9.3° for the cruise case.

Maximum lift coefficients for all airfoils were taken as the computed values as calculated by the MCARFA computer code. These results are presented with other source values when possible. Cruise lift coefficients were taken as the design c_l of 0.4 for the NLF and the SM701 airfoils. Cruise c_l values for the AG9301 cases and the

Wortmann airfoil were calculated by requiring the same stall and cruise speed for the AG9301 and Wortmann airfoils as for the known NLF(1)-0416 airfoil.

Lift coefficient comparisons (Fig. 102) show the AG9301 with the 30° deflection case has the highest c_{lmax} value with the AG9301 with the 20° deflection somewhat lower. The SM701, NASA NLF(1)-0416, and FX 79-K-144/17 airfoils all had significantly lower c_{lmax} values. Drag coefficient results show the Wortmann airfoil has the lowest c_d at the low lift coefficients (Fig. 103). The AG9301 20° deflection case had the highest drag at a given lift coefficient for most of the c_l range. The AG9301 30° deflection case had a lower drag than the 20° case, but still higher than the other airfoils at a given lift value through most of the c_l range. The L/D ratio results confirm the c_d conclusions that the AG9301 cases have lower L/D ratios at a given lift coefficient than the other airfoils (Fig. 104). However, because of the significantly higher c_{lmax} values obtained with the AG9301 configurations, the cruise c_l values are also higher and therefore the actual cruise L/D ratios are much more competitive. The moment coefficient results show the AG9301 30° deflection case has the highest moment coefficient, followed by the AG9301 20° deflection case (Fig. 105). The other airfoils had moment coefficients roughly a third that of the AG9301 30° deflection case. A high moment coefficient is generally considered undesirable in an airfoil because of the trim drag penalty that is usually associated with a higher moment coefficient. This concern is somewhat overblown for fixed geometry airfoils like the AG9301 airfoil because the effect of the pitching moment on the aircraft can be greatly reduced, if not eliminated, by proper positioning of the wing on the airframe. This is not possible with variable geometry airfoils for all conditions because, unlike the fixed geometry configurations, the moment coefficient changes

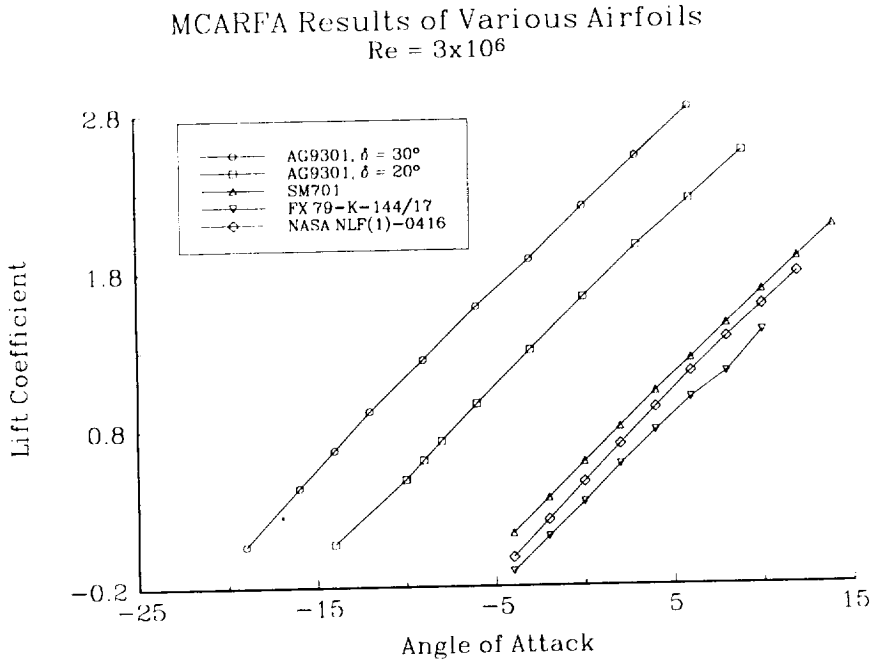

Fig. 102 Lift coefficient comparison of various airfoils

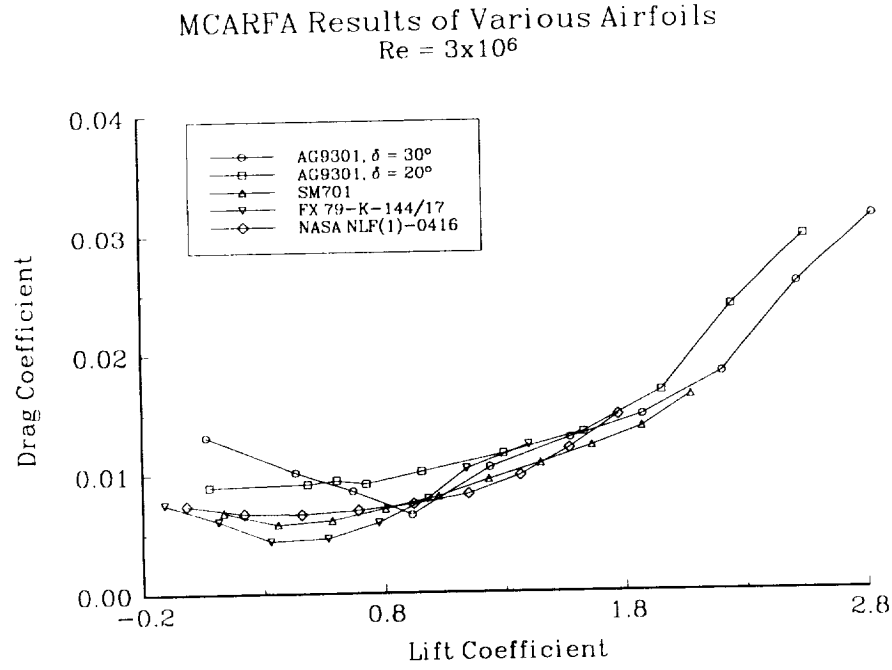

Fig. 103 Drag coefficient comparison of various airfoils

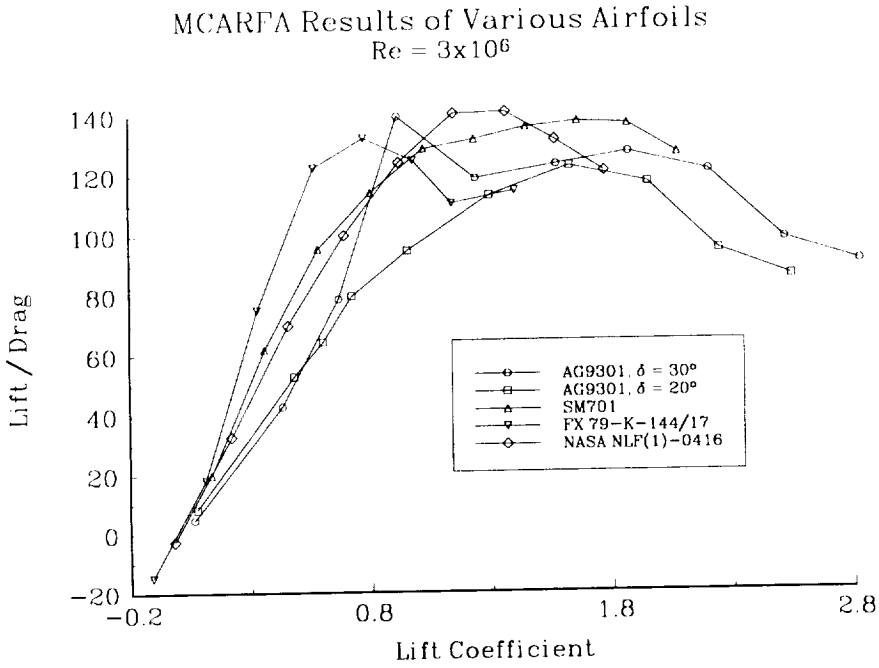

Fig. 104 L/D ratio comparison of various airfoils

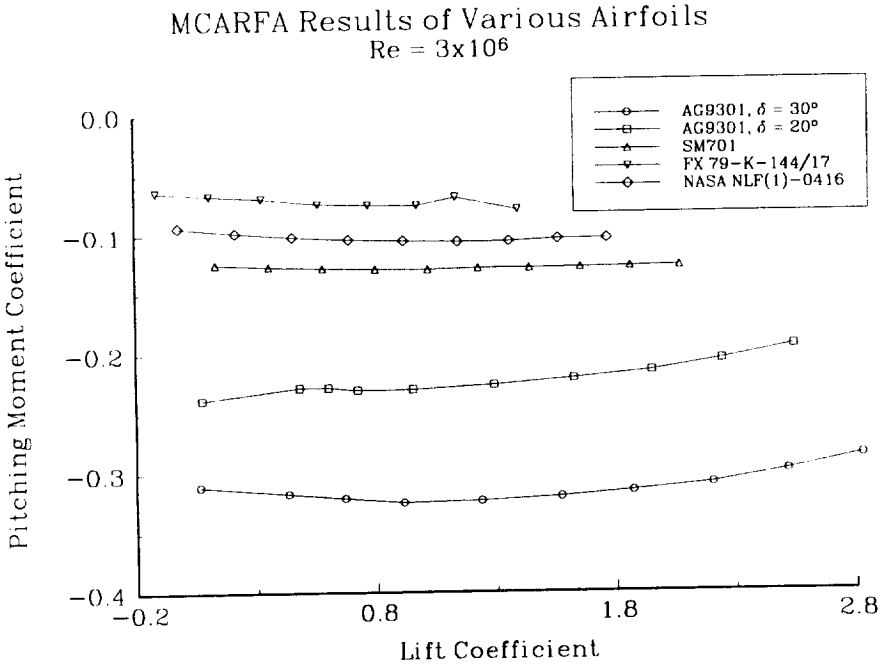

Fig. 105 Moment coefficient comparison of various airfoils

significantly with different flap deflections and therefore the proper positioning for one flap deflection will not be the optimum for a different flap deflection.

Table 4 lists the MCARFA results at a Reynolds number of $3x10^6$ for the various critical parameters associated with the airfoil comparison. Comparisons of the AG9301 results with the NASA NLF(1)-0416 airfoil are particularly important comparisons because the NLF airfoil is, with minor modifications, the primary profile in the AG9301 configuration so the comparisons are very much that of the effect of adding the secondary element. From the table it is clear that both the AG9301 configurations offer significantly higher c_{lmax} values. The 30° deflection case has a nearly 60% higher c_{lmax} than the NLF airfoil and the 20° deflection case has an approximately 44% higher c_{lmax} than the NLF airfoil. The AG9301 30° deflection configuration has a higher L/D at the cruise case than any of the other airfoils and over 19% higher than the NLF airfoil. The AG9301 20° deflection case has a cruise L/D slightly higher than the NLF(1)-0416 airfoil.

Table 4 Airfoil comparison at Reynolds number of $3x10^6$

Airfoil	c_{lmax}	$c_{lcruise}$	L/D_{cruise}
AG9301 - 30°	2.827	.63	72.67
AG9301 - 20°	2.545	.57	61.06
NLF(1)-0416	1.77	.4	60.92
SM701	1.87	.4	67.97
FX 79-K-144/17	1.40	.31	70.18

On the basis of L/D ratio alone, the AG9301 airfoil offers significant improvement in the cruise case, but the real benefit is apparent when accounting for the significantly higher c_{lmax} value as well. The higher c_{lmax} value allows the wing

planform to be significantly smaller for the same stall speed than a wing based on the other airfoils. The c_{lmax} value obtained with the 30° deflection case for the AG9301 airfoil allows a 46% smaller planform than the NASA NLF(1)-0416 airfoil. The wing makes up approximately 30% of the total weight of a sailplane[49] and, in a first order approximation, the wing weight is proportional to the wing planform; therefore, the smaller planform wing will be roughly 46% lighter than the NLF based wing. This corresponds to a nearly 14% lighter aircraft. Since the lift must equal the weight for level flight and the aircraft weighs 14% less, the lift required is also 14% less. This also results in 14% less wing drag at the same L/D ratio. When combining the weight savings and the increased L/D at cruise, a wing based on the AG9301 30° deflection case airfoil will have over 27% less drag at the cruise case than a wing based on the NLF(1)-0416 airfoil. This drag improvement is for a generic sailplane with the same stall speed and the same cruise speed in both cases, the only difference is the wing based on the different airfoils. Following a similar set of calculations, a wing based on the 20° deflection case of the AG9301 will have about 11.75% less wing drag at the cruise case than a wing based on the NLF(1)-0416 airfoil.

Transition Location

Numerical results for the transition location are presented for the AG9301 airfoil in the 30° and 20° deflection cases in Figures 106 and 107 respectively. It can be seen that the AG9301 30° deflection case has significantly more laminar flow on the upper surface than the NASA NLF(1)-0416 airfoil. The NLF airfoil does have a small amount more laminar flow on the lower surface than the AG9301 airfoil. At the cruise lift coefficient the AG9301 has approximately 25% laminar flow on the lower surface and 80% laminar flow on the upper surface. No separated flow is calculated on either surface. The AG9301 20° deflection case has less laminar flow on the upper surface

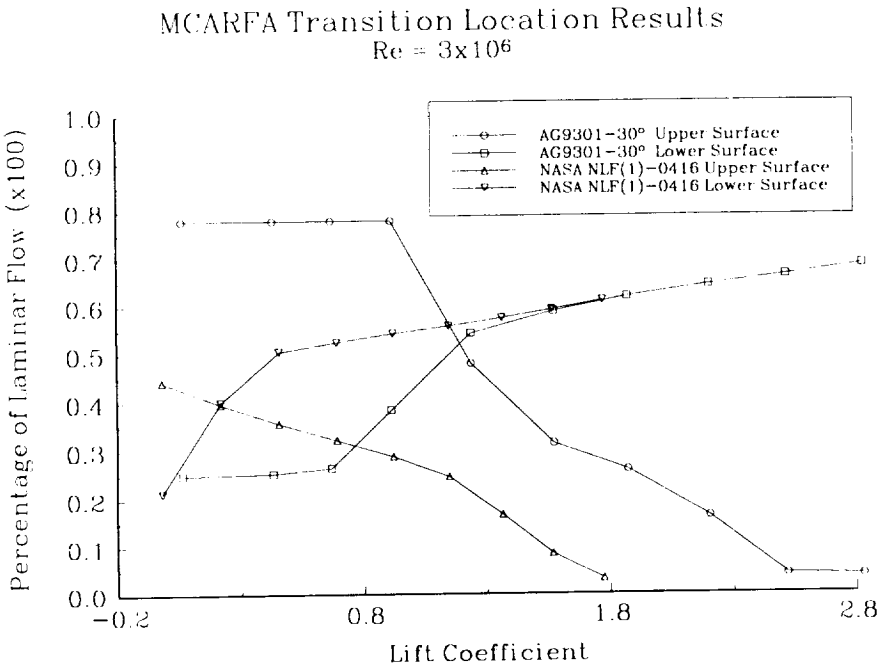

Fig. 106 Numerical transition location, $\delta = 30°$

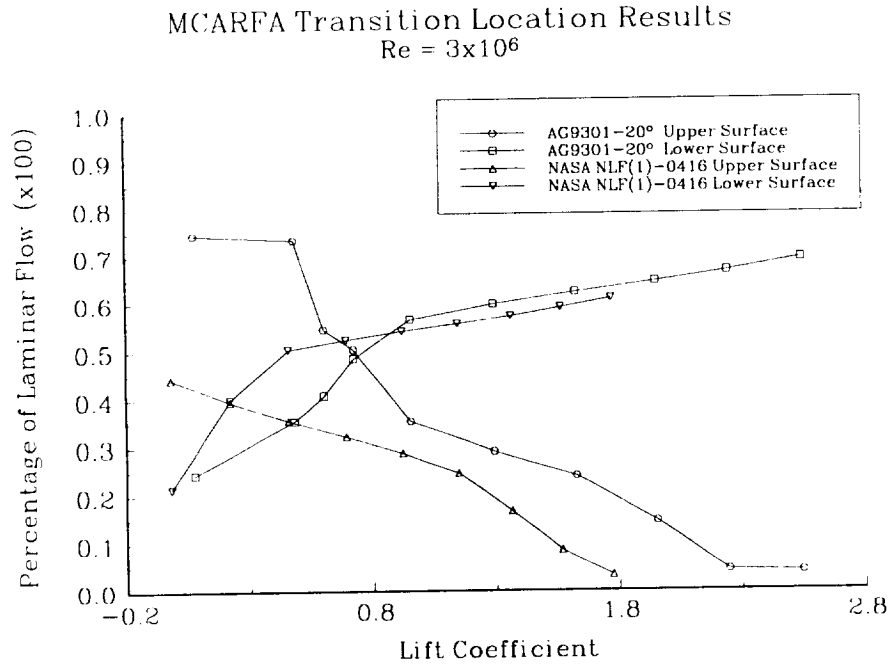

Fig. 107 Numerical transition location, $\delta = 20°$

than the 30° deflection case, but still more than the NLF(1)-0416 airfoil. The 20° deflection case has more laminar flow on the lower surface than the 30° deflection case, but still less than the NLF airfoil at cruise lift coefficients. At the cruise lift condition, the AG9301 20° deflection case has approximately 35% laminar flow on the lower surface and 70% laminar flow on the upper surface.

EXPERIMENTAL TOOLS

Experimental surface and wake pressure data, along with flow visualization measurements of transition location, were obtained for various AG9301 airfoil configurations in the Texas A&M University Low Speed Wind Tunnel.[50]

Wind Tunnel

The wind tunnel is of the closed circuit, single return type. Figure 108 presents a plan view of the wind tunnel circuit. Total circuit length at the centerline is 121.3 meters. The tunnel cross section is circular and of steel plate construction from the power section at the exit of the diffuser around to the entrance of the contraction section. The maximum diameter of 9.15 meters occurs in the settling chamber. Turning vanes are installed at each corner of the circuit. A single screen is located at the settling chamber entrance and a double screen just upstream of the contraction section to improve dynamic pressure uniformity and to reduce the flow turbulence level.

The contraction section which acts as a transition piece from circular to rectangular cross section is of reinforced concrete construction. The contraction ratio is 10.4 to 1 in a length of 9.15 meters.

Diffusion takes place immediately downstream of the test section in a concrete diffuser which also returns the flow to a circular cross section. The horizontal expansion angle is 1.43° and the vertical angle is 3.38° in an overall length of 14.17 meters.

The 3.81 meter diameter, four-blade Curtiss Electric propeller driven at 900 RPM by a 1250 kVA synchronous electric motor provides the air flow in the wind tunnel. Blade tips are inset into the tunnel wall to minimize tip interference effects.

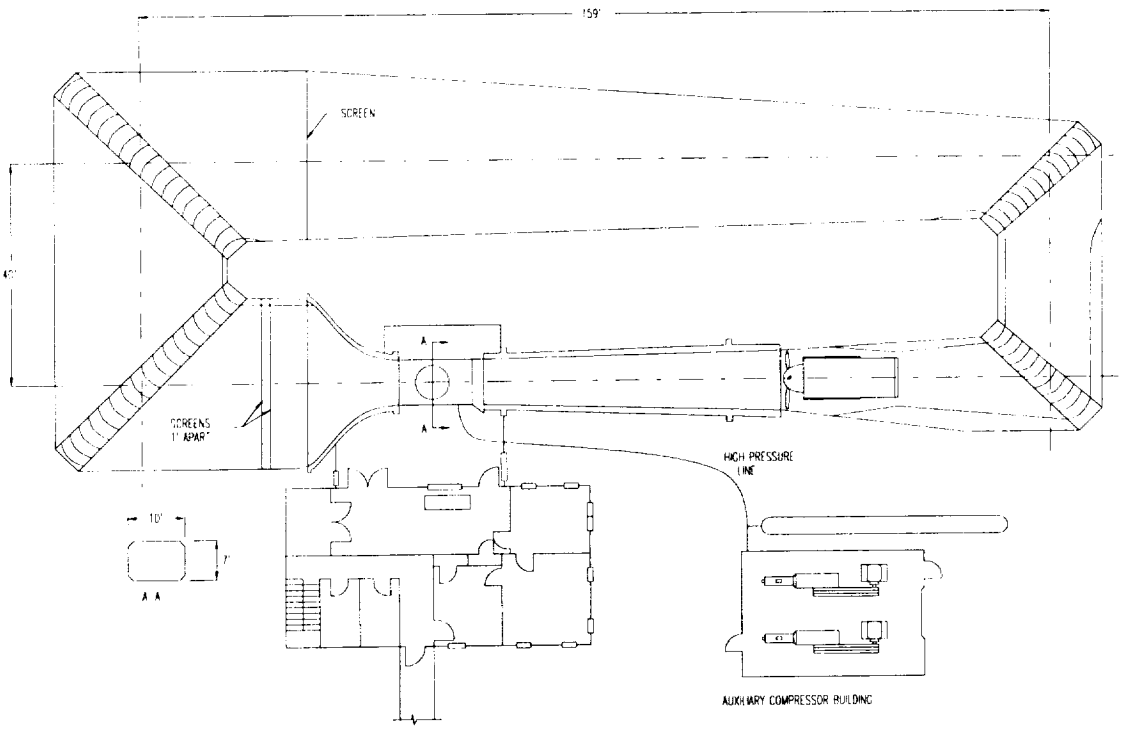

Fig. 108 TAMU-LSWT facility diagram

Any desired test section dynamic pressure between zero and 5 kiloPascals can be obtained by proper propeller blade pitch angle positioning.

The rectangular test section is 2.13 meters high, 3.05 meters wide, and 3.66 meters long. The corners have 31 centimeter fillets which house fluorescent lamps to provide photographic lighting. Cross sectional area of the test section is 6.32 square meters. Eight centimeter wide vertical venting slots in the side walls at the test section exit maintain near atmospheric static pressure. The test section side walls diverge about 2.5 centimeters in 3.66 meters to account for boundary layer growth. A turntable 2.13 meters in diameter built into the test section floor rotates with the external balance system to provide remote model positioning.

Test section dynamic pressure is measured by a differential pressure transducer accurate to ±2.4 Pascals. The set dynamic pressure reading is actually the difference

between two static pressure rings; one located in the settling chamber and one just upstream of the test section. A third order calibration curve, obtained by comparison with an accurate pitot-static probe, is then applied to the set dynamic pressure to obtain the uncorrected actual dynamic pressure in the test section.

The longitudinal turbulence intensity level was previously measured in the test section at dynamic pressures up to 4.7 kPa. The longitudinal turbulence intensity, in percent, is defined as:[29]

$$\%T = \frac{\sqrt{\overline{u'^2}}}{U_\infty} \times 100$$

Figure 109 shows the turbulence intensity vs. dynamic pressure as measured by a hot film anemometer system.[51] It is seen the turbulence intensity is less than 0.2% for dynamic pressures less than 1.68 kPa. The turbulence intensity increases to a peak of about 0.8% at a dynamic pressure near 2.40 kPa, and then decreases with increasing dynamic pressure. The AG9301 was tested at four different dynamic pressures corresponding to turbulence intensity levels of approximately: 0.22%, 0.19%, 0.75%, and 0.65%. A longitudinal turbulence intensity value of 0.05% is generally accepted as the desired level for good laminar flow airfoil testing. The primary effect of the higher than ideal turbulence intensity values in the TAMU-LSWT was to cause earlier transition from laminar to turbulent flow than would be the case in free air.

Airfoil Model

A model of the AG9301 airfoil was designed and built to experimentally verify the section characteristics predicted by the numerical analysis. The model had a total chord of 61 centimeters. The primary airfoil AG9301A had a 46 cm chord and the secondary airfoil NACA 4412 had a 15 cm chord.

The primary element was constructed around a 5x10 cm steel box beam used as a wing spar. Two steel templates were cut to the final desired profile shape and then one template was welded to the spar. Eighteen 51 mm thick sections of Ren Shape were roughly cut to the profile shape and slid onto the spar and pinned to each other, then the final steel template was welded into place. The center Ren Shape section had sixty-three pressure ports installed by drilling through the rough cut outline and gluing 1 mm steel tubing protruding normal to the surface. Vinyl tubing was then connected to the internal side of the steel tubing and routed through the spar to the transducer location. The final profile was obtained by sanding the Ren Shape down to the steel templates and painting the finished shape.

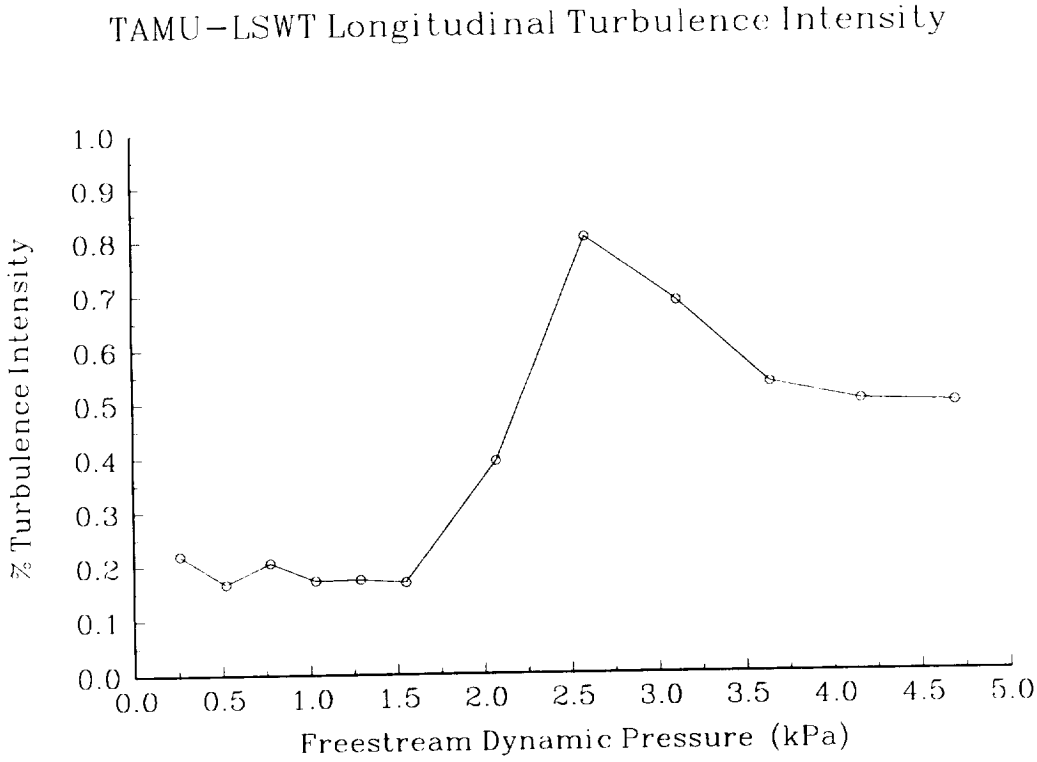

Fig. 109 Freestream longitudinal turbulence intensity

The secondary element was fabricated similar to the primary element, except due to size constraints, it was not possible to put a solid spar inside the model. The secondary model was, therefore, built of solid Ren Shape with steel templates at the ends and two steel alignment pins connecting each Ren Shape section. Twenty-six pressure ports were installed on the secondary airfoil using the same technique as the primary shape. The vinyl pressure tubing was run through a hole drilled in the Ren Shape and out the bottom of the model. The tubing was then run along the secondary element bracket to the transducer location.

The secondary element was connected to the primary by steel brackets at both the top and the bottom of the model. The brackets had fixed mounting holes on the primary element and variable locations for mounting on the secondary element to allow various second element relative positions to be tested.

The initial model design called for an accurate profile shape on the center 0.91 meters of the model and then an approximate shape on the outer 0.61 meter sections. This was to reduce construction time but still keep a two-dimensional section. Material and mounting problems led to the elimination of the outer 0.61 m sections, thus making the model effectively a three-dimensional shape with a span of 0.91 meters. Upon examination of initial wind tunnel data on the model, it was determined that the 0.91 meter span model was not giving truly two-dimensional results. Circular aluminum endplates 775 mm in diameter were added to the ends of the 0.91 meter span. Also during initial testing of the AG9301 airfoil, the secondary element was observed to deflect under load, effectively closing the gap between the two airfoil sections. Additional brackets were added to the 20° and 30° cases at the 95%, -1.5% leading edge location and the model was re-run for critical conditions.

As previously stated, pressure ports were located on both airfoil sections near the center of the span. Ports were offset 2.5 mm spanwise to eliminate the risk of upstream ports contaminating the data downstream. Sixty-three ports on the primary element and twenty-six ports on the secondary element were distributed based on surface curvature with regions of high curvature having more ports. Figure 110 shows the final profile shapes with pressure port locations.

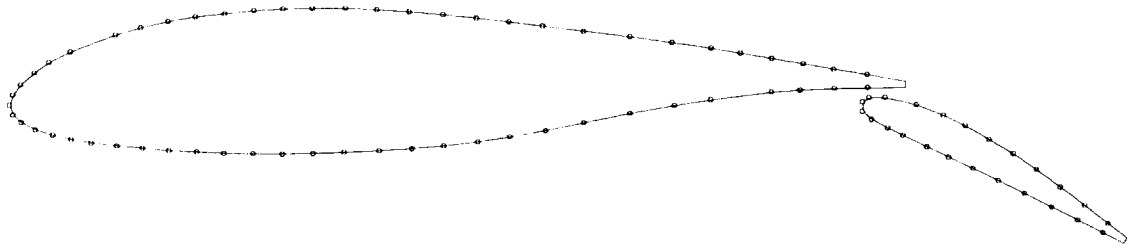

Fig. 110 AG9301 pressure port locations

The airfoil model was installed with the span vertical in the TAMU-LSWT test section. The LSWT external balance was used as a mounting system allowing the turntable to be utilized for angle of attack changes. The airfoil model was constructed with a steel mounting plate at the base which bolted to the tunnel's Large Base Mount Support. The Base Mount Support was located in the center of the turntable with the top 11 cm below the floor. A two piece floorplate was installed with a small clearance around the spar to eliminate any air transfer between the test section and the balance room below. A rotating pin was used at the ceiling to carry some of the wind load and reduce model deflections. Figure 111 shows a drawing of the airfoil model installed in the TAMU-LSWT test section.

The model was aligned with the chord of the primary element parallel to the geometric tunnel centerline. Angle of attack changes were accomplished by rotating

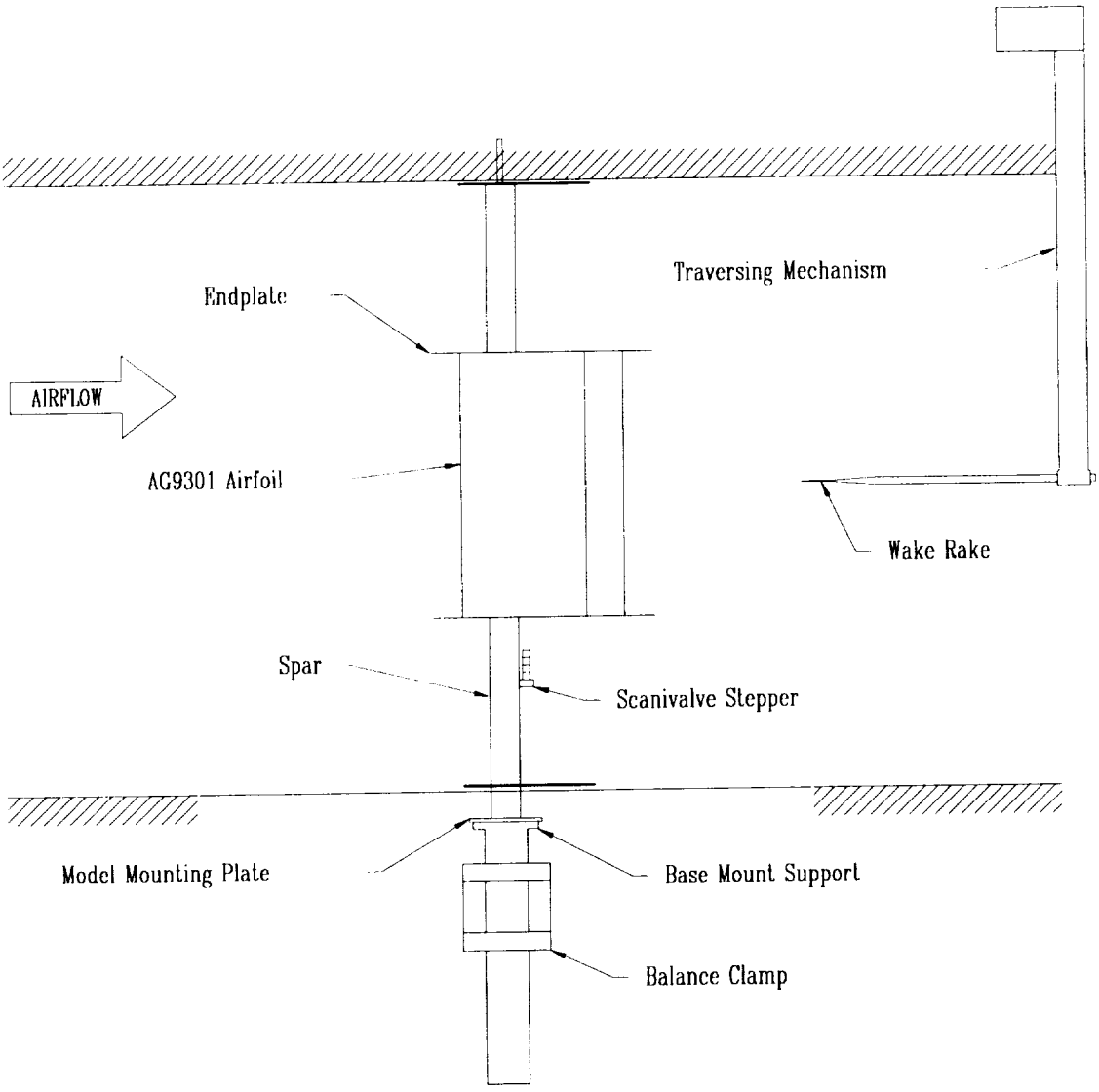

Fig. 111 AG9301 airfoil installed in TAMU-LSWT

the turntable in the floor of the test section. All angle of attack values were defined relative to the primary element chord line.

Instrumentation

All pressures were measured by Validyne pressure transducers on the initial runs. Two ranges of transducers were used. A 20 kPa transducer was used on the upper surfaces of the two airfoils, a 6.9 kPa transducer was used on the lower surfaces

of the airfoils, and a 6.9 kPa transducer was used on the wake rake. The TAMU-LSWT 16-bit Preston A/D system was used to convert the analog transducer readings to digital values in the Perkin-Elmer 3210 super mini-computer. One thousand samples of analog data were taken at 1000 Hz. and averaged to obtain a single pressure reading. A settling time of 2 seconds was used between consecutive pressure readings.

Two Scanivalve stepper systems were used to allow multiple pressure readings by a single transducer. Two 48 port heads on the first Scanivalve were installed on the wing spar just below the model base and shielded from the wind by a small fairing. The second 48 port Scanivalve was installed on the tunnel's traversing mechanism near the wake rake. The two heads connected to the airfoil model were of the 1 mm style and the one head measuring the wake rake pressures was of the 1.6 mm style. During the second set of wind tunnel runs, the TAMU-LSWT PSI-8400 pressure measurement system was used to measure the wake rake pressures instead of the second Scanivalve system.

A forty port total pressure wake rake was used to obtain pressure measurements for the calculation of profile drag. Total port spacing was 6.4 mm between centerlines yielding a 250 mm span. The rake has an additional five static ports evenly spaced along its span to obtain dynamic pressures in the wake. The rake was mounted to the TAMU-LSWT traversing mechanism allowing remote positioning of the rake when desired. The rake was positioned one chord length behind the trailing edge of the airfoil model.

A digital optical encoder on the LSWT turntable provided the model angle of attack reading. This reading, the freestream dynamic pressure, and the temperature were read by the Perkin-Elmer D/D system by taking 100 samples of each counter output and averaging to obtain a data point.

Data Reduction

Pressures were calculated from the measured transducer voltages according to the following equation:

$$p = (V - WOZ) \times SLOPE$$

where p is the pressure, V is the transducer voltage, WOZ is the initial transducer voltage with no wind on, and SLOPE is the linear calibration slope obtained on-line by reading a known calibration pressure and corresponding voltage. Pressure coefficients were then obtained from the raw pressures by:

$$C_p = \frac{(p - p_s)}{(p_t - p_s)}$$

where C_p is the pressure coefficient, p is the local pressure, and p_t and p_s are the freestream total and static pressures from a pitot-static probe respectively.

The two element drag coefficient was calculated by the momentum loss method from the dynamic pressure wake rake data using the relation:[52]

$$c_d = 2\int\left(\sqrt{\frac{q}{q_0}} - \frac{q}{q_0}\right)\frac{dy}{c}$$

Two-dimensional airfoil normal and axial force coefficients were obtained for each element by integrating the local pressure coefficient data. The two element moment coefficient was also calculated from the surface pressures by:[52]

$$c_n = \frac{1}{c} \times \int_0^c (C_{p_l} - C_{p_u})dx$$

$$c_a = \frac{1}{c} \times \int_0^c \left(C_{p_u} \frac{dy_u}{dx} - C_{p_l} \frac{dy_l}{dx} \right) dx$$

$$c_{m_{c/4}} = \frac{1}{c^2} \left[\int_0^c \left(C_{p_u} - C_{p_l} \right) \times \left(x - x_{c/4} \right) dx + \int_0^c \left(C_{p_u} \frac{dy_u}{dx} \right) y_u dx - \int_0^c \left(C_{p_l} \frac{dy_l}{dx} \right) y_l dx \right]$$

Two element normal and axial coefficients were calculated from the single element information and using the previously calculated drag coefficient. The lift and chordwise force coefficients were then obtained from the normal, axial, and drag force coefficients by: [53]

$$c_N = c_{n_1} + (c_{n_2} \times \cos\delta_2) - (c_{a_2} \times \sin\delta_2)$$

$$c_A = \frac{\left(c_d - (c_N \times \sin\alpha) \right)}{\cos\alpha}$$

$$c_l = (c_N \times \cos\alpha) + (c_A \times \sin\alpha)$$

Once the raw force and moment data were obtained, they were corrected for two-dimensional wind tunnel effects by the following procedure:[52]

$$\lambda = 0.3$$

$$\sigma = \frac{\pi^2}{48} \times \left(\frac{c}{10} \right)^2$$

$$\varepsilon_{sb} = \lambda \times \sigma$$

$$\varepsilon = \varepsilon_{sb} + \varepsilon_{wb}$$

$$c_{f,m} = \frac{c_{f,m}}{(1 + 2\varepsilon)}$$

$$\alpha = \alpha + \left(\frac{57.3 \times \sigma}{2 \times \pi} \times c_l \right) + (4 \times c_m)$$

$$c_l = c_l \times (1 - \sigma - 2\varepsilon)$$

$$c_d = c_d \times (1 - 3\varepsilon_{sb} - 2\varepsilon_{wb})$$

$$c_m = \left[c_m \times (1 - 2\varepsilon)\right] + \left(\sigma \times \frac{c_l}{4}\right)$$

$$\frac{L}{D} = \frac{c_l}{c_d}$$

The angle of attack reading was corrected to account for three-dimensional effects due to the model not entirely spanning the LSWT test section. This correction was: [4]

$$\alpha = \alpha_u - \frac{(180 \times c_l)}{(\pi^2 \times 2.5741)}$$

for the first set of data without the endplates and:

$$\alpha = \alpha_u - \frac{(180 \times c_l)}{(\pi^2 \times 4.0640)}$$

for the second set of data with the endplates. The aspect ratio correction to angle of attack was obtained by calculating the effective aspect ratio based on the experimental data from the AG9301A case at a Reynolds number of 7.5×10^5 and the AG9301 20° deflection case at a Reynolds number of 1×10^6 respectively and then using this calculated aspect ratio to correct all other wind tunnel data.

Flow Visualization

Surface flow visualization was performed at various dynamic pressures and model angle of attack settings for the AG9301 final configuration. The flow visualization solution was a mixture of white tempera paint and diesel fuel brushed on

the airfoil surface. While the mixture was wet, the tunnel was brought up to the desired wind speed and the mixture was allowed to dry, leaving the tempera paint residue on the surface. This technique allowed clear and accurate assessments of the regions of laminar, turbulent, and separated flow, transition locations, and separation bubbles. Photographs were taken of all tested configurations for later use in measuring the transition locations and flow characteristics.

EXPERIMENTAL RESULTS AND DISCUSSION

Experimental results were obtained in the Texas A&M University Low Speed Wind Tunnel to verify the AG9301 airfoil numerical design. Results were initially obtained for both the primary element alone and the two element combination before improvements were made to the wind tunnel model. Additional experimental values were obtained on the AG9301 airfoil with the 20° and 30° secondary element deflection cases after the additional secondary element brackets and endplates were added. Numerical results, of both the design shape and the actual measured and smoothed[54] model profile shape, are included for comparison with the wind tunnel results.

AG9301A Primary Element Alone

Aerodynamic load data were measured on the AG9301A primary element alone at Reynolds numbers of 7.5×10^5 and 2.25×10^6 based on the 46 cm chord. Comparisons on this single element airfoil are possible, not only with the MCARFA computer code results, but also the PROFIL computer code analysis.

Lift coefficient values at the 7.5×10^5 Reynolds number case show essentially the same c_{lmax} value in both the experiment and numerically predicted data (Fig. 112). The design shape does have a slightly higher c_{lmax} value than the actual constructed shape. The zero lift angle of attack is essentially the same as the MCARFA predicted value. The somewhat non-linear shape of the experimental lift curve suggests the model was not seeing truly two dimensional flow. Numerical and experimental c_d values agree quite well with the experimental data slightly higher through most of the c_l range (Fig. 113). The L/D ratio results follow the c_d values and show generally quite good agreement (Fig. 114). The PROFIL computer code does appear to most

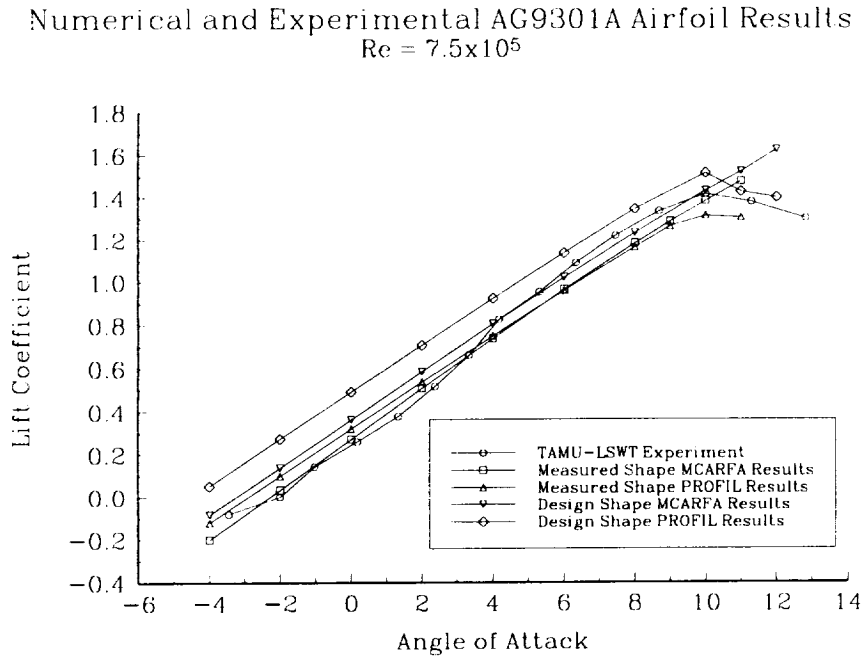

Fig. 112 Experimental AG9301A lift coefficient results, Re = 7.5x10^5

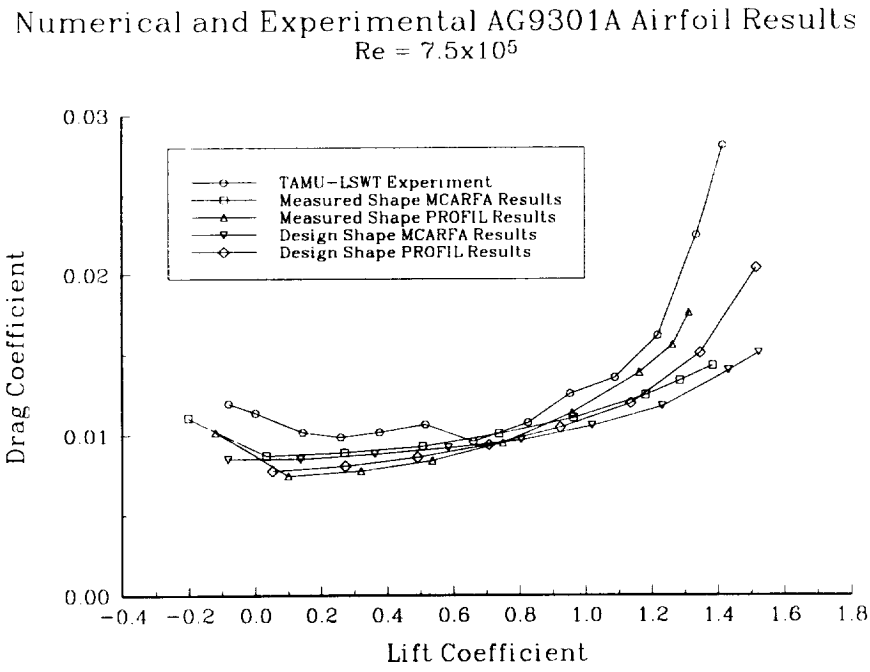

Fig. 113 Experimental AG9301A drag coefficient results, Re = 7.5x10^5

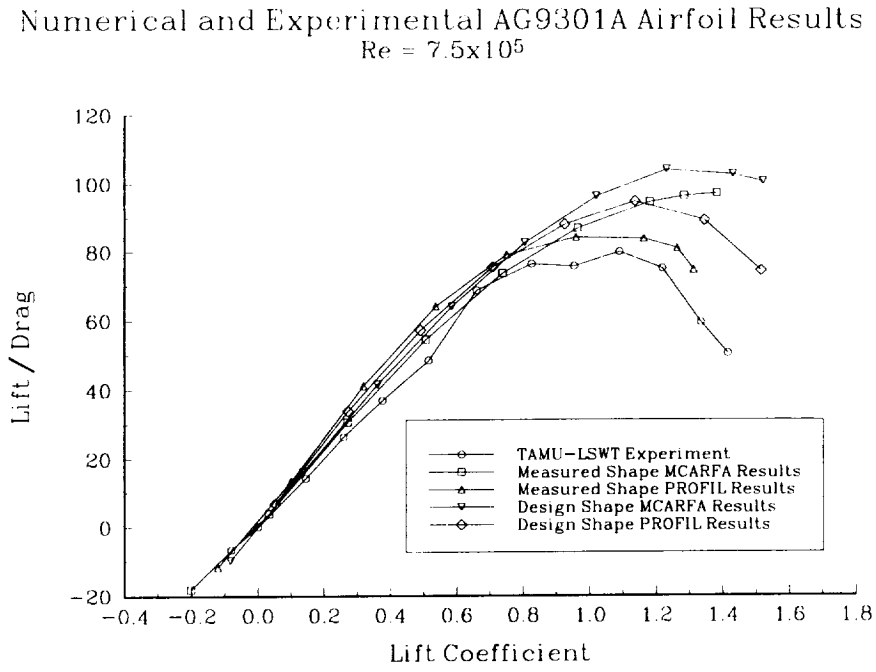

Fig. 114 Experimental AG9301A L/D ratio results, Re = $7.5x10^5$

accurately predict the measured values, especially at higher lift coefficients. Moment coefficient results vary substantially between all four types of numerical data and the experimental results (Fig. 115).

Similar single element results were obtained on the AG9301 at a Reynolds number of $2.25x10^6$. Experimental values were only obtained through the cruise lift coefficient range because of model mounting loads and available pressure transducer ranges. Lift coefficient results show generally good agreement with the zero lift angle of attack much closer to the numerically predicted value than at the lower Reynolds number case (Fig. 116). Drag coefficient results again show good agreement with the experimental data slightly higher through the entire c_l range (Fig. 117). The experimental L/D ratio values also correspond to the numerically predicted answers, but are somewhat lower because of the higher c_d results (Fig. 118). The moment

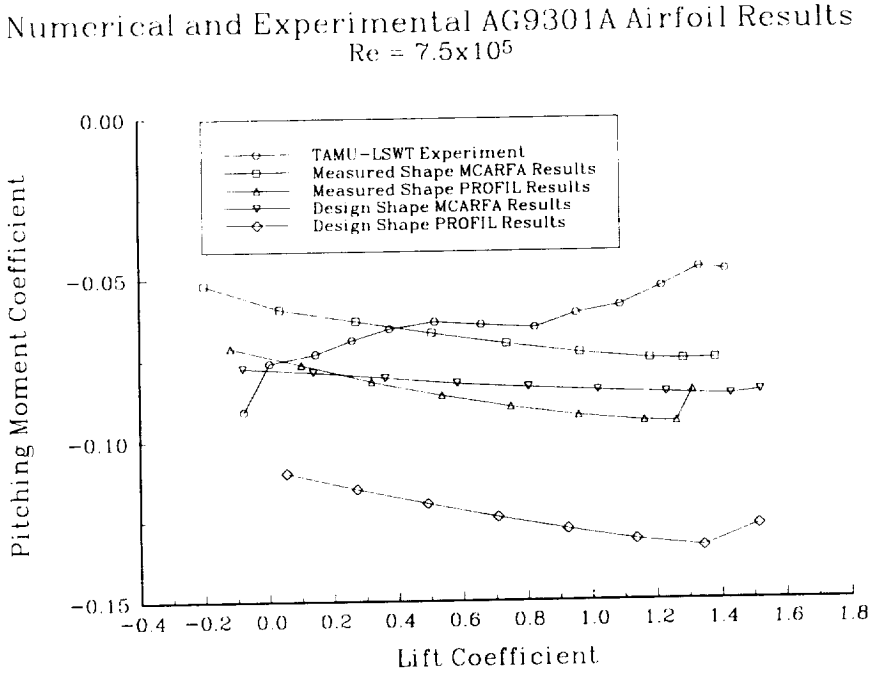

Fig. 115 Experimental AG9301A moment coefficient results, Re = 7.5x10^5

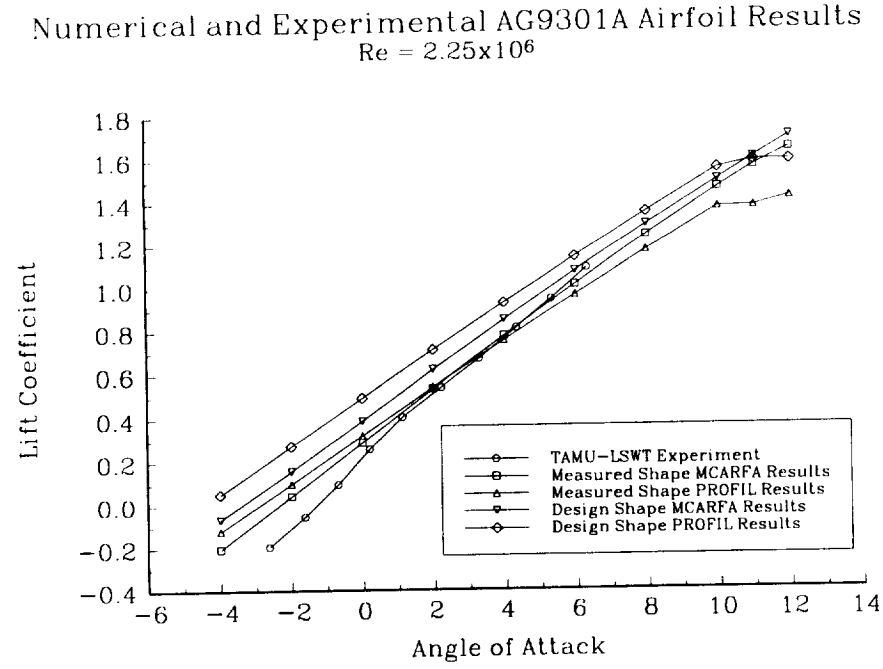

Fig. 116 Experimental AG9301A lift coefficient results, Re = 2.25x10^6

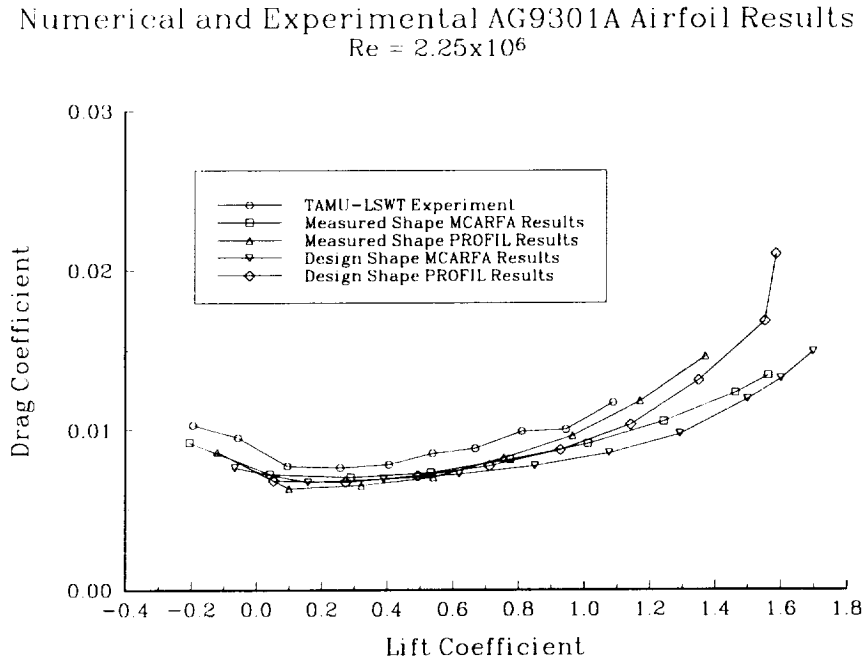

Fig. 117 Experimental AG9301A drag coefficient results, Re = 2.25x10^6

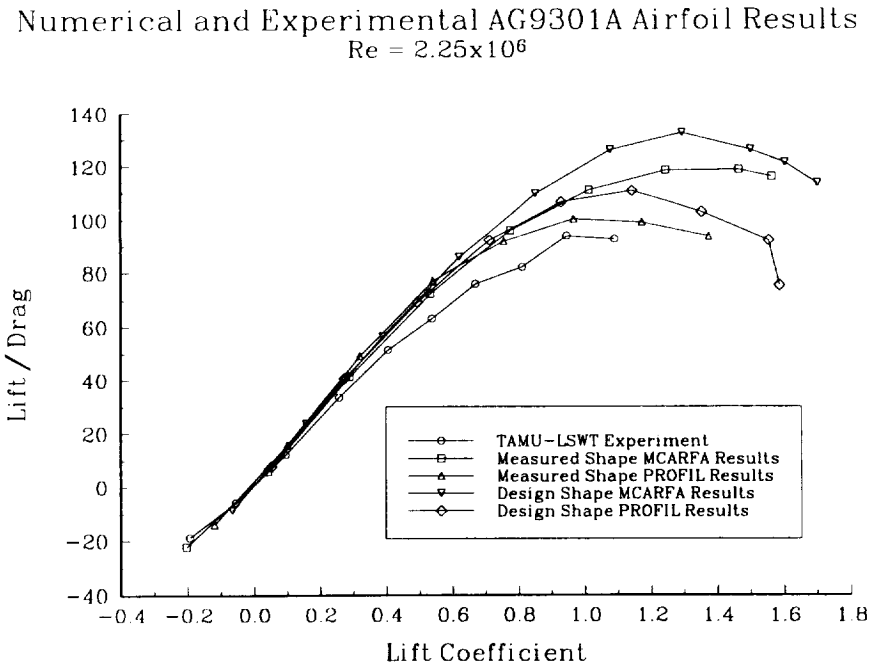

Fig. 118 Experimental AG9301A L/D ratio results, Re = 2.25x10^6

coefficient values again vary significantly between the different sources (Fig. 119). The experimental moment is the lowest of any of the types of data.

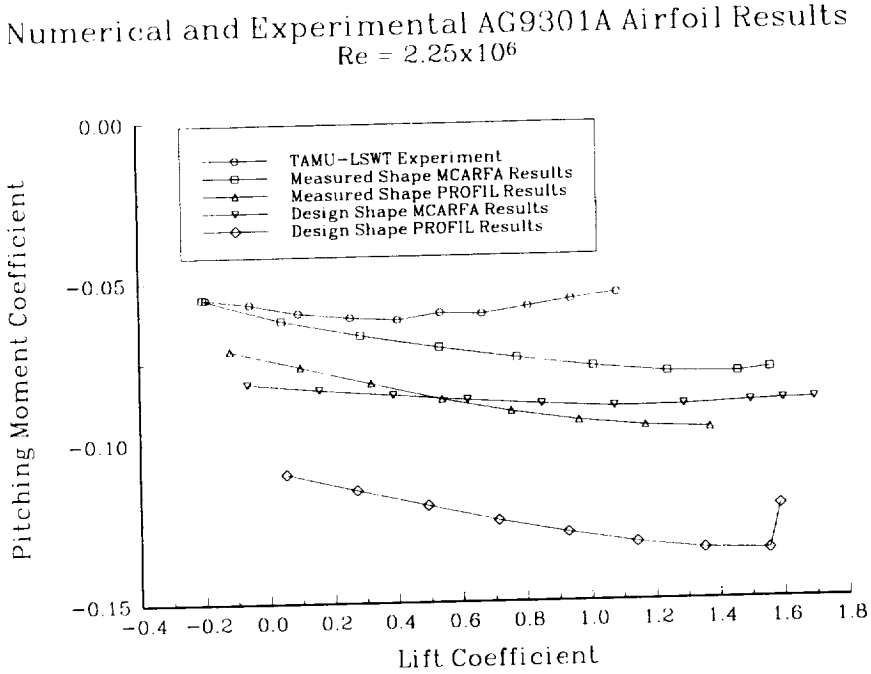

Fig. 119 Experimental AG9301A moment coefficient results, Re = 2.25x10^6

Overall, the AG9301A single element airfoil was experimentally verified. The numerically predicted maximum lift coefficient values were also measured. The drag coefficient was measured higher than predicted, but within the expected range based on the higher turbulence intensity and the model construction techniques. The moment coefficient was also within the predicted range, although really good correlation between any of the sets of moment data were not observed.

Relative Position

Experimental data was obtained to verify the optimum position of the second element with respect to the first. As with the numerical data, the second element was moved through a grid with the leading edge of the secondary element varied from 94% through 96% behind the leading edge of the primary element and from 1% through 2% below the primary element. Results were obtained through the cruise lift coefficients for the AG9301 with the secondary element deflected 30° at a Reynolds number of $3x10^6$ based on the total chord.

The experimental L/D results for the 94%, -1% secondary element position show very poor agreement with the numerically predicted values (Fig. 120). Significant differences also exist between the design and constructed shape results at this position. These differences are assumed to be due primarily to the finite trailing edge thickness on the constructed shape and the near zero thickness on the design shape. Moment coefficient results show a experimentally measured moment roughly two thirds that of the predicted case (Fig. 121).

Somewhat better correlation between numerical and experimental data was obtained at the 94%, -1.5% position. Lift to drag ratio results still show a significantly lower experimental L/D than predicted (Fig. 122). Moment coefficient results, while again closer, still are significantly different between the numerical and experimental values (Fig. 123). Results very similar to the 94%, -1.5% case were obtained for the 94%, -2% condition. Again, a lower experimental L/D (Fig. 124) and moment coefficient (Fig. 125) were observed.

Results at the 95% horizontal position follow the trends observed in the 94% cases. The experimental 1% below L/D results (Fig. 126) and moment coefficient results (Fig. 127) show very poor agreement with the numerically predicted

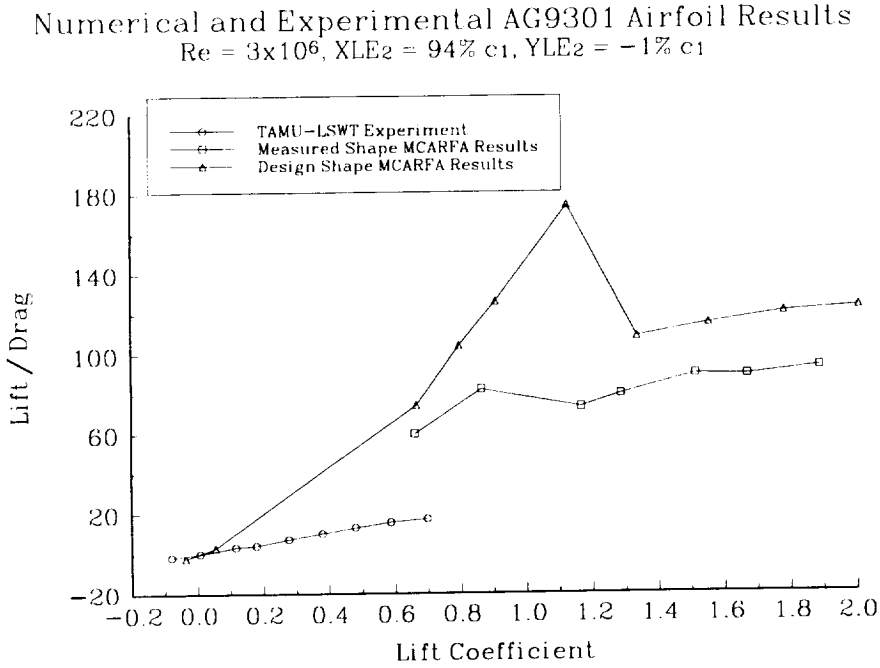

Fig. 120 AG9301 experimental L/D ratio, 94%, -1% position, δ=30°

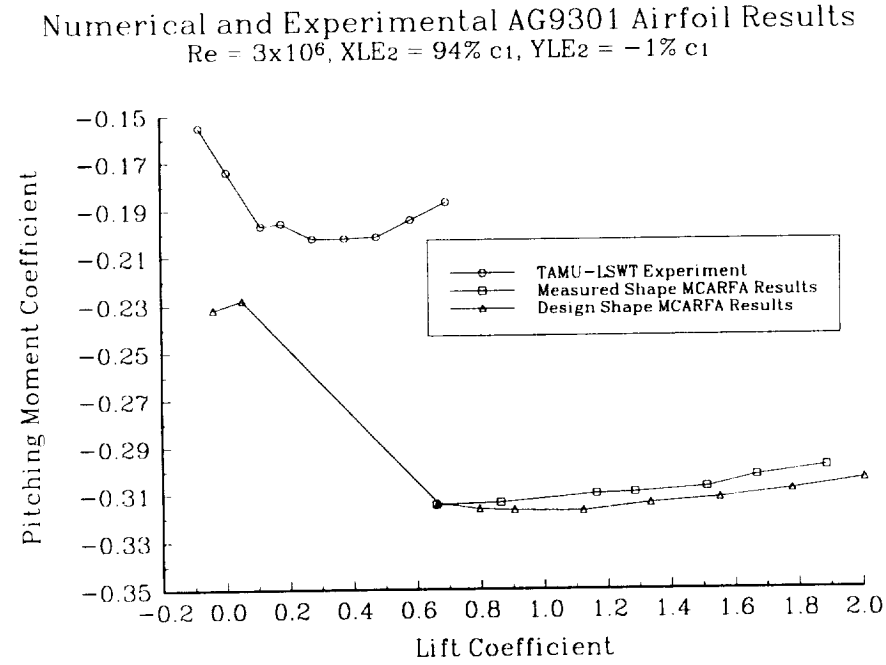

Fig. 121 AG9301 experimental moment coefficient, 94%, -1% position, δ=30°

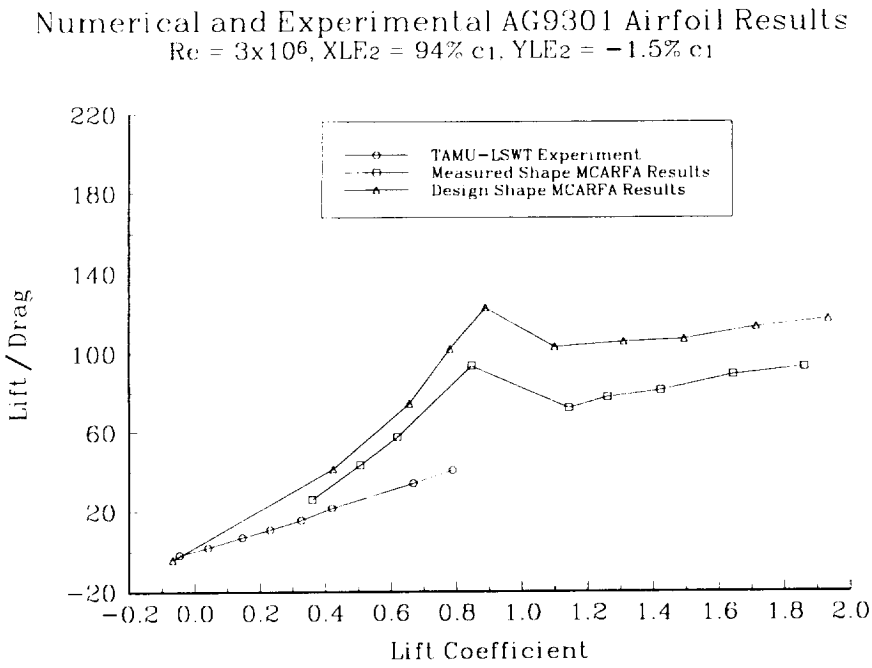

Fig. 122 AG9301 experimental L/D ratio, 94%, -1.5% position, δ=30°

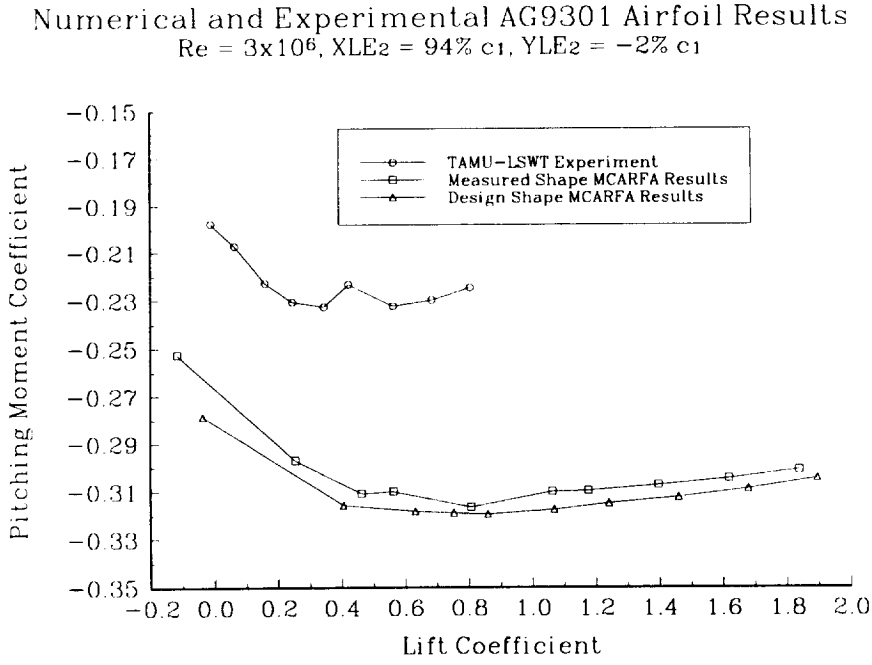

Fig. 123 AG9301 experimental moment coefficient, 94%, -1.5% position, δ=30°

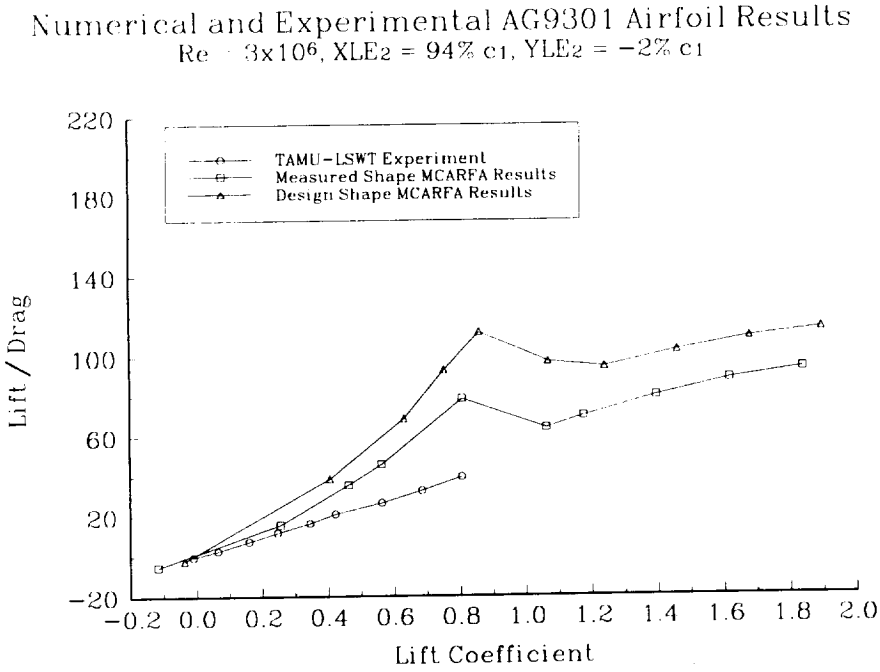

Fig. 124 AG9301 experimental L/D ratio, 94%, -2% position, δ=30°

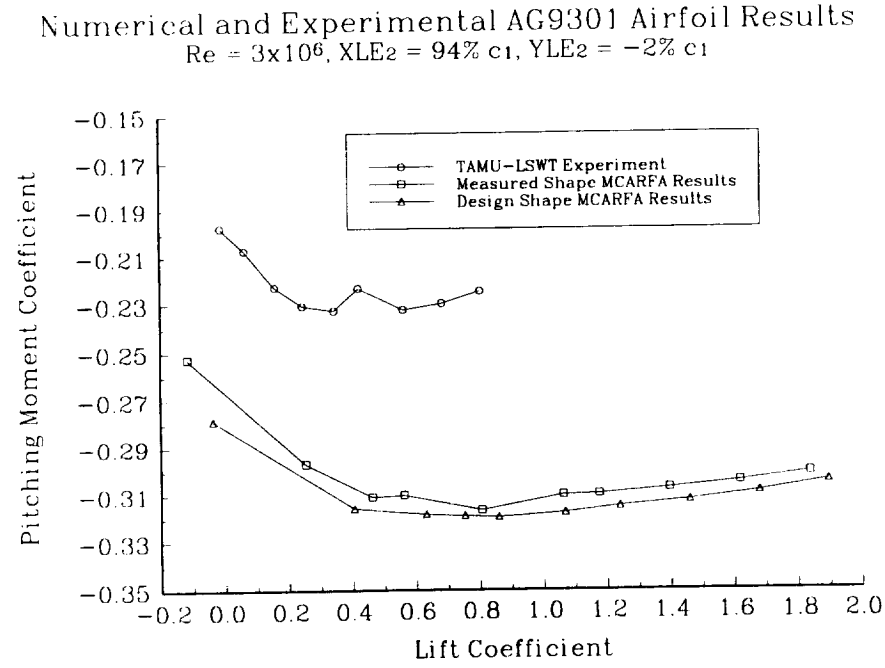

Fig. 125 AG9301 experimental moment coefficient, 94%, -2% position, δ=30°

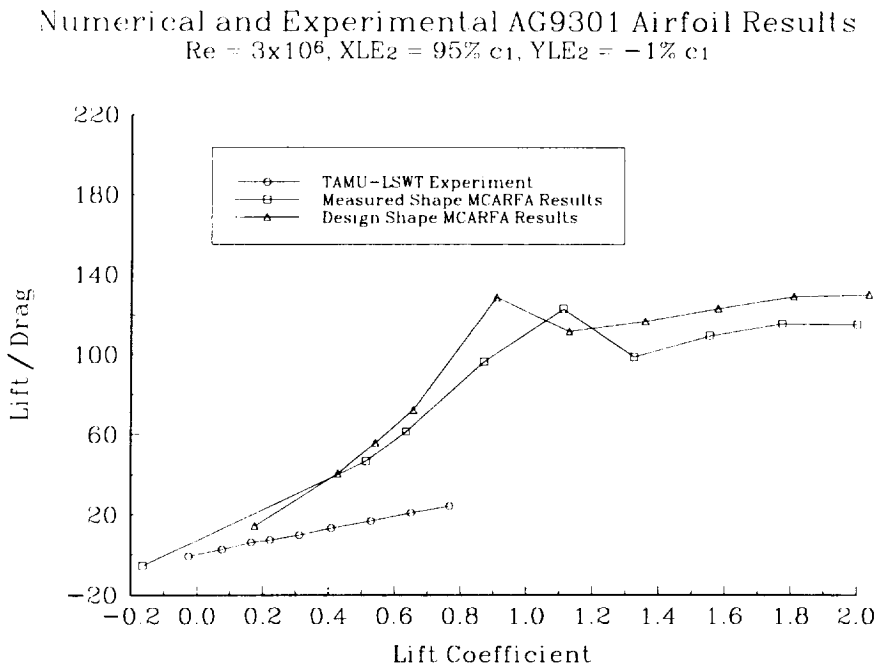

Fig. 126 AG9301 experimental L/D ratio, 95%, -1% position, δ=30°

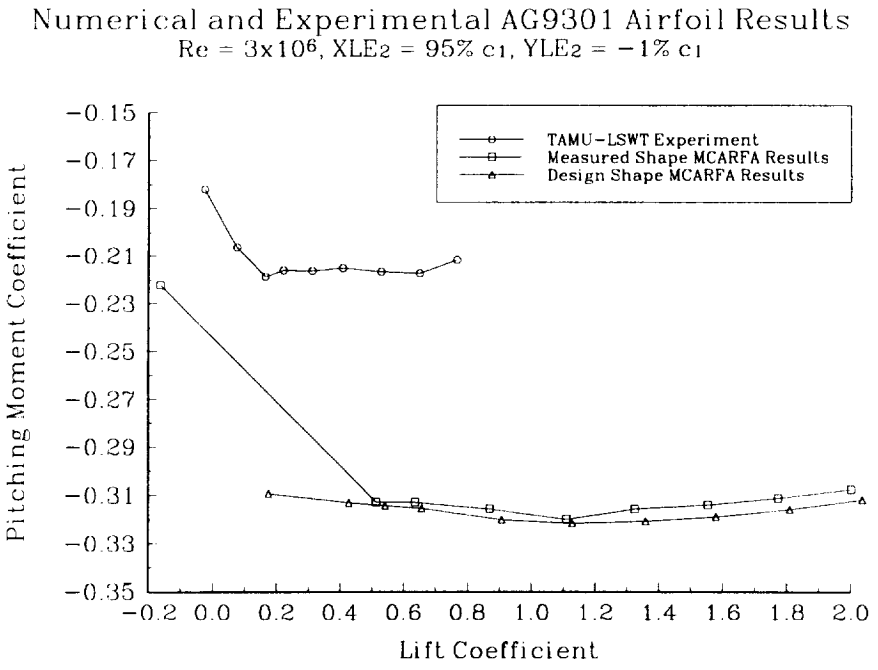

Fig. 127 AG9301 experimental moment coefficient, 95%, -1% position, δ=30°

information. The experimental 1.5% below L/D results (Fig. 128) and moment coefficient results (Fig. 129) and the 2% below answers (Figs. 130-131) show better agreement with the numerical values, but still are significantly lower.

The 96%, -1% position again exhibited very poor agreement with the numerical cases. Both the L/D results and moment coefficient values were significantly lower (Figs. 132-133). The 96%, -1.5% experimental L/D values showed very good agreement with the numerically predicted case (Fig. 134). Moment coefficient values were still measured to be significantly lower than predicted (Fig. 135). Fair agreement was also obtained with the L/D data for the 96%, -2% case (Fig. 136). However, the moment coefficient comparison was still poor (Fig. 137).

As previously discussed, the secondary element was observed to significantly deflect under an applied load. It is believed this deflection is the cause of the poor correlation between the experimental and numerical results. The best comparisons came with the largest gap conditions, where deflections would have the least effect. In addition, the significantly lower moment suggests lower lift values on the aft portions of the airfoil, thus further supporting the hypothesis of second element deflection being the cause of the poor agreement.

Due to the poor agreement between the experimental and numerical data, the optimum relative position could not be verified.

Transition Location

The transition location was measured on the primary element of the AG9301 airfoil using the flow visualization method discussed earlier. Results for the 30° deflection case of the AG9301 airfoil at a Reynolds number of $3x10^6$ show less laminar flow across the entire c_l range on the upper surface than predicted (Fig. 138). However, more laminar flow was measured than predicted on the lower surface. This difference

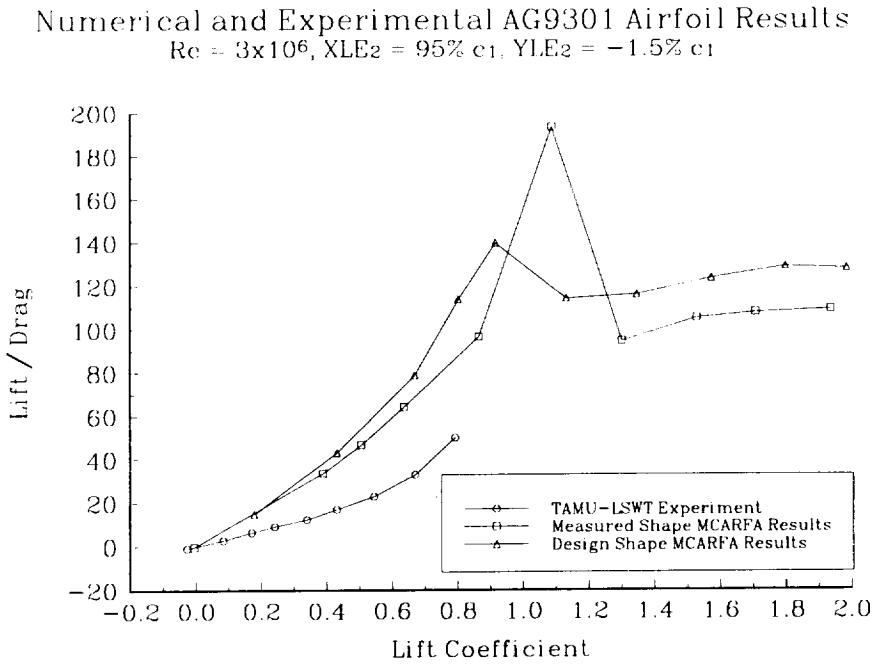

Fig. 128 AG9301 experimental L/D ratio, 95%, -1.5% position, δ=30°

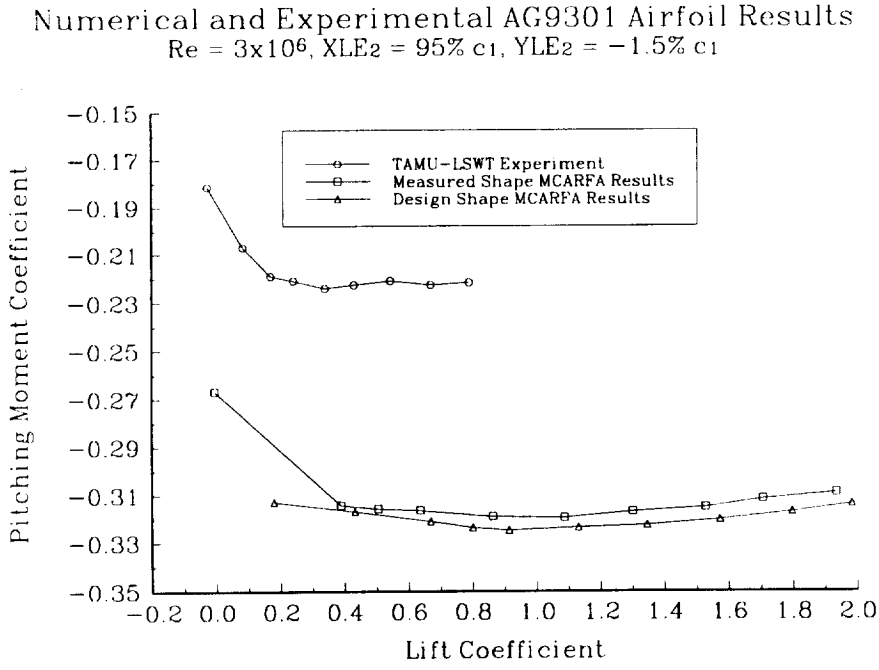

Fig. 129 AG9301 experimental moment coefficient, 95%, -1.5% position, δ=30°

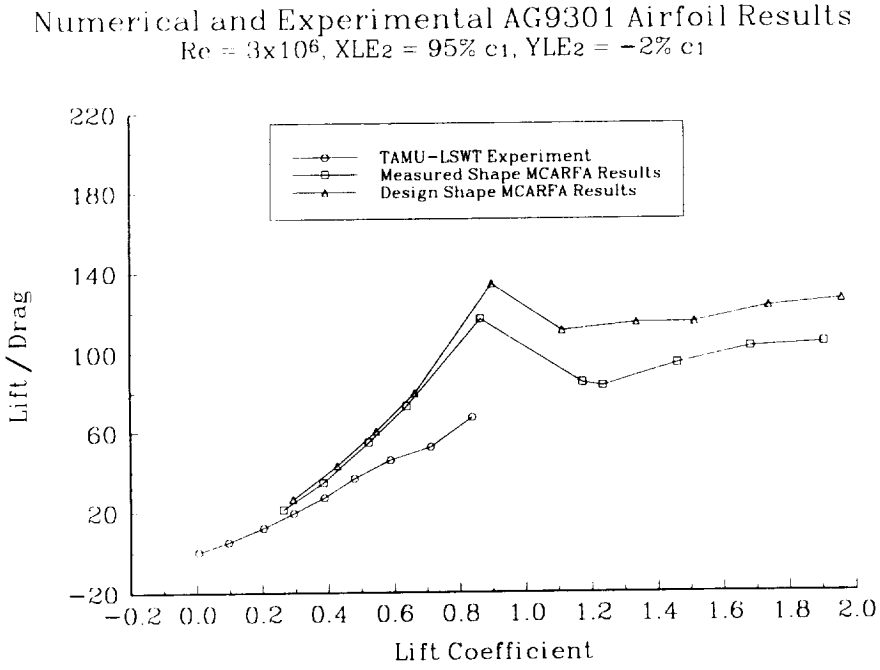

Fig. 130 AG9301 experimental L/D ratio, 95%, -2% position, δ=30°

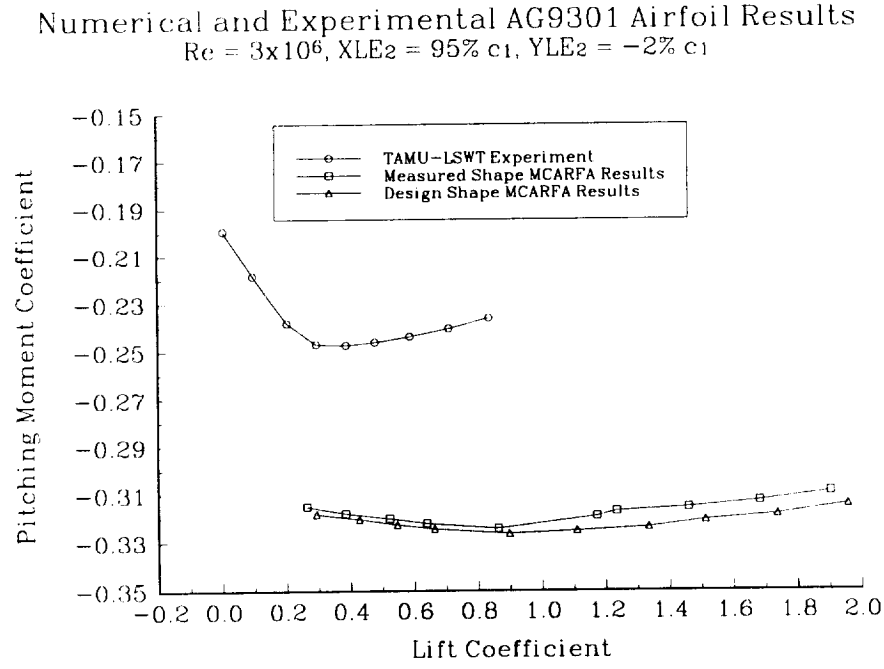

Fig. 131 AG9301 experimental moment coefficient, 95%, -2% position, δ=30°

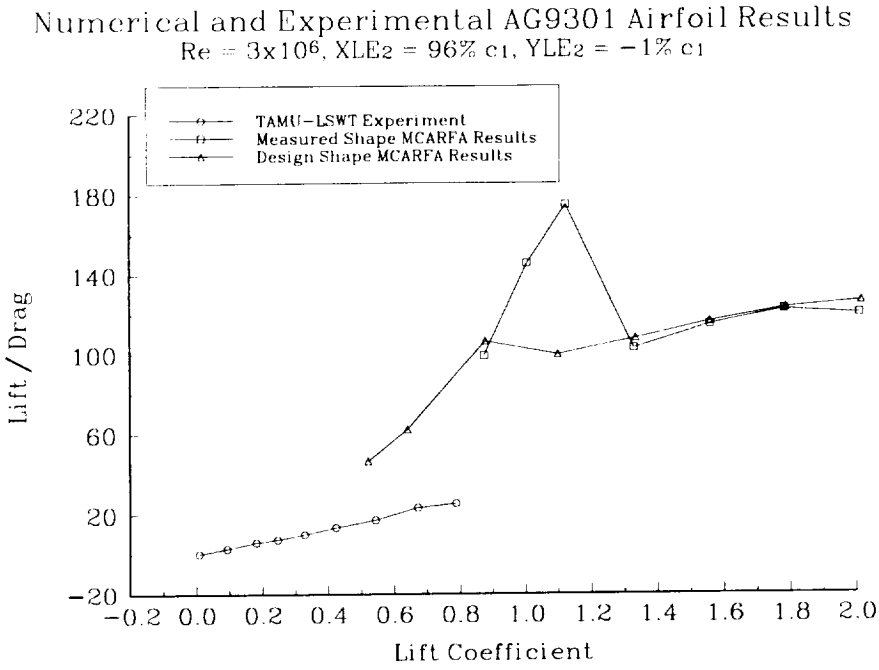

Fig. 132 AG9301 experimental L/D ratio, 96%, -1% position, δ=30°

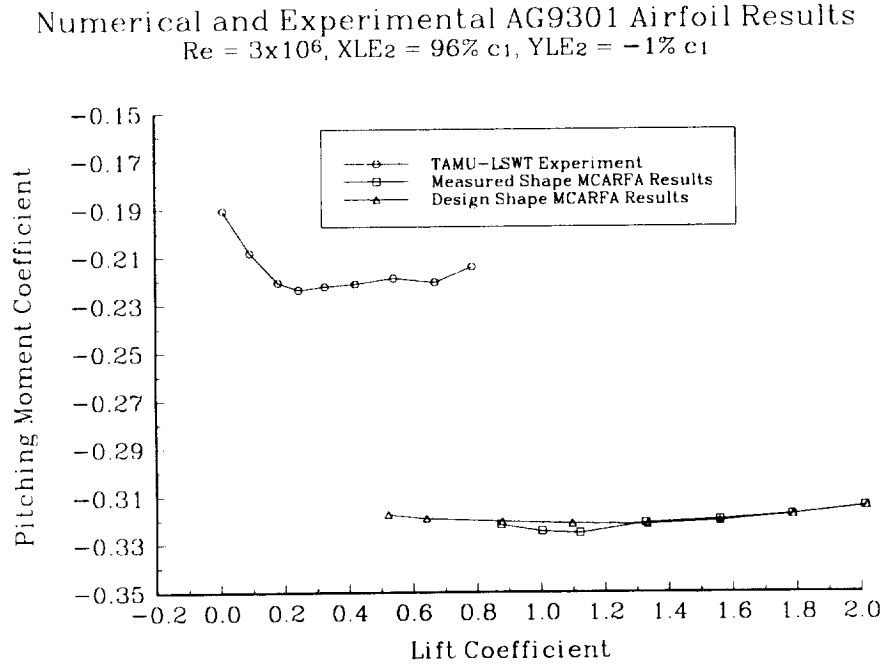

Fig. 133 AG9301 experimental moment coefficient, 96%, -1% position, δ=30°

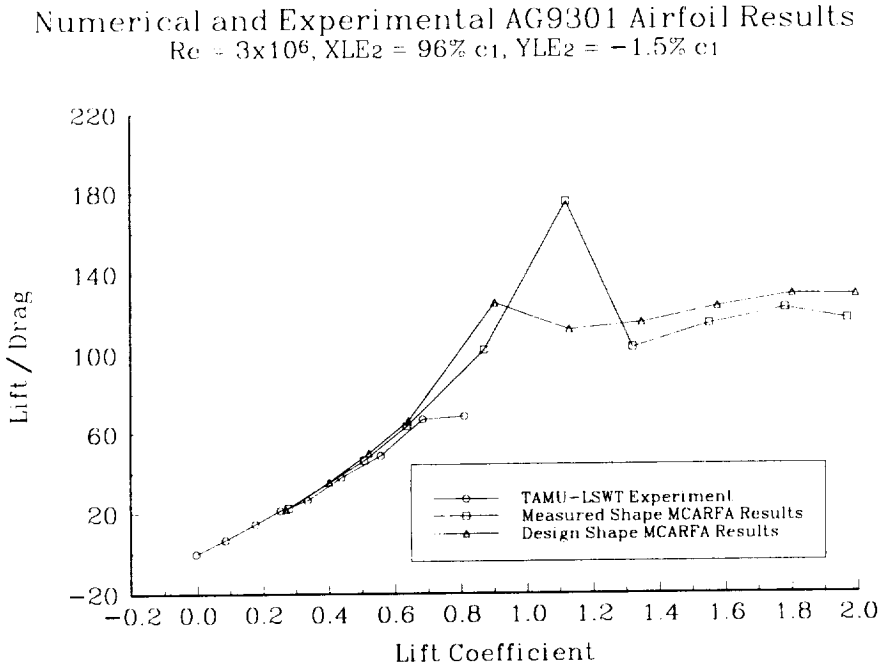

Fig. 134 AG9301 experimental L/D ratio, 96%, -1.5% position, δ=30°

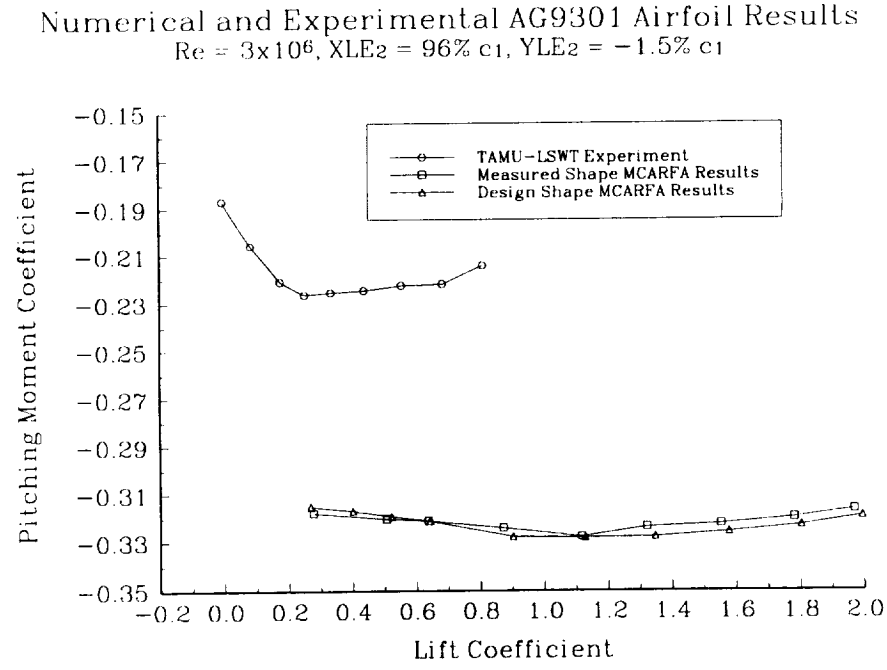

Fig. 135 AG9301 experimental moment coefficient, 96%, -1.5% position, δ=30°

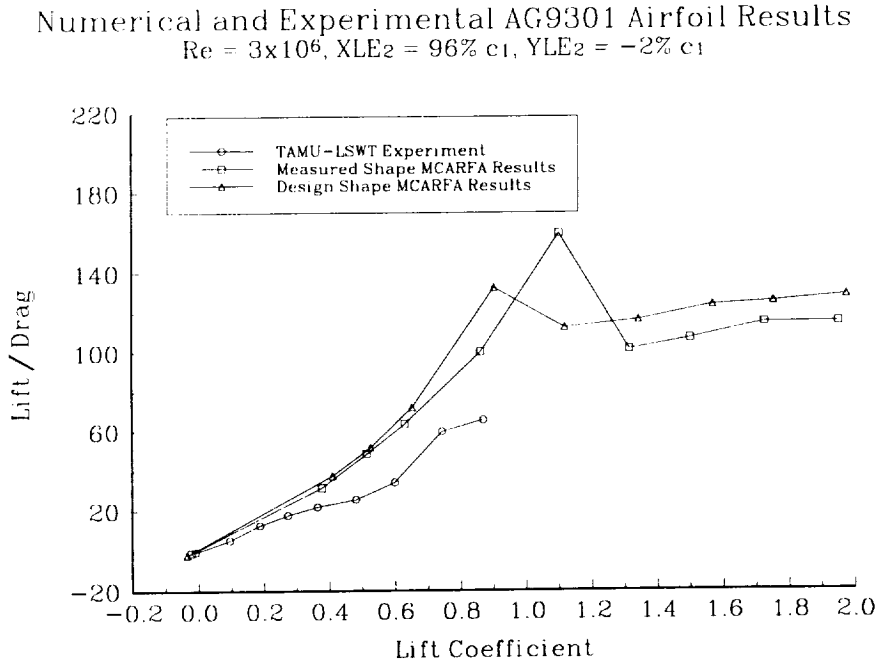

Fig. 136 AG9301 experimental L/D ratio, 96%, -2% position, δ=30°

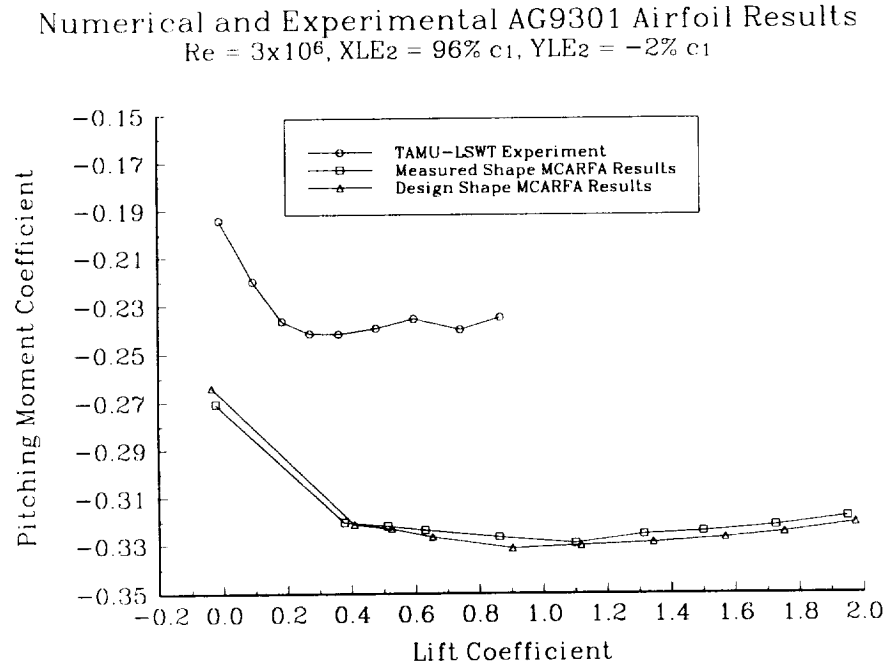

Fig. 137 AG9301 experimental moment coefficient, 96%, -2% position, δ=30°

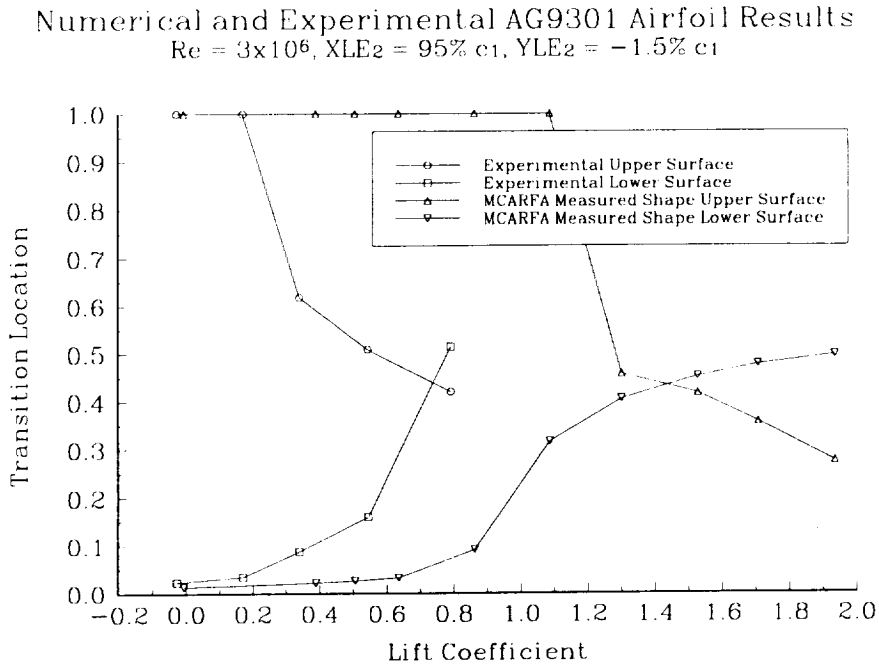

Fig. 138 AG9301 experimental transition location, $\delta = 30°$

is again likely to be caused by the secondary element deflection. It is possible that the surface finish of the model or the freestream turbulence intensity level in the wind tunnel were also contributing to the differences.

Comparisons were made between the experimental wind tunnel data and the numerically predicted values with transition fixed at the experimentally observed locations on the primary element in order to determine the effects of the increased freestream turbulence on the results. Lift coefficient answers show very little change between the numerical fixed and natural transition locations (Fig. 139). Drag coefficient results show a nearly 55% increase in drag coefficient at a c_l of about 0.73 with the transition fixed (Fig. 140). Moment coefficient results show very little change with the different transition locations (Fig. 141) and the L/D ratio follows the c_d trends with a significantly lower L/D for the fixed transition case (Fig. 142).

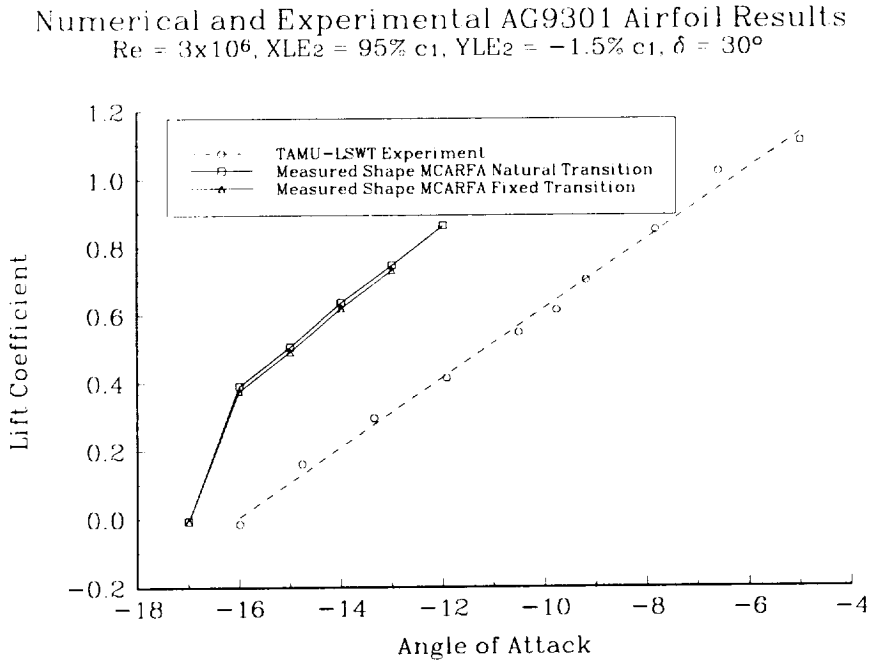

Fig. 139 AG9301 fixed transition effect on lift coefficient, δ = 30°

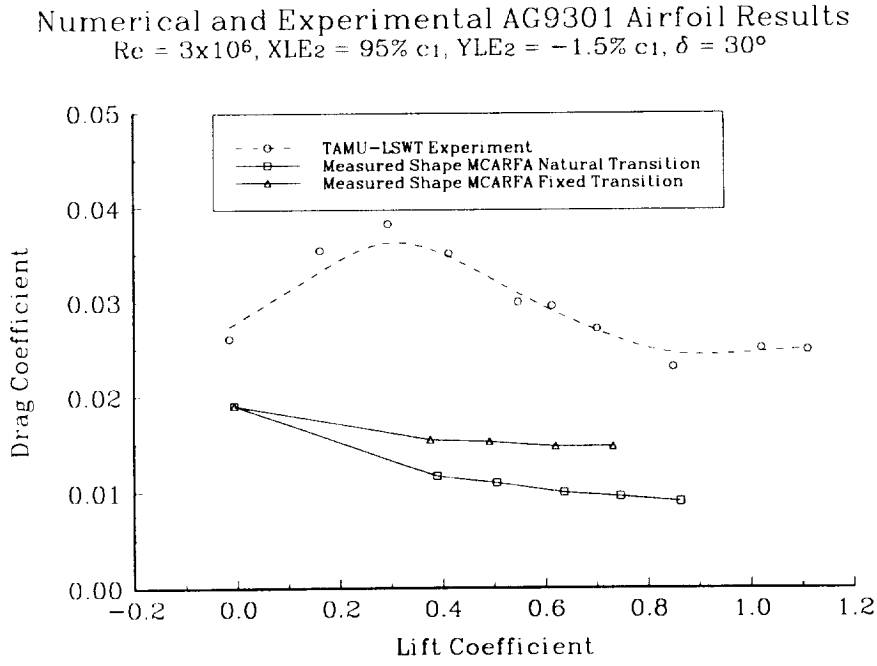

Fig. 140 AG9301 fixed transition effect on drag coefficient, δ = 30°

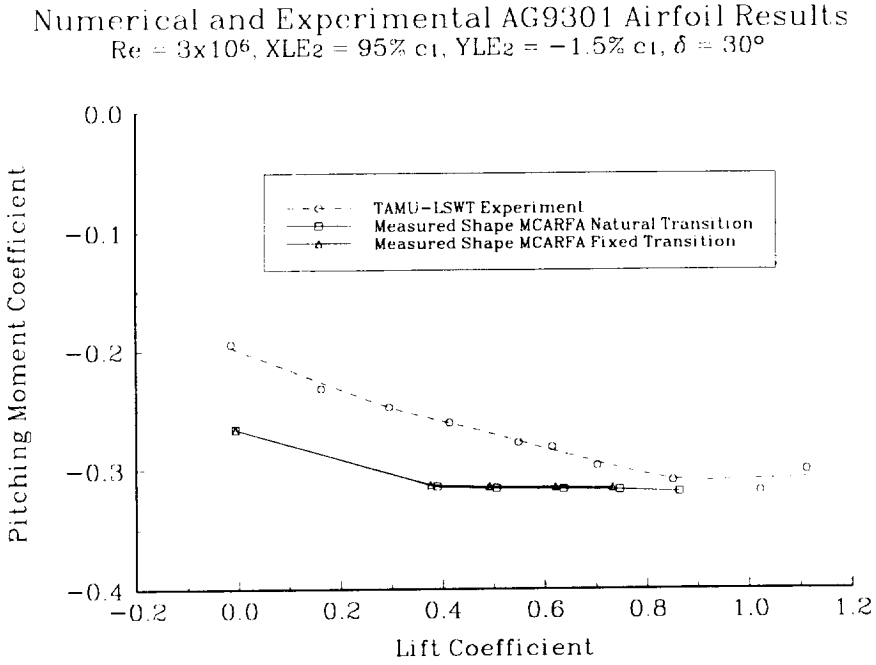

Fig. 141 AG9301 fixed transition effect on moment coefficient, δ = 30°

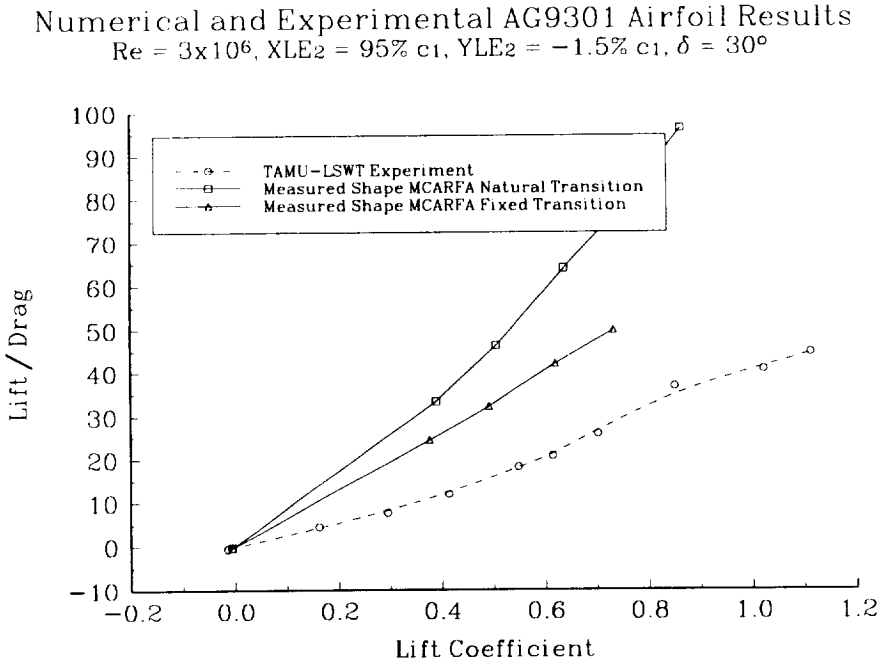

Fig. 142 AG9301 fixed transition effect on L/D ratio, δ = 30°

Improved Wind Tunnel Model

Improvements to the wind tunnel model, as previously discussed, were completed and new aerodynamic load data at Reynolds numbers from $1x10^6$ through $3x10^6$ were obtained for both the 30° and 20° deflection cases of the AG9301 airfoil. Results were again compared to both the design and measured shape numerical data from the MCARFA computer code.

Lift coefficient data for the AG9301 30° deflection case at a Reynolds number of $8x10^5$ shows a significant change in the zero lift angle of attack when compared with the numerically predicted data (Fig. 143). The maximum lift coefficient value was also significantly lower at approximately 2.2 rather than the 2.8 predicted. Drag and moment coefficient data were not obtained at this Reynolds number because of the accuracy of the pressure measurement system at reading the extremely low pressures at this condition.

Lift coefficient data at the $1x10^6$ Reynolds number case for the AG9301 30° deflection condition again shows a significant change in the α_0 value (Fig. 144). The experimentally measured c_{lmax} was about 2.3 for this case. Drag coefficient data shows the measured c_d quite a bit higher than predicted (Fig. 145). The numerical and experimental L/D curves generally follow the same trends, but the experimental values are a significant amount lower (Fig. 146). The experimental moment coefficient values are also lower than the numerically predicted case (Fig. 147).

The $2x10^6$ Reynolds number case lift coefficient results show a change in the lift curve slope between the experimental and numerical data (Fig. 148). Experimental drag coefficient values, while following the shape of the curve well, are higher than predicted (Fig. 149). Experimental L/D results (Fig. 150) and moment coefficient values (Fig. 151) are both lower than predicted.

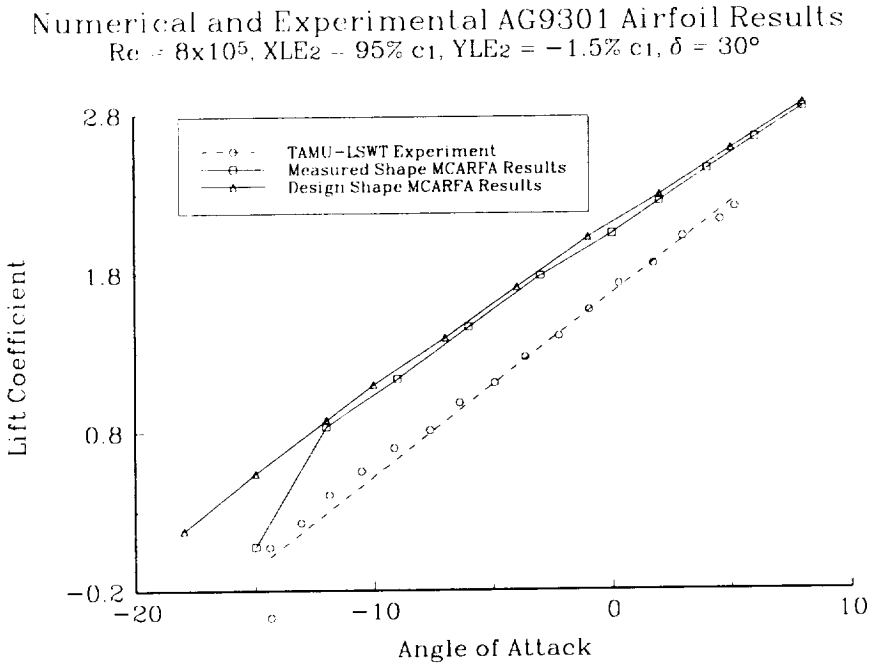

Fig. 143 AG9301 experimental lift coefficient, $\delta = 30°$, Re = $8x10^5$

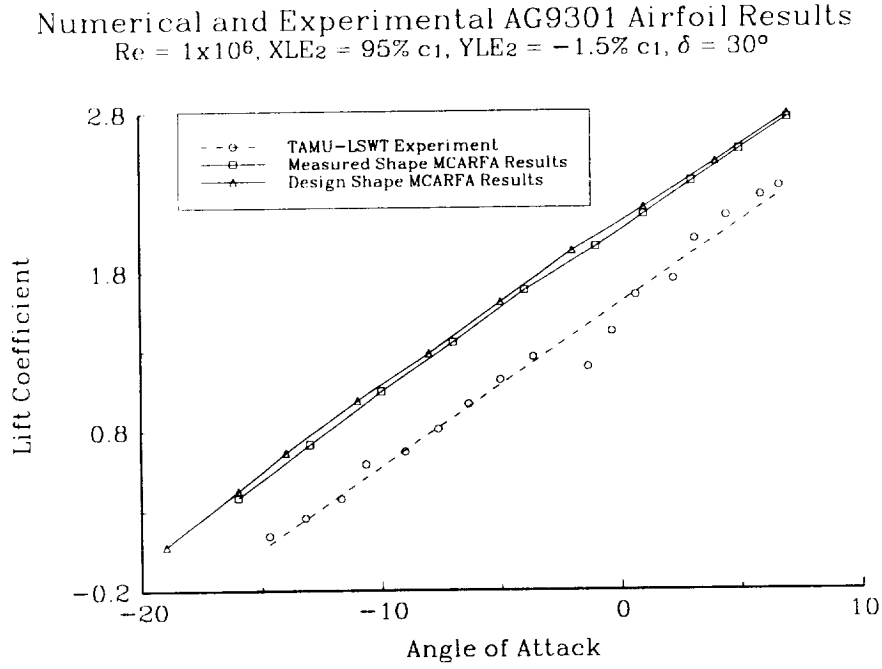

Fig. 144 AG9301 experimental lift coefficient, $\delta = 30°$, Re = $1x10^6$

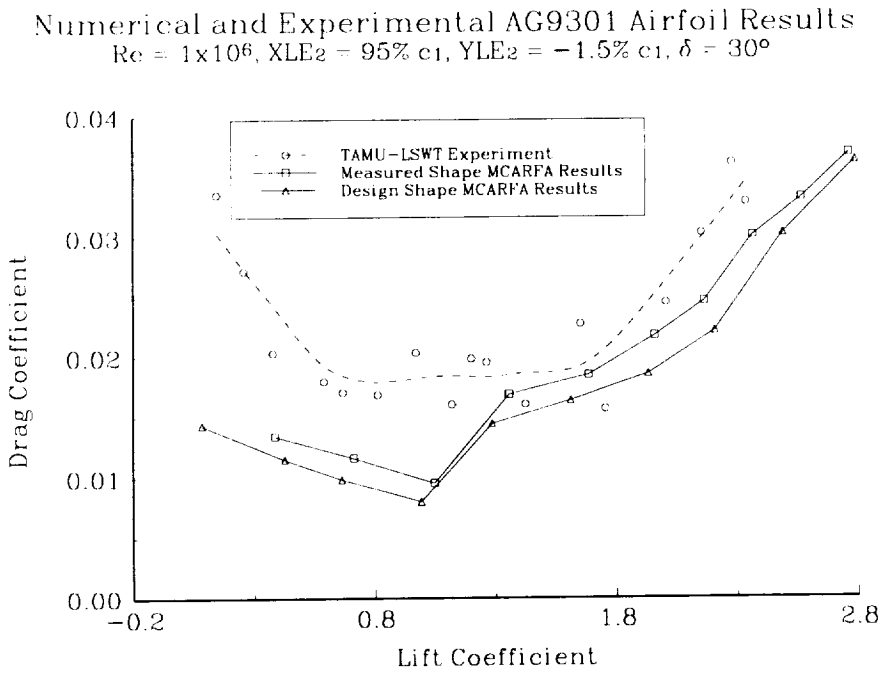

Fig. 145 AG9301 experimental drag coefficient, δ = 30°, Re = 1x10^6

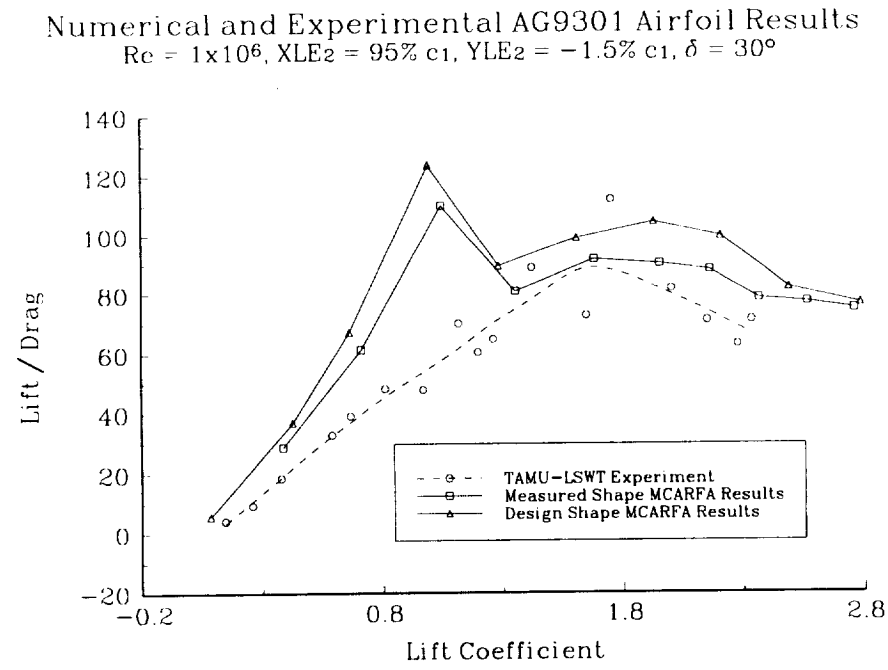

Fig. 146 AG9301 experimental L/D ratio, δ = 30°, Re = 1x10^6

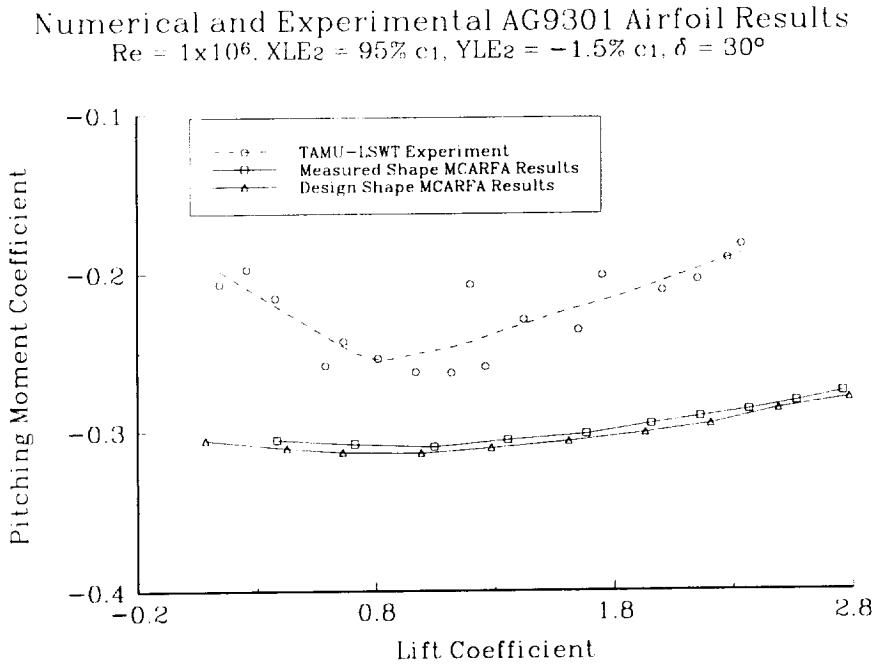

Fig. 147 AG9301 experimental moment coefficient, δ = 30°, Re = 1x10^6

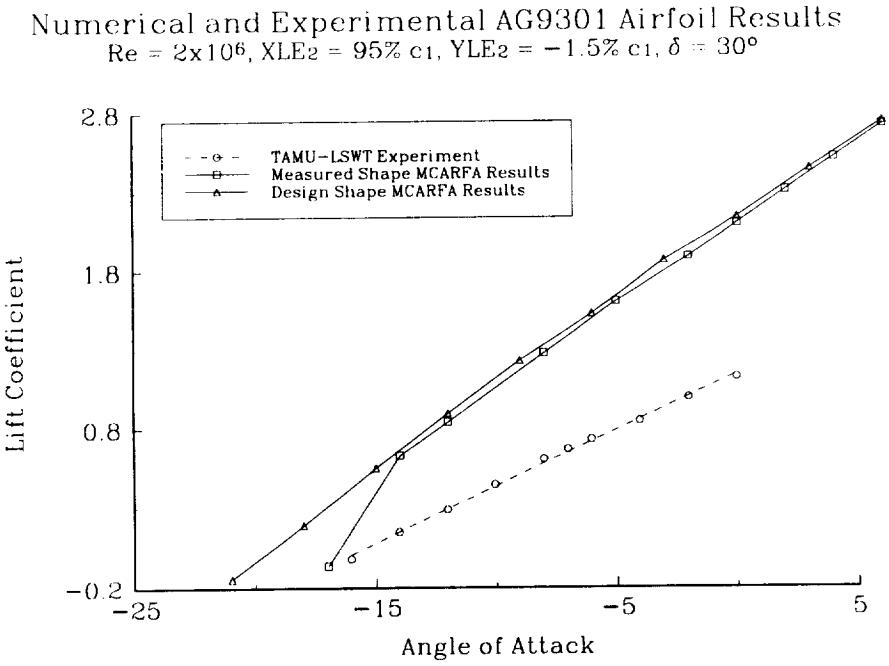

Fig. 148 AG9301 experimental lift coefficient, δ = 30°, Re = 2x10^6

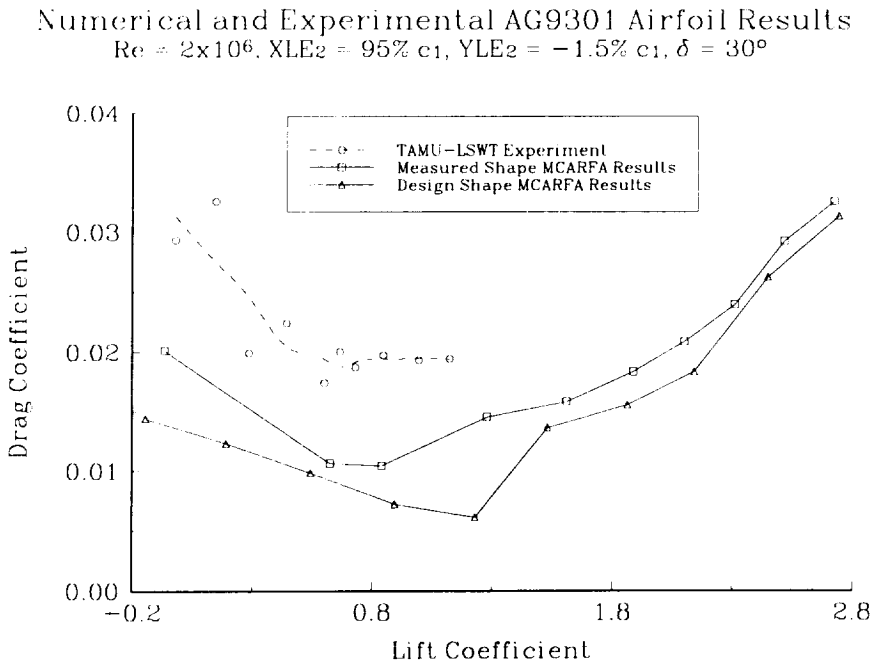

Fig. 149 AG9301 experimental drag coefficient, δ = 30°, Re = 2x10^6

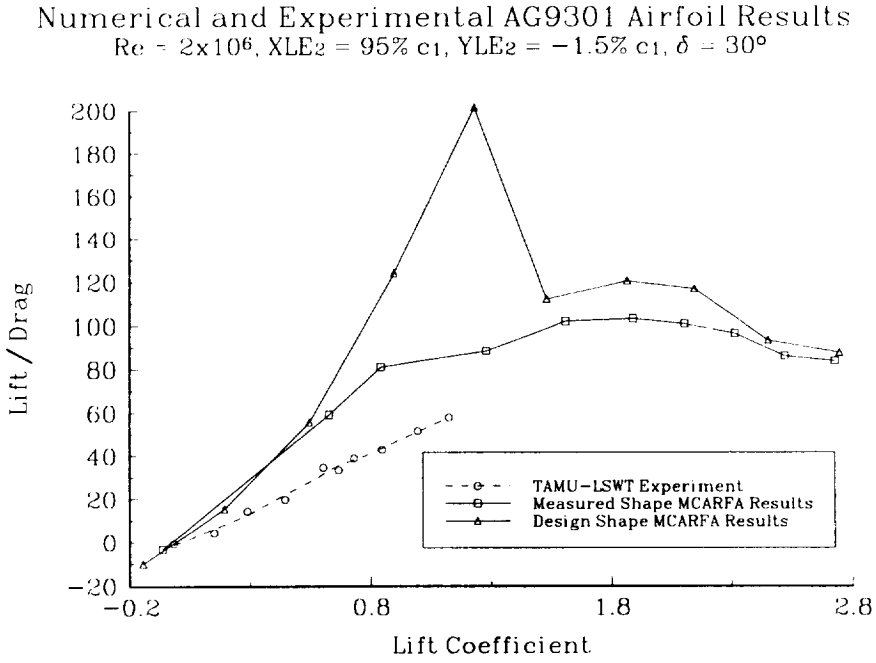

Fig. 150 AG9301 experimental L/D ratio, δ = 30°, Re = 2x10^6

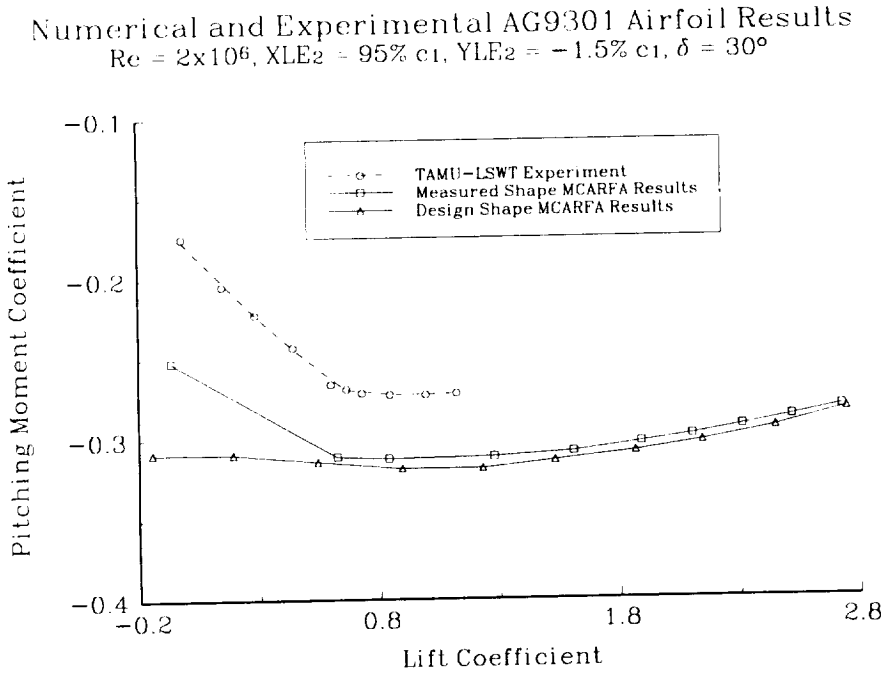

Fig. 151 AG9301 experimental moment coefficient, $\delta = 30°$, Re = $2x10^6$

Lift coefficient results at a Reynolds number of $3x10^6$ show the lift curve slope matches the numerical value well, but again a large shift in α_0 value is observed (Fig. 152). The drag coefficient for this case is significantly higher than predicted (Fig. 153) and consequently the L/D results are lower (Fig. 154). Moment coefficient trends do not match the shape of the predicted curve (Fig. 155).

Experimental lift coefficient results for the 20° deflection case of the AG9301 airfoil at a Reynolds number of $1x10^6$ show fair agreement with the numerically predicted data (Fig. 156). The zero lift angle of attack is shifted approximately 1.5° between the numerical and experimental data. The c_{lmax} value was predicted to be 2.63 and measured to be 2.28, some 13% lower. The experimental drag coefficient was higher than numerically predicted through the low c_l range, but generally followed the shape of the curve well (Fig. 157). Because of the higher c_d, the experimental L/D ratio

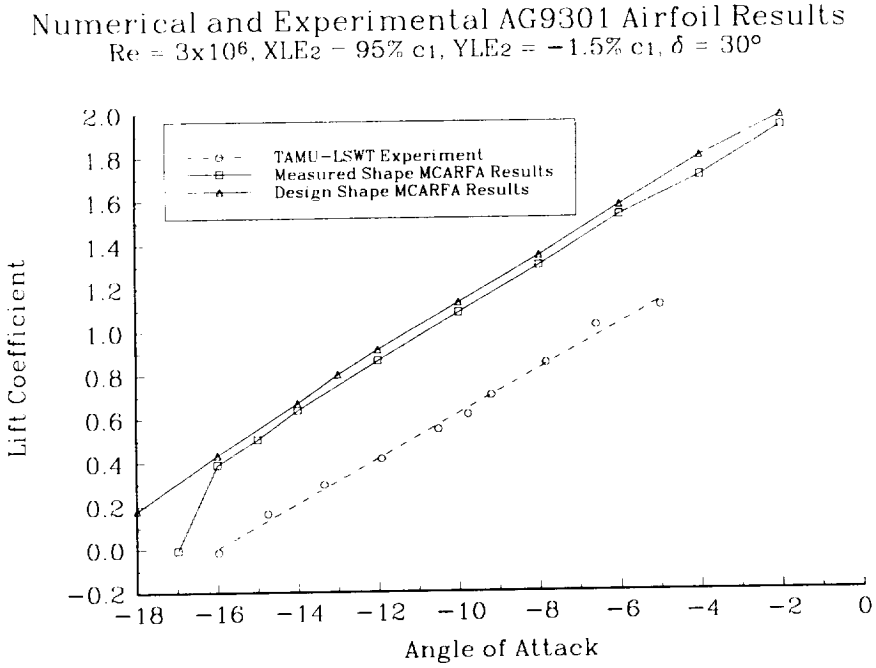

Fig. 152 AG9301 experimental lift coefficient, δ = 30°, Re = 3x10^6

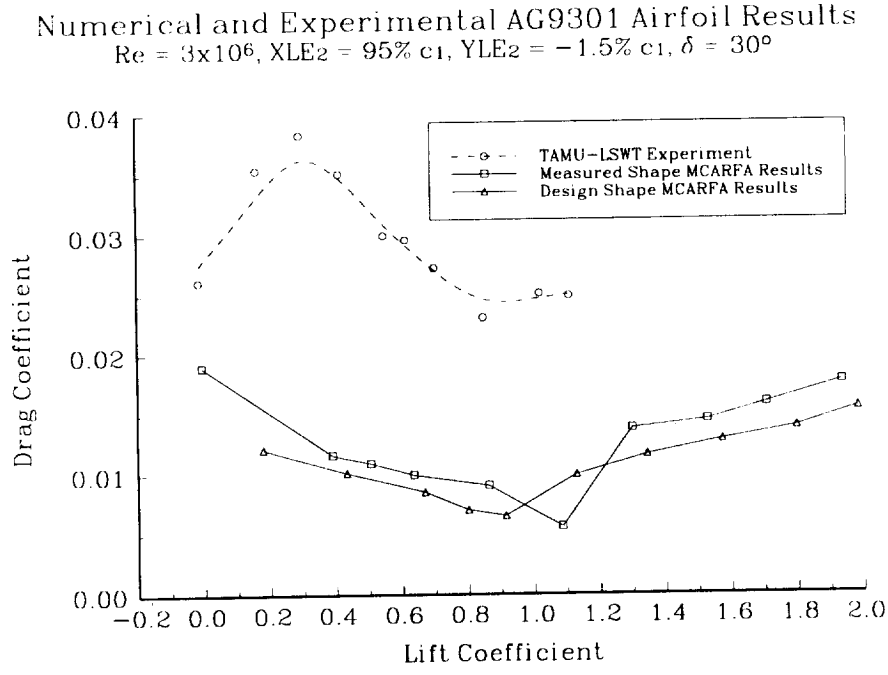

Fig. 153 AG9301 experimental drag coefficient, δ = 30°, Re = 3x10^6

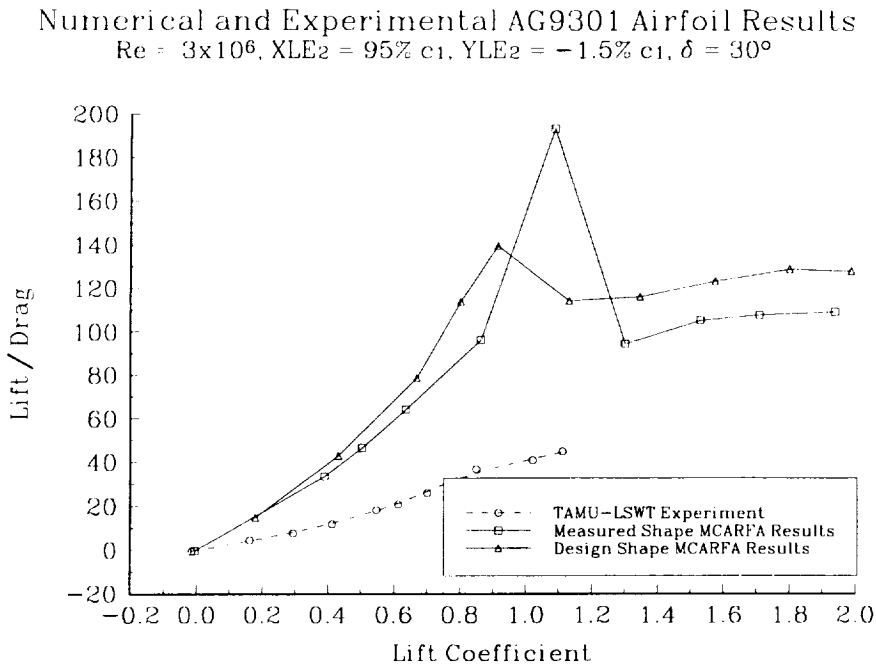

Fig. 154 AG9301 experimental L/D ratio, δ = 30°, Re = 3x10^6

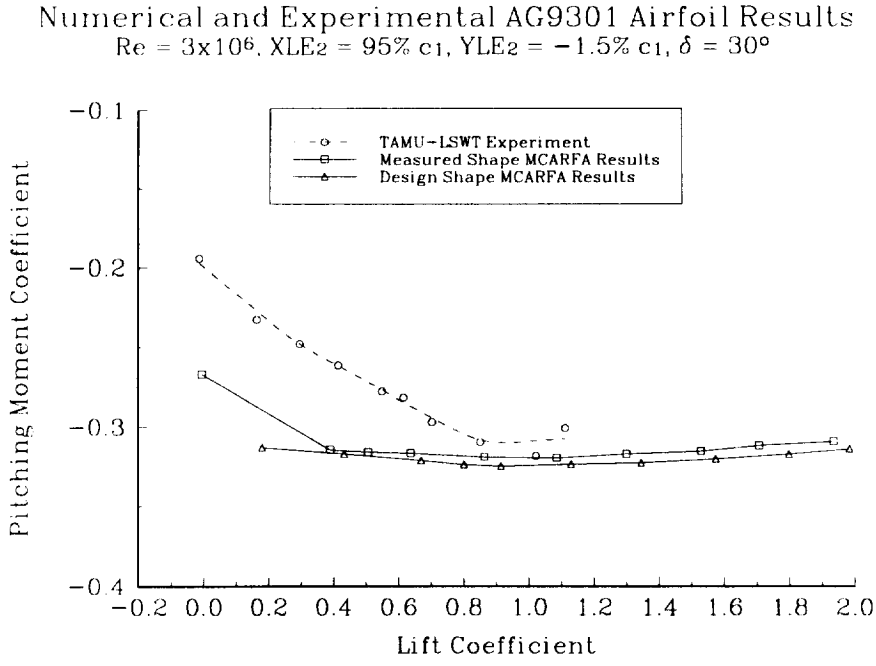

Fig. 155 AG9301 experimental moment coefficient, δ = 30°, Re = 3x10^6

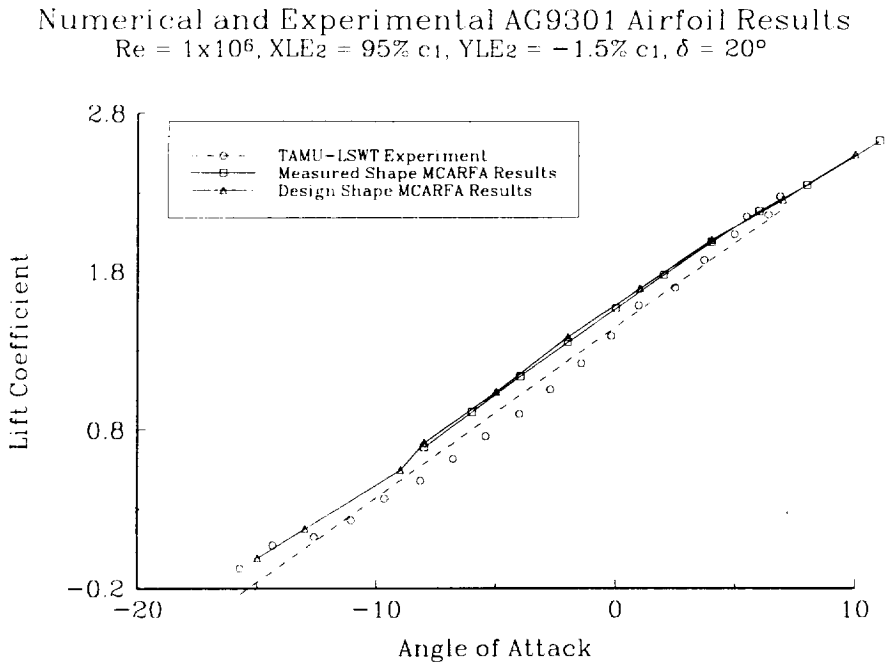

Fig. 156 AG9301 experimental lift coefficient, $\delta = 20°$, Re = 1x10^6

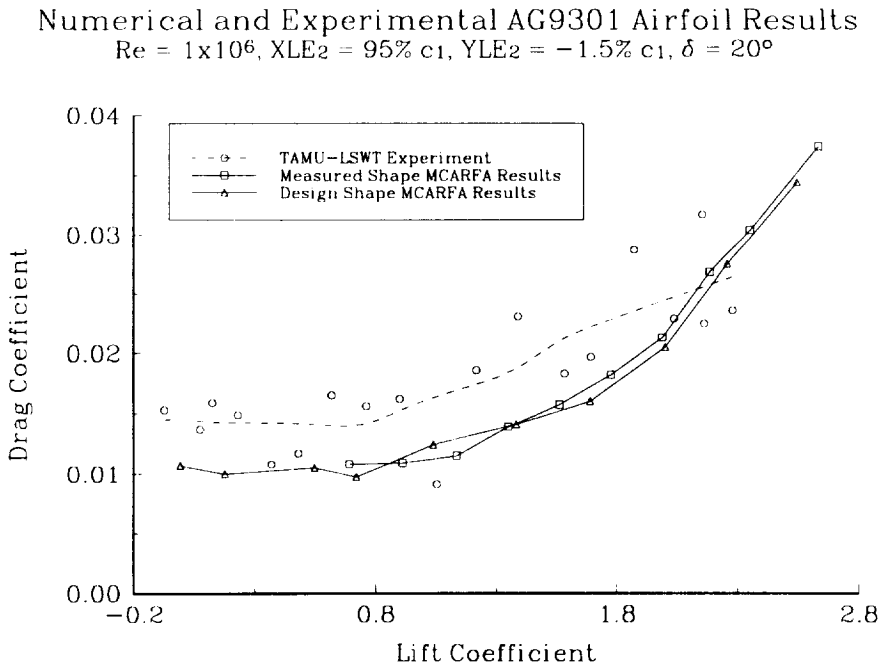

Fig. 157 AG9301 experimental drag coefficient, $\delta = 20°$, Re = 1x10^6

values were lower than predicted, but again the shape of the curves were very similar (Fig. 158). Moment coefficient values show excellent agreement between the numerical predictions and the experimentally measured data (Fig. 159).

The $2x10^6$ Reynolds number lift coefficient data shows the slope of the experimental lift curve to be more shallow than numerically predicted (Fig. 160). The experimental and numerical α_0 values were very close. Drag coefficient data was again higher experimentally (Fig. 161). The L/D values show reasonably good agreement between the numerical and experimental data (Fig. 162). The moment coefficient data for this Reynolds number case shows the experimental c_m to be lower than the predicted value (Fig. 163).

Results at a Reynolds number of $3x10^6$ follow the same trends as the $2x10^6$ case. The experimental lift curve slope is more shallow than predicted but the α_0 values agree well (Fig. 164). Experimental drag coefficient data is again higher than predicted (Fig. 165). The experimentally measured L/D values again agree quite well with the predicted values (Fig. 166). The moment coefficient was measured to be lower than numerically predicted (Fig. 167).

Some evidence still suggests true two-dimensional flow is not being obtained at all lift values even with the endplates installed on the model. The slope of the experimental lift curve changes fairly significantly with different Reynolds numbers. Figure 168 presents the experimental lift curve results for the 20° deflection case of the AG9301 airfoil at Reynolds numbers from $1x10^6$ through $3x10^6$. The lower slope at the higher Reynolds numbers is evidence that the airfoil model is not fully two dimensional. Drag coefficient values did not show a significant change with Reynolds number (Fig. 169). The experimental L/D values were generally the same at different Reynolds number, but the $3x10^6$ case did show a somewhat higher L/D curve

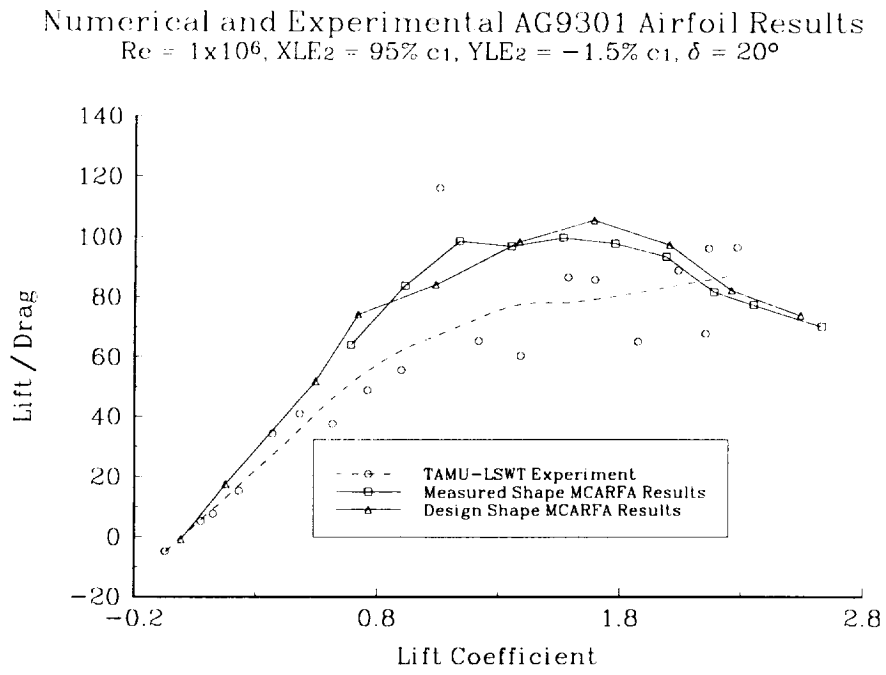

Fig. 158 AG9301 experimental L/D ratio, δ = 20°, Re = 1x10^6

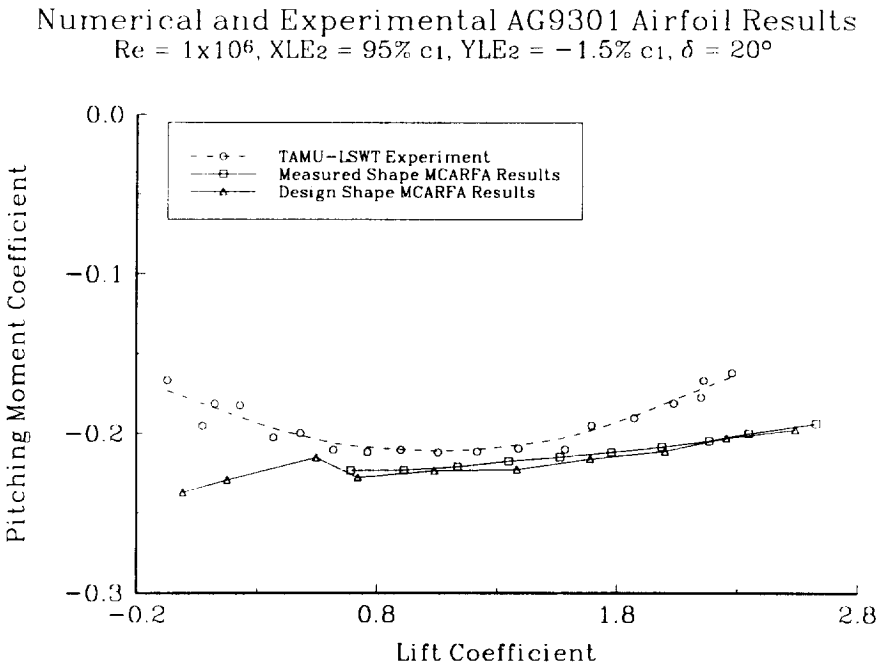

Fig. 159 AG9301 experimental moment coefficient, δ = 20°, Re = 1x10^6

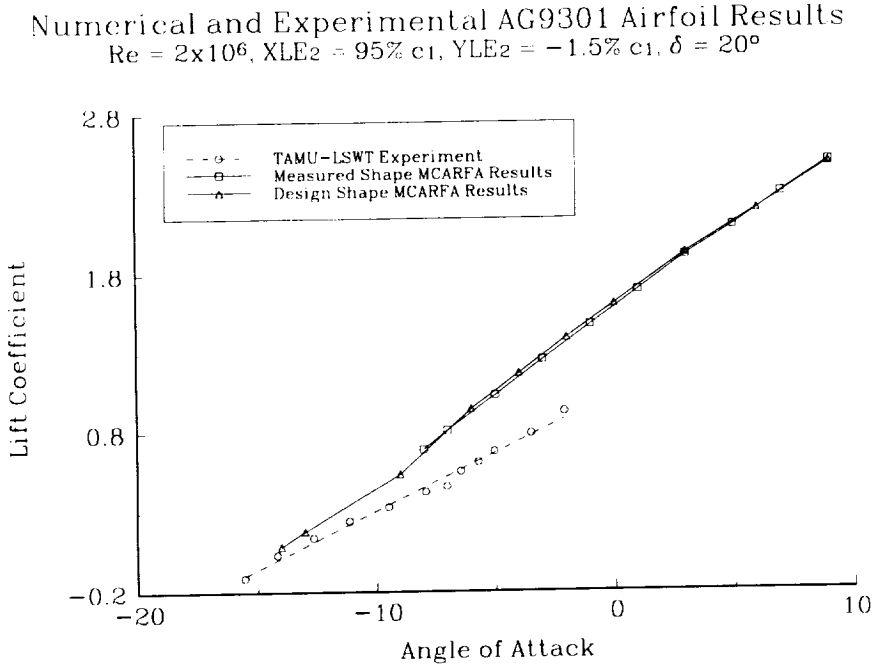

Fig. 160 AG9301 experimental lift coefficient, $\delta = 20°$, Re = 2x10^6

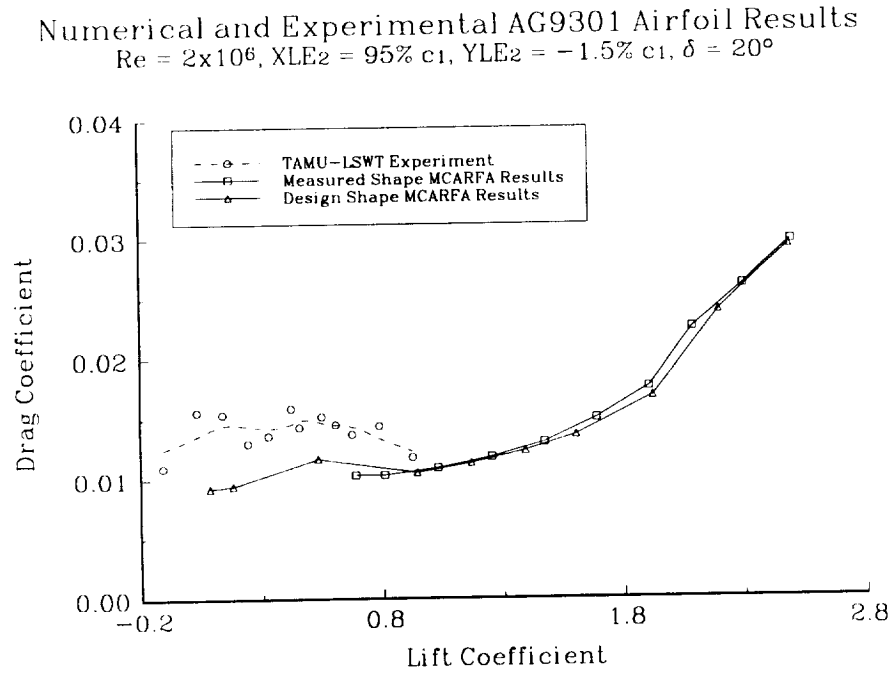

Fig. 161 AG9301 experimental drag coefficient, $\delta = 20°$, Re = 2x10^6

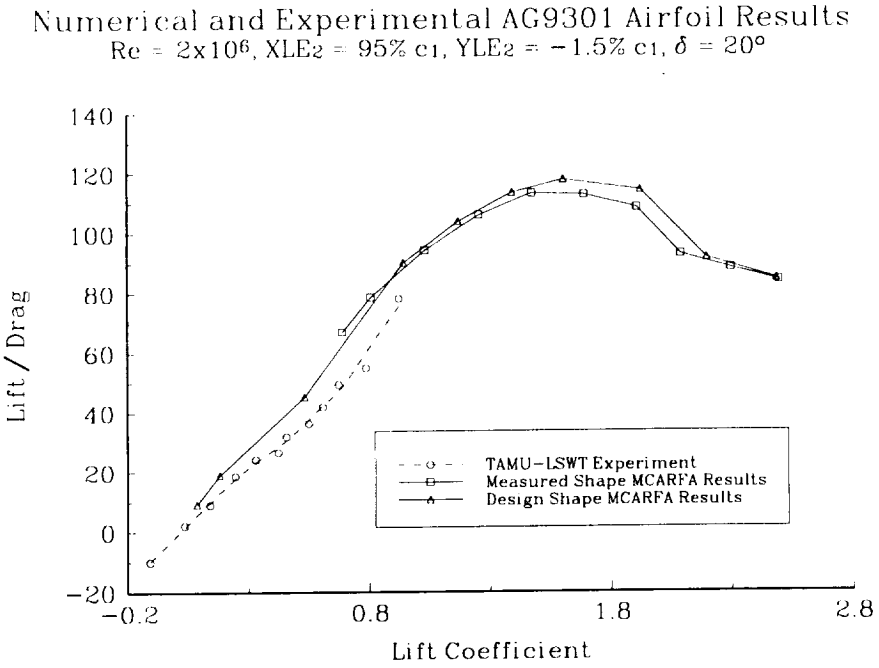

Fig. 162 AG9301 experimental L/D ratio, $\delta = 20°$, $Re = 2x10^6$

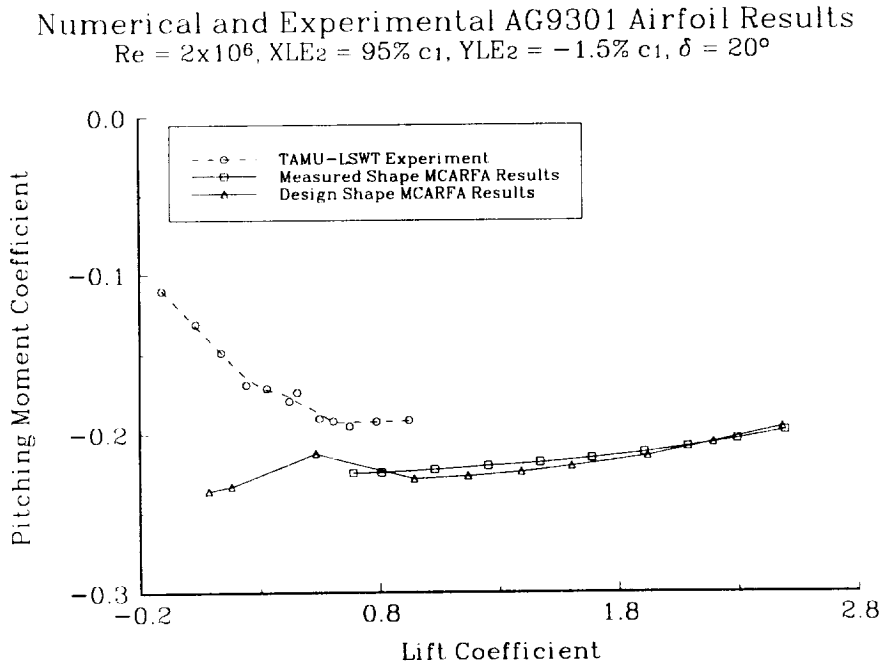

Fig. 163 AG9301 experimental moment coefficient, $\delta = 20°$, $Re = 2x10^6$

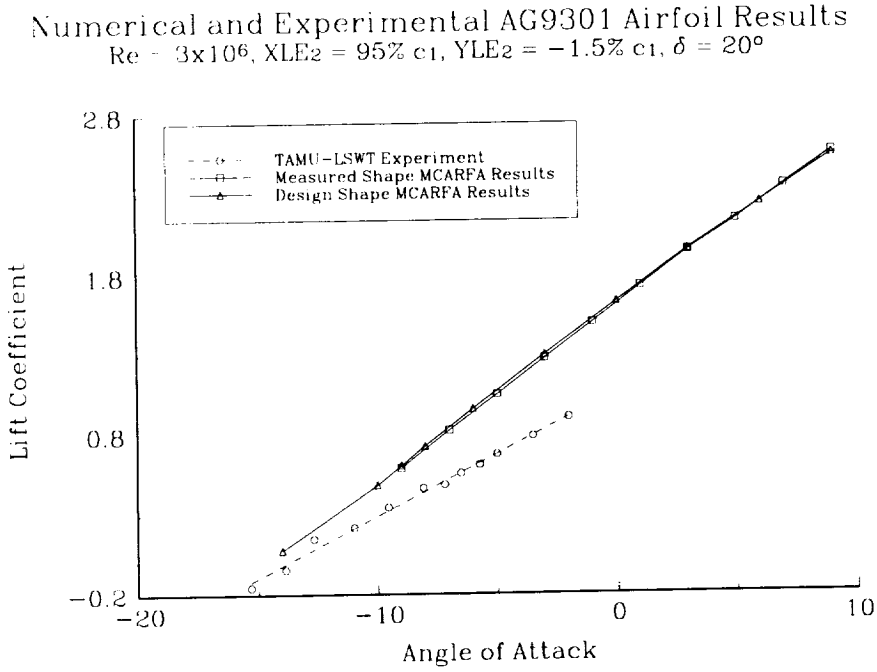

Fig. 164 AG9301 experimental lift coefficient, δ = 20°, Re = 3x10^6

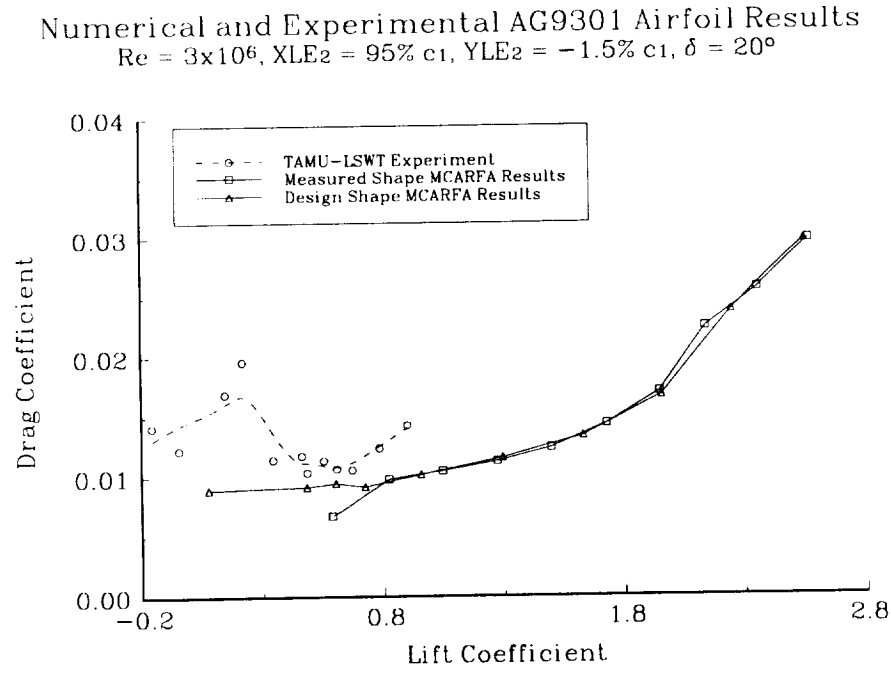

Fig. 165 AG9301 experimental drag coefficient, δ = 20°, Re = 3x10^6

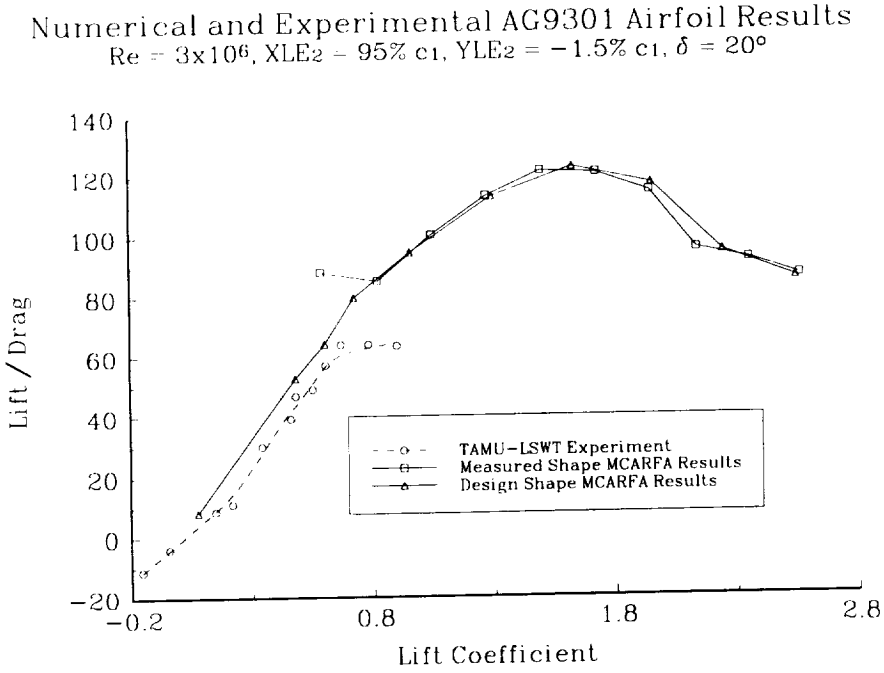

Fig. 166 AG9301 experimental L/D ratio, $\delta = 20°$, $Re = 3x10^6$

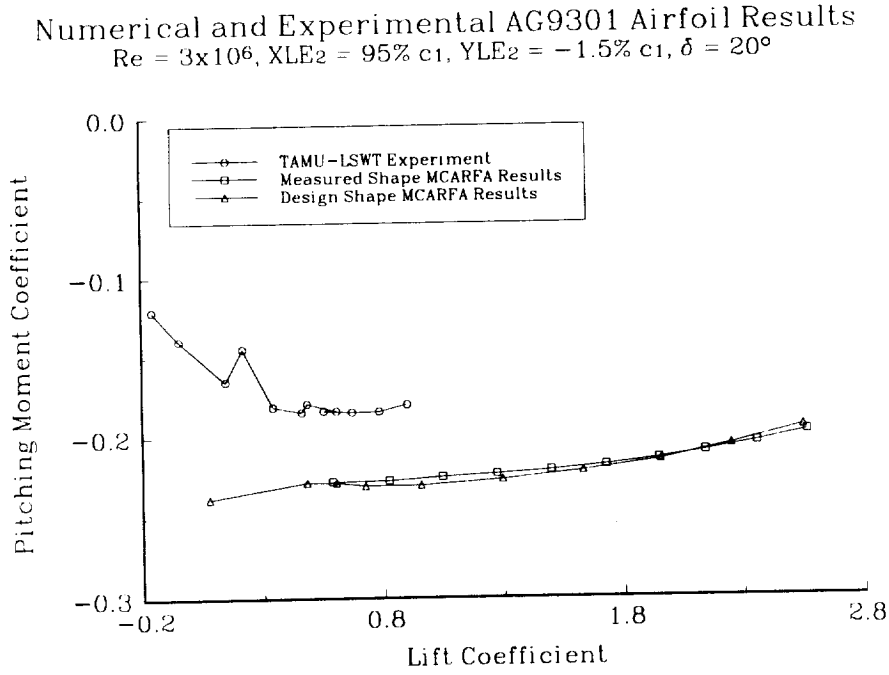

Fig. 167 AG9301 experimental moment coefficient, $\delta = 20°$, $Re = 3x10^6$

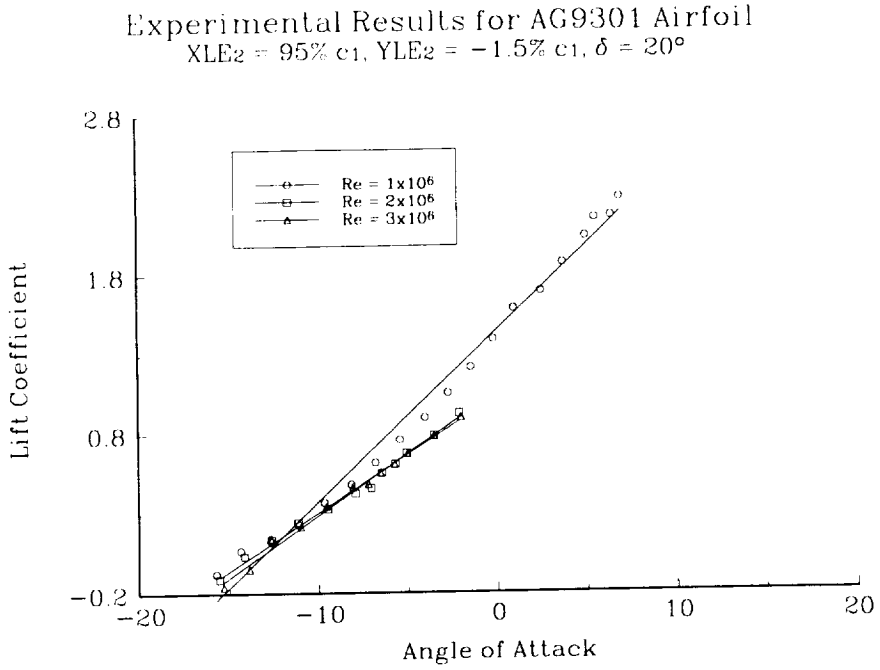

Fig. 168 Reynolds number effect on experimental lift coefficient

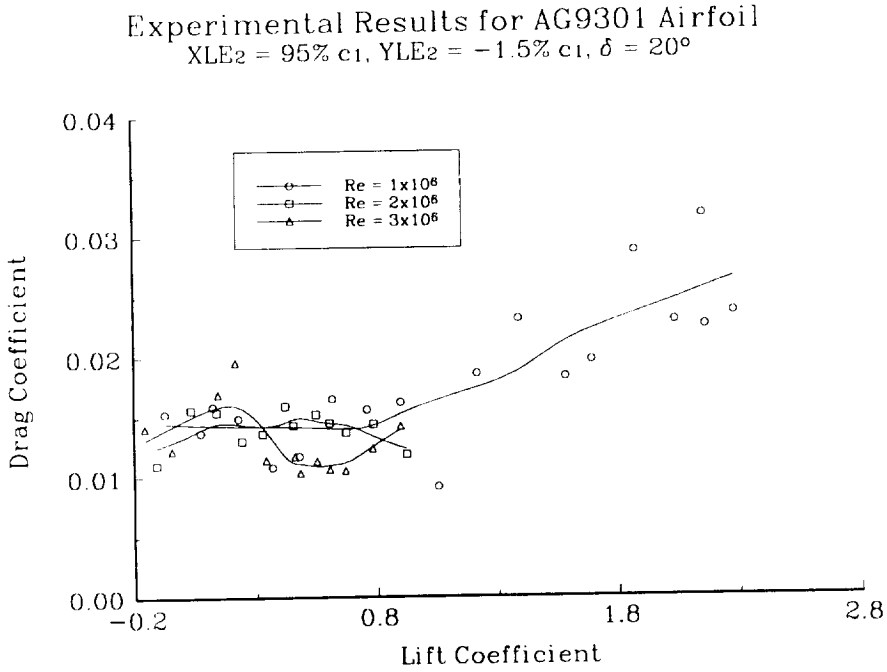

Fig. 169 Reynolds number effect on experimental drag coefficient

(Fig. 170). The $2x10^6$ and $3x10^6$ Reynolds number case c_m values were lower than the $1x10^6$ Reynolds number case (Fig. 171).

Based on the above data, the AG9301 case with the secondary element deflected 20° from the primary element was experimentally verified by fair agreement at all conditions. The 30° deflection case could not be experimentally verified. Neither the numerically predicted c_{lmax} or the L/D values for this case were observed in the wind tunnel data.

Uncertainty Analysis and Data Repeatability

An uncertainty analysis as described by Kline and McClintock[55] was performed on the wind tunnel data to determine the uncertainty in the force coefficients due to instrumentation and measurement accuracy. Figures 172 through 174 present the c_l, c_d, and L/D results for the AG9301 airfoil 20° deflection case at a Reynolds number of $1x10^6$, respectively. It is clear that the uncertainty in the results due to the instrumentation and measurement accuracy is not as large as the apparent scatter in the data.

A test of the repeatability of the wind tunnel data was also performed on the AG9301 airfoil deflected 30° at a Reynolds number of $3x10^6$. This repeatability check was performed during the initial set of wind tunnel runs before improvements were made to the model. Lift coefficient results show generally good agreement, but definite differences do exist between the two sets of measured data at the same test conditions (Fig. 175). The drag coefficient results show a significant difference between the two sets of experimental data (Fig. 176). Moment coefficient repeatability results show the same trends in both of the experimental cases (Fig. 177), but again definite differences do exist. The L/D ratio results, as the drag coefficient, show significant differences between the two sets of experimental data (Fig. 178). The differences between the two

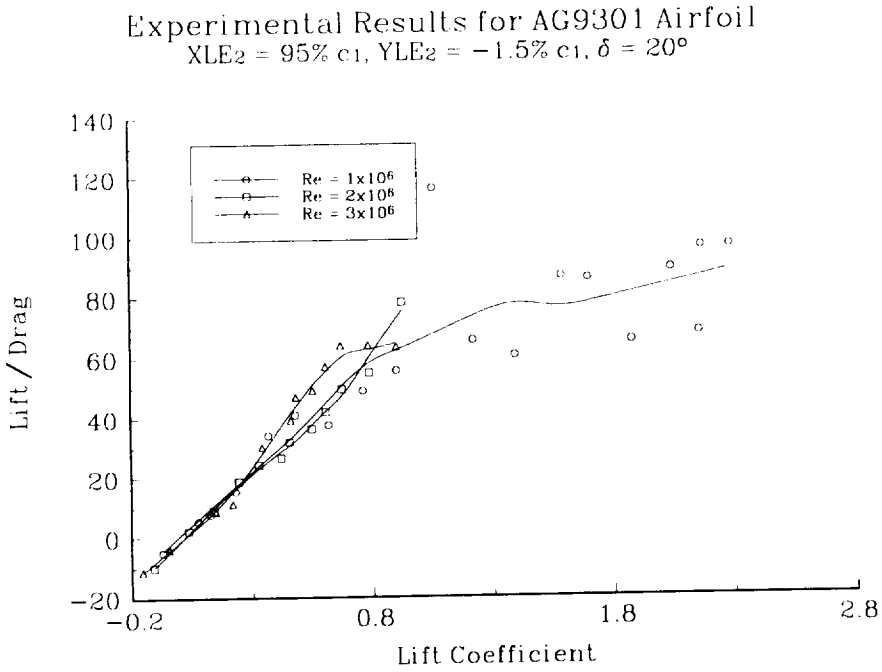

Fig. 170 Reynolds number effect on experimental L/D ratio

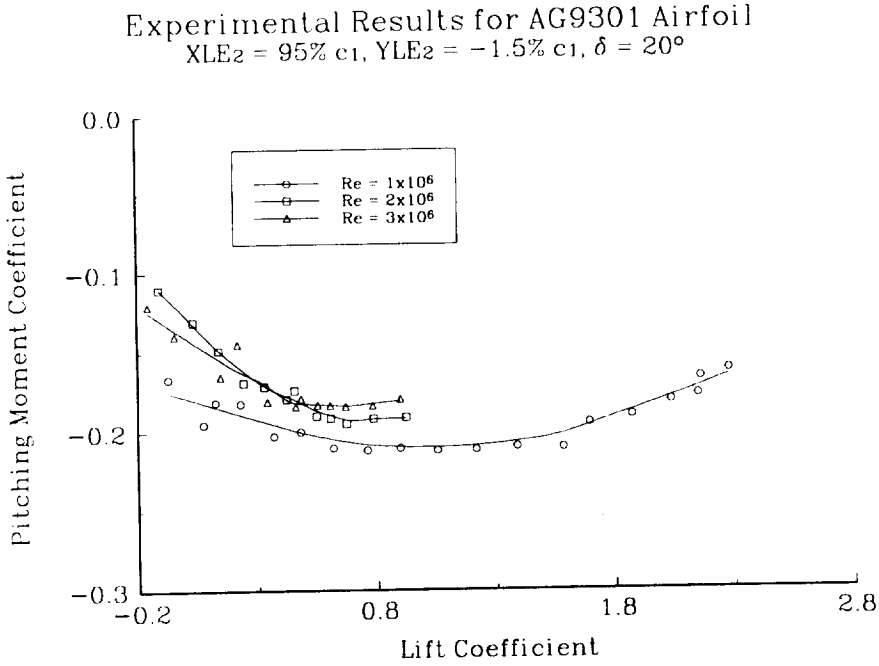

Fig. 171 Reynolds number effect on experimental moment coefficient

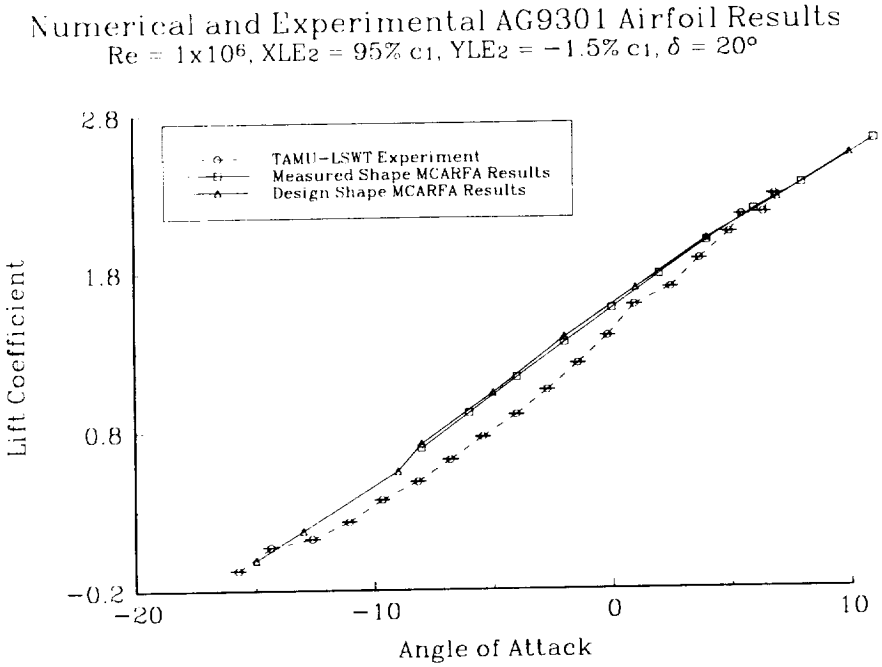

Fig. 172 Uncertainty analysis of experimental lift coefficient

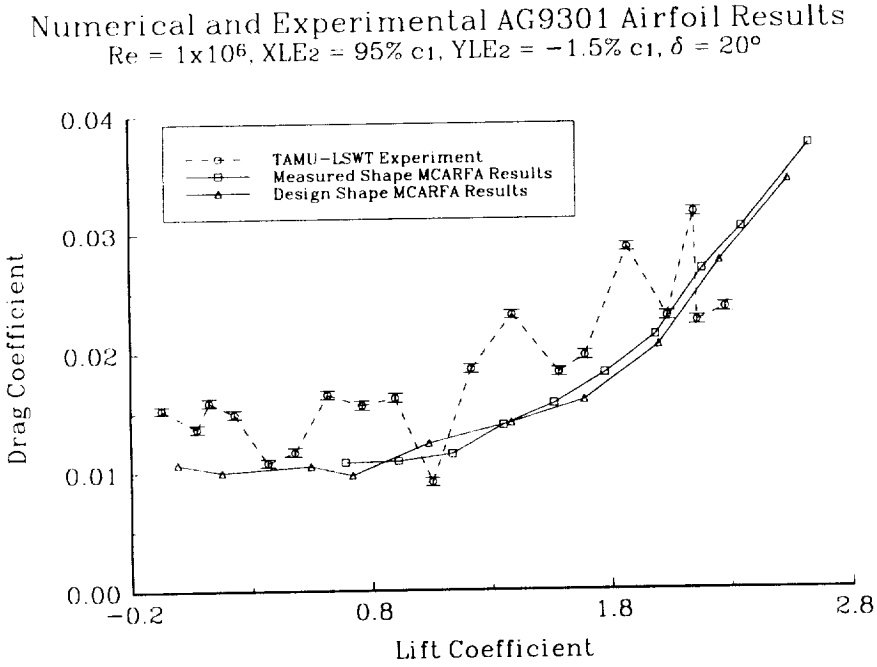

Fig. 173 Uncertainty analysis of experimental drag coefficient

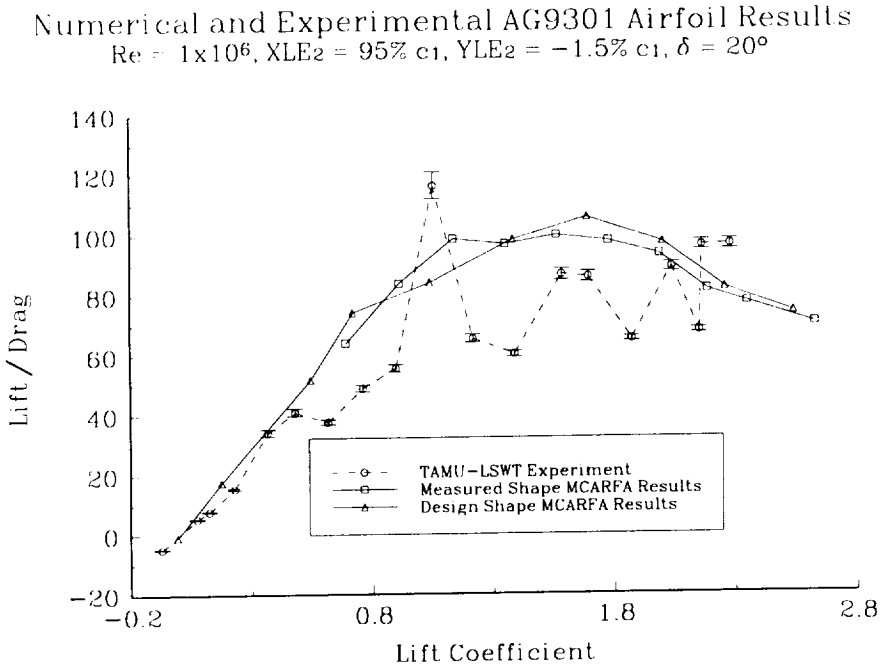

Fig. 174 Uncertainty analysis of experimental L/D ratio

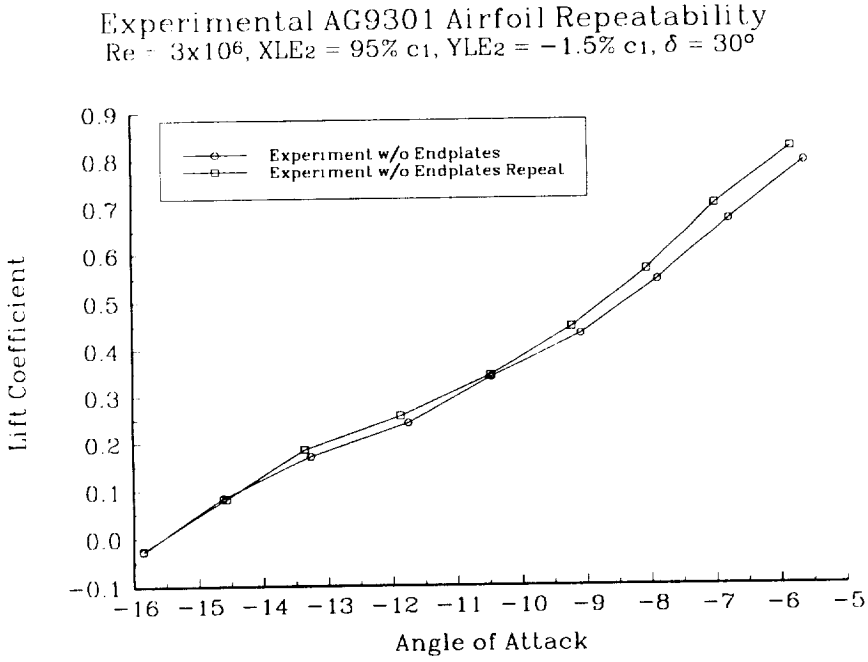

Fig. 175 Repeatability of experimental lift coefficient

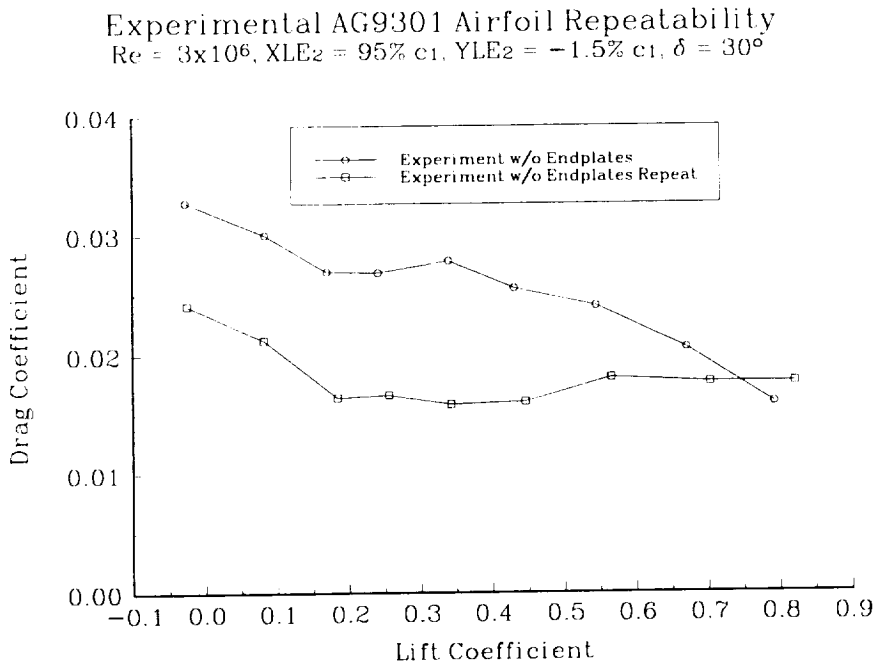

Fig. 176 Repeatability of experimental drag coefficient

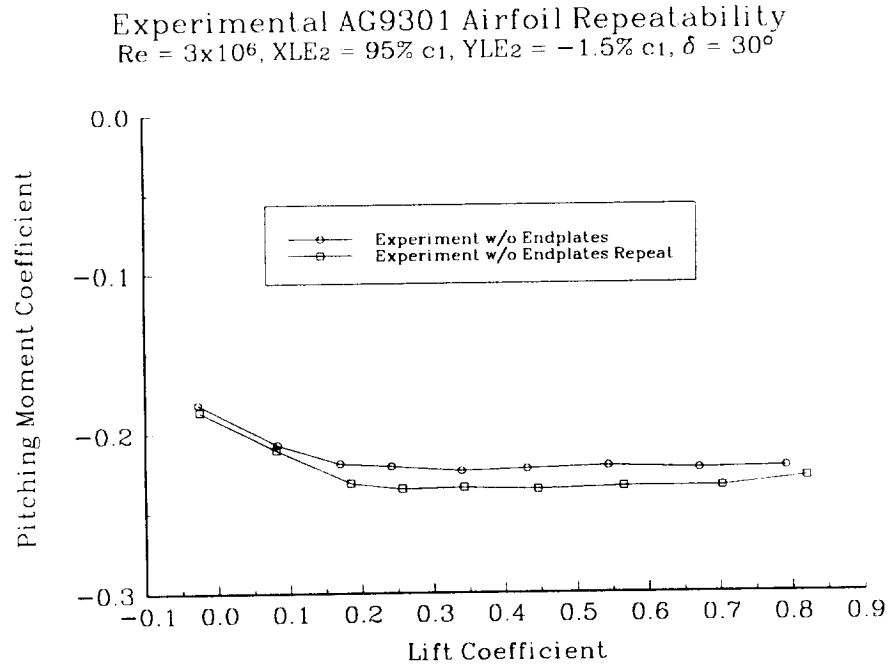

Fig. 177 Repeatability of experimental moment coefficient

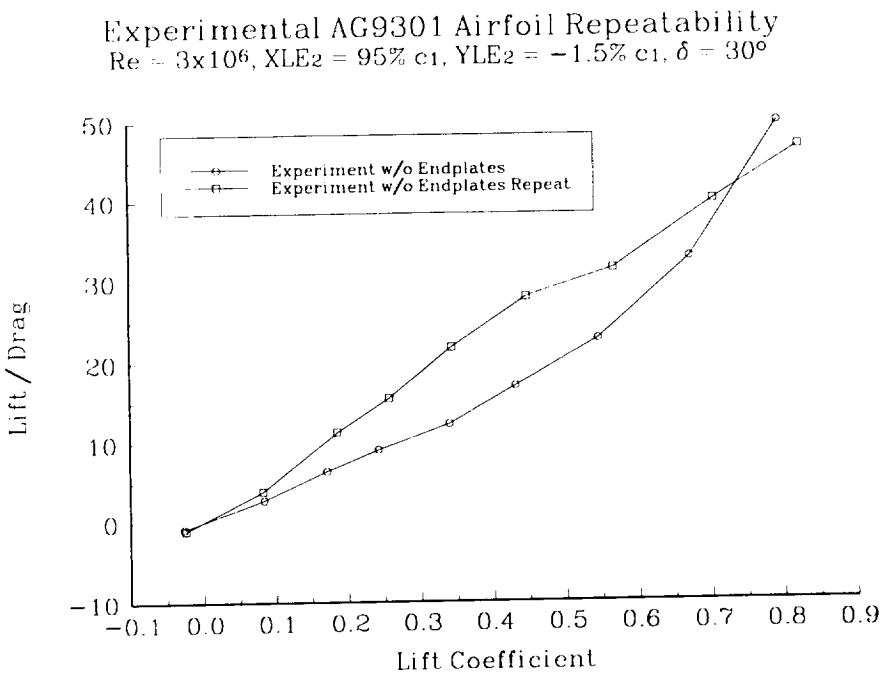

Fig. 178 Repeatability of experimental L/D ratio

sets of experimental data for all forces and moments are larger than the uncertainty analysis predicts. A likely explanation for the differences is the way the Scanivalve measurement system acquires data. The data is acquired sequentially over a total time of approximately 4 minutes for each data point. Some differences in the freestream conditions can take place during this time, but the freestream total and static pressure readings used in data reduction are only acquired during a discrete time period during the entire 4 minutes.

Spanwise Drag Variation

Some concern existed over how the experimentally measured drag coefficient would vary at different span stations. This variation could be due to differences in surface finish quality or profile shape. The additional brackets added to reduce the secondary element deflections could also have had an effect on the drag coefficient

value. The drag coefficient was normally measured in the center of the span of the wind tunnel model, but to explore the variation of the c_d with span station, drag measurements were taken in five centimeter increments from 5 cm below the center span to 20 cm above the center span location. The additional secondary element bracket was located 18 cm from the center span station. Results for the AG9301 airfoil with a secondary element deflection of 20° at a Reynolds number of $3x10^6$ and at a lift coefficient of approximately 0.54 show little variation in the experimental c_d with span station at locations away from the secondary element brackets (Fig. 179). An increase in the measured c_d is observed near the secondary element bracket, but this is to be expected.

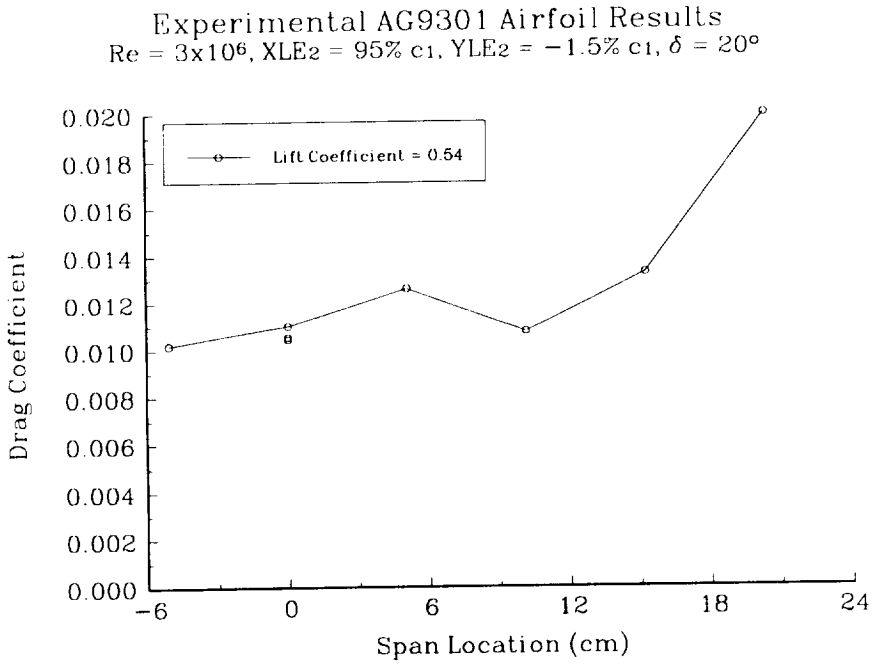

Fig. 179 AG9301 spanwise drag coefficient, δ = 20°, Re = $3x10^6$

CONCLUSIONS

The concept of a two element fixed geometry laminar flow airfoil for the cruise case in an incompressible flight regime has been numerically and experimentally verified. Results show a generic sailplane wing based on the final configuration AG9301 airfoil will have a 11.75% reduction in total wing drag when compared with a current general aviation airfoil. The new two element airfoil was numerically designed using the NASA Langley Multi Component Airfoil Analysis Code (MCARFA) and experimentally verified in the Texas A&M University Low Speed Wind Tunnel.

Referring back to Table 4, numerical results show the optimum configuration to include the secondary element deflected 30°. With this 30° deflection, the AG9301 airfoil has a lift to drag ratio at cruise of 72.67. This is over 19% higher than the NASA NLF(1)-0416 airfoil upon with the AG9301 was based. The maximum lift coefficient for this case was calculated to be nearly 60% higher than the NLF(1)-0416 airfoil. Overall a 28% reduction in wing drag for a generic sailplane was calculated based on this new case when compared with the NLF(1)-0416 airfoil. At the cruise lift coefficient of 0.63 and a Reynolds number of $3x10^6$, the new airfoil has 80% laminar flow on the upper surface and 25% laminar flow on the lower surface.

While the 30° deflection case numerically showed better performance characteristics, the secondary element deflected 20° also showed good results. The maximum lift coefficient was calculated to be 44% higher than the NLF(1)-0416 airfoil and the cruise L/D ratio was slightly higher for the AG9301 airfoil. Overall a 11.75% reduction in overall wing drag for a generic sailplane was calculated based on the 20° deflection case when compared to the NLF(1)-0416 airfoil. The moment coefficient for the 20° deflection case was approximately two thirds that of the 30° deflection case.

The 20° deflection case has 70% laminar flow on the upper surface and 35% laminar flow on the lower surface and the cruise lift coefficient of 0.57 and a Reynolds number of $3x10^6$.

Experimental results show the 20° deflection case values agree fairly well with the numerically calculated answers. The measured drag coefficient was higher than numerically predicted, but the shape of the curve agreed well. The numerically calculated values at the 30° deflection case could not be experimentally verified. Significantly higher drag and lower lift were measured than numerically predicted.

Based on the experimental verification, the lower moment coefficient, and the somewhat more conservative design, the final configuration for the AG9301 airfoil uses the 20° secondary element deflection.

The final configuration of the AG9301 airfoil is made up of two distinct components; the primary element is a modified profile named the AG9301A based on the NASA NLF(1)-0416 airfoil and the secondary element is a NACA 4412 airfoil. The primary component chord is 75% of the total chord and the secondary element chord is 25% of the total. The leading edge of the secondary element is located 95% of the primary chord length behind and 1.5% of the primary chord length below the leading edge of the primary element. The secondary element is deflected down 20° with respect to the primary element.

The most likely location for future improvement to the two element cruise airfoil concept is the lower surface of the primary element. Results show slightly less laminar flow on the lower surface of the AG9301 airfoil than on the original NASA NLF(1)-0416. This is largely due to the negative angle of attack of the primary element at the cruise case. Further design, without decreasing the c_{lmax} value, of the lower surface should increase the cruise performance.

Another possibility for future study would be the variation of the secondary element deflection angle during flight. The current study explored the concept of a fixed geometry airfoil, but the increased complexity of a variable geometry configuration is often determined to be of net value. This possibility would not be a significant change for the AG9301 airfoil because of the pre-existing structure to support the distinct secondary element.

REFERENCES

[1]Anderson, J.D., Jr., *Introduction to Flight*, Second Edition, McGraw-Hill Book Company, New York, 1985.

[2]Schweizer, P.A., "An International One-Design Class and the Olympics," *Technical Soaring*, Vol XIII, No. 2, April 1989, pp. 42-44.

[3]Abbott, I.A., von Doenhoff, A.E. and Stivers, L.S., "Summary of Airfoil Data," NACA Report No. 824, 1945.

[4]Abbott, I.A. and von Doenhoff, A.E., *Theory of Wing Sections*, Dover Publications, New York, 1959.

[5]Duddy, R.R., "High-Lift Devices and Their Uses," *Journal of Royal Aeronautical Society*, Vol. 53, 1949, p. 859.

[6]Gad-el-Hak, M., "Control of Low-Speed Airfoil Aerodynamics," *AIAA Journal*, Vol. 28, No. 9, 1990, pp. 1537-1552.

[7]Liebeck, R.H., "A Class of Airfoils Designed for High Lift in Incompressible Flow," *Journal of Aircraft*, Vol. 10, No. 10, 1973, pp. 610-617.

[8]Liebeck, R.H., "Design of Subsonic Airfoils for High Lift," *Journal of Aircraft*, Vol. 15, No. 9, 1978, pp. 547-561.

[9]McGhee, R.J., Viken, J.K., Pfenninger, W., Beasley, W.D. and Harvey, W.D., "Experimental Results for a Flapped Natural-Laminar-Flow Airfoil with High Lift/Drag Ratio," NASA TM-85788, 1984.

[10]Morgan, H.L., "High-Lift Flaps for Natural Laminar Flow Airfoils," *Laminar Flow Aircraft Certification*, NASA CP-2413, 1985.

[11]Murri, D.G., McGhee, R.J., Jordan, F.L., Davis, P.J., and Viken, J.K., "Wind Tunnel Results of the Low-Speed NLF(1)-0414F Airfoil," *Research in Natural Laminar Flow and Laminar-Flow Control*, NASA CP-2487 Part 3, 1987.

[12]Ormsbee, A.I. and Chen, A.W., "Multiple Element Airfoils Optimized for Maximum Lift Coefficient," *AIAA Journal*, Vol. 10, Dec. 1972, pp. 1620-1624.

[13]Page, F.H., "The Handley Page Wing," *The Aeronautical Journal*, June 1921, pp. 263-289.

[14]Somers, D.M., "Design and Experimental Results for a Flapped Natural-Laminar-Flow Airfoil for General Aviation Applications," NASA TP-1865, 1981.

[15]Spitzmiller, T., "Flaps and Their Effects," *Air Progress*, Vol. 54, May 1992, pp. 34-36.

[16]Viken, J.K., Viken, S.A., Pfenninger, W., Morgan, H.L., and Campbell, R.L., "Design of the Low-Speed NLF(1)-0414F and the High-Speed HSNLF(1)-0213 Airfoils with High-Lift Systems," *Research in Natural Laminar Flow and Laminar-Flow Control*, NASA CP-2487 Part 3, 1987.

[17]Smith, A.M.O., "High-Lift Aerodynamics," *Journal of Aircraft*, Vol. 12, No. 6, 1975, pp. 501-530.

[18]Bauer, A.B., "The Laminar Airfoil Problem," *Eighth Annual Symposium of the National Free-Flight Society*, 1975, pp. 40-45.

[19]Stevens, W.A., Goradia, S.H., and Braden, J.A., "Mathematical Model for Two-Dimensional Multi-Component Airfoils in Viscous Flow," NASA CR-1843, 1971.

[20]Stevens, W.A., Goradia, S.H., Braden, J.A. and Morgan, H.L., "Mathematical Model for Two-Dimensional Multi-Component Airfoils in Viscous Flow," AIAA Paper 72-2, San Diego, CA, Jan. 1972.

[21]Brune, G.W. and Manke, J.W., "An Improved Version of the NASA-Lockheed Multielement Airfoil Analysis Computer Program," NASA CR-145323, 1978.

[22]Brune, G.W. and Manke, J.W., "A Critical Evaluation of the Predictions of the NASA-Lockheed Multielement Airfoil Computer Program," NASA CR-145322, 1978.

[23]Morgan, H.L., "A Computer Program for the Analysis of Multielement Airfoils in Two-Dimensional Subsonic, Viscous Flow," *Aerodynamic Analyses Requiring Advanced Computers*, NASA SP-347 Part II, 1975, pp. 713-747.

[24]Smetana, F.O., Summey, D.C., Smith, N.S. and Carden, R.K., "Light Aircraft Lift, Drag, and Moment Prediction - A Review and Analysis," NASA CR-2523, May 1975.

[25]Allison, D.O. and Waggoner, E.G., "Prediction of Effects of Wing Contour Modifications on Low-Speed Maximum Lift and Transonic Performance for the EA-6B Aircraft," NASA TP-3046, 1990.

[26]Oellers, H.J., "Incompressible Potential Flow in a Plane Cascade Stage," NASA TT F-13,982, 1971.

[27]Goradia, S.H., *Confluent Boundary Layer Flow Development With Arbitrary Pressure Distribution*, Ph. D. Thesis, Georgia Institute of Technology, Atlanta, GA, 1971.

[28]Cohen, C.B. and Reshotko, E., "The Compressible Laminar Boundary Layer with Heat Transfer and Arbitrary Pressure Gradient," NACA Rep. 1294, 1956.

[29]Schlichting, H., *Boundary-Layer Theory*, McGraw-Hill, New York, 1987.

[30]Truckenbrodt, E. "A Method of Quadrature for Calculation of the Laminar and Turbulent Boundary Layer in Case of Plane and Rotationally Symmetric Flow," NACA TM-1379, 1955.

[31]Nash, J.F. and Hicks, S.G., "An Integral Method Including the Effects of Upstream History on the Turbulent Shear Stress," *Computation of Turbulent Boundary Layers*, AFOSR-IFP-Stanford Conference, August 1968.

[32]Williams, B.R., "An Exact Test Case for the Plane Potential Flow About Two Adjacent Lifting Aerofoils," R&M No. 3717, Aeronautical Research Council, London, 1973.

[33]Platt, R.C. and Abbott, I.H., "Aerodynamic Characteristics of NACA 23012 and 23021 Airfoils with 20-percent-chord External-airfoil Flaps of NACA 23012 Section," NACA Report No. 573, 1936.

[34]Wenzinger, C.J. and Delano, J.B., "Pressure Distribution over an NACA 23012 Airfoil with a Slotted and a Plain Flap," NACA Report No. 633, 1938.

[35]Wenzinger, C.J., "Pressure Distribution over an NACA 23012 Airfoil with an NACA 23012 External-airfoil Flap," NACA Report No. 614, 1938.

[36]Wenzinger, C.J. and Harris, T.A., "Wind-tunnel Investigation of an NACA 23012 Airfoil with Various Arrangements of Slotted Flaps," NACA Report No. 664, 1939.

[37]Eppler, R., *Airfoil Program System User's Guide*, Universität Stuttgart, Stuttgart, Germany, March 27, 1991.

[38]Eppler, R., *Airfoil Design and Data*, Springer-Verlag, Berlin, 1990.

[39]Eppler, R. and Somers, D.M., "A Computer Program for the Design and Analysis of Low-Speed Airfoils," NASA TM-80210, 1980.

[40]Eppler, R. and Somers, D.M., "Supplement To: A Computer Program for the Design and Analysis of Low-Speed Airfoils," NASA TM-81862, 1980.

[41]Nicks, O.W., Steen, G.G., Heffner, M. and Bauer, D., "Wind Tunnel Investigation and Analysis of the SM701 Airfoil," Technical Soaring, Vol. XVI, No. 4, Presented at the XXII OSTIV Congress, Uvalde, Texas, 1991, pp. 109-115.

[42]Reed, R.C., "Wortmann FX 79-K-144/17 Airfoil Low Speed Wind Tunnel Test," Report No. TR-9231, Aerospace Engineering Division, Texas Engineering Experiment Station, Texas A&M University System, November 1992.

[43]Carlson, L.A., "Derivation of the Biot-Savart Law," AERO 472 Class Notes, Texas A&M University, 1978.

[44]Eppler, R., "Direct Calculation of Laminar and Turbulent Bled-Off Boundary Layers," NASA TM-75328, 1978.

[45]Somers, D.M., "Design and Experimental Results for a Natural-Laminar-Flow Airfoil for General Aviation Applications," NASA TP-1861, 1981.

[46]Wentz, W.H. and Ostowari, C., "Additional Flow Field Studies of the GA(W)-1 Airfoil with 30-Percent Chord Fowler Flap Including Slot-Gap Variations and Cove Shape Modifications," NASA CR-3687, 1983.

[47]Somers, D.M. and Maughmer, M.D., "The SM701 Airfoil: An Airfoil for World Class Sailplanes," Presented at the XXIII OSTIV Congress, Uvalde, Texas, August 1991.

[48]Johnson, R.H., "Flight Testing/Performance Improvements Through Wing Profile Correction," *Technical Soaring*, Vol. XIII, No. 3, pp. 84-89.

[49]Roskam, J., *Airplane Design Part V: Component Weight Estimation*, Roskam Aviation and Engineering Company, Ottawa, Kansas, 1985.

[50]"Low Speed Wind Tunnel Facility Handbook," Aerospace Engineering Division, Texas Engineering Experiment Station, Texas A&M University System, 1985.

[51]Haffermalz, D.S. and Steen, G.G., "Freestream Turbulence Intensity Measurements in the Texas A&M University Low Speed Wind Tunnel," Report No. TR-9211, Aerospace Engineering Division, Texas Engineering Experiment Station, Texas A&M University System, July 1992.

[52]Rae, W.H. and Pope, A., *Low-Speed Wind Tunnel Testing*, Second Edition, John Wiley and Sons, New York, 1984.

[53]Anderson, J.D., Jr., *Fundamentals of Aerodynamics*, Second Edition, McGraw-Hill, Inc., New York, 1991, pp. 70-71.

[54]Morgan, H.L., Jr., "Computer Programs for Smoothing and Scaling Airfoil Coordinates," NASA TM-84666, 1983.

[55]Kline, S.J. and McClintock, F.A., "Describing Uncertainties in Single-Sample Experiments," *Mechanical Engineering*, Vol. 25, No. 1, Jan. 1953.

APPENDIX A

CASE LIST

Case	Primary Airfoil	Primary Hinge	Primary Size	Second Airfoil	Second Hinge	Second Size	Delta Flap	Freestream Alpha	RN
1	3717 A	0,0	1	3717 A	0,0	1	30	0, 10	0.5
2	3717 B	0,0	1	3717 B	0,0	1	10	0, 10	0.5
3	63,4-420	.824, -.187	2	63,4-420	.824, -.187	0.5	25	-10 to 8, del = 2	6
4	63,4-420	.824, -.187	2	63,4-420	.824, -.187	0.5	25	-10 to 8, del = 2	3
5	63,4-420	.824, -.187	2	63,4-420	.824, -.187	0.5	25	-10 to 8, del = 2	1
6	23012	1.032, -.054	0.8333	23012	.25, -.10	0.1667	20	-8 to 8, del = 2	1.05
7	23012	1.032, -.054	0.8333	23012	.25, -.10	0.1667	20	-6 to 8, del = 2	3
8	(1)-0416		2					-4 to 12, del = 2	3
9	(1)-0416	.98, -.03	1.25	12	0, 0	0.4167	20	-10 to 8, del = 2	3
10	(1)-0416	.98, -.03	1.25	2412	0, 0	0.4167	20	-10 to 8, del = 2	3
11	(1)-0416	.98, -.03	1.25	4412	0, 0	0.4167	20	-10 to 8, del = 2	3
12	(1)-0416	.92, -.03	1.25	4412	0, 0	0.4167	20	-10 to 8, del = 2	3
13	(1)-0416	.93, -.03	1.25	4412	0, 0	0.4167	20	-10 to 8, del = 2	3
14	(1)-0416	.94, -.03	1.25	4412	0, 0	0.4167	20	-10 to 8, del = 2	3
15	(1)-0416	.95, -.03	1.25	4412	0, 0	0.4167	20	-10 to 8, del = 2	3
16	(1)-0416	.96, -.03	1.25	4412	0, 0	0.4167	20	-10 to 8, del = 2	3
17	(1)-0416	1.00, -.03	1.25	4412	0, 0	0.4167	20	-10 to 8, del = 2	3
18	(1)-0416	1.02, -.03	1.25	4412	0, 0	0.4167	20	-10 to 8, del = 2	3
19	(1)-0416	.93, -.02	1.25	4412	0, 0	0.4167	20	-10 to 8, del = 2	3
20	(1)-0416	.94, -.02	1.25	4412	0, 0	0.4167	20	-10 to 8, del = 2	3
21	(1)-0416	.95, -.02	1.25	4412	0, 0	0.4167	20	-10 to 8, del = 2	3
22	(1)-0416	.96, -.02	1.25	4412	0, 0	0.4167	20	-10 to 8, del = 2	3
23	(1)-0416	.98, -.02	1.25	4412	0, 0	0.4167	20	-8 to 8, del = 2	3
24	(1)-0416	.92, -.02	1.25	4412	0, 0	0.4167	20	-10 to 8, del = 2	3
25	(1)-0416	.98, -.03	1.25	23012	0, 0	0.4167	20	-8 to 8, del = 2	3
26	(1)-0416	.92, -.04	1.25	4412	0, 0	0.4167	20	-10 to 8, del = 2	3
27	(1)-0416	.93, -.04	1.25	4412	0, 0	0.4167	20	-10 to 8, del = 2	3
28	(1)-0416	.94, -.04	1.25	4412	0, 0	0.4167	20	-10 to 8, del = 2	3
29	(1)-0416	.95, -.04	1.25	4412	0, 0	0.4167	20	-10 to 8, del = 2	3
30	(1)-0416	.96, -.04	1.25	4412	0, 0	0.4167	20	-10 to 8, del = 2	3
31	(1)-0416	.98, -.04	1.25	4412	0, 0	0.4167	20	-10 to 8, del = 2	3
32	(1)-0416	1.00, -.04	1.25	4412	0, 0	0.4167	20	-10 to 8, del = 2	3
33	(1)-0416	1.02, -.04	1.25	4412	0, 0	0.4167	20	-10 to 8, del = 2	3
34	(1)-0416	.92, -.015	1.25	4412	0, 0	0.4167	20	-10 to 8, del = 2	3
35	(1)-0416	.93, -.015	1.25	4412	0, 0	0.4167	20	-10 to 8, del = 2	3
36	(1)-0416	.94, -.015	1.25	4412	0, 0	0.4167	20	-10 to 8, del = 2	3
37	(1)-0416	.95, -.015	1.25	4412	0, 0	0.4167	20	-10 to 8, del = 2	3
38	(1)-0416	.96, -.015	1.25	4412	0, 0	0.4167	20	-8 to 8, del = 2	3
39	(1)-0416	.98, -.015	1.25	4412	0, 0	0.4167	20	-6 to 8, del = 2	3
40	12		2					-4 to 14, del = 2	3
41	2412		2					-4 to 14, del = 2	3.1
42	4412		2					-4 to 12, del = 2	3
43	23012		2					-4 to 14, del = 2	3
44	(1)-0416	.92, -.02	1.25	2412	0, 0	0.4167	20	-10 to 8, del = 2	3
45	(1)-0416	.93, -.02	1.25	2412	0, 0	0.4167	20	-10 to 8, del = 2	3
46	(1)-0416	.94, -.02	1.25	2412	0, 0	0.4167	20	-10 to 8, del = 2	3
47	(1)-0416	.95, -.02	1.25	2412	0, 0	0.4167	20	-10 to 8, del = 2	3
48	(1)-0416	.96, -.02	1.25	2412	0, 0	0.4167	20	-10 to 8, del = 2	3

Case	Primary Airfoil	Primary Hinge	Primary Size	Second Airfoil	Second Hinge	Second Size	Delta Flap	Freestream Alpha	RN
49	(1)-0416	.98, -.02	1.25	2412	0, 0	0.4167	20	-10 to 8, del = 2	3
50	(1)-0416	.92, -.02	1.25	4412	0, 0	0.4167	10	-6 to 12, del = 2	3
51	(1)-0416	.93, -.02	1.25	4412	0, 0	0.4167	10	-6 to 12, del = 2	3
52	(1)-0416	.94, -.02	1.25	4412	0, 0	0.4167	10	-6 to 12, del = 2	3
53	(1)-0416	.95, -.02	1.25	4412	0, 0	0.4167	10	-6 to 12, del = 2	3
54	(1)-0416	.92, -.02	1.25	4412	0, 0	0.4167	15	-8 to 10, del = 2	3
55	(1)-0416	.93, -.02	1.25	4412	0, 0	0.4167	15	-8 to 10, del = 2	3
56	(1)-0416	.94, -.02	1.25	4412	0, 0	0.4167	15	-8 to 10, del = 2	3
57	(1)-0416	.95, -.02	1.25	4412	0, 0	0.4167	15	-8 to 10, del = 2	3
58	(1)-0416	.96, -.02	1.25	4412	0, 0	0.4167	15	-8 to 10, del = 2	3
59	(1)-0416	.98, -.02	1.25	4412	0, 0	0.4167	15	-8 to 10, del = 2	3
60	(1)-0416	.92, -.02	1.25	4412	0, 0	0.4167	25	-12 to 6, del = 2	3
61	(1)-0416	.93, -.02	1.25	4412	0, 0	0.4167	25	-12 to 6, del = 2	3
62	(1)-0416	.94, -.02	1.25	4412	0, 0	0.4167	25	-12 to 6, del = 2	3
63	(1)-0416	.95, -.02	1.25	4412	0, 0	0.4167	25	-12 to 6, del = 2	3
64	(1)-0416	.96, -.02	1.25	4412	0, 0	0.4167	25	-12 to 6, del = 2	3
65	(1)-0416	.98, -.02	1.25	4412	0, 0	0.4167	25	-12 to 6, del = 2	3
66	(1)-0416	.92, -.02	1.25	4412	0, 0	0.4167	30	-14 to 4, del = 2	3
67	(1)-0416	.95, -.02	1.25	4412	0, 0	0.4167	30	-14 to 4, del = 2	3
68	(1)-0416	.93, -.02	1.25	4412	0, 0	0.4167	30	-14 to 4, del = 2	3
69	(1)-0416	.94, -.02	1.25	4412	0, 0	0.4167	30	-14 to 4, del = 2	3
70	(1)-0416	.96, -.02	1.25	4412	0, 0	0.4167	30	-14 to 4, del = 2	3
71	(1)-0416	.98, -.02	1.25	4412	0, 0	0.4167	30	-12 to 4, del = 2	3
72	(1)-0416	.96, -.02	1.25	4412	0, 0	0.4167	30	-15 to -6, del = 1	3
73	(1)-0416	.93, -.015	1.25	4412	0, 0	0.4167	30	-14 to 4, del = 2	3
74	(1)-0416	.94, -.015	1.25	4412	0, 0	0.4167	30	-14 to 4, del = 2	3
75	(1)-0416	.95, -.015	1.25	4412	0, 0	0.4167	30	-14 to 4, del = 2	3
76	(1)-0416	.96, -.015	1.25	4412	0, 0	0.4167	30	-14 to 4, del = 2	3
77	(1)-0416	.98, -.015	1.25	4412	0, 0	0.4167	30	-14 to 4, del = 2	3
78	(1)-0416	.93, -.01	1.25	4412	0, 0	0.4167	30	-14 to 4, del = 2	3
79	(1)-0416	.94, -.01	1.25	4412	0, 0	0.4167	30	-14 to 4, del = 2	3
80	(1)-0416	.95, -.01	1.25	4412	0, 0	0.4167	30	-14 to 4, del = 2	3
81	(1)-0416	.96, -.01	1.25	4412	0, 0	0.4167	30	-14 to 4, del = 2	3
82	(1)-0416	.95, -.015	1.25	4412	0, 0	0.4167	30	-18 to -9, del = 1	3
83	(1)-0416	.95, -.015	1.25	4412	0, 0	0.4167	30	-8 to 1, del = 1	3
84	(1)-0416	.95, -.015	1.25	4412	0, 0	0.4167	30	2 to 11, del = 1	3
85	GS01A	.9799,-.008	1.25	4412	.0155,.0031	0.4167	30	-14 to 2, del = 4	3
86	GS02A	.95,-.015	1.25	4412	0, 0	0.4167	30	-14 to 4, del = 2	3
87	GS03A	.95,-.015	1.25	4412	0, 0	0.4167	30	-14 to 4, del = 2	3
88	GS03AU	.95,-.015	1.25	4412	0, 0	0.4167	30	-10 to 4, del = 2	3
89	(1)-0416	.95, -.015	1.25	4412	0, 0	0.4167	30	-14 to 4, del = 2	1
90	(1)-0416		2					-4 to 12, del = 2	1
91	GS02A	.95, -.015	1.25	4412	0, 0	0.4167	30	-18 to -9, del = 1	3
92	GS02A	.95, -.015	1.25	4412	0, 0	0.4167	30	-8 to 1, del = 1	3
93	GS02A	.95, -.015	1.25	4412	0, 0	0.4167	30	2 to 11, del = 1	3
94	GS04A	.95, -.015	1.25	4412	0, 0	0.4167	30	-14 to 4, del = 2	3
95	GS05A	.95, -.015	1.25	4412	0, 0	0.4167	30	-14 to 4, del = 2	3
96	GS06A	.95, -.015	1.25	4412	0, 0	0.4167	30	-14 to 4, del = 2	3

Case	Primary Airfoil	Primary Hinge	Primary Size	Second Airfoil	Second Hinge	Second Size	Delta Flap	Freestream Alpha	RN
97	GS02A	.94, -.015	1.25	4412	0, 0	0.4167	30	-14 to 4, del = 2	3
98	GS02A	.96, -.015	1.25	4412	0, 0	0.4167	30	-14 to 4, del = 2	3
99	GS02A	.94, -.01	1.25	4412	0, 0	0.4167	30	-14 to 4, del = 2	3
100	GS02A	.95, -.01	1.25	4412	0, 0	0.4167	30	-14 to 4, del = 2	3
101	GS02A	.96, -.01	1.25	4412	0, 0	0.4167	30	-14 to 4, del = 2	3
102	GS02A	.94, -.02	1.25	4412	0, 0	0.4167	30	-14 to 4, del = 2	3
103	GS02A	.95, -.02	1.25	4412	0, 0	0.4167	30	-14 to 4, del = 2	3
104	GS02A	.96, -.02	1.25	4412	0, 0	0.4167	30	-14 to 4, del = 2	3
105	GS02A	.95, -.015	1.25	4412	0, 0	0.4167	30	-18 to -9, del = 1	1
106	GS02A	.95, -.015	1.25	4412	0, 0	0.4167	30	-8 to 1, del = 1	1
107	GS02A	.95, -.015	1.25	4412	0, 0	0.4167	30	2 to 11, del = 1	1
108	GS02A	.95, -.015	1.25	4412	0, 0	0.4167	30	-17 to -9, del = 1	0.75
109	GS02A	.95, -.015	1.25	4412	0, 0	0.4167	30	-8 to 1, del = 1	0.75
110	GS02A	.95, -.015	1.25	4412	0, 0	0.4167	30	2 to 11, del = 1	0.75
111	GS02A	.95, -.015	1.25	4412	0, 0	0.4167	30	-18 to -9, del = 1	2
112	GS02A	.95, -.015	1.25	4412	0, 0	0.4167	30	-8 to 1, del = 1	2
113	GS02A	.95, -.015	1.25	4412	0, 0	0.4167	30	2 to 11, del = 1	2
114	SM701		2					-4 to 14, del = 2	3
115	79-K-144		2					-4 to 14, del = 2	3
116	GS02A	.95,-.015	1.25	4412	0, 0	0.4167	20	-8 to 8, del = 2	3
117	AG9301A-ACT		1.4967					-4 to 12, del = 2	0.79
118	AG9301A-ACT		1.4967					-4 to 12, del = 2	2.302
119	AG9301A-ACT	.96,-.02	1.4967	4412-ACT	0, 0	0.4967	30	-17 to -2	3.134
120	AG9301A-ACT	.96,-.015	1.4967	4412-ACT	0, 0	0.4967	30	-17 to -2	3.074
121	AG9301A-ACT	.96,-.01	1.4967	4412-ACT	0, 0	0.4967	30	-17 to -2	3.022
122	AG9301A-ACT	.95,-.02	1.4967	4412-ACT	0, 0	0.4967	30	-12 to -2	2.983
123	AG9301A-ACT	.95,-.015	1.4967	4412-ACT	0, 0	0.4967	30	-17 to -2	2.96
124	AG9301A-ACT	.95,-.01	1.4967	4412-ACT	0, 0	0.4967	30	-16 to -2	2.929
125	AG9301A-ACT	.94,-.02	1.4967	4412-ACT	0, 0	0.4967	30	-17 to -2	2.931
126	AG9301A-ACT	.94,-.015	1.4967	4412-ACT	0, 0	0.4967	30	-17 to -2	2.93
127	AG9301A-ACT	.94,-.01	1.4967	4412-ACT	0, 0	0.4967	30	-14 to -2	2.919
128	AG9301A-ACT	.95,-.015	1.4967	4412-ACT	0, 0	0.4967	20	-9 to 4	3.079
129	AG9301A-ACT	.95,-.015	1.4967	4412-ACT	0, 0	0.4967	30	-15 to 8	0.801
130	AG9301A-ACT	.95,-.015	1.4967	4412-ACT	0, 0	0.4967	30	-16 to 7	1.073
131	AG9301A-ACT	.95,-.015	1.4967	4412-ACT	0, 0	0.4967	30	-17 to 6	2.063
132	AG9301A	.96,-.02	1.5	4412	0, 0	0.5	30	-17 to -2	3
133	AG9301A	.96,-.015	1.5	4412	0, 0	0.5	30	-17 to -2	3
134	AG9301A	.96,-.01	1.5	4412	0, 0	0.5	30	-15 to -2	3
135	AG9301A	.95,-.02	1.5	4412	0, 0	0.5	30	-17 to -2	3
136	AG9301A	.95,-.015	1.5	4412	0, 0	0.5	30	-18 to -2	3
137	AG9301A	.95,-.01	1.5	4412	0, 0	0.5	30	-18 to -2	3
138	AG9301A	.94,-.02	1.5	4412	0, 0	0.5	30	-18 to -2	3
139	AG9301A	.94,-.015	1.5	4412	0, 0	0.5	30	-18 to -2	3
140	AG9301A	.94,-.01	1.5	4412	0, 0	0.5	30	-16 to -2	3
141	AG9301A	.95,-.015	1.5	4412	0, 0	0.5	20	-13 to 2	3
142	AG9301A	.95,-.015	1.5	4412	0, 0	0.5	30	-18 to 8	0.8
143	AG9301A	.95,-.015	1.5	4412	0, 0	0.5	30	-19 to 7	1
144	AG9301A	.95,-.015	1.5	4412	0, 0	0.5	30	-21 to 6	2

Case	Primary Airfoil	Primary Hinge	Primary Size	Second Airfoil	Second Hinge	Second Size	Delta Flap	Freestream Alpha	RN
145	AG9301A		1.5					-4 to 12, del = 2	0.75
146	AG9301A		1.5					-4 to 12, del = 2	2.25
147	AG9301A	.95,-.015	1.5	4412	0, 0	0.5	30	-19 to 6	3
148	AG9301A-ACT	.95,-.015	1.4967	4412-ACT	0, 0	0.4967	30	-17 to 7	2.96
149	AG9301A	.95,-.015	1.5	4412	0, 0	0.5	20	-14 to 11	0.8
150	AG9301A	.95,-.015	1.5	4412	0, 0	0.5	20	-15 to 10	1
151	AG9301A	.95,-.015	1.5	4412	0, 0	0.5	20	-14 to 9	2
152	AG9301A	.95,-.015	1.5	4412	0, 0	0.5	20	-14 to 9	3
153	AG9301A-ACT	.95,-.015	1.4967	4412-ACT	0, 0	0.4967	20	-8 to 11	0.9
154	AG9301A-ACT	.95,-.015	1.4967	4412-ACT	0, 0	0.4967	20	-8 to 9	1.9
155	AG9301A-ACT	.95,-.015	1.4967	4412-ACT	0, 0	0.4967	20	-9 to 9	2.9

VITA

Gregory Glen Steen was born [redacted] Mr. Steen graduated from Helena High School in Helena, Montana in the spring of 1984. Mr. Steen entered Texas A&M University in the fall of 1984 and graduated with his Bachelor of Science in Aerospace Engineering degree in December of 1988. During college, Mr. Steen participated in the University's Cooperative Education program working three work terms at the Texas A&M University Low Speed Wind Tunnel. After graduation, Mr. Steen accepted a position as a Research Specialist at the Low Speed Wind Tunnel. He entered the Master's program in Aerospace Engineering on a part time basis in the fall of 1989.

Mr. Steen is married to the former Kathy Boeckman and has one son. He may be reached through his parents Harvey and Ila Steen at 735 Sixth Avenue in Helena, Montana 59601.